Mesures de la luminosité absolue à l'expérience LHCb

Plamen Hopchev

UNIVERSITÉ DE GRENOBLE

THÈSE

Pour obtenir le grade de

DOCTEUR DE L'UNIVERSITÉ DE GRENOBLE

Spécialité : **Physique Subatomique & Astroparticules**

Arrêté ministérial : 7 août 2006

Présentée par

Plamen Hopchev

Thèse dirigée par **Bolek Pietrzyk**

préparée au sein du
Laboratoire d'Annecy-le-Vieux de Physique des Particules
et de l'**École Doctorale de Physique, Grenoble**

Absolute luminosity measurements at LHCb

Thèse soutenue publiquement le **25 Novembre 2011**,
devant le jury composé de :

Dr. Lucia Di Ciaccio
LAPP (Annecy), Président
Dr. Massimiliano Ferro-Luzzi
CERN, Rapporteur
Dr. Witold Kozanecki
CEA(Saclay), Rapporteur
Dr. Jaap Panman
CERN, Examinateur
Dr. Bolek Pietrzyk
LAPP(Annecy), Directeur de thèse

Abstract

Absolute luminosity measurements are of general interest for colliding-beam experiments at storage rings. These measurements are necessary to determine the absolute cross-sections of reaction processes and are valuable to quantify the performance of the accelerator. LHCb has applied two methods to determine the absolute scale of its luminosity measurements for proton-proton collisions at the LHC running at a centre-of-mass energy of 7 TeV. In addition to the classic "van der Meer" scan method a novel technique has been developed which makes use of direct imaging of the individual beams using both proton-gas and proton-proton interactions. The beam imaging method is made possible by the high resolution of the LHCb vertex detector and the close proximity of the detector to the beams, and allows beam parameters such as positions, angles and widths to be determined. We describe both methods and compare the two results. In addition, we present the techniques used to transport the absolute luminosity measurement to the full data-taking period.

Résumé

Les mesures de la luminosité intégrée pour les expériences auprés de collisionneur ont un intérêt majeur. Ces mesures participent à la détermination des sections efficaces de production des processus étudiés, elles quantifient également les performances de l'accélérateur et des expériences. Deux méthodes ont été utilisées par l'expérience LHCb pour déterminer la mesure de la luminosité absolue enregistrée durant la campagne 2010 de prise de données des collisions proton-proton à une énergie de 7 TeV dans le centre de masse : outre la méthode classique applelée "van der Meer scan" une nouvelle technique est développée permettant une détermination directe des paramètres de chaque faisceau en localisant les interactions faisceau-faisceau et les interactions faisceau-gaz résiduel. Cette méthode n'est possible que grace à la résolution du détecteur de vertex de LHCb et sa proximité avec la zone des faisceaux de protons et les paramètres tels la position, les angles et les largeurs des faisceaux peuvent être mesurés. Les deux methodes sont décrites et leurs résultats discutés. De plus les techniques utilisées pour étendre les mesures de luminosité absolue à l'ensemble de la prise de données 2010 sont décrites.

Contents

Acknowledgements

I am greatly indebted to many people for help, both direct and indirect, in writing this PhD thesis. I am grateful to the French *Ministère de l'Enseignement Supérieur et de la Recherche* who provided the financial support for the preparation of the thesis, and to *Laboratoire d'Annecy-le-Vieux de Physique des Particules* (LAPP) who offered me a very friendly and stimulating working environment. I profited a lot, both in personal and scientific aspect, from my interaction with the members of the LAPP–LHCb group. I am truly thankful to Philippe Ghez, Vincent Tisserand and Stéphane T'Jampens for sharing their expertise and experience with me. Most of all I am grateful to Marie-Noëlle Minard and to my supervisor Bolek Pietrzik for their guidance and vigorous support throughout my thesis.

I am obliged to my colleagues from the LHCb luminosity group for numerous fruitful discussions and for providing figures and text included in this thesis. I would like to thank Jaap Panman for being a shining example of a researcher and a gentleman, Massimiliano Ferro-Luzzi for his invaluable help during my first steps in LHCb and for providing the opportunity for me to work on the beam-gas imaging method, and Vladislav Balagura for sharing his passion about science and for showing me how to be a better physicist. Being able to work with and learn from them has been an honour.

Going back in time I cannot miss to acknowledge my professors and colleagues at the University of Sofia. I am truly indebted and thankful to Leandar Litov, who sparked my interest in particle physics and who supported me even when I decided to leave the CMS group in Sofia.

The *dernière ligne droite* may be straight, but may have bumps as well. This is why I owe a sincere thankfulness to Sabine Elles for her limitless support, helpful initiatives and for all memorable discussions on way to the local *restaurant inter entreprises*.

Finally, I would like to thank my parents Daniela and Hristo, without whose love and support I would not have made it this far.

Preface

The collision energy and the luminosity are essential characteristics of a particle collider. The high-energy collisions allow massive particles to be produced and the fundamental laws of nature to be explored at otherwise inaccessible energy scales. The luminosity characterises the collision rate between the particles and its knowledge is essential for the experimental determination of the cross-section (probability) of the collision reactions. The measured and theoretically calculated cross-sections can be used to test the theoretical description and to extract new information about the colliding particles and the mechanisms of the interaction process.

The Large Hadron Collider beauty experiment (LHCb) [1, 2, 3] is dedicated to studies of CP violation and rare decays of charm and beauty hadrons. LHCb records the events produced in proton-proton collision provided by the LHC [4, 5]. Owing to its unparalleled energy and instantaneous luminosity reach the LHC is the most copious source of beauty hadrons in the world. The LHCb measurements of b-hadron branching ratios and particle-antiparticle asymmetries provide a highly sensitive test of the Standard Model and open a window for observing the effects of yet-unknown particles and interactions (New Physics). In these and other ratio measurements the luminosity cancels and therefore its accurate determination does not improve the measurement precision. Other LHCb measurements determine the cross-section for producing particles like $b\bar{b}$, J/ψ and W and Z bosons. For these, the precise knowledge of the integrated luminosity is essential. The experimental determination of the particle production cross-sections in the unique phase-space region covered by LHCb provides the possibility to perform cross-checks of the Quantum Chromodynamics (QCD) predictions and to acquire new information about the internal structure of the proton.

Various methods have been employed in the past to measure the absolute luminosity in particle colliders. Some of them use processes, where precise and reliable theoretical cross-section calculations can be made (*e.g.* Bhabha scattering in e^+e^- colliders). Others use the theoretical knowledge of the behaviour of the scattering cross-section in a certain part of the phase-space (*e.g.* the optical theorem and the Coulomb scattering methods). All these methods are referred to as *indirect*, as they do not have relation to the physical properties of the colliding beams. On the other hand, the *direct* methods, like the van der Meer (VDM) scan and wire scan, allow absolute luminosity calibration to be made by measuring geometrical properties of the colliding beams.

The development of precise vertex detectors opened the possibility for the application of a new direct method for absolute luminosity determination. The beam-gas imaging (BGI) method [6] uses the vertex detection of beam-gas interactions to measure the individual beam shapes, slopes, and offsets at the interaction point, which are then used in the absolute luminosity determination. The BGI method was applied for a first time in LHCb using the first LHC data collected at the end of 2009 [7, 8, 9]. The achieved precision of 15% allowed the most accurate absolute cross-section normalisation in the LHC run at $\sqrt{s} = 900$ GeV to be made [7]. This thesis describes the LHCb absolute luminosity calibration with the VDM and BGI methods, using $\sqrt{s} = 7$ TeV data collected in 2010.

Chapter 1 of this thesis discusses the relevance of precise luminosity determination for obtaining fundamental physics results. Also, an overview is made of some of the existing methods for absolute luminosity determination and the precision achieved in their previous application.

In Chapter 2 essential LHC characteristics are presented. Emphasis is given to the accelerator physics concepts and the machine parameters relevant to the luminosity determination.

Chapter 3 provides an overview of the LHCb detector. A description is given of the tracking, calorimeter and trigger systems, which are used in the absolute luminosity determination and whose performance is directly related to the measurement precision. Particular emphasis is given to the VELO vertex detector and the online selection of beam-gas interactions.

With most methods for absolute luminosity determination an estimate of the absolute luminosity is obtained only for short periods of data-taking. Once the absolute scale is set, it can be propagated through the entire data-set collected by the experiment with the help of a procedure called relative luminosity measurement. Chapter 4 describes the techniques used for the systematic determination of the relative luminosity in all data-taking periods.

The application of any direct method for absolute luminosity determination requires the knowledge of the number of protons contained in the colliding bunches. Chapter 5 summarises the bunch population data analysis which uses measurements provided by the LHC beam current transformers and ghost charge estimates provided by LHCb.

Finally, the LHCb measurements using data collected in 2010 and providing absolute calibration of the luminosity are described. The experimental determination of an effective reference cross-section with the VDM and BGI methods are presented in Chapters 6 and 7, respectively. The results presented in these chapters are published in [10]. The author has no direct contribution to the analysis leading to the absolute luminosity normalisation with the VDM method. The text describing the measurements with the VDM method (Chapter 6) is reproduced from [10] and is included in this thesis for a comparison with the BGI method and its results.

The author's personal thesis contributions include the development of the LHCb hardware (L0) and software (HLT) online selections for events containing beam-gas interactions, the implementation of the HLT beam-gas trigger, the measurement of the ghost charge in the LHC fills used for absolute luminosity calibration, and participation in the analysis leading to the absolute luminosity determination with BGI method.

Chapter 1

Luminosity

The luminosity of a particle collider is determined by the rate of the particle collisions it produces. The *instantaneous** luminosity, L, is defined as the ratio between the rate of interactions of a certain type, R, and the cross-section (probability) for the reaction of interest, σ:

$$L = R\,/\sigma \tag{1.1}$$

Knowledge of the instantaneous luminosity is necessary for the estimation of the expected signal and background rates, while a precise knowledge of the integrated luminosity is employed in a number of fundamental physics measurements, which allow us to improve our understanding of the theories describing the particle interactions. Also, the luminosity can be used to characterise the accelerator performance on an absolute scale.

The Large Hadron Collider beauty experiment has been designed for a study of rare b-hadron decays and CP-violation. Its core measurements aim at determining particle production asymmetries and branching fractions of specific decay channels. These rely on relative measurements, which do not involve knowledge of the luminosity. However, LHCb is a forward spectrometer with a unique rapidity coverage. This offers the possibility to study the properties of particle production in hadron collisions in a hitherto unexplored kinematical region. As discussed in Section 1.1, the cross-section measurements of charm and beauty hadrons provide new constraints on the existing particle production models, while the Drell-Yan and electroweak boson production processes offer the possibility to extract new information about the structure of the proton, which plays an essential role in the theoretical calculations. The uncertainty of the absolute luminosity contributes directly to the precision of the measured cross-sections and has therefore direct impact on the possibility to achieve these new insights. Later in this section we look in more detail into the luminosity precision goal imposed by the relevant cross-section measurements and theoretical calculations.

* Unless otherwise stated, throughout this thesis the term *luminosity* refers to the *instantaneous* luminosity, which usually is measured in units of $\mathrm{cm}^{-2}\mathrm{s}^{-1}$ or $\mathrm{b}^{-1}\mathrm{s}^{-1}$, and the letter L is used. The *integrated* luminosity, usually measured in units of cm^{-2} or b^{-1}, is denoted with the calligraphic symbol $\mathcal{L}$.

An overview of some of the most accurate methods for absolute luminosity determination at the LHC is given in Section 1.2. These include the van der Meer (VDM) and beam-gas imaging (BGI) methods, which have been used by the LHC experiments for absolute luminosity normalisation of the data taken in 2009 and 2010 [10, 11, 12].

1.1 Relevance of absolute luminosity measurements

For most of the measurements foreseen by the LHC experiments [13] a good understanding of the hard processes occurring in hadron collisions plays a crucial role. These processes are described by perturbative quantum chromodynamics (QCD), whose predictions are in agreement with the measurements performed at the Tevatron [14].

From the theory side, the factorisation theorem [15] provides the possibility to calculate a wide variety of hard-scattering inclusive and differential cross-sections in hadron-hadron collisions. The theoretical results for several benchmark hard-scattering processes can be seen in Fig. 1.1. In an experiment, the absolute cross-section for a certain process can be measured from the rate at which this process occurs and the luminosity (see Eq. (1.1)). Therefore, a precise knowledge of the absolute luminosity is necessary for an accurate comparison between theory and experiment. Given the available event statistics at the LHC, the measurements✦ have the potential to further constraint the theoretical models (*e.g.* the models describing the proton structure) and the precision of the luminosity determination should not be a limiting factor.

In this chapter we discuss the potential gains that a comparison between theory and experiment can bring and the corresponding precision goal for the luminosity normalisation. Before this, however, a brief overview is made of several key aspects of the hard-interaction QCD formalism.

1.1.1 Hard-scattering QCD formalism

The physics processes occurring in high-energy colliders are dominated by the strong interactions and, naturally, QCD provides their description. The hadron scattering processes can be classified as soft or hard. The soft processes include elastic and diffractive interactions and play an important role in the calculations related to the total cross-section and the underlying event. The soft QCD processes are dominated by non-perturbative QCD effects which are still difficult to calculate. On the other hand, the hard QCD interactions involve a large momentum exchange and can be calculated with good precision using perturbation theory [14]. Typical hard scattering processes are Drell-Yan (quark-antiquark annihilation producing a lepton pair with large invariant mass; the process can be mediated by a virtual photon or a W or Z

✦ The presently available LHCb measurements of some benchmark processes are discussed in Section 1.1.2.

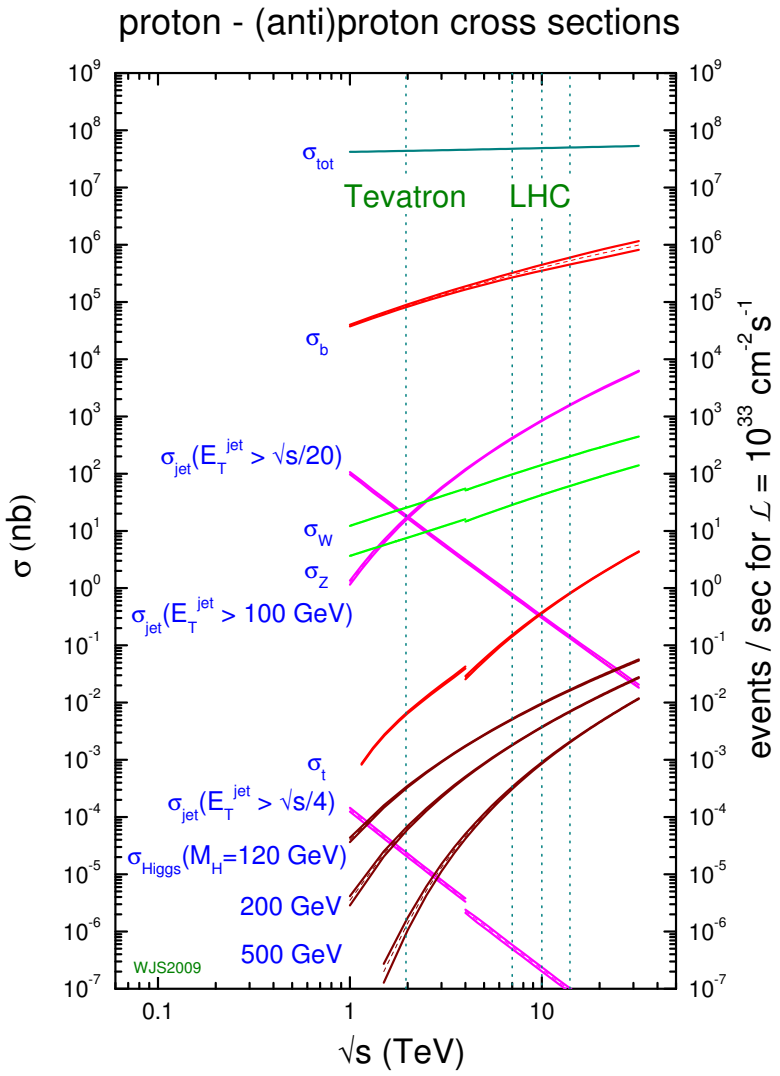

Figure 1.1: Cross-sections for a selection of hard processes versus $\sqrt{s}$, the center-of-mass energy of the colliding hadrons. The energy domains of the Tevatron (proton-antiproton collisions) and the LHC (proton-proton collisions) are indicated by dashed vertical lines. The production cross-sections for objects with a fixed mass or jets with fixed transverse energy E_T grow with $\sqrt{s}$, because of the increase in the number of partons carrying small fraction of the total proton momentum. On the other hand, the production cross-sections for jets with transverse momentum that is a fixed fraction of $\sqrt{s}$ fall with $\sqrt{s}$ due to the quadratic decrease of the partonic cross-sections with E_T. The discontinuity at $\sqrt{s} \sim 4$ TeV is due to the different initial states (pp vs $p\bar{p}$) considered in the calculations below and above that value. More details can be found in [14]. Figure from [16].

boson) and the heavy-quark, Higgs boson or high transverse momentum jet production processes. These processes play central role in the physics programme of the LHC experiments.

The essential condition for the application of perturbative QCD for calculations of hard scattering processes of hadrons is the possibility to separate (factorise) the

interaction between the partons of the two incoming hadrons from the interactions of the partons inside each of the hadrons. The viability of such an assumption and the domains of its applicability have been formulated in several factorisation theorems [15]. As the name suggests, the factorisation theorem states that in hard hadron-hadron scattering, where the partons of the incoming hadrons interact at short distance (*i.e.* at large momentum transfer Q^2), we can separate the sensitivity to dynamics at different scales. Almost all applications of perturbative QCD use factorisation properties of some kind. With its help the cross-section for a generic hard hadron process $\sigma_{AB\to X}$ can be written in the following way:

$$\sigma_{AB\to X} = \int dx_1 dx_2 \times \sum_{i,j} f_i(x_1, Q^2)\ f_j(x_2, Q^2)\ \hat{\sigma}_{ij\to X} \quad , \tag{1.2}$$

where $f_{i,j}(x, Q^2)$ are the densities of partons of type i and j in the two colliding hadrons, called *parton distribution functions* (PDFs). The PDFs are functions of the momentum fraction carried by the corresponding parton, x (also known as Bjorken-x), and the momentum transferred in the scattering process, Q^2. $\hat{\sigma}_{ij\to X}$ is the relevant elementary *partonic* cross-section, which may depend on a number of quantities like coupling strength between the quarks i and j and the mass of the final state particle X. From this equation we can see the potential gains from a precise absolute luminosity determination – its uncertainty determines the experimental precision of all measured cross-sections $\sigma_{AB\to X}$.

Parton distribution functions The proton PDFs $f_i(x, Q^2)$ describe the probability for finding partons (quarks and gluons) inside the proton that carry certain fraction of its momentum. The dependence of the PDFs on the momentum transferred in the scattering process, Q^2, is described by the DGLAP equation [§] [17]. The proton PDFs are universal in the sense that they do not depend on the exact nature of the scattering process. For example, the proton structure obtained from fits to deep-inelastic scattering data is the same as the one obtained in fixed target experiments or in hadron colliders. However, as will be detailed later, different experiments access different regions in the (x, Q^2) plane and therefore the most complete description of the proton structure is possible only by combining the available experimental data. Currently a number of groups produce publicly available PDFs using different data-sets and analysis frameworks. Three of them, namely MSTW [16], CTEQ [18] and NNPDF [19], provide *global* PDFs obtained from global fits of data from HERA, Tevatron and fixed target experiments.

Calculation of partonic cross-section The hard-scattering partonic cross-sections $\hat{\sigma}_{ij\to X}$, which appear in Eq. (1.2) are calculated in the framework of perturbative QCD. The standard approach is to express the scattering amplitude for a given process as

[§] Named after its authors Dokshitzer, Gribov, Lipatov, Altarelli and Parisi.

a series expansion in powers of the gauge coupling constant α_s. The terms in the perturbative expansion can be represented with the help of Feynman diagrams, where their physical meaning becomes clear. The number of vertices in each Feynman diagram is related to the order of the coupling constant in the perturbative expansion.

Naturally, the calculation of the terms corresponding to each order of the coupling constant is not possible and therefore in QCD calculations approximations need to be made. A leading order (LO) calculation of a certain process involves only the terms in the perturbative expansion which contain the lowest possible power of the coupling constant. In many cases LO calculations are sufficient to describe principal features of the process under study and provide the first estimate of its cross-section. Expressions for the LO cross-section of many processes are widely available in the literature [20]. Higher order calculations include the contributions from more complicated Feynman diagrams, which involve larger number of interaction vertices. For example, a next-to-leading order (NLO) calculation includes all terms to order α_s compared to the LO term. Higher-order calculations account for extra partonic processes that are possible only beyond the LO and therefore provide more precise estimates of the related quantities. The higher order QCD calculations offer significant challenges due to infrared divergences occurring from real and virtual radiation with vanishing momentum [14]. Consequently, for many processes the NLO calculations represent the most accurate theoretical predictions and NNLO (next-to-next-to-leading order) calculations are available only for a handful of processes of primary interest to the physics at high-energy colliders. The latter include the Drell-Yan process, mediated by a virtual-photon and the W and Z boson production [21].

The uncertainties in the calculations of cross-sections of hard-scattering processes come from the renormalisation scale [22], imperfect knowledge of the PDFs, from the uncertainty of the strong coupling $\alpha_S(M_Z^2)$, and others. In addition, non-perturbative effects, like the fragmentation of the hard-scattering products, affect the precision of the theoretical predictions. The absolute contribution of each of these uncertainties depends on the specific process. From Eq. (1.2) it can be concluded that the comparison between the experimental measurements and the theoretical predictions can bring new information in two main directions. Processes, which have large uncertainty in the partonic cross-section, like the production of J/ψ and $b\bar{b}$, can be used to establish the correctness of different theoretical models and to improve the understanding of QCD calculations. On the other hand, the processes for which high-precision partonic cross-section are available, like Drell-Yan and electroweak boson production, can be used to improve our knowledge of the parton distribution functions. This will then result in improved QCD predictions for all related quantities [23]. Naturally, sufficiently precise experimental results are needed to make useful comparisons. Later in this section we discuss the current level of uncertainty in the theoretical predictions for the cross-section of several benchmark hard-scattering processes at the LHC and we show that the most stringent requirement on the accuracy of the measured cross-sections, in particular on the precision of the absolute luminosity, comes from the possibility to

constrain the PDFs by considering the processes of W and Z boson production.

1.1.2 Cross-section measurements

Several absolute cross-section measurements, listed below, have been performed by LHCb. They provide insight into the processes of particle production in a unique rapidity and p_T region of the phase space. In addition, there is a big number of important measurements of cross-section ratios, which are not subject to a luminosity uncertainty and are not included in the following considerations. The results which one bases on luminosity measurements are:

1. Strange particle production cross-sections:
   - prompt ❖ K^0_S [7];
   - inclusive ϕ [24].
2. Hidden charm and beauty production cross-sections:
   - prompt J/ψ [25];
   - prompt double J/ψ [26];
   - inclusive ψ(2S) [27];
   - prompt Υ(1S) [28].
3. Open charm and beauty production cross-sections:
   - prompt charm mesons [29, 30];
   - b-hadrons (using decays to J/ψ [25] or semi-leptonic decays [31]).
4. W and Z production cross-sections [32];
5. Exclusive J/ψ, ψ(2S), χ_c and non-resonant dimuon production cross-sections [33].

Both J/ψ and $b\bar{b}$ production are typical processes used for comparison between theory and experiment. Below we discuss the relevant LHCb results and their consistency with the theoretical predictions, paying special attention to the magnitude of the corresponding uncertainties.

J/ψ production The LHCb measurement of the prompt J/ψ production cross-section as function of p_T is shown in Fig. 1.2, along with different theoretical predictions based on colour singlet (CSM), non-relativistic QCD (NRQCD), and colour evaporation (CEM) models [25]. Figure 1.3 shows the results for J/ψ from b-decay. These measurements provide the determination of the differential cross-sections for the production of prompt J/ψ and J/ψ from b-decay in the forward region at $\sqrt{s} = 7$ TeV.

The LHCb measurements are in good agreement with earlier measurements of the J/ψ production cross-section performed by CMS in the rapidity region common to both experiments, $2.0 < y < 2.5$ [25]. The LHCb measurement of the prompt J/ψ cross-section is in excellent agreement with the high-p_T theoretical predictions based on the

❖ The *prompt* particle production includes both direct and indirect (*i.e.* feed-down from short-lived massive states) contributions.

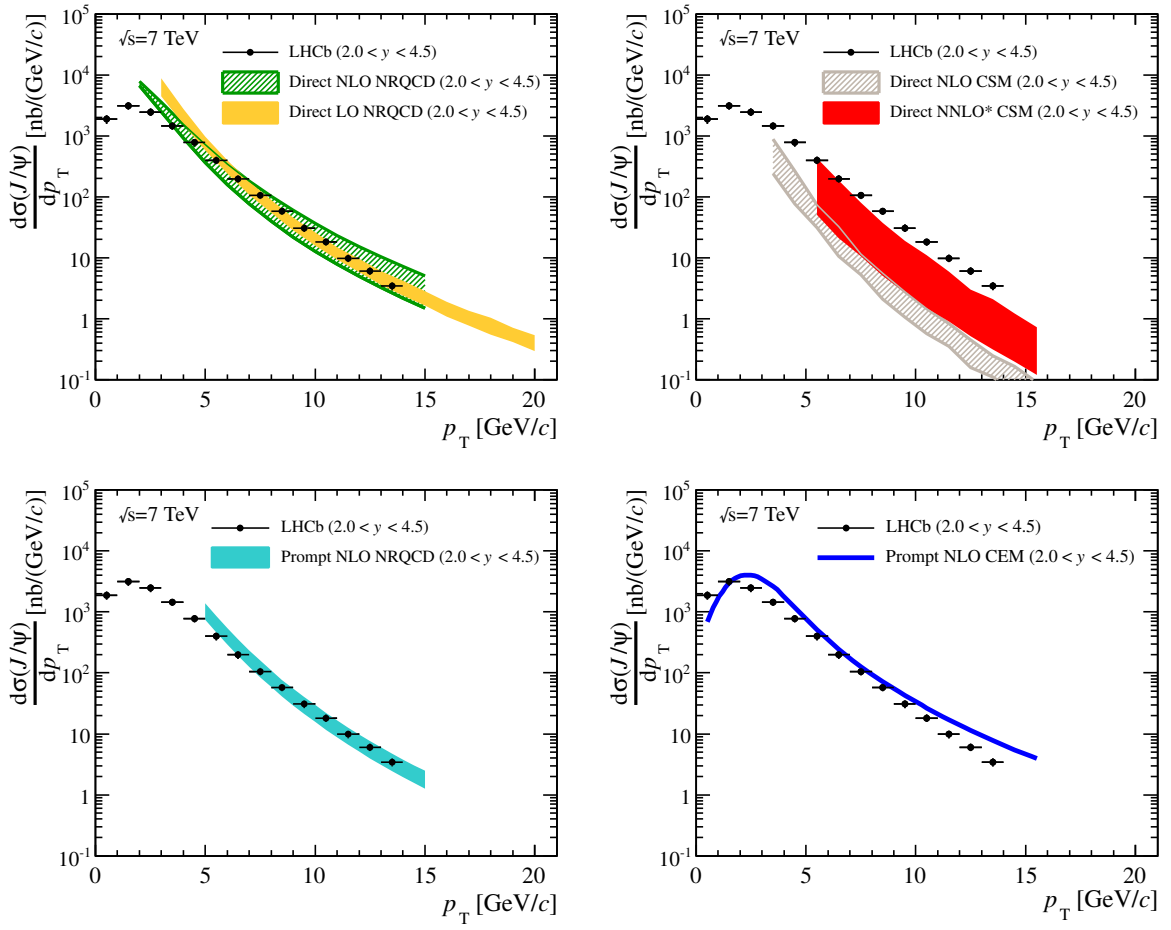

Figure 1.2: Prompt J/ψ production cross-section as function of p_T. The LHCb measurements (circles with error bars) of prompt J/ψ production are compared to different theoretical calculations (filled or hatched bands) of direct (top panels) and prompt (bottom panels) production of unpolarised J/ψ. From [25].

NRQCD, while the fixed-order next-to-leading-logarithm (FONLL) QCD calculations describe very well the differential cross-section for J/ψ from b.

***b$\bar{b}$* production** LHCb has performed two measurements of the inclusive $b\bar{b}$ production cross-section in pp collisions at $\sqrt{s} = 7$ TeV, using two different methods. The first method uses decays of b-hadrons into final states containing a D^0 meson and a muon, and estimates the total $b\bar{b}$ cross-section to be $284 \pm 20(stat.) \pm 39(syst.) \pm 28(lumi.)$ μb [31]. The 10% luminosity error is larger than the statistical, but smaller than the systematic uncertainty of the measurement. The latter is dominated by the uncertainty of the tracking efficiency. The second method uses J/ψ from b-hadron decays and yields a total $b\bar{b}$ cross-section of $288 \pm 4(stat.) \pm 38(syst.) \pm 29(lumi.)$ μb [25]. In this measurement, the 10% luminosity error is larger than the statistical, but smaller than the systematic uncertainty of the measurement. The latter is dominated by the

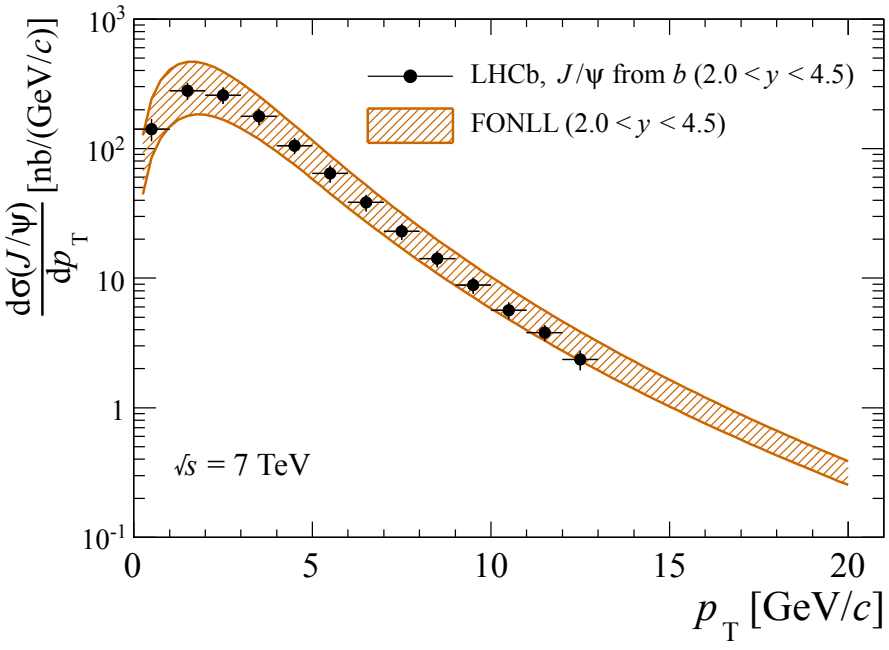

Figure 1.3: Production cross-section for J/ψ from b as function of p_T, assuming unpolarised J/ψ. The LHCb measurements are shown as circles with error bars, while the theoretical prediction based on a FONLL calculation is represented by a hatched band. From [25].

error from extrapolation to the full polar angle and the uncertainty of the tracking efficiency. The agreement between the results of the two methods is excellent. The comparison of the differential $b\bar{b}$ production cross-section, obtained from b-hadron decays into $D^0\mu\nu X$ with the theoretical predictions shows a good agreement as well (see Fig. 1.4).

Experimental and theoretical uncertainties As can be seen in Fig. 1.2 the experimental precision is sufficient to distinguish between some of the most popular theoretical models. In the presented LHCb measurements the experimental uncertainty is dominated by the absolute luminosity error and the tracking efficiency error. For the case of the prompt J/ψ the lack of knowledge of the polarisation brings an additional uncertainty, which will be reduced by measuring its polarisation. At the time of these measurement the luminosity precision was 10%, while the overall theoretical uncertainties are significantly larger than the experimental ones. Therefore, the improved LHCb results with 2010 or 2011 data, which include the presently available luminosity uncertainty of 3.5%, will encourage further progress in the theoretical calculations. The discrimination between the different theoretical models using only differential cross-sections is not easy with the current level of theoretical precision. Additional observables, like the polarisation in the case of J/ψ production, will certainly play an important role in this comparison. In addition, a higher experimental precision and therefore a lower error on the luminosity can be useful in the comparison of the

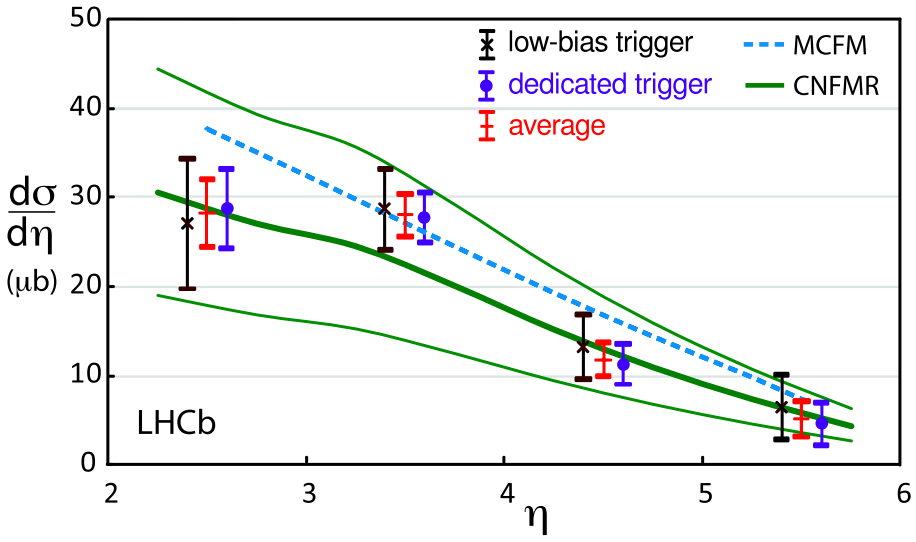

Figure 1.4: Cross-section for the production of b-hadrons in the geometric acceptance of LHCb as function of pseudorapidity. The LHCb measurements have been obtained by using samples of b-hadrons decaying to $D^0\mu\nu X$, selected online either by a low-bias (crosses) or a dedicated (circles) trigger. Their average is indicated by the symbol '+'. The experimental uncertainty does not include the systematic errors. The predictions of the MCFM and CNFMR models are shown with a dashed and a thick solid line, respectively. The thin solid lines indicate the theoretical uncertainties on the CNFMR model. Figure reproduced from [31].

results between the LHC experiments, as it will allow important cross-check of the measurement systematics to be made.

1.1.3 Parton distribution functions

Figure 1.5 shows the accessible ranges of parton momentum fraction, x, and momentum transfer, Q^2, in fixed target experiments, at HERA and at the LHC. The limited geometrical acceptance of the experiments prevents the exploration of the full kinematical coverage of the accelerator. For example, the ALICE, ATLAS and CMS experiments are essentially instrumented in the central region and cover rapidity ranges of about $|y| < 2.5$. According to Fig. 1.5, the W and Z bosons produced with central rapidity at the LHC can be used as a probe of the parton distributions around $x = 5 \times 10^{-3}$ (such values are typical for the *sea* quarks and gluons in the proton). On the other hand, LHCb covers the rapidity range of $1.9 < y < 4.9$ and therefore it will be able to probe the distributions of partons at very high and very low x. Therefore, the LHCb measurements of Drell-Yan and electroweak boson production will provide insight into a hitherto unexplored kinematical region. At the same time, the measurements in the rapidity range common to all LHC experiments, $1.9 < y < 2.5$, will allow direct comparison of their results to be made.

In many cases the uncertainties in the PDFs limit the precision of the theoretical

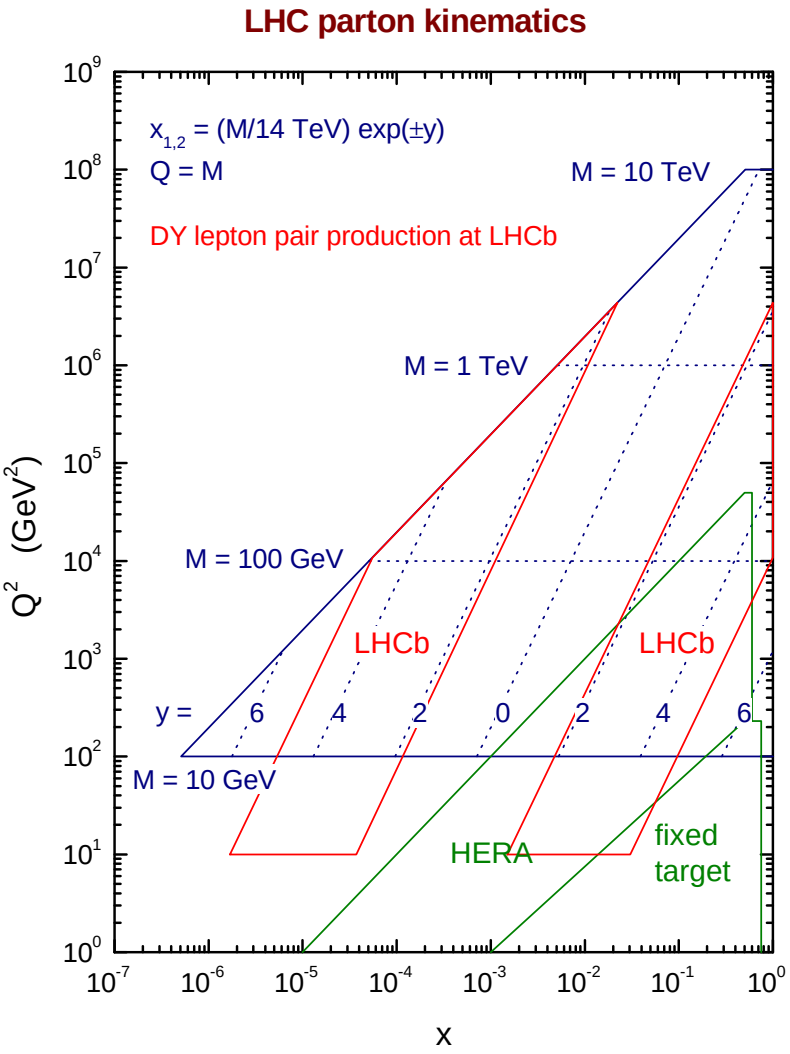

Figure 1.5: The kinematic range of x and Q^2 accessible at fixed target experiments, at HERA and at the LHC. Thanks to its superior center-of-mass energy the LHC extends the rapidity coverage of the Tevatron (not shown). At LHC the central rapidity region, $|y| < 2.5$, which is sensitive to distributions of partons with medium and small momentum fraction x will be explored by the ALICE, ATLAS and CMS experiments. The unique rapidity coverage of LHCb ($1.9 < y < 4.9$) will allow complementary studies of the distributions of partons with very high and very low x to be made. Figure from [23].

cross-section calculations [34]. The relative uncertainties due to PDFs on the cross-sections for Drell-Yan and electroweak boson production are shown in Fig. 1.6. The precision of the calculations decreases at high rapidity because of the relatively less constrained sea quarks with very low Bjorken-x ($\mathrm{O}(10^{-5})$). For example, a Drell-Yan scattering process involving a virtual photon with mass $M = 10$ GeV and rapidity $y = 4.5$ will probe the distributions of quarks with $x_{1,2} = (M/\sqrt{s})e^{\pm y} = (10/7000)e^{\pm 4.5}$ and therefore $x_1 \approx 0.13$ and $x_2 \approx 2 \times 10^{-5}$. As shown in Fig. 1.5, the LHCb experiment is well suited for measurements of relatively low-mass Drell-Yan lepton pairs produced

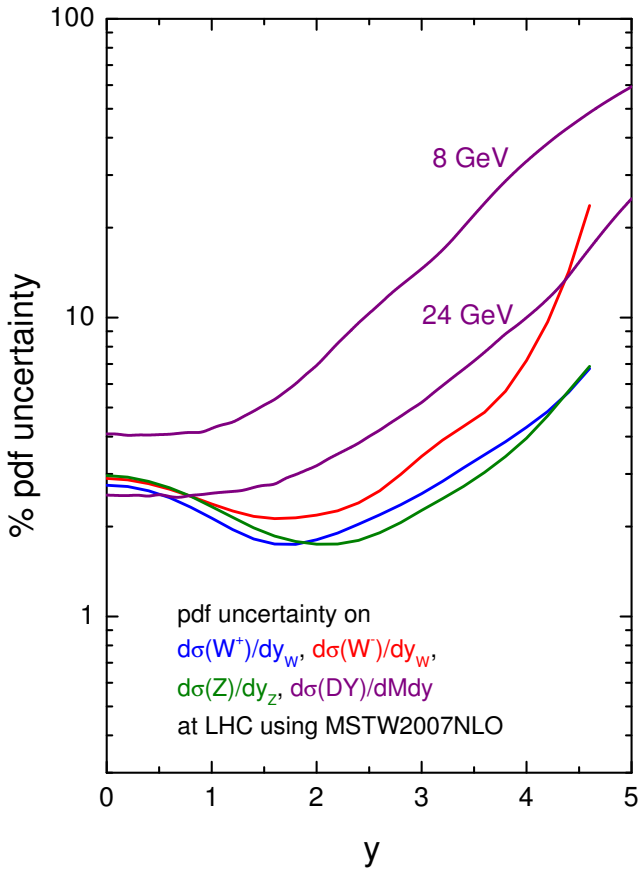

Figure 1.6: Theoretical uncertainties on the cross-sections for Drell-Yan and electroweak boson production at the LHC, arising from uncertainties on the PDFs. As explained in the text, at high rapidity the processes involve partons with lower Bjorken-x, whose distributions are less well constrained by existing collider data, resulting in an increased cross-section uncertainty. At fixed rapidity, a Drell-Yan pair with lower invariant mass (the curve labeled "8 GeV" to be compared with the curve labeled "24 GeV") has larger uncertainty as it involves an interaction of a parton with a lower x. Figure from [23].

at high rapidity. The theoretical predictions for this process show sizable variation as one goes from LO to NLO to NNLO [23]. This instability is attributed to the increasing divergence of terms in the perturbative expansion as one increases the order of the calculation (α_S is relatively large at this energy scale). Therefore, the measurements on low-mass Drell-Yan production are important for our understanding of the convergence of the perturbative series in QCD. When the reliability of the theoretical predictions is established, the process of low-mass Drell-Yan production can be used to determine the distributions of partons with very small $x \sim 10^{-5} - 10^{-6}$ inside the proton. Recent work [35, 36] demonstrates the prospects for these measurements at LHCb and provide preliminary results on the expected improvements of the PDFs. Naturally, the precision of the measured cross-sections depends directly on the uncertainty of the absolute luminosity normalisation. Therefore, the precision on the luminosity will be a key for

constraining the PDFs.

The W and Z boson production have the best theoretical precision. The uncertainty on the partonic cross-sections is at the 2% level [37], while the uncertainty from the knowledge of the PDFs is larger. In Fig. 1.6 it is shown that at high rapidity the results obtained with the MSTW2007NLO PDF set include significant uncertainty (O(10%)) due to the PDFs. Comparison of the total cross-sections for different benchmark processes, obtained with different PDF sets shows agreement within $\pm$ 5% [38] (see Fig. 1.7). The expected ultimate experimental precision for the measurement of the Drell-Yan and electroweak gauge boson production, excluding the uncertainty of the luminosity, is below 1% [37, 39]. Therefore, with a luminosity error below 5% one will be able to make a distinction between different PDF sets. At present, the precision goal for the uncertainty of the absolute luminosity is set by the theoretical uncertainty of the partonic cross-section for W boson production, namely 2% [37].

In summary, the precise measurement of the cross-sections for processes like Drell-Yan and electroweak boson production will allow improvement of the knowledge of the proton PDFs to be made. This will then result in improved QCD predictions. Absolute luminosity measurement with uncertainty of 2% will be useful even now. Precise cross-section measurements of processes with a smaller dependence on the PDFs can be used for accurate comparison of the predicted and measured cross-sections and for improving our understanding of QCD.

1.2 Methods for absolute luminosity determination

The luminosity is related to the rate of collisions and it can be defined with the help of Eq. (1.1), where it plays the role of a proportionality factor between the rate and the cross-section of a given process. The methods for luminosity determination, based on the measurement of the rate of occurrence of a process with a known cross-section are called *indirect* methods. One possibility is to use the theoretical prediction or a previous measurement of the *absolute value* of the cross-section for the process of interest. Other approaches use the theoretical knowledge of the *behaviour* of the differential pp cross-section in a certain part of the phase-space. The choice of a process with reliable and precise theoretical predictions, which at the same time allows its rate to be accurately measured in an experiment, is essential for the indirect methods of absolute luminosity determination. The *direct* methods provide an estimate of the luminosity through the determination of the geometric properties and particle distributions inside the colliding beams. Often not all parameters of interest are accessible by the experiment itself, making the application of the direct methods possible only by combining the information from different experiment- and accelerator instruments.

The precision of the indirect methods relies on the knowledge of trigger and selection efficiencies for the relevant processes, while the direct methods are subject to different systematic effects, like magnet hysteresis or vertex resolution. There is a strong

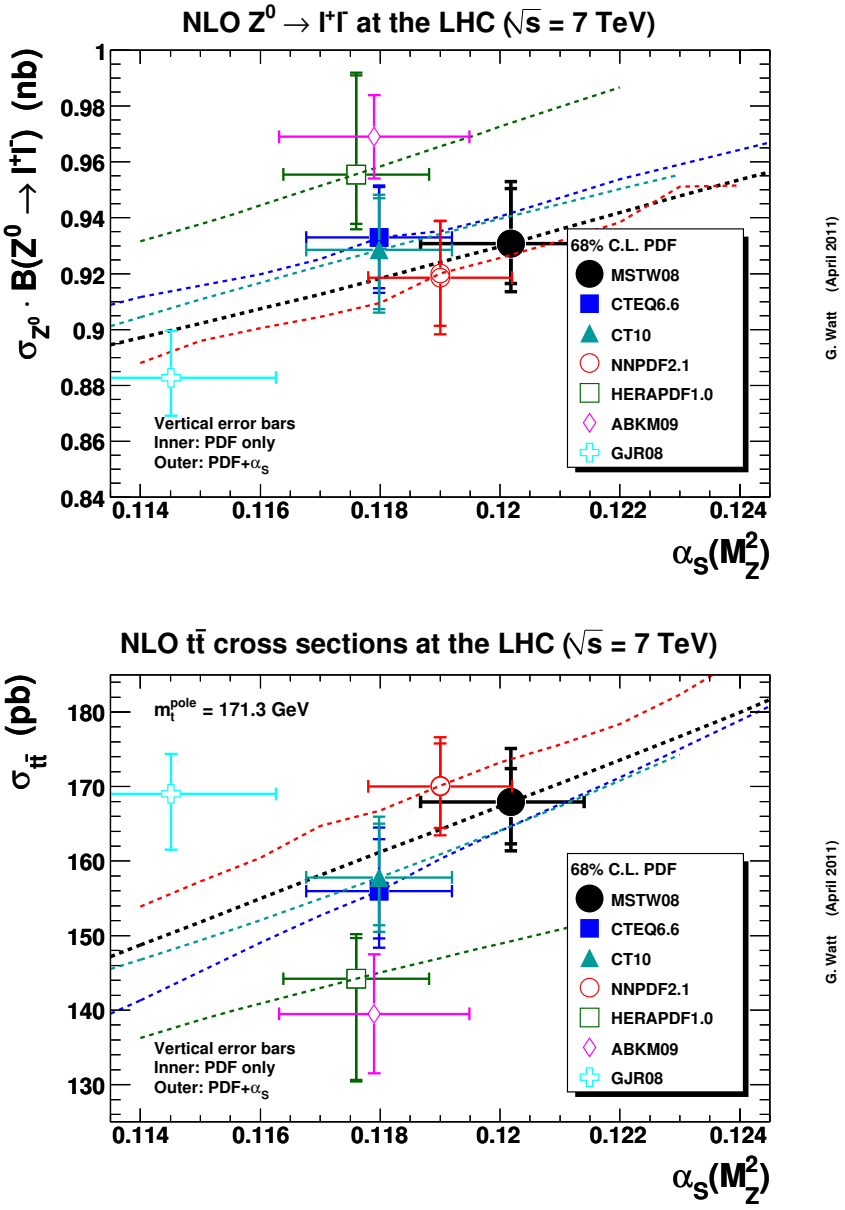

Figure 1.7: Theoretical predictions for the NLO cross-section for Z boson (top panel) and $t\bar{t}$ (bottom panel) production in pp collisions at $\sqrt{s}$ =7 TeV. The different points correspond to different PDF sets. The horizontal error bars indicate the uncertainty in $\alpha_s(M_Z^2)$, while the inner (outer) vertical error bars show the cross-section uncertainty due to PDFs (PDFs and α_s). Figures from [16].

motivation to use several methods, affected by different systematics, to determine the absolute luminosity. Usually, the determination of the absolute luminosity scale is the product of a comprehensive analysis, using data taken during a limited period of time. However, once the absolute scale is set, it can be *propagated* through the entire data-set collected by the experiment with the help of a comparably simpler procedure, usually called *relative* luminosity measurement or *luminosity monitoring*.

In this section we describe some of the existing methods for absolute luminosity determination. Section 1.2.1 concentrates on the indirect methods to be employed at the LHC, while Section 1.2.2 presents the theoretical concepts of the traditional van der Meer scan and the novel beam-gas imaging methods. The latter two are used for the absolute luminosity normalisation of the data taken by LHCb at $\sqrt{s} = 0.9$ and 7 TeV.

1.2.1 Indirect methods

The indirect methods for absolute luminosity determination involve interaction processes, for which reliable and precise theoretical predictions are available. One possibility is to employ Eq. (1.1) in conjunction with a cross-section, which is *calculable on an absolute scale*, and a measurement of the rate of the corresponding process. In principle, any QED process, with sufficient event rate, can be used in this approach. For example, in e^+e^- colliders the commonly used reference process is the low- or large-angle Bhabha scattering ($e^+e^- \to e^+e^-$), which has a total theoretical error of about 0.05% and allows the absolute luminosity to be determined with a similar precision [40, 41]. At the LHC, cross-section predictions with accuracy better than 1% are available for the process of elastic dilepton production via photon-photon fusion $pp \to pp + l^+l^-$ [42]. Another class of indirect methods for absolute luminosity determination use the theoretical knowledge of the *behaviour* of the pp cross-section. Widely used examples include the method based on the optical theorem [43] and the method measuring the cross-section for elastic proton-proton scattering in the Coulomb-nuclear interference region [44].

Before discussing in more detail these methods and the plans for their application at the LHC we would like to point out that the use of a certain process for setting the absolute luminosity scale is appropriate only when we don't anticipate to use this process to extract new information from precise comparison of data and theory. For example, it may be preferable to use the precisely calculable processes of W and Z production to constrain the proton PDFs (see Section 1.1.3) instead of using them for indirect determination of the absolute luminosity [37].

Elastic dilepton production via photon-photon fusion The cross-section for the process of elastic production of a lepton pair via photon-photon fusion (see Fig. 1.8) can be calculated within pure QED and there are no strong interactions between the leptons in the final state. On the other hand, the variant of the same process where one or both leading protons dissociate during the collision (*inelastic* dilepton production via photon-photon fusion) is subject to larger theoretical uncertainties and needs to be considered as a background [42]. Suppression of this background is possible by requiring small transverse momentum of the lepton pair ($p_t^{l_1} + p_t^{l_2} < 30$ MeV). Also, in this kinematic domain the cross-section corrections due to strong interactions between the protons (rescattering) is negligible [45]. When the produced lepton pair is e^+e^- these conclusions are valid only if the transverse momentum of each lepton is small [45].

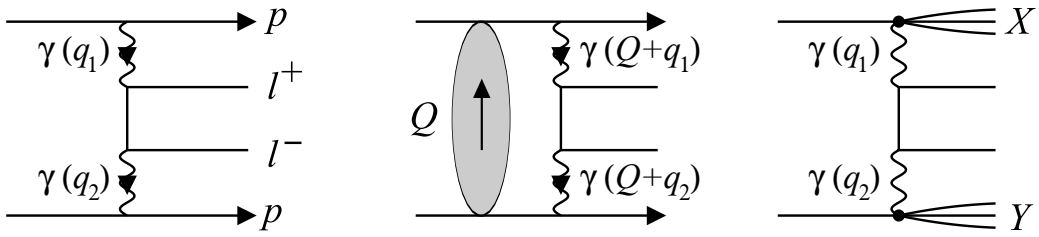

Figure 1.8: Feynman diagrams of processes of dilepton production via photon-photon fusion. The elastic case (left) is shown along with one of its corrections due to rescattering (center) and the inelastic case (right), where one or both leading protons dissociate during the collision.

The latter requirement makes the process with an electron pair less favorable from an experimental point of view than the one with a muon pair. In the following we concentrate specifically on the dimuon process.

The theoretical uncertainty of the cross-section for elastic dimuon production is less than 0.5 % and its main contribution comes from the knowledge of the proton form factors [42]. The practical usage of this process as a luminometer is challenging due to the low signal rate, the presence of backgrounds and the difficulty to trigger on dilepton pairs with low invariant mass. In addition to the already mentioned *inelastic* dilepton production via photon-photon fusion other processes with signal-like signatures include: dimuon production via Drell-Yan ($\gamma^*/Z \to \mu^+\mu^-$), dimuon production via double pomeron exchange, and photon-pomeron-mediated production of a particle decaying into two muons, *e.g.* a J/ψ (see Fig. 1.9). Contamination from $c\bar{c}$ or $b\bar{b}$ events, where both quarks decay semi-leptonically into muons ($c/b \to \mu X$) and from combinatorial backgrounds due to pion and kaon misidentification is expected as well. The estimation of the correction, which takes into account the inefficiency due to multiple interactions plays an essential role in the measurement of the signal rate. A comprehensive LHCb study, based on simulations [39] shows that the best way to

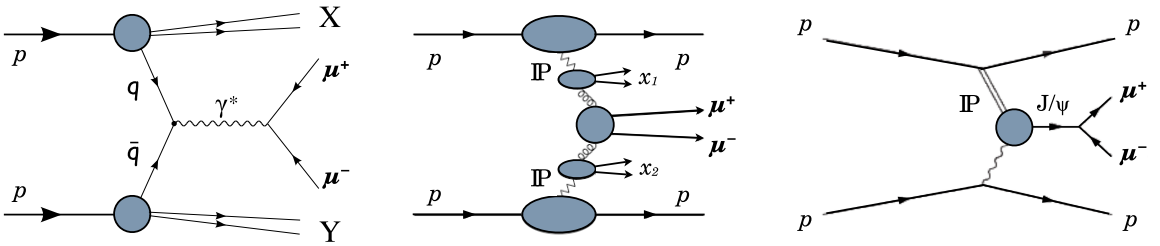

Figure 1.9: Feynman diagrams of background processes to elastic dimuon production via photon-photon fusion. Dimuon production via Drell-Yan (left), dimuon production via double pomeron exchange (center) and J/ψ production mediated by photon-pomeron interactions (right).

distinguish these background processes is to use the transverse momentum and the invariant mass of the dimuon pair, the dimuon acoplanarity (a function of the transverse momenta of the muon pair), and the total charged-particle multiplicity of the event. The expected number of recorded and reconstructed signal $pp \to pp + \mu^+\mu^-$ events in 1 fb^{-1} (*i.e.* half year of data-taking at nominal conditions) of LHCb data is about 5000. The anticipated background, retained after the offline selection, is about 5% of the signal. One fb^{-1} of data makes an absolute luminosity measurement with precision 1.9% possible [39].

Cross-section measurements of various exclusive dimuon processes have been published recently by LHCb, using 36 pb^{-1} of data at $\sqrt{s} = 7$ TeV [46]. The measured cross-sections for the exclusive production of J/ψ, ψ(2S), χ_{c0}, χ_{c1} and χ_{c2} confirm the theoretical predictions for the corresponding processes. In addition, these measurements pave the way towards better understanding of the background to the process of elastic dimuon production via photon-photon fusion. The cross-section of the latter reaction has also been measured, yielding the result $67 \pm 10(stat.) \pm 7(syst.) \pm 15(lumi.)$ pb. Here, the luminosity uncertainty takes into account the error of the integrated luminosity corresponding to the used data-set (10%) and the additional error related to the fact that only events with a single interaction are used in the analysis. This result is consistent with the theoretically predicted value, 42 ± 0.4 pb [46].

Optical theorem: TOTEM-CMS and ALFA-ATLAS The optical theorem can be applied to the process of *elastic* scattering of protons [¶] as a method to measure the total proton-proton cross-section and the absolute luminosity. The optical theorem relates the imaginary part of the forward scattering amplitude to the total cross-section:

$$\sigma_{\text{tot}}(s) = \frac{4\pi}{s} \operatorname{Im} A(s, t = 0) \tag{1.3}$$

σ_{tot} is the total proton-proton cross-section, s is the center-of-mass energy, $A(s, t = 0)$ is the (forward) scattering amplitude evaluated at vanishing momentum transfer, t [✠] [47]. Using also the definition of the differential elastic cross-section, at $t = 0$:

$$\left(\frac{\mathrm{d}\sigma_{\text{el}}(s)}{\mathrm{d}t}\right)_{t=0} = \frac{\pi}{s^2} \left|A(s, t = 0)\right|^2 \tag{1.4}$$

and

$$\rho(s) = \frac{\operatorname{Re} A(s, t = 0)}{\operatorname{Im} A(s, t = 0)} \tag{1.5}$$

[¶] Valid also if one or both scattering particles is an anti-proton.

[✠] More precisely, t is the Mandelstam variable defined by $t = (p_i^{init} - p_i^{final})^2$, where p_i^{init} and p_i^{final} are the initial and final four-momenta of each scattering proton ($i = 1, 2$). In the relativistic limit and for small scattering angles θ, the following approximation is valid: $t \approx -p^2\theta^2$.

the following expression is obtained (omitting the explicit s-dependence):

$$\left(\frac{\mathrm{d}\sigma_{\mathrm{el}}}{\mathrm{d}t}\right)_{t=0} = \frac{(1+\rho^2)\sigma_{\mathrm{tot}}^2}{16\pi} \tag{1.6}$$

By substituting σ_{el} with R_{el}/L and one of the powers of σ_{tot} with $(R_{\mathrm{el}}+R_{\mathrm{inel}})/L$, from Eq. (1.6) an expression for the total proton-proton cross-section in terms of observable elastic and inelastic event rates can be obtained:

$$\sigma_{\mathrm{tot}} = \frac{16\pi}{1+\rho^2}\,\frac{(\mathrm{d}R_{\mathrm{el}}/\mathrm{d}t)_{t=0}}{R_{\mathrm{el}}+R_{\mathrm{inel}}} \tag{1.7}$$

In addition, a similar expression for the luminosity can be derived:

$$L = \frac{R_{\mathrm{el}}+R_{\mathrm{inel}}}{\sigma_{\mathrm{tot}}} = \frac{(1+\rho^2)(R_{\mathrm{el}}+R_{\mathrm{inel}})^2}{16\pi\,(\mathrm{d}R_{\mathrm{el}}/\mathrm{d}t)_{t=0}} \tag{1.8}$$

Therefore, the optical theorem allows the independent determination of the total proton-proton cross-section and the absolute luminosity to be made by measuring:

- the rate of elastic interactions with small scattering angle (see below);
- the total interaction rate, *i.e.* $R_{\mathrm{el}}+R_{\mathrm{inel}}$.

The optical theorem has been used extensively in previous experiments for the measurement of the total proton-(anti)proton cross-section. At CERN's Intersecting Storage Rings (ISR), a precision of 0.6% was reached and simultaneously the reliability of the new (at that time) van der Meer scan method for absolute luminosity determination was demonstrated to within ±0.9% [48]. The uncertainty of the total cross-section measurements performed at the SPS was 2.4% [49], while at the Tevatron two independent measurements by the CDF and E811 experiments provided precisions of about 2.8% [50, 51]. The absolute luminosity normalisation of the most recent Tevatron data uses the *inelastic* proton-antiproton cross-section obtained from averaging and extrapolating the results of the CDF and E811 measurements at $\sqrt{s}$ =1.8 TeV [52]. The overall luminosity uncertainty at the Tevatron includes contributions from the modelling of diffractive processes and the long-term stability of the luminosity monitors and has a value of about 6%.

At the LHC, measurements of the elastic, diffractive and total proton-proton cross-sections are foreseen by the combined TOTEM-CMS and ALFA-ATLAS experiments. These measurements will bring new insight into the soft hadronic processes, which represent a significant fraction of the total pp or $p\bar{p}$ cross-section and play an important role in the modelling of the processes at hadron colliders. The new constraints from the elastic and diffractive measurements will help to choose among the large variety of existing models. The TOTEM-CMS and ALFA-ATLAS measurement programmes include also the determination of the absolute luminosity with the use of Eq. (1.8) [43, 44, 53]. This allows luminosity monitors to be calibrated. The TOTEM detectors are planned to be fully compatible with the CMS data acquisition system

and therefore to allow common as well as stand-alone readout of both detectors. The ALFA-ATLAS experiments are discussed later in this section.

TOTEM consists of tracking telescopes T1 and T2, located inside CMS at about 10 m from the CMS interaction point (IP5), and a system of Roman Pot stations at distances 147 m, 180 m and 220 m from the interaction point. The detectors are placed symmetrically along the beam axis, covering both sides of IP5. The combined TOTEM and CMS geometrical acceptance can be seen in Fig. 1.10.

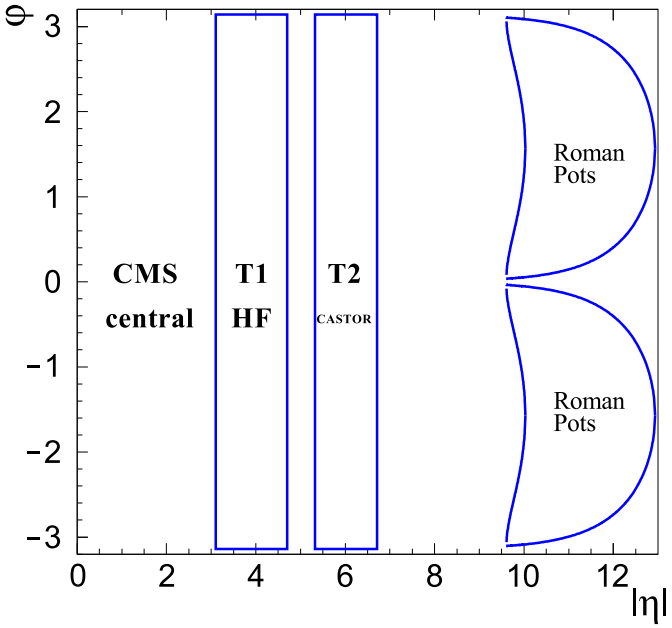

Figure 1.10: The combined TOTEM-CMS acceptance in the pseudorapidity-azimuthal plane. The TOTEM tracking telescopes T1 and T2 cover the pseudorapidity region $3 \lesssim |\eta| \lesssim 6.5$ and overlap with the CMS Hadronic Forward calorimeter (HF) and the CASTOR calorimeter [54]. The Roman Pot system detect particles in the very forward region, $10 \lesssim |\eta| \lesssim 13$.

The total inelastic interaction rate is measured with the TOTEM tracking telescopes T1 and T2, while the elastic events are detected with the Roman Pot system. The deflection angle of the elastically scattered protons, θ, is deduced from their transverse offset at the place where they are detected. This allows the momentum transfer to be estimated ($|t| \approx p_{beam}^2 \theta^2$). The precision of the measured momentum transfer can be improved by using special (parallel-to-point) beam optics and by decreasing the beam *divergence*. The latter can be achieved by decreasing the transverse beam emittance and increasing the $\beta^\star$. Two running scenarios with $\beta^\star = 90$ m and $\beta^\star = 1540$ m are foreseen for the measurement of high- and low-t elastic scattering [55]. In addition, no crossing angle should be present and parasitic (offset in z) collisions should be avoided with a filling scheme with increased bunch spacing.

Several running scenarios have been developed in order to cover the full range in momentum transfer needed for the study of elastic and diffractive phenomena. The smallest accessible $|t|$-value is about 2×10^{-3} GeV^2 (see Fig. 1.11). This value is determined by the center-of-mass energy and the aperture restrictions defined by the LHC – the detectors are allowed to approach the beam to a distance of a few mm [43]. The

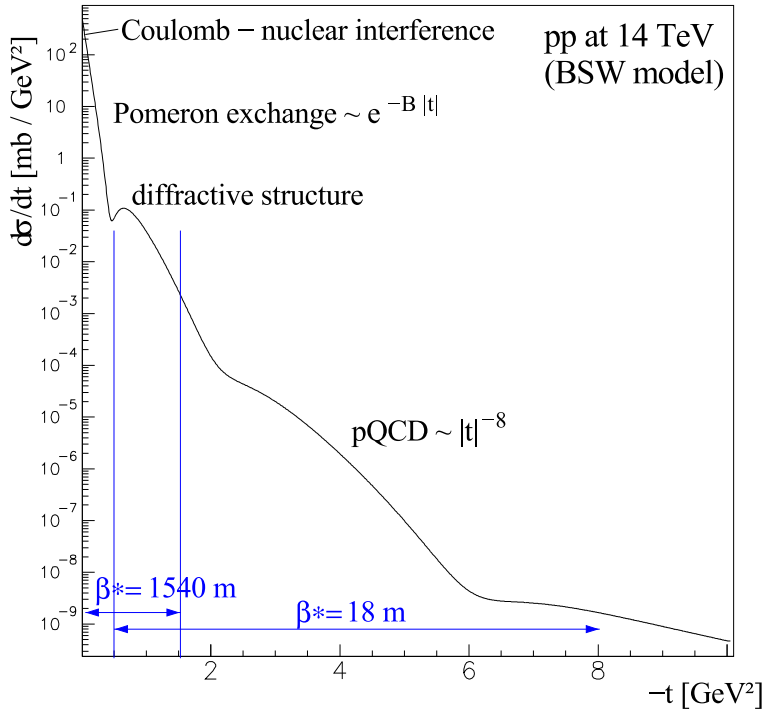

Figure 1.11: Differential cross-section for elastic pp scattering, according to the BSW model [47], characterised by several t-regions with different behaviour. The TOTEM experiment envisages different running scenarios for the measurement of the elastic cross-section over a large t-range (note the big variation of the cross-section over the shown t-range). The extrapolation of the measurements in the 'Pomeron exchange' (nuclear) region are used in the determination of the absolute luminosity.

Coulomb scattering may play a non-negligible role once t-values below a few times 10^{-2} GeV^2 are reached. The nuclear part of the cross-section, which is used for the extrapolation to $t = 0$ and the determination of the absolute luminosity, needs to be separated with the help of a theoretical model. It is expected that the model dependence of the determined cross-section slope will add an uncertainty of several per mille to the extrapolation. Other sources of uncertainty are related to the knowledge of the beam parameters (energy and crossing angle), the knowledge of the effective length between the IP and the Roman Pots, the measurement itself (detector alignment, trigger and geometrical efficiency, background estimation) and ρ (see Eq. (1.5)), which is taken as an external parameter. The target overall precision on σ_{tot} and the luminosity is

about 1% [43].

Coulomb interference region: ALFA-ATLAS At very low t the elastic pp scattering cross-section reveals a structure due to the interference between the electromagnetic and nuclear components of the elastic pp interaction [56]. The value of t where the Coulomb amplitude equals the nuclear amplitude depends on the center-of-mass energy. For nominal LHC energy ($\sqrt{s}$ =14 TeV) the corresponding value is expected to be $|t| = 0.65 \times 10^{-3}$ GeV^2 [44] (see Fig. 1.12). Previous measurements at the

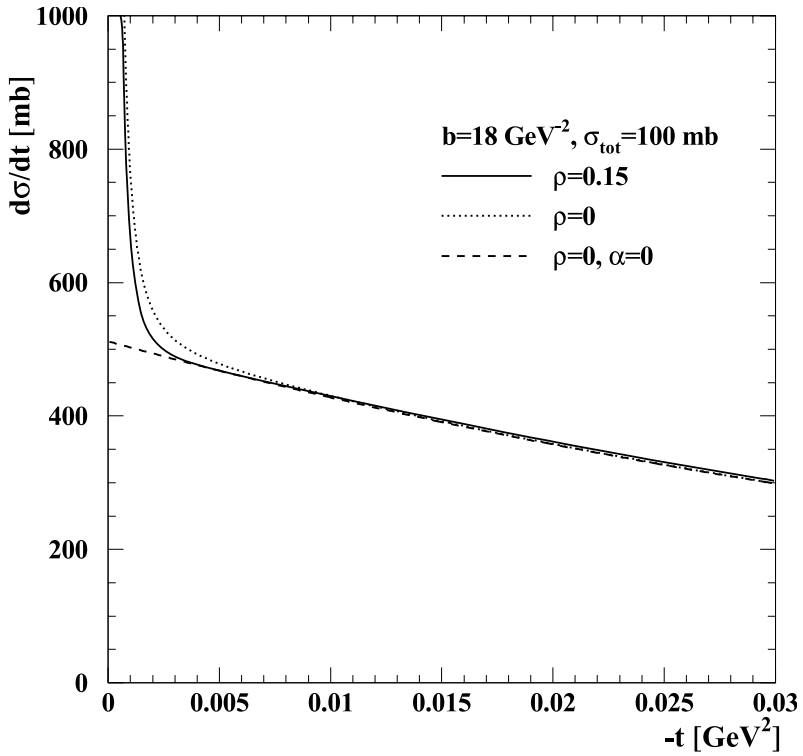

Figure 1.12: Calculated differential cross-section for elastic pp scattering [44]. The behaviour at $|t| \gtrsim 0.005$ is determined by the strong interaction, whose contribution is indicated by the dashed line (electromagnetic coupling equal to zero). At $|t| \lesssim 0.001$ the cross-section is dominated by Coulomb scattering. The region in between is the Coulomb-nuclear interference region. The cross-section behaviour in this t-region can be used to determine, among others, the luminosity and the ρ-parameter.

SPS were able to access the Coulomb interference region by measuring elastically scattered protons with angles down to 140 μrad [57]. At the LHC, because of the higher center-of-mass energy, measurements of protons deflected to 3.5 μrad are necessary. Measurements in the Coulomb interference region will be attempted by the ALFA detector, which consists of a set of scintillating fiber detectors, placed in Roman Pots on both sides of the ATLAS interaction point (IP1) and located at a distance of about 240 m from it [44]. The Coulomb interference region will not be accessible to TOTEM

with its nominal $\beta^\star = 1540$ m optics mentioned above. However, studies are continuing on the design of suitable optics to allow TOTEM to extend its measurements down to $t \approx 10^{-4}$ GeV^2 [43].

The measurement of the differential cross-section for elastic pp scattering in the t-region where the Coulomb cross-section and the nuclear cross-section are of the same order of magnitude can be used to measure the luminosity. The functional form of the elastic cross-section as function of t is known and a fit to the measured differential cross-section can be used to extract the luminosity, the ρ-parameter, the total elastic cross-section and the slope of the nuclear elastic cross-section [44, 48]. The latter is a variable which is measured by TOTEM in order to extrapolate the nuclear elastic cross-section to t =0. It is worth to point out that the 'Coulomb interference' (CI) method uses a value of the ρ-parameter, obtained from the same measurement, while the ρ-parameter needs to be taken as external input in the method based on the optical theorem. The uncertainty of the absolute luminosity measured with the CI method at UA4 was about 3% [57] and a similar precision is expected in the measurement foreseen by ALFA [44].

The need to measure protons scattered at angles of a few micro-radian imposes very stringent requirements on the beam optics and the ALFA detectors. Similarly to the conditions needed by TOTEM, the small-t elastic scattering measurements of ALFA require parallel-to-point beam focusing and low beam divergence. The nominal running scenario foresees $\beta^\star = 2625$ m and sensitive detectors approaching the circulating beams at a distance of 1-2 mm. The conditions needed for an absolute luminosity measurement with satisfactory precision are close to the expected performance and safety limits of the machine. Therefore, alternative approaches for absolute luminosity determination have been envisaged by ALFA-ATLAS in the case that the Coulomb interference region is not reached. One possibility is to use the method based on the optical theorem and the extrapolation of the nuclear part of the elastic cross-section (see page 16). The ATLAS pseudorapidity coverage is somewhat limited in this context and the determination of the inelastic rate, needed for this measurement, depends on the Monte-Carlo based extrapolation to full phase-space. The accuracy of this method for absolute luminosity determination will most probably be limited by the uncertainty of the inelastic pp rate [44]. A second alternative approach has been studied as well. It is also based on the optical theorem and the determination of the nuclear part of the elastic cross-section at $t = 0$, but the measurement of the inelastic rate is avoided by using σ_{tot} from an independent measurement, *e.g.* the value obtained by TOTEM (see Eq. (1.8)) [44].

1.2.2 Direct methods

In a circular collider the instantaneous luminosity of one pair of colliding bunches can be expressed as [58, 59]:

$$L = N_1 N_2 f \sqrt{(\vec{v}_1 - \vec{v}_2)^2 - \frac{(\vec{v}_1 \times \vec{v}_2)^2}{c^2}} \int \rho_1(x,y,z,t)\, \rho_2(x,y,z,t)\, \mathrm{d}x\, \mathrm{d}y\, \mathrm{d}z\, \mathrm{d}t\,, \quad (1.9)$$

where N_i $(i = 1, 2)$ are the number of particles in the two bunches, f is the revolution frequency, $\vec{v}_i$ are the particle velocities [‡], c is the speed of light, and ρ_i are the position- and time-dependent bunch densities, normalised such that their individual integrals over full space are unity at any time t. The integral in formula (1.9) is known as the beam overlap integral. In the relativistic limit and for small crossing angle between the beams, the square root factor, known as Møller factor [60], can be approximated with $2c\cos^2\alpha \approx 2c$, where α is the half crossing angle.

The direct methods for measuring the absolute luminosity employ several strategies to determine the various parameters entering Eq. (1.9). The *wire scan* method allows the beam profiles to be measured by scanning a thin wire across the beams [61]. Alternatively, the beam properties can be inferred from a theoretical calculation of the beam optics. The wire scan method and the theoretical calculation are not very precise as they both rely on detailed knowledge of the beam optics. For the wire scan method this is due to the fact that in order not to interfere with the experimental particle physics detectors, the wires can only be installed far from the interaction region. Next in this section we describe in more detail the approaches of the van der Meer scan method, where a reference cross-section can be determined by measuring the rate of the corresponding reaction when the two colliding beams are scanned across each other, and the novel beam-gas imaging method which allows the individual beam angles, positions and shapes to be determined from the reconstruction of beam-gas interaction vertices. Recently, another method was proposed, which allows the individual beam profiles to be determined when the two beams probe each other such as during a van der Meer scan. Unlike the beam-gas imaging, the *beam-beam imaging* method [62] uses only vertex measurements of pp events.

Van der Meer scan (VDM) method The VDM method provides a direct determination of an effective cross-section σ_{vis} [⊛] by separating the two colliding beams and measuring a counting rate proportional to the rate of inelastic pp interactions [63]. It has been demonstrated that irrespective of the beam shape, the integral of the counting rate curve obtained from sweeping the two beams across each other over the entire region where pp collision occur, can be used to evaluate an effective cross-section. The original proposal envisaged the application of the method at the ISR, where the beams

[‡] In the approximation of zero emittance the velocities are the same within one bunch.

[⊛] The measured σ_{vis} is a detector-dependent cross-section, related to a process whose measurement is straightforward. For more details see Section 4.1.

were not bunched and collided with a crossing angle in the horizontal plane. Therefore a scan only in the vertical plane was necessary. An extension of the method was proposed for its application in the SPS, where the colliding beams were bunched and collided head-on [64]. In this case a scan of the plane perpendicular to the beam ($x-y$ plane) was needed. It has been shown that if the beam shapes are factorisable in their x and y components, the procedure can be simplified to two scans in both transverse directions, avoiding the need to perform a scan of the full transverse plane. Recently, a rigorous proof has been given of the validity of the VDM method for bunched beams colliding with an arbitrary crossing angle and for arbitrary orientation of the scanning plane [62]. Consequently, for the VDM scans at the LHC, the following general formula can be used:

$$\sigma_{\text{eff}} = \frac{\int R(\Delta_x, \Delta_{y_0})\mathrm{d}\Delta_x \int R(\Delta_{x_0}, \Delta_y)\mathrm{d}\Delta_y}{N_1\, N_2\, f\, \cos\alpha\, R(\Delta_{x_0}, \Delta_{y_0})} \tag{1.10}$$

where N_1 and N_2 are the intensities of the two colliding bunches, which need to be taken from an independent measurement, f is the revolution frequency, α is the half crossing angle and $R(\Delta_x, \Delta_y)$ are the event rates corresponding to the process with cross-section σ_{eff}. These rates are measured when the beams are displaced by Δ_x and Δ_y with respect to the nominal "working" point (x_0, y_0). The range of the displacements Δ_x and Δ_y need to ensure that the full profiles of the beams are explored. In addition, the relation between the transverse displacement parameters (currents in the steering magnets) and the actual displacement needs to be known on an absolute scale. For this purpose, a dedicated length-scale calibration needs to be done with the help of the vertex detector of the experiment. Finally, in the application of the VDM method several effects need to be taken into account: tails of the transverse bunch distribution and bunch evolution during the scans (shape distortions or transverse kicks due to beam-beam effects, emittance growth, bunch-current decay). It is assumed that these effects either are negligible or can be corrected for.

As already mentioned, the VDM method has been applied at the ISR. The reported uncertainty is about 1% and is dominated by the knowledge of the absolute value of the displacements during the scan [48, 65]. Subsequently the VDM method becames a standard tool for absolute luminosity determination at hadron and heavy-ion colliders, surpassing the precision achieved with other direct methods. The LHCb absolute luminosity measurements performed with the April and October 2010 VDM scans are described in Chapter 6.

Beam-gas imaging (BGI) method The BGI method [6] is based on the reconstruction of interaction vertices between beam protons and nuclei of the residual gas in the beam vacuum pipe. This allows one to obtain an image of the transverse bunch profile along its trajectory and to determine the positions and the angles of the beams. The precision of the measured beam parameters can be improved by using the constraint provided by the luminous region. The measured beam parameters are then used to calculate the overlap integral of a given pair of colliding bunches and to estimate

the corresponding luminosity. In other words, the BGI method uses Eq. (1.9) directly. Neglecting the crossing angle and beam positioning offsets Eq. (1.9) reduces to:

$$L = \frac{N_1 \, N_2 \, f}{2\pi \sqrt{(\sigma_1^{x2} + \sigma_2^{x2}) \left(\sigma_1^{y2} + \sigma_2^{y2}\right)}} \tag{1.11}$$

where $\sigma_{1,2}^{x,y}$ are the Gaussian beam widths (for a more exact formula see (7.1)).

For the application of the BGI method a vertex resolution is needed that is comparable or smaller than the transverse beam widths. Also, the geometrical acceptance of the vertex detector should allow the detection of a large fraction of the interaction products of the beam-gas interactions in the vicinity of the IP. The residual gas in the beam vacuum pipe consists mainly of relatively light elements such as hydrogen, carbon and oxygen. The hydrogen gas, H_2, is dominant. Therefore, the expected rate of beam-gas interactions for one bunch of N protons traversing a region with length d and density n is $R \approx 2\, n\, d\, \sigma_{pp}\, f\, N$. For LHCb, approximate realistic values are $n = 10^{13}$ molecules/m^3 [66], $d = 1$ m, $\sigma_{pp} = 37$ mb (inelastic cross-section of 7 TeV protons on protons at rest, *i.e.* $\sqrt{s} = 81$ GeV) [67], $f = 11245$ Hz and $N = 10^{11}$ protons. Thus, the expected rate of beam-gas interactions which can be reconstructed with the LHCb vertex detector is about 0.08 Hz per bunch (assuming full acceptance and reconstruction efficiency). An important prerequisite for the application of the BGI method is that, in case of inhomogeneity, the transverse profile of the residual gas should be known.

Compared to the VDM method, the disadvantage of a small rate is balanced by the advantages that the method is non-disruptive, the beams do not move and, at least in principle, the method can be applied while taking physics data. The beam-gas rate can be increased by a limited, controlled increase of the residual vacuum pressure in the vertex detector without danger to the experiment. Similarly to the VDM method, the BGI method relies on an independent measurement of the bunch intensities.

Chapter 2

The Large Hadron Collider

The Large Hadron Collider (LHC) has been designed to produce high-energy proton-proton collisions whose study allows us to improve our understanding of the fundamental laws of Nature. In this chapter an overview is given of the LHC layout, its operation and the physics goals of its experiments. Attention is drawn to technical details, operational procedures and beam instrumentation devices that play an essential role for the luminosity production and determination. These details complement the description of the LHCb detector and the analysis methods discussed in the subsequent chapters of this thesis.

2.1 CERN and the Large Hadron Collider

CERN accelerator complex

The current flagship of CERN's particle physics research is the Large Hadron Collider (LHC) [4, 5]. It is a 27-km long circular accelerator designed to produce proton-proton collisions with the unprecedented center-of-mass energy 14 TeV. Before the protons reach this high energy they pass through several stages of acceleration. A schematic of the system of particle accelerators at CERN is shown in Fig. 2.1.

Only a subset of the large number of accelerators is used to deliver protons to the LHC. Initially, a gas cylinder supplies hydrogen atoms to the source chamber of a linear accelerator. There the hydrogen atoms are ionised, yielding bare protons and electrons. The protons go in packets (bunches) through all their steps of acceleration. First, at LINAC2, the particles reach a kinetic energy of 50 MeV. Later they get accelerated by the Proton Synchrotron Booster, a versatile circular accelerator with four parallel rings. At a kinetic energy of about 1.4 GeV the protons are transferred to the Proton Synchrotron (PS), where they are further accelerated and reach an energy of about 25 GeV. For the fourth and last-before-LHC stage of acceleration the proton packets are injected into the Super Proton Synchrotron (SPS). The 7-km circumference SPS accelerates the protons to 450 GeV before injecting them into LHC via two transfer lines. At the LHC the proton beams are accelerated to 7 TeV and

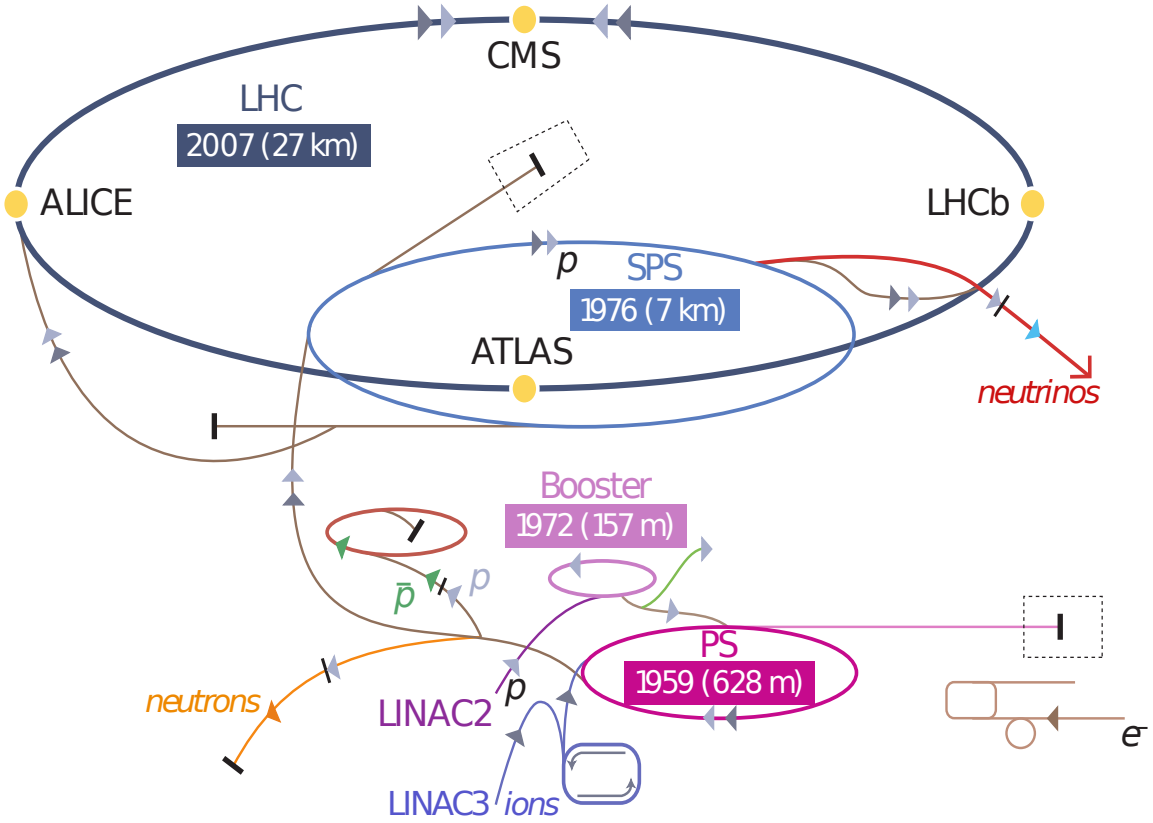

Figure 2.1: A schematic of the system of particle accelerators at CERN, indicating the startup year and the length of some of the major devices. The LHC proton accelerator chain includes the linear accelerator LINAC2 and the circular accelerators Proton Synchrotron Booster (Booster), Proton Synchrotron (PS), Super Proton Synchrotron (SPS) and finally, the LHC. For the LHC operation with ions, lead nuclei are accelerated in LINAC3 and the Low Energy Ion Ring (LEIR) before they enter the PS and follow the same path as protons.

travel in opposite directions in separate vacuum beam pipes. The two beams intersect at four points along the LHC ring where four detector complexes register the products of their collisions.

Large Hadron Collider

The LHC is a two-ring superconducting hadron accelerator and collider, designed to provide proton-proton collisions with center-of-mass energy of 14 TeV [5]. The LHC is situated in an underground tunnel with circumference 27 km, which hosted the Large Electron-Positron Collider (LEP) between 1989 and 2000. The LHC lies between 45 m and 170 m below the surface and has eight straight sections and eight arcs with radius of almost 3 km. In the middle of four of the straight sections there are underground caverns hosting the detector complexes of the four main LHC experiments. The other four straight sections accommodate major collider systems: the radio-frequency (RF) system, which accelerates the beams and keeps them bunched is located in insertion

region 4 (IR4)⋆, the beam dump system, which is used for extracting the beams from the LHC is located in IR6, and beam cleaning devices, which are essential for the machine protection are placed in IR3 and IR7 (see Fig. 2.2).

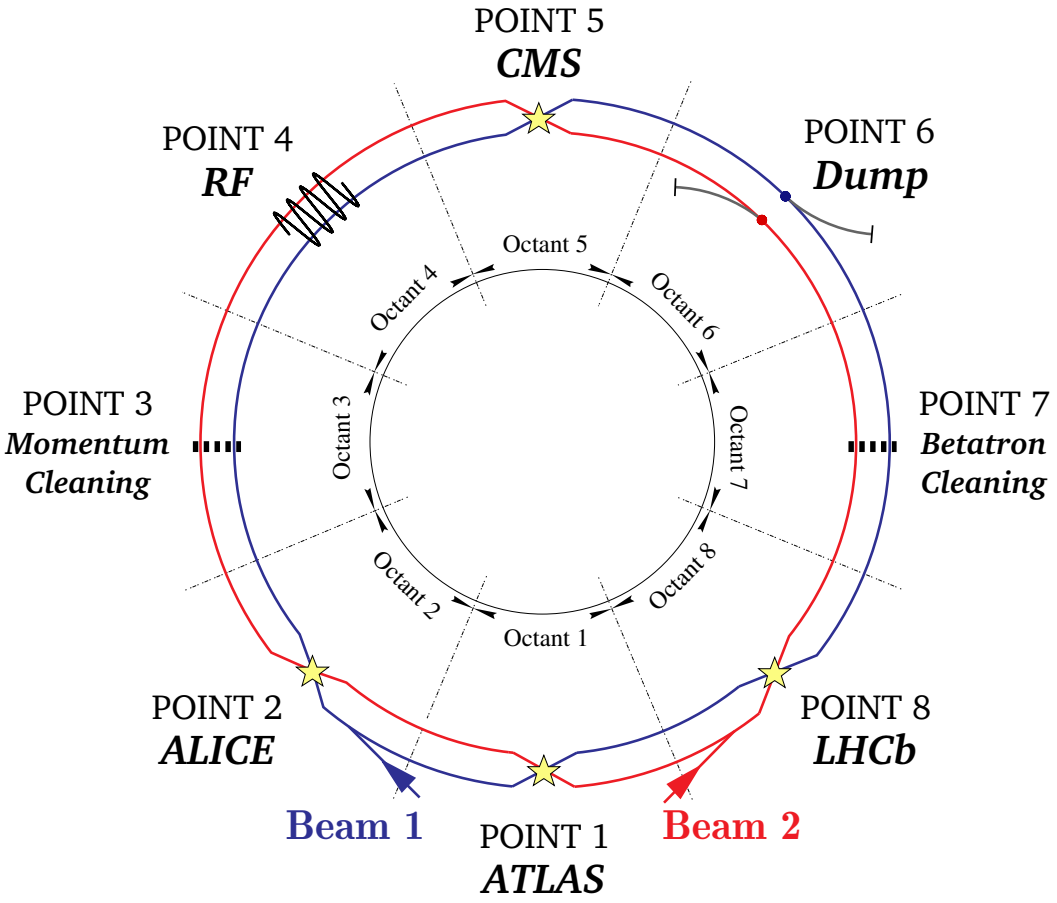

Figure 2.2: Layout of the LHC. The two beams circulating in opposite directions intersect at four points. The detector complexes of the ATLAS (IR1), ALICE (IR2), CMS (IR5) and LHCb (IR8) experiments surround the intersection points and register the products of the colliding beams. The RF, dump and beam cleaning systems are located at the other four insertion regions.

The curved sections along the LHC ring are equipped with more than a thousand cryodipoles which can provide a magnetic field greater than 8 T to guide the high-energy beams along the circular trajectory. The various functions of the straight sections are fulfilled by a variety of normal and superconducting magnets [5]. A unique feature of the LHC magnet system is the use of NbTi superconducting windings cooled by superfluid helium at 1.9 K. In addition, almost all of LHC superconducting magnets adopt the "two-in-one" design, where the windings for the two beam channels are accommodated in a common cold mass and cryostat (see Fig. 2.3).

⋆ An insertion region (IR) is a part of the accelerator, located between two neighbouring arcs. The interaction points (IP) are located in the middle of the insertion regions (except for IP8, see section 2.2.4) [5].

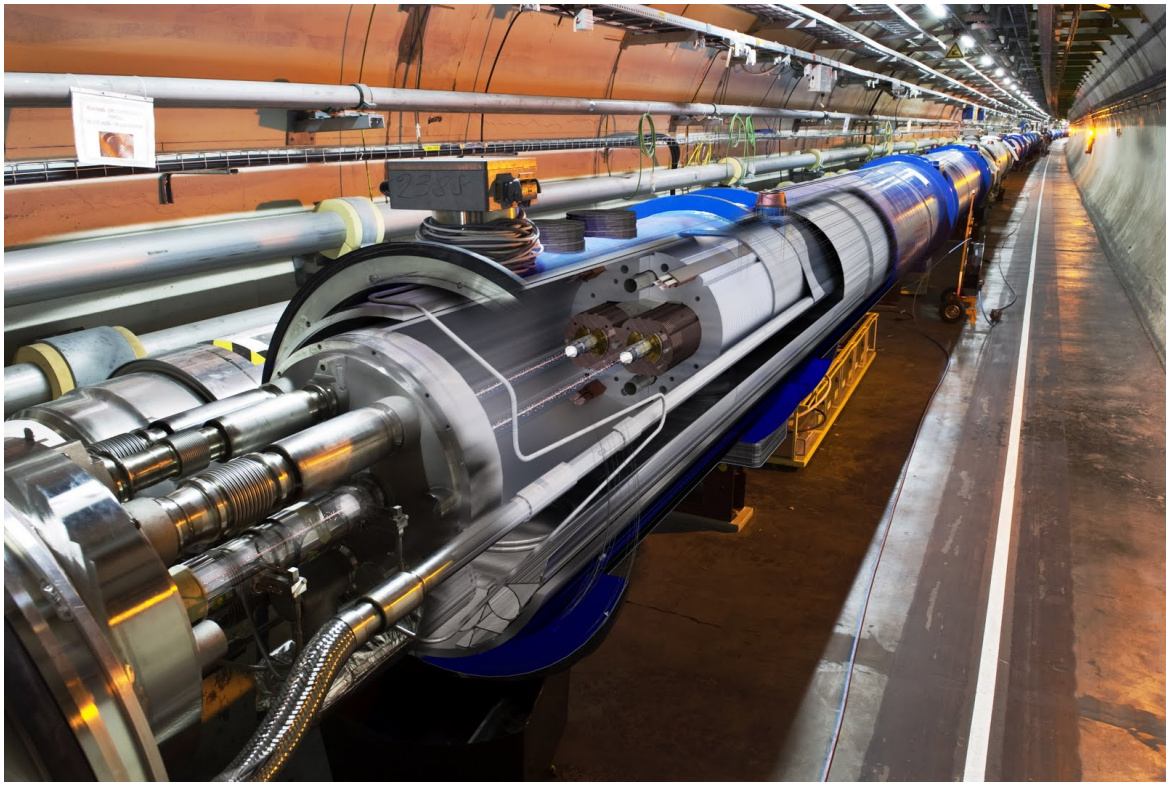

Figure 2.3: An illustration of the LHC tunnel, where the inner structure of one of the superconducting dipoles and the complex interconnection with a neighbouring magnet can be seen. The twin aperture of these dipoles allows a single cryostat to be used for both magnets.

Physics goals of the LHC project

The primary goals of the LHC and its experiments are to test the *Standard Model* (SM) description of particle physics and to look for direct or indirect evidence of the existence of new particles and interactions:

- there are indications that, if it exists, the Higgs boson should be observed at the LHC [68];
- at these very high energies particles beyond the SM predictions are also likely to be produced. For instance, particles arising from supersymmetry (SUSY) are hoped to be seen;
- high-precision b-physics measurements will attempt to unravel *New Physics* via rare decay channels or subtle CP violation effects;
- in dedicated runs the LHC will provide heavy ion collisions (*e.g.* Pb-Pb), instead of *pp* collisions, to study the behaviour of nuclear matter in extreme conditions and the formation of a quark-gluon plasma.

Two of the LHC experiments, ATLAS (A Toroidal LHC Apparatus System) [69], located at Interaction Point 1 (IP1, see Fig. 2.2) and CMS (Compact Muon Solenoid) [54], located at IP5, are referred to as general-purpose detectors (GPDs). Their physics goals include all of the points mentioned in the list above. Generally speaking, both detector

complexes comprise subsystems with similar functions, but because of different technical approaches and different emphasis on each of the subsystems, the two GPDs differ in performance and complement each other.

The other two LHC experiments have specialised purposes. ALICE (A Large Ion Collider Experiment) [70], located at IP2, is designed for the detection of heavy ion collisions and the study of the quark-gluon plasma. The LHCb (Large Hadron Collider beauty) experiment [1, 2, 3], located at IP8, is optimised for precise studies of CP violation in the B-meson systems and searches for *New Physics* through rare B-meson decays. The specialised LHC experiments have chosen detector geometries and technical approaches that are complementary to those of the GPDs and are tailored to their specific physics goals.

LHC startup

The first proton beams circulated in the LHC in September 2008. Several days later an incident damaged a fraction of the bending magnets and the decision was taken to resume operation at a lower energy and only after the installation of a new magnet protection system. The LHC delivered its first collisions at injection energy (0.45 TeV per beam) in the end of 2009 and shortly thereafter set a new world energy record by accelerating protons to 1.18 TeV. In 2010 the LHC operated at half its nominal energy and produced collisions at 7 TeV center-of-mass energy (3.5 TeV per beam). During its first year of operation the world's most powerful accelerator showed steady progress, increasing the collision rate from merely a fraction of a Hz to about 3 MHz, and delivered about 40 pb^{-1} to the ATLAS, CMS and LHCb experiments✦.

Further progress marked 2011 as well: the total number of bunches per beam increased to 1380 thanks to the reduced bunch spacing, the individual bunch populations exceeded the nominal value of 1.15×10^{11} protons and the beams were focused even stronger at the interaction points. With these beam parameters the LHC was able to deliver luminosity larger than 10^{33} cm^{-2} s^{-1} and to set a world record for luminosity at hadron colliders. According to the current schedule the nominal LHC energy (14 TeV in the center-of-mass) and luminosity (10^{34} cm^{-2} s^{-1}) will be reached only after the shutdown planned for 2013–2014.

2.2 Characteristics and operation

2.2.1 Beam dynamics

As a type of accelerator the LHC is a synchrotron, meaning that the magnitude of the magnetic field used to bend the particles is increased synchronously with their energy. The motion of the individual (charged) particles is governed by the

✦ For its optimal operation the ALICE detector requires lower instantaneous luminosity and measures were taken to reduce the proton-proton interaction rate at IP2.

Lorentz force, $\vec{F}$:

$$\vec{F} = e\left(\vec{E} + \vec{v} \times \vec{B}\right) \ , \tag{2.1}$$

where e is the electric charge of the particle, $\vec{v}$ is its velocity, and $\vec{E}$ and $\vec{B}$ are the electric and magnetic fields. This force is applied as a *bending* force (using dipole magnets) to guide the particles along a predefined ideal trajectory (also called *reference orbit*) and as *focusing* force (using quadrupole magnets) to confine the particles in the vicinity of the ideal path [§]. The single particle motion in the directions transverse to the reference orbit has the form of a pseudo-harmonic oscillation with varying amplitude [71]:

$$\xi(s) = A\sqrt{\beta_\xi(s)}\cos(\phi_\xi(s) + \phi_0) \ , \tag{2.2}$$

where $\xi = x, y$ and s are the transverse and longitudinal coordinates, respectively, $\beta_\xi(s)$ and $\phi_\xi(s)$ are determined by the arrangement of magnets along the design orbit (accelerator *lattice*), and A and ϕ_0 are constants that depend on the initial conditions and define individual particle trajectories [❖]. This oscillation around the reference orbit is called betatron motion and $\beta_\xi(s)$ - *betatron function*. The symbol $\beta^\star$ is used to signify the value of the betatron function at the point where the two beams collide. The amplitude of the betatron oscillations depend on the lattice and the constant A, whose square is referred to as transverse *emittance* ϵ.

The transverse spread of a particle ensemble around the reference orbit can be characterised by the area the particles occupy in the (x, x', y, y') phase space [72]. Here, x and y are the transverse coordinates and x' and y' are the momentum slopes p_x/p_z and p_y/p_z. Using this phase space area several definitions of the transverse *beam emittance* can be given [72]. The transverse beam emittance describes the compactness of the beam in (ξ, ξ') phase space and together with the betatron function it determines the transverse beam width σ at a given point along the reference orbit s:

$$\sigma_\xi(s) = \sqrt{\beta_\xi(s)\,\epsilon_\xi(s)} \ , \ \xi = x, y \tag{2.3}$$

When the beam is accelerated its emittance is reduced, due to the increase of its longitudinal momentum. On the other hand, the transverse *normalised* emittance $\epsilon_n = \beta_r\gamma_r\epsilon$ does not change during acceleration (under certain conditions) and is used as an essential beam characteristic. Here, β_r and γ_r are the relativistic velocity and γ-factor. The nominal transverse normalised emittance of the LHC beam is 3.75 μm rad in both transverse coordinates [¶].

[§] A single quadrupole focuses in one of the planes transverse to the beam direction and de-focuses in the other. At the LHC the "strong focusing" mechanism is used, where focusing in both transverse planes is achieved with alternating focusing/defocusing quadrupoles.

[❖] We assume that the motion in the two transverse coordinates is decoupled.

[¶] Smaller than nominal values of the transverse beam emittance have been achieved and used in physics fills.

2.2.2 Filling scheme

The beam injected in the LHC is captured, accelerated and stored using a 400 MHz superconducting radio-frequency (RF) system. The frequency of the RF system determines the spacing between consecutive RF buckets, where proton bunches can be stored. For the LHC the bucket-spacing is 2.5 ns and, taking into account the accelerator length, the total number of RF bunch slots is 35640. However, according to the design, only every 10^{th} RF bucket can be filled with protons, which leads to a minimal bunch separation of 25 ns. As explained below, due to different constraints not all of the allowed 3564 slots will be filled with particles.

As mentioned in Section 2.1, the proton bunches are created and accelerated in the LHC injector complex and then delivered to the LHC via two transfer lines. The particular sequence of filled and empty bunch slots is called *filling scheme*. A number of constraints need to be taken into account in the design of a filling scheme [73, 74]: the rise time of the LHC injection and dump *kickers*, the displacement of the LHCb interaction point (see Section 2.2.4) and others. The principal filling scheme of the LHC foresees a total number of 2808 bunches per beam, distributed into 39 batches (or *trains*) of 72 bunches. The bunches in each train occupy consecutive bunch slots and therefore are separated by 25 ns, corresponding to a distance of about 7.5 m.

In the early running period of 2010 the beams consisted of only a few bunches, separated by a hundred or more empty 25 ns slots. Later in the year, when the intensity limit imposed by the machine protection was increased, multi-bunch injections were performed allowing the LHC to be filled faster. The individual bunches in these trains were separated by 150 ns.

The individual bunches are identified by the RF bucket they occupy. In LHCb, the bunch-crossing identifier (BCID) is used to label the 3564 25 ns slots and is associated to the RF bucket of beam1 by the relation BCID = (RF bucket + 9)/10 [75]. For beam2 the correspondence is BCID = (RF bucket + 9)/10 + 894, modulo 3564. To have a collision between two bunches at LHCb their bucket numbers must satisfy the following relation: RF bucket beam1 − RF bucket beam2 = 8940. The LHCb bunch ID counting ensures that bunches with equal BCID in the two beams collide at the LHCb IP.

2.2.3 Beam instrumentation

In this section a brief description is given of the devices used to measure the *intensity* and the *position* of the two LHC beams.

Beam current transformers

The measurement of the absolute bunch intensity at the LHC is provided by two separate types of current transformers [76, 77, 78]. One type, the DCCT (DC Current Transformer), measures the total current circulating in each ring, irrespective of the

bunch structure of the beams. The other type, the FBCT (Fast Beam Current Transformer), is capable of measuring the bunch populations in each of the 3564 nominal (25 ns) bunch slots. Separate devices are used to measure the intensity of the two LHC beams. For both types of current transformers two identical and independent systems (A and B) are used. The system A is primarily used for measurements, while system B is intended for tests and development. In the April-May 2010 running period both DCCT systems were stable and provided reliable information, while only the FBCT system A could be used for analysis.

The beam current transformers are an essential part of the LHC beam instrumentation. The beam intensity measurements they provide are necessary for evaluating the beam presence, safe beam conditions and beam lifetime. While their machine protection functions demand high reliability and availability, their role in the absolute luminosity determination adds the most stringent precision requirements. The beam intensity measurements used in the absolute luminosity determination with the van der Meer and beam-gas imaging methods are described in Chapter 5.

Beam position monitors

Beam position monitors (BPMs) are necessary for the determination of beam orbit and associated parameters. The BPMs provide essential information needed for the operation of the accelerator. The BPM system at the LHC consists of about a thousand monitors, spread all over the two LHC rings [5]. All BPMs measure the beam position in both horizontal and vertical planes. Depending on the specific type, the BPMs contain four button electrodes or four striplines, positioned in a plane perpendicular to the beam trajectory. The detection of the electromagnetic signal induced by the passage of the beam allows the transverse beam position to be determined.

All four interaction points of the LHC are equipped with directional stripline position monitors (BPMSW [5]), which provide independent measurements for the two beams[✠]. At the insertion regions of the four experiments the directional BPMs are located inside the final focusing quadrupoles Q1 (see Fig. 2.4) and their measurements can be used to determine the beam angles at the IP [79].

2.2.4 Operational aspects

Beam crossing angle

The high design luminosity at the LHC requires an operation with a large number of bunches. The small distance between consecutive bunches (25 ns) and the large length of the sections where the two beams travel in a common vacuum chamber (about one hundred meters) implies that along with the nominal beam-beam encounters at the experiment interaction points there will be a large number of parasitic collision

✠ Note that the use of directional BPMs is needed only in the regions where the two beams travel in a common vacuum pipe.

points[‡]. As these parasitic encounters degrade the beam stability and lifetime, and may cause unwanted background for the experiments, the beam trajectories must be adjusted such that the two beams collide with a small crossing angle [80, 81]. The LHC baseline foresees crossing angle in the vertical plane at IR1 and IR2, and crossing angle in the horizontal plane at IR5 and IR8 [5]. Half crossing angles of about 100 μrad provide sufficient separation between the bunches in the nominal parasitic collision points. The crossing angle reduces the overlap of the two beams at the interaction point and therefore has the effect of decreasing the luminosity, see Eq. (7.10).

The detector setup of the ALICE and LHCb experiments includes powerful dipole magnets. These magnets induce an additional "internal" crossing angle in the corresponding IP. The effect of the experiment dipoles on the beam orbit is compensated with other magnets ("compensators") located near the interaction point (see Fig. 2.4). The net crossing angle at the interaction point is determined by the sum of the internal and the "external" crossing angles, where the latter is defined by crossing angle bumps aimed at avoiding parasitic collisions in the common vacuum chamber of the two beams.

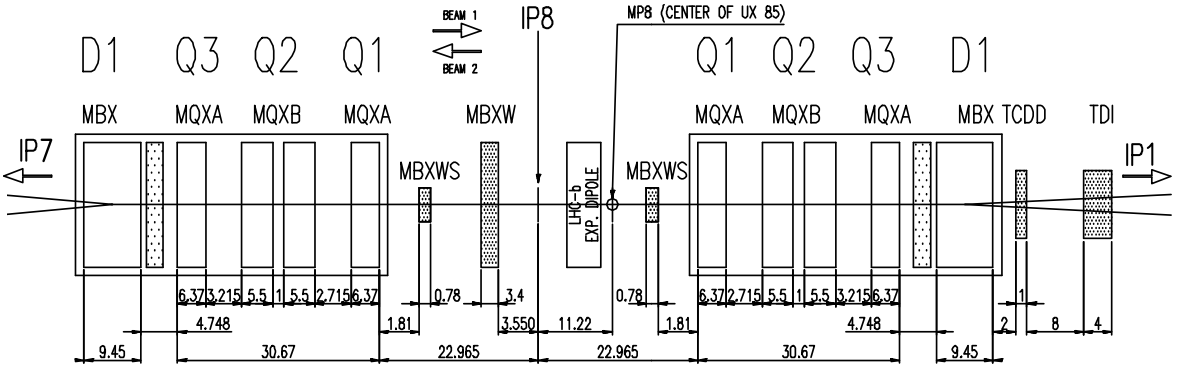

Figure 2.4: Arrangement of magnets in the vicinity of the LHCb interaction point. The dipole magnets D1 steer the two beams in the transition from separate to common vacuum chambers. The quadrupole triplets Q1-Q3 provide the final focusing of the two beams before they collide. The LHCb interaction point (IP8) is displaced from the centre of LHC octant 8 (MP8) (see Fig. 2.2) by 11.22 m to allow the LHCb experimental setup to fit into the existing underground cavern. Also indicated are the LHCb dipole magnet and its three compensator magnets MBXW(S). All distances are in meters.

A somewhat relevant peculiarity of the LHCb interaction point is that it is shifted by 1.5 bunch-spacings, *i.e.* by about 11.22 m towards IP7 in order to accommodate the experimental setup of LHCb in the already existing underground cavern. This shift leads to complications in the design of filling schemes which provide maximal

[‡] The spatial separation between two collision points in the common vacuum chamber is $d \approx c\,\Delta t/2 \approx 3.75$ m, where we approximate the bunch velocity with the speed of light c, and Δt is the bunch time separation. Therefore, the number of parasitic collision points at IR8, which is equipped with a 126 m long common vacuum chamber, is 32 [4].

number of colliding bunches for all experiments, and to the fact that different bunches will collide a different number of times per turn. The consequences of the latter on the beam dynamics are discussed in [82].

Filling sequence and control of the beam position at the IP

The operational procedure of the LHC includes several stages, represented schematically in Fig. 2.5. Initially, bunches of particles are accumulated at the LHC by consecutive injection from the SPS. At this stage the beam energy is 450 GeV and the $\beta^\star$ is 11 m and 10 m at IP1/IP5 and IP2/IP8, respectively [83]. Then, the two beams are accelerated until the desired energy is reached (energy "ramp"). The next step is to reduce the beam size at the interaction points by increasing the strength of the final focusing magnets (beam "squeeze").

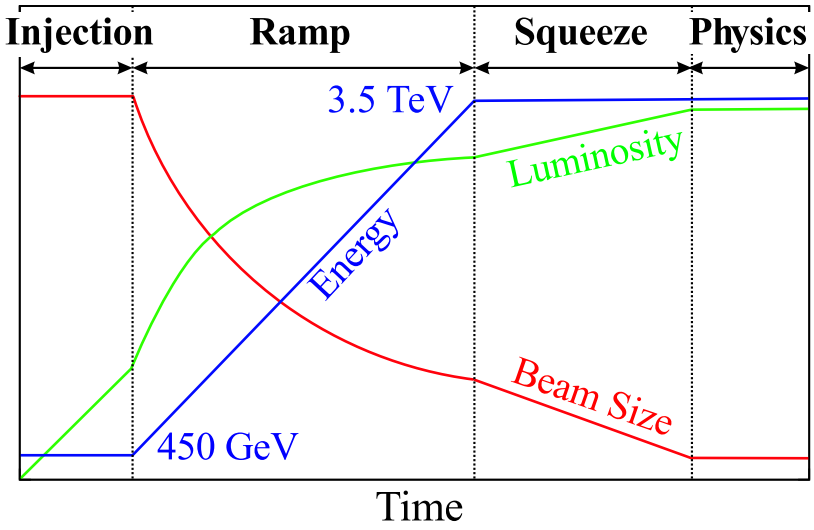

Figure 2.5: Essential steps during a physics fill and the relative evolution of the beam energy, the beam size and the theoretical luminosity (the shown luminosity trend neglects the fact that the beams are kept separated at the IP before reaching "Physics"). Initially the beams are injected at the LHC with energy of 450 GeV. During "Ramp" the beam is accelerated. As a consequence, the transverse beam emittance decreases, which leads to a decrease of the transverse beam size and to an increase in the theoretical luminosity (see Eqs. (2.3) and (1.11)). In the "Squeeze" step, the $\beta^\star$ is reduced in order to decrease additionally the beam size at the IP. During "Physics" stable colliding beams are provided to the experiments. Figure reproduced from [79].

During all these steps, which nominally take a total time of less than an hour [4], the two beams are kept separated at the interaction points in order to avoid collisions and beam disturbance during the ramp and squeeze stages. Then, the beams are brought into collision and the experiments start taking data ("physics" mode). A detailed description of the different accelerator and beam modes can be found in [84]. During the time the two beams collide the luminosity decreases due to an increase of

the transverse beam size and a decrease of the beam intensity ⊛. After a certain period of time (roughly, 10 hours) it becomes more profitable from the integrated luminosity point of view to dump the beams and start a new fill. Also, a number of unforeseen events can lead to premature dump of the beams as well. After a beam dump the LHC magnet currents need to be ramped down to their injection values before the preparation of a new fill can start.

The separation of the beams at the interaction point is controlled by six orbit corrector magnets [79]. The MCBC and MCBY magnets are located far from the IP and control the two beams independently, while the MCBX magnets are located in the region with common vacuum chamber and steer the two beams simultaneously. The orbit corrector magnets are needed to centre precisely the two beams at the collision point. The luminosity optimisation is done with the help of the LHC luminosity monitors, located some 100 meters away from the IP [85], and the luminosity reported to the LHC by the experiments. The same orbit corrector magnets are used also for steering the beams during the van der Meer scans.

It should be noted that unexpected beam orbit behaviour has been observed when the MCBX magnets were used to steer the beams [79], a possible explanation being large hysteresis effects in these magnets. The observed magnet errors imply that the MCBX magnets should not be used for fine tuning and optimisation of the beam position at the IP. The use of the distant corrector magnets of type MCBC and MCBY alone provides the necessary flexibility, but certain restrictions on the beam orbit arise from machine protection point of view [79]. These restrictions do not present a problem during normal operation, where only small variations of the beam position are needed to centre the two beams. The van der Meer scan procedure requires larger beam displacement at the IP in order to measure the full beam overlap. It has been found that the beam displacement margins corresponding to the use of the MCBC and MCBY magnets alone are sufficient for the application of the van der Meer method when the two beams are initially separated and then moved in opposite directions [79].

⊛ The "luminosity leveling" procedure used in LHCb allows the luminosity to be kept constant (and lower than the maximal achievable) during the fill by adjustment of the relative transverse position of the two beams at the IP.

Chapter 3

The LHCb experiment

The Large Hadron Collider beauty experiment (LHCb) [1, 2, 3] is dedicated to precise measurements of CP violation and rare decays of charm and beauty hadrons. A significant part of the physics programme involves searches for indirect evidence of *New Physics**. For example, one of the decay modes where sizeable effects of yet-unknown particles could be found is $B_s^0 \to \mu^+\mu^-$. LHCb will measure the very small branching fraction of this decay down to the value predicted precisely by the Standard Model ($3.2 \pm 0.2 \times 10^{-9}$ [86]) and therefore will be able to give conclusive answer if this decay mode is influenced by New Physics. Another place where LHCb will be able to improve the current experimental precision is the measurement of the mixing-induced CP-violating phase in $B_s^0 \to J/\psi\phi$ decays. A detailed description of these and several other heavy-flavor subjects, where LHCb can make large impact already during the early period of data-taking, can be found in [87]. The LHCb physics programme includes also precision electroweak measurements, studies of lepton flavor violation and various exotic searches.

As detailed in Section 1.1, the precise measurement of the absolute luminosity is essential for the determination of cross-sections for different processes. The comparison between the measured and theoretically calculated cross-sections will improve our understanding of QCD and of the structure of the proton. Consequently, this will allow better theoretical predictions to be made for the processes within the Standard Model and therefore will facilitate the search for New Physics.

This chapter begins with a brief overview of the LHCb experiment. Later are described the components which play an essential role in the absolute luminosity measurement at LHCb: the tracking system, the calorimeters and the trigger system.

No description is given of the Ring Imaging Cherenkov (RICH) and muon detectors, as their measurements are not used in the present analysis. Detailed description of these detector systems can be found in the respective technical design documents, [88] and [89], and in a more recent LHCb detector paper [1].

* Usually, the term *New Physics* refers to theoretical models which go beyond the well established *Standard Model* of particle physics. Particles and interactions which do not have explanation within the Standard Model are generically called "New Physics".

3.1 Overview

b-hadron production

Owing to its unparalleled energy and instantaneous luminosity reach, the LHC is the most copious source of b-hadrons ✦ in the world. All known types of b-mesons and b-baryons are produced. The dominant heavy-quark production processes at the LHC are the quark-antiquark annihilation and the gluon fusion (see Fig. 3.1).

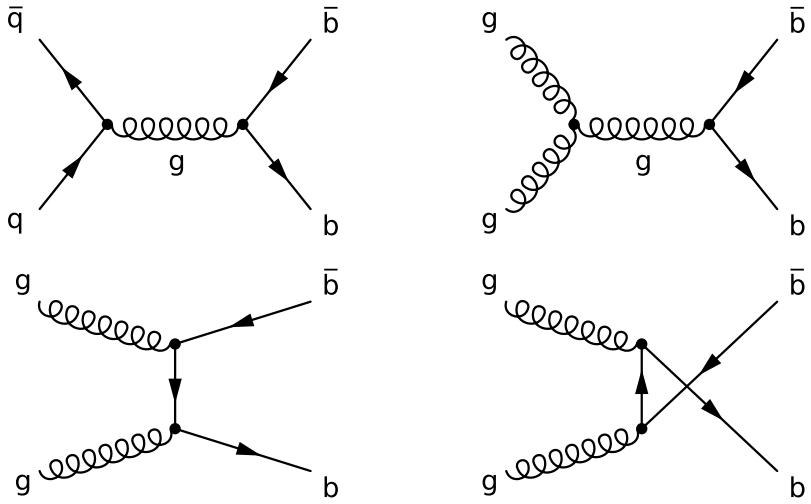

Figure 3.1: Feynman diagrams of leading order contributions to the process of $b\bar{b}$ production in hadron collisions. The diagrams correspond to quark-antiquark annihilation (top left) and gluon fusion (the rest).

An estimate of the expected heavy-flavored hadron yields can be obtained with the help of the production cross-section for the relevant process. As explained in Section 1.1.1, the cross-section calculations for hard processes can be done in the framework of perturbative QCD. The cross-section predictions based on next-to-leading order (NLO) calculations for selected LHC benchmark processes can be seen in Fig. 1.1. In particular, the total b-quark production cross-section in 14 TeV pp collisions is estimated to be 633 μb [2].

An important property of the b-hadrons produced at the LHC is their angular distribution. In high-energy pp collisions the beauty hadrons are predominately produced in pairs in the forward or backward cone, see Fig. 3.2. Taking into account the LHCb acceptance and using a conservative approximation of 500 μb for the total $b\bar{b}$ production cross-section at 14 TeV, the yield of b-hadrons in LHCb has been estimated to 10^{12} per nominal year [2].

As mentioned in Section 1.1.2, LHCb has measured the total and differential b-hadron production cross-section at $\sqrt{s}$ =7 TeV, using two different methods. The obtained total $b\bar{b}$ cross-sections are $288 \pm 4 \pm 48$ μb [25] and $284 \pm 20 \pm 49$ μb [31]. Both

✦ Here, the term "b-hadron" is used to designate hadrons containing a b or $\bar{b}$-quark.

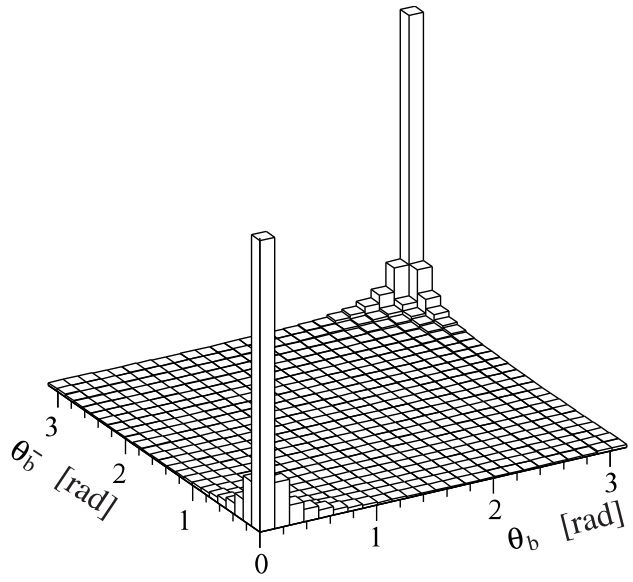

Figure 3.2: Polar angle distribution of the b and $\bar{b}$-hadrons produced in pp collisions at LHC energies generated with PYTHIA. The two hadrons are predominantly produced both forward ($\theta \approx 0$) or both backward ($\theta \approx \pi$). (From [3]).

the inclusive and the transverse-momentum differential cross-section measurements show an excellent agreement with the theoretical predictions.

Detector layout

The LHCb detector is a single-arm forward spectrometer with a polar angle coverage from 10 to 300 mrad in the bending (horizontal) plane and from 10 to 250 mrad in the non-bending (vertical) plane, see Fig. 3.3.

The detector geometry has been optimised for the detection of b-hadrons, which are predominately produced in the forward or backward cone (see Fig. 3.2). In order of increasing distance to the interaction point, the LHCb detector components are: the vertex detector (VELO), the first RICH detector (RICH1), the Tracker Turicensis (TT), the spectrometer magnet, three tracking stations (T1-T3), each consisting of independent silicon and straw tube tracking detectors, the second RICH detector (RICH2), the calorimeter system, comprising a scintillating pad detector (SPD), pre-shower detector (PS) and electromagnetic and hadronic calorimeters (ECAL and HCAL) and five muon stations (M1-M5).

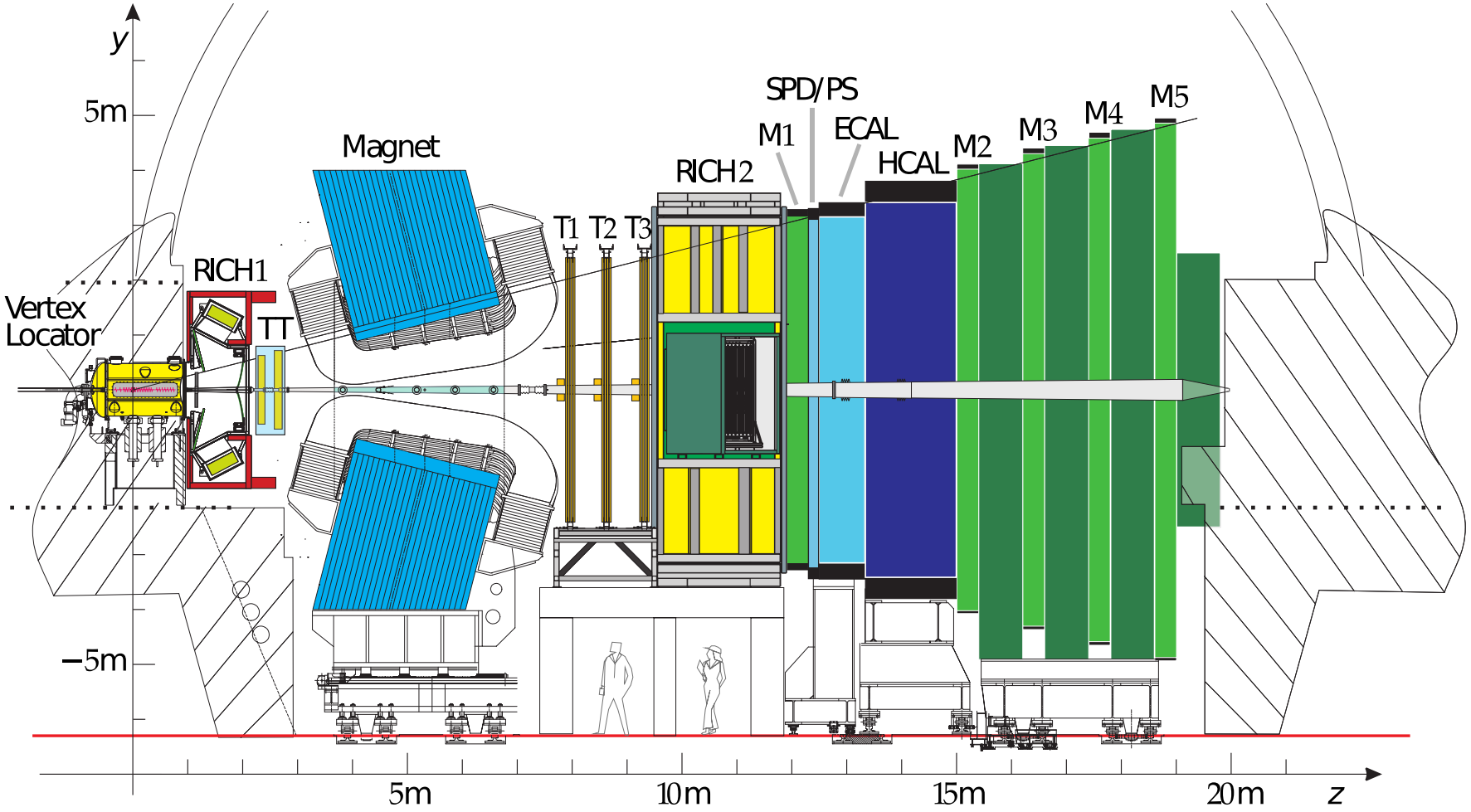

Figure 3.3: Side view of the LHCb spectrometer with labels for the main detector sub-systems: vertex detector 'Vertex Locator', particle identification detectors 'RICH1' and 'RICH2', tracking stations on either side of the dipole magnet - 'TT' and 'T1' to 'T3', calorimeter system including scintillating pad detector 'SPD', preshower 'PS', electromagnetic and hadronic calorimeters ('ECAL' and 'HCAL') and five muon detectors 'M1' to 'M5'.

A standard right-handed coordinate system has been adopted, where the z axis is aligned with the direction of beam1 and the y axis is along the vertical. The polar angle is defined with respect to the z axis. In terms of pseudorapidity [§] the LHCb acceptance is approximately $1.9 < \eta < 5.3$.

The design instantaneous luminosity for LHCb is $2 \times 10^{32}\text{cm}^{-2}\text{s}^{-1}$ [1]. This value, albeit 50 times lower than the expected reach of LHC, has been found optimal for the physics goals of LHCb as it incorporates high pp interaction rate and low probability for multiple interactions in a single bunch-crossing [❖]. The latter requirement arises from the need to measure secondary vertices of b-hadrons, which typically are displaced by a few mm from the primary interaction. The probability for different number of pp interactions per bunch-crossing as function of the instantaneous luminosity is shown in Fig. 3.4.

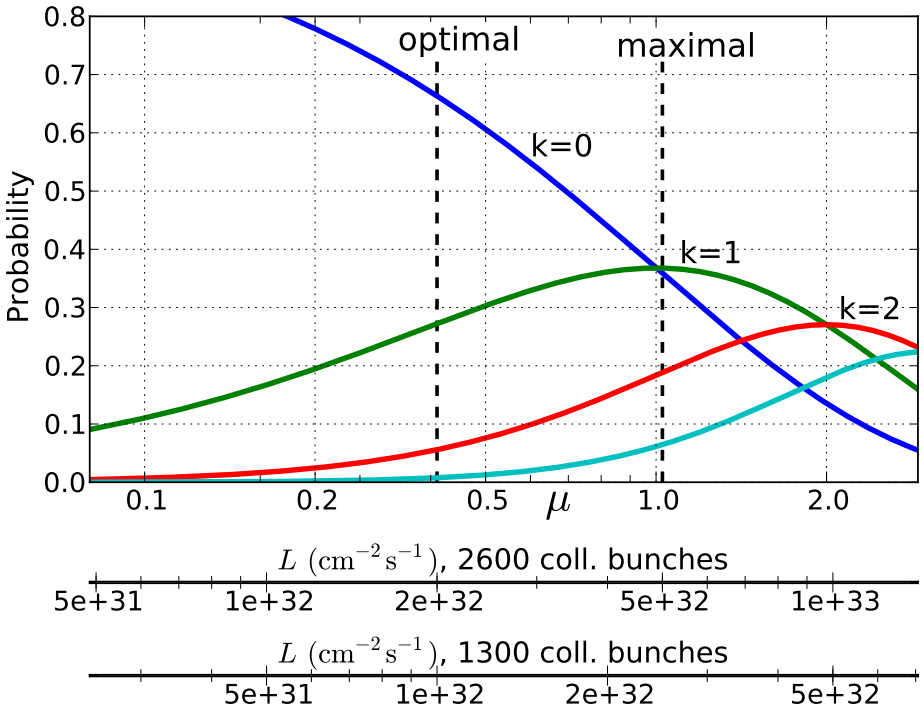

Figure 3.4: Poisson probability of crossings with 0, 1, 2 and 3 pp interactions, as a function of the average number of interactions per crossing, μ. The pp interaction cross-section has been assumed to be 60 mb, which corresponds approximately to the cross-section for a pp collision to produce at least two tracks in the VELO. The two scales at the bottom indicate the corresponding instantaneous luminosity in the cases of 2600 and 1300 bb crossings. The dashed vertical lines mark the designed optimal (2×10^{32} cm^{-2} s^{-1}) and maximal (5×10^{32} cm^{-2} s^{-1}) luminosities at nominal conditions (2600 bb crossings).

[§] The pseudorapidity of a particle is defined as $\eta = -\ln\left(\tan\frac{\theta}{2}\right)$, where the θ is the polar angle.
[❖] In 2010-2011 it was shown with real data that the capabilities of LHCb make it possible to run with higher luminosity.

3.2 Tracking system

The tracking system of LHCb provides a measurement of the trajectories and the momenta of the charged particles traversing the LHCb detector. This allows the primary interaction to be localised. Furthermore, by combining the information from the tracking system and the RICH detectors, the calorimeters and the muon system, certain particle species can be identified. The charged particle trajectories are measured by the VELO, which surrounds the interaction region and by four planar tracking stations: the Tracker Turicensis (TT), located upstream of the LHCb dipole magnet and T1-T3, positioned downstream of the magnet. VELO and TT are silicon microstrip detectors. The T1-T3 stations are divided in inner (*i.e.* close to the beam pipe) and outer regions. In the inner region silicon strip detectors, collectively known as Inner Tracker (IT), are used, while in the other region gas-filled straw-tubes are employed (Outer Tracker, OT). The TT and IT are united in a common project called Silicon Tracker (ST). In this section we make a short review of the LHCb tracking detectors, the pattern recognition and the overall performance of the tracking system.

3.2.1 Vertex Locator

The Vertex Locator (VELO) [1, 90] provides precise measurements of track coordinates in the region immediately surrounding the interaction point. The detector geometry is optimised for the measurement of tracks with small angles with respect to the beam line and the detection of secondary vertices of charm and beauty hadron decays. The VELO is composed of a series of silicon strip detectors positioned along the beam line. The detector is split into two retractable halves which allows the VELO to keep safe distance from the beams while the beams are being prepared for collision and to be as close as possible to the interaction point during data-taking (see Fig. 3.5).

The VELO covers the angular acceptance of the downstream detectors and is able to detect particles with pseudorapidity in the range $1.6 < \eta < 4.9$ and emerging at $z = 0$. The possibility to detect backward going tracks with pseudorapidity in the range $-3.3 < \eta < -1.6$ is used for improving the reconstruction of primary vertices. The packing of the VELO sensors is more dense near the interaction point (IP) so that the average extrapolation distance from the first measured hit to the vertex is reduced. The two most upstream VELO stations are occupied by the sensors of the *pile-up veto system* (PU). The PU system provides input to the LHCb level-0 trigger and plays an essential role in the online selection of beam-gas interactions.

In order to minimise the amount of material in the detector acceptance the VELO is placed in a vacuum vessel. The VELO sensors and the LHC beams are separated by a 0.3 mm thick corrugated foil of aluminium alloy. The foil provides protection of sensitive detectors from radio frequency (RF) pickup from the LHC beams and is therefore called RF-foil. It has a complex shape which minimises the amount of

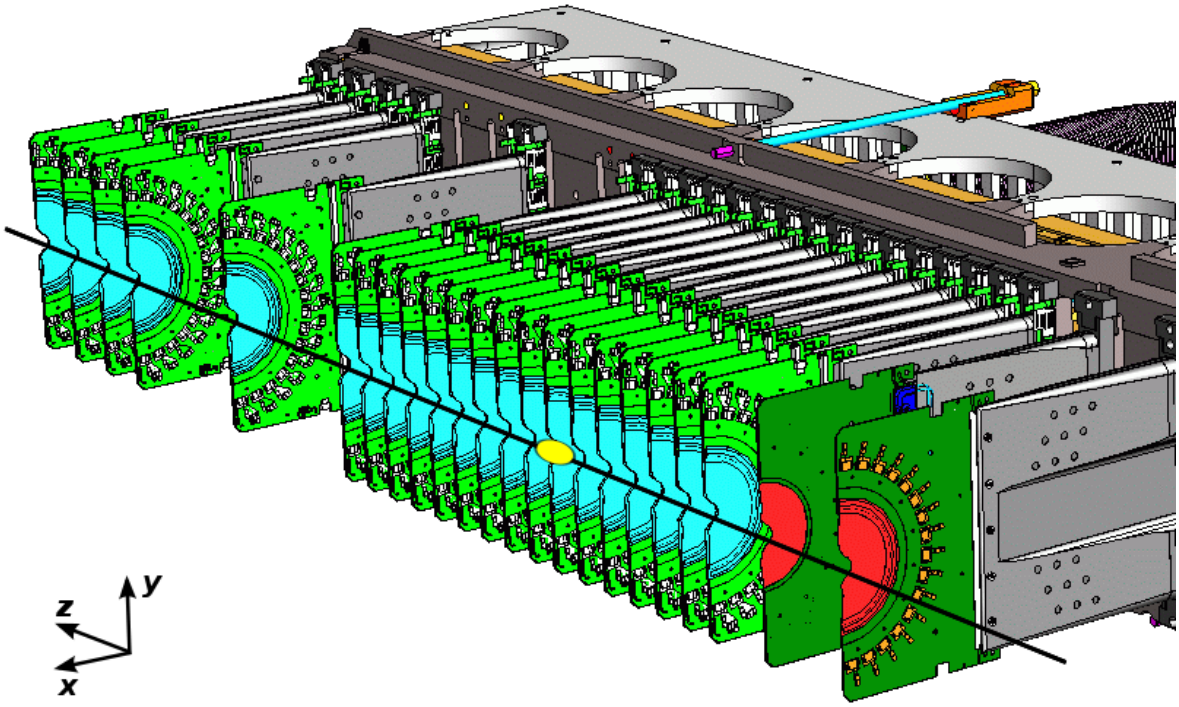

Figure 3.5: One half of the VELO detector, consisting of 21 modules with r- and ϕ-measuring sensors (cyan) and two additional r-measuring modules of the pile-up veto system (red). The z axis, which is the approximate trajectory of the two beams, is indicated by a black line and the origin of the LHCb coordinate frame and nominal position of the luminous region - by an yellow ellipse.

material traversed by a charged particle before it reaches the sensors and allows the two halves of the VELO to overlap ¶ when in closed position.

Each of the 21 modules of the VELO half contains two silicon sensors mounted back-to-back and provides full spatial information of the position of the ionising particle. The strips of one of the sensors (r-sensor) follow a circular path centred at the z axis. This type of sensors provides a measurement of the radial coordinate of the charged particles. In order to reduce the occupancy the sensor is subdivided into four 45° regions (see Fig. 3.6). The other type of sensors provides a measurement of the ϕ-coordinate and is referred to as ϕ-sensor. These sensors have straight strips and are subdivided into inner and outer region. In order to improve the pattern recognition the strips of the ϕ-sensor are tilted with respect to the radial. An opposite-sign skew of approximately 20° and 10° is used in the inner and outer regions, respectively (see Fig. 3.6). The VELO modules are placed in a way such that adjacent ϕ-sensors have

¶ A small overlap in the x-y plane is required for the VELO sensors in order to cover the full azimuthal acceptance and to facilitate the alignment. The overlapping is achieved by shifting the position of one VELO half with respect to the other by 15 mm along the z axis.

an opposite skew with respect to each other. The minimum strip pitch is about 40 μm. Table 3.1 summarises some of the principal sensor characteristics.

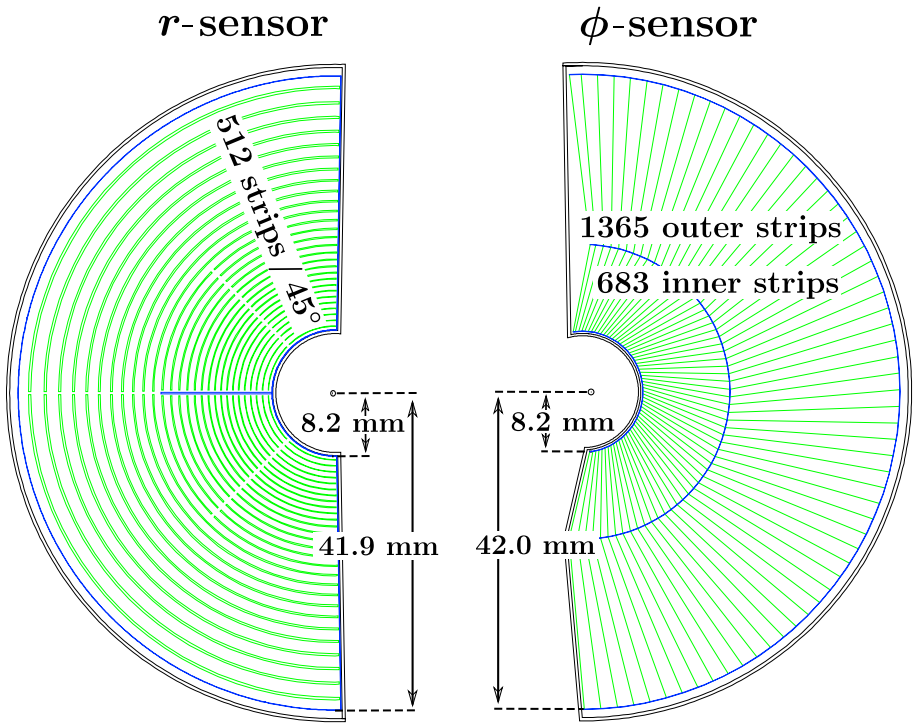

Figure 3.6: Layout of the VELO r- and ϕ-sensors. The inner and outer radius of the active area for both sensors is 8.2 and 42 mm, respectively, and both sensors comprise 2048 readout channels. The strips of the r-sensor follow circular paths and are divided into four 45° regions, while the strips of the ϕ-sensor are straight and have different skew with respect to the radii in the inner and outer regions.

The r-ϕ module design was preferred over the ordinary rectilinear configuration because of the possibility for fast identification of high impact parameter tracks in the High Level Trigger. The varying strip pitch provides a more homogeneous occupancy throughout the sensor, since the particle flux is highest close to the beam axis, where the strip pitch is small, and decreases away from the beam, where the pitch is larger.

The PU system [1, 91] consists of four sensors situated in two planes upstream of the VELO ($z \approx -228$ and -308 mm). The PU sensors have a layout similar to the r-sensors of the VELO and provide measurements of the radial coordinate of the traversing charged particles. The number of readout channels per sensor is 512. The PU system was designed with the goal to provide means to distinguish and reject bunch-crossings with multiple pp interactions (pile-up veto) at the first trigger level (L0). This is achieved by connecting the hits from the same 45° sector of two PU sensors with a straight line and extrapolating to the z axis. The distribution of those z coordinates allows one to identify events with multiple interactions. Details about the use of the PU system in the online selection of beam-gas interactions can be found

Table 3.1: Principal characteristics of the VELO sensors.

	r-sensor	ϕ-sensor
number of sensors	42 + 4 (PU)	42
readout channels per sensor	2048	2048
sensor thickness	300 μm	300 μm
smallest pitch	40 μm	38 μm
largest pitch	102 μm	97 μm
inner radius of active area	8.2 mm	8.2 mm
outer radius of active area	42 mm	42 mm
angular coverage	182°	≈182°
average occupancy	1.1%	1.1/0.7% inner/outer

in Section 3.4.2.

3.2.2 Tracker Turicensis, Inner Tracker and Outer Tracker

Tracker Turicensis (TT) The TT [1, 92] (originally called "Trigger Tracker") is located upstream of the magnet at $z \approx 2.5$ m. It consists of four layers of silicon strip detectors, covering the full LHCb acceptance (see Fig. 3.7). The 4 detection layers are arranged in two pairs, (x, u) and (v, x), that are separated by approximately 30 cm along the z axis. The silicon strips in the x-layers are oriented vertically, while the strips in the u- and v-layers are rotated by 5° in opposite directions along the z axis. The silicon sensors are 500 μm thick and have lateral size of 9.64 × 9.44 cm. Each sensor has 512 readout strips with a strip pitch of 183 μm. Simulation studies have shown that the average strip occupancy of the innermost modules does not exceed 3.5% in b-hadron events. The spatial resolution of the TT detector modules was measured in test beams and was found to be about 50 μm [1].

Inner Tracker (IT) The IT [1, 92] occupies the inner part of the three tracking stations, located downstream of the magnet at $z \approx 8.0$, 8.6 and 9.2 m. The IT covers a small part of the surface of the tracking stations, where the particle flux is highest. Each tracking station has four IT layers, arranged in an (x, u, v, x) configuration, similar to the TT (see Fig. 3.8). The IT layers contain silicon strip sensors with sizes 7.6 × 11 cm. Each sensor has 384 readout strips with a strip pitch of 198 μm. The optimisation of the signal-to-noise ratio and the material budget necessitated the use of single sensors below and above the beam pipe, and double sensors on the two sides of the beam pipe. The expected strip occupancy for b-hadron events is about 2.5% in the innermost region. As for the TT, the spatial resolution measured in test beams is about 50 μm [1].

Outer Tracker (OT) The OT [1, 93] covers the outer region of the three T-stations, located downstream of the LHCb magnet. Each OT station is composed of four layers

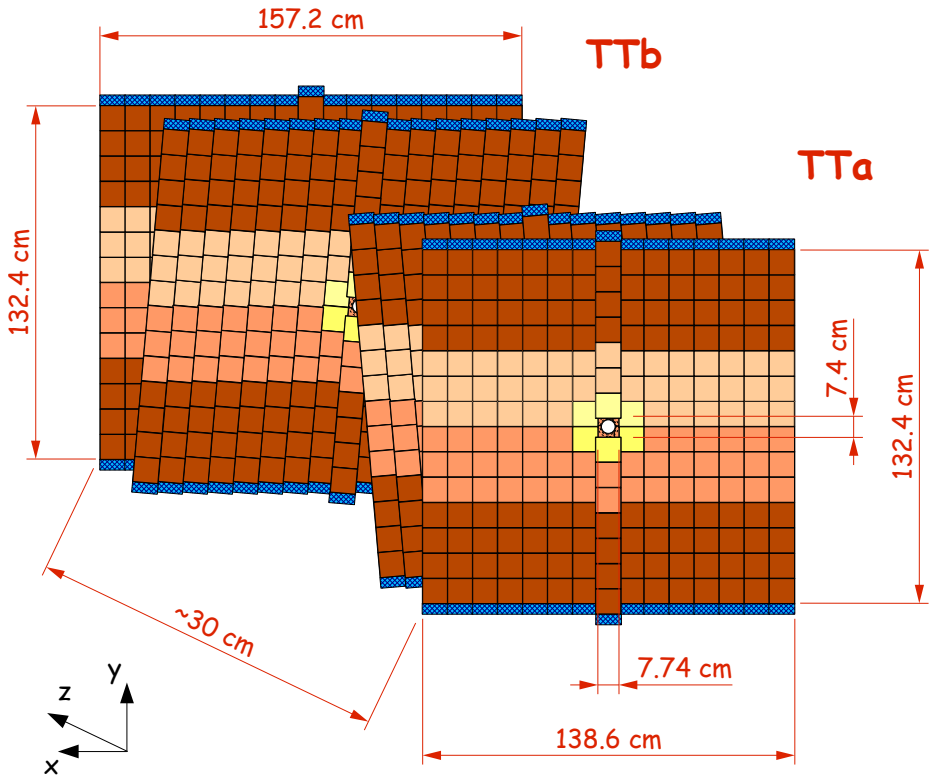

Figure 3.7: Layout of the TT detector. Each of the two stations, TTa and TTb, is composed of two layers of silicon strip sensors. The different colours of the sensors correspond to the different way their strips are bonded together and connected with the readout hybrids.

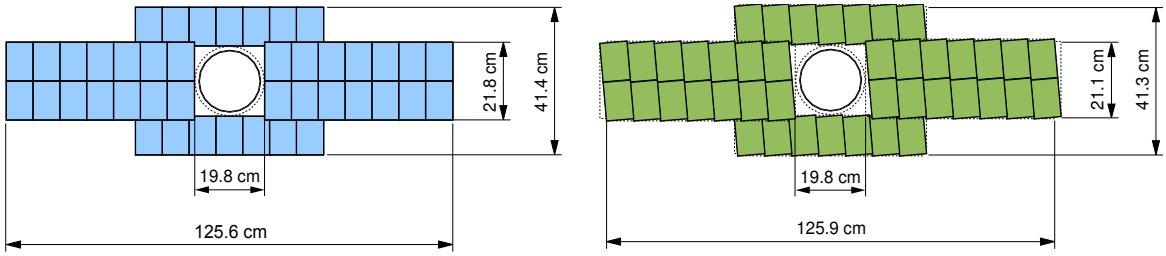

Figure 3.8: Layout of an x (left) and u (right) detection layers in one of the IT stations. A cross-section of the beam pipe is drawn in the middle of the two layers.

of drift-tube modules (see Fig. 3.9a). Similar to the IT, the OT layers are arranged in an (x, u, v, x) configuration. Each OT layer is composed of an array of drift-tube modules. Each module contains two staggered layers of straw-tubes, filled with a mixture of Argon (70%) and CO_2 (30%) (see Fig. 3.9b). The inner diameter of the straws is 4.9 mm and the pitch between two straws is 5.25 mm. Each module layer is composed of two types of modules. Shorter modules are used below and above the region covered by the IT (see 3.9a), while longer modules cover the remaining OT area. The complete OT detector consists of 96 short and 168 long modules and comprises

about 55000 single straw-tube channels.

All three OT stations are of equal size and each of them covers the full LHCb acceptance (polar angle of 300 mrad in the horizontal plane and 250 mrad in the vertical plane). At nominal running conditions the OT occupancy does not exceed 10%. Test beam measurements have shown that hit efficiencies larger than 99% in the centre of the straw (and dropping at its outer edge) and spatial resolution better than 200 μm can be achieved [1].

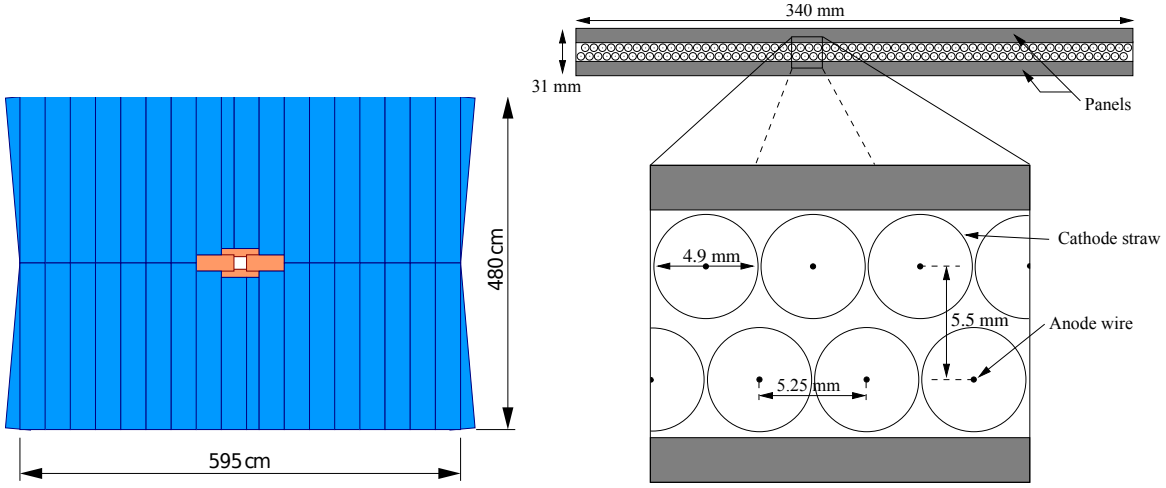

(a) Front view of the T-stations

(b) Cross-section of an OT module

Figure 3.9: (a) Front view of the T-stations, with the IT and OT covering the regions near and far from the beam-pipe, respectively. (b) Cross-section of an OT module, with a magnified insert, showing the straw-tubes placed in between the module support panels.

3.2.3 Magnet

The LHCb dipole magnet [1, 94] is used to deflect charged particles flying in the LHCb acceptance so that their momentum can be measured. The magnet has been designed as a warm magnet with saddle-shaped coils. Its magnetic field is oriented along the vertical and its polarity can be reversed, which can be used to control systematic errors and to minimise apparatus asymmetries in high-precision CP-violation studies. Inevitably, the field of the LHCb dipole magnet acts on the primary proton beams and generates an "internal" crossing angle in the horizontal plane. In total three compensator magnets are installed on both sides of LHCb to balance the effect of the LHCb dipole (see Fig. 2.4).

The total bending power of the LHCb spectrometer is $\int B_y \, \mathrm{d}l \approx 4$ Tm. In Fig. 3.10 the principal component of the magnetic field is shown as a function of the z-coordinate along the beam line. The magnetic field strength is highest in the centre of the magnet and decreases slowly away from it. The magnetic field non-uniformity in the transverse

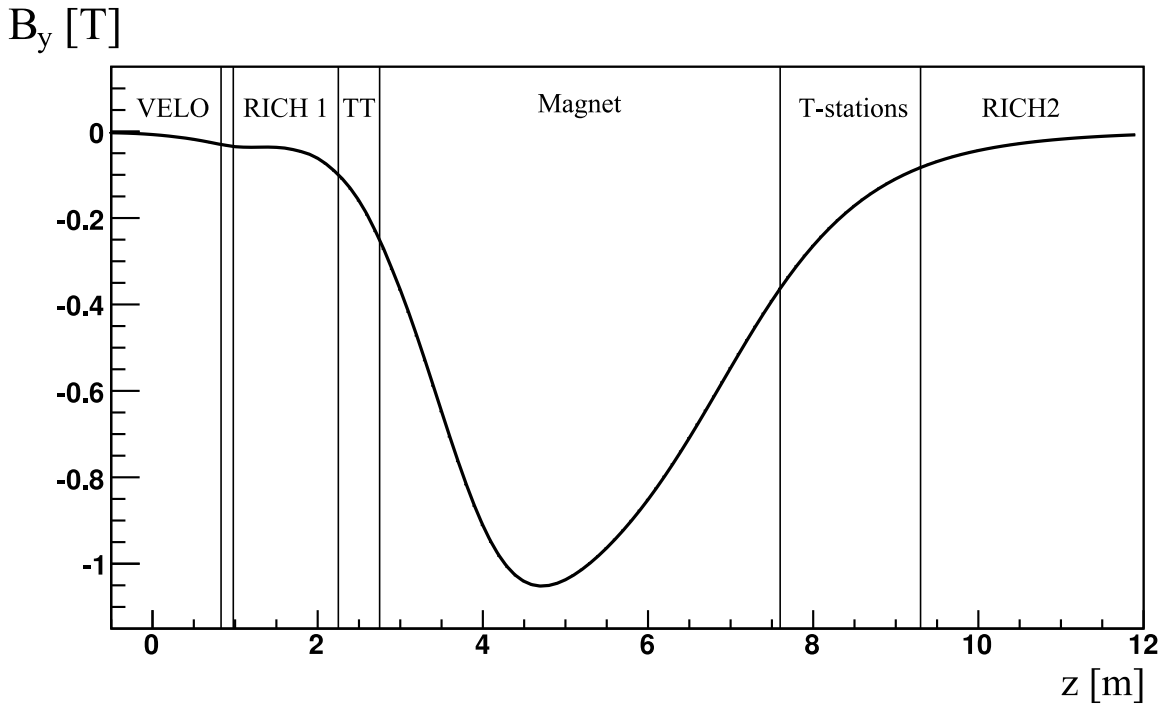

Figure 3.10: The principal (y) component of the magnetic field of the LHCb dipole magnet along the z axis, used in the LHCb Monte Carlo simulation.

directions does not exceed 1% in x-y planes of 1 m^2 from $z = 3$ m to $z = 8$ m.

3.2.4 Track reconstruction

The pattern recognition phase of the event reconstruction aims at finding all tracks which leave sufficient hits in one or more of the tracking detectors. In the track reconstruction software the hit patterns in the VELO, the TT, the IT and the OT detectors are analyzed and the groups of hits belonging to the same particle are identified. Later, the track candidates are fitted in order to determine more precisely the particle trajectories. Finally, the quality of the produced tracks is examined and doubly reconstructed tracks and random hit combinations are rejected. In this section we describe briefly these distinct steps comprising the track reconstruction procedure. A more detailed account can be found in [95] and the references therein.

Depending on the traversed tracking detectors the following classes of tracks are defined (see Fig. 3.11):

- **VELO tracks** are measured only in the VELO. Typically they have large polar angle or fly in the backward direction. These tracks improve the primary vertex reconstruction. Tracks made from VELO hits only are used in the first stage of the LHCb software trigger (see Section 3.4.1.2);
- **Upstream tracks** traverse only the VELO and the TT-stations. In general these tracks come from lower momentum particles, bent out of the detector acceptance

by the magnetic field;

- **Long tracks** leave hits in all tracking detectors and therefore provide the most precise momentum estimates. These tracks are used in most of the physics studies;
- **Downstream tracks** have measurements only in the TT and the T-stations. Typically the source of such tracks are particles decaying outside the VELO acceptance, such as K_S^0 and Λ;
- **T tracks** have hits only in the T-stations and are usually produced in secondary interactions (downstream tracks out of the TT acceptance).

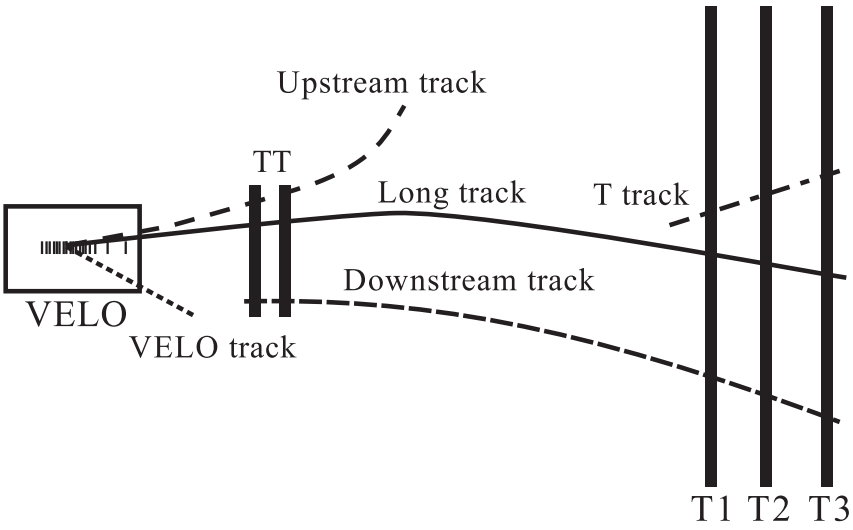

Figure 3.11: A schematic illustration of the various track types, defined according to the set of tracking detectors being traversed.

The pattern recognition can be divided into two logical steps. Initially, the track "seeds" are reconstructed from hits in the VELO or the T-stations. Later, complementing hits in the remaining tracking detectors are searched for.

Reconstruction of seed tracks. The VELO seed reconstruction consists of three steps. First, hits in the r-sensors of the VELO are used to find particle trajectories in the r-z plane. The following assumptions are made: the particle trajectory is considered a straight line, which is motivated by the fact that the integral magnetic field in the VELO region is sufficiently small, and the particles originate from the interaction region. The straight-line trajectories allow the hits to be searched only in the same 45° sectors of the adjacent r-sensors. Initial VELO track seeds of three or four hits are extended by linear projection to the surrounding sensors, resulting into r-z VELO tracks. In the second step of the VELO seed reconstruction ϕ-sensor hits are added to the r-z track to form a three-dimensional track candidate called a 3D VELO track. Multiple 3D candidates may be found for the same r-z track as the only available information for the azimuthal coordinate of the r-z track comes from the relevant sector

(*i.e.* the search window for ϕ hits is 45° wide). This ambiguity is resolved later by fitting a straight line to the 3D track candidates and imposing a minimal requirement on the resulting χ^2 per degree of freedom. Finally, the candidate with largest number of ϕ hits is retained. In the third and final step of the VELO seed reconstruction an additional search for tracks, not necessarily originating from the interaction region, is made with the unused VELO r and ϕ hits. In this algorithm space points are formed from one r and one ϕ hit in the same VELO module. These space points are combined using a procedure similar to the one used in the search for r-z tracks. Again, 3D tracks are constructed from space point sequences compatible with a straight line. In both the r-z and the "space point" approach a 3D track is required to comprise at least three r and three ϕ hits.

The reconstruction of T track seeds uses only hits in the IT and OT. In the vertical plane the particle trajectories are straight lines, while in the horizontal plane the trajectories need to be parametrised with a parabola due to the sizeable magnetic field in the T-stations area (see Fig. 3.10). Initially, hits in the two outermost x layers are connected with a straight line, a search window is defined around this hypothetical path and hits in the inner layers are looked for. Later, a second seed finding algorithm is executed, which considers only the remaining unused hits. Here, the starting point is a sequence of four hits in a single IT-station, which are compatible with a straight line, and the extension of the T track candidate is made to the other T-stations. Finally, the hit collections are fitted to a straight line in the vertical plane and a parabola in the horizontal plane. An estimation of the track momentum can be made from the measured curvature and independently using the assumption that the particle originates from the interaction region. Selection criteria are applied on the hit multiplicity and the fit likelihood before accepting the seed candidates.

Reconstruction of "composite" tracks. Using the seed tracks reconstructed from VELO and T-station hits a search for complementing hits in the other tracking detectors is made. First we look for long tracks and then for upstream and downstream tracks. VELO and T tracks are made from the left-over seeds.

The reconstruction of long tracks uses two independent approaches. In the *forward* tracking approach VELO seeds are combined with single hits in the T-stations. After parametrising the expected trajectory other T-station hits are added. Long tracks are created from the combination of the VELO seed and the T-station hits when sufficient number of hits are collected and good quality trajectory is obtained. In the track *matching* approach VELO and T track seeds are extrapolated to the downstream end of the VELO ($z = 830$ mm). The T seed trajectory is extrapolated through the magnet using its momentum estimate, while the VELO seed is extrapolated as a straight line. The correspondence between the position and slope parameters of the two segments determines if they belong to the same track. In both the forward and matching approaches TT hits located near the obtained trajectory are added to the track. All used VELO and T seeds are discarded in the successive search for other

track types.

The search for upstream tracks starts with a straight line extrapolation of VELO seed tracks to the TT. The hits within a predefined search window are examined for compatible hit collections. Significant difference between the slopes in the horizontal plane is allowed in order to compensate for the lack of momentum information. The best upstream track candidates are refitted by a Kalman filter (see below) and finally the candidate with lowest χ^2 per degree of freedom is selected.

A downstream track is created from a T-station seed and TT hits. Using the momentum estimate of the T seed, the expected particle trajectory is calculated and TT hits inside a certain search window are added. A refined momentum estimate is made using the assigned TT hits. In addition to the usual hit multiplicity and χ^2 selection criteria, we require that the value of the refined momentum estimate and the initial estimate from the T seed are compatible.

Track fitting. After tracks have been found their trajectories are refitted using a least-squares method called Kalman filter. This provides more precise information about the particle paths, momenta and the associated uncertainties. The fitting is performed for all track types. The Kalman filter fit uses track "states", which encapsulate the position, the slope and the momentum of the track at certain points along its path. The parameters of each state are updated in a number of iterations, using the corresponding tracking detector hits. Before passing to the next hit the Kalman filter takes into account the amount of material traversed and applies multiple-scattering and energy-loss corrections. The whole procedure is performed twice, starting from the most downstream hit towards the most upstream one and vice-versa, and finally the obtained track parameter values are combined. The resulting collection of states represents the best estimate of the path of a particle at discrete points in the LHCb detector.

Clone removal. The track reconstruction concludes with the execution of algorithms searching for track duplicates. If two tracks or segments of tracks share hits, the one with the smaller overall number of hits is discarded. In addition, the quality of the tracks and the probability for being a *clone* (two tracks are called clones of each other if they share a certain amount of hits) or a *ghost* (a track not corresponding to a real particle) is recorded for use in offline analyses.

3.2.5 Primary vertex reconstruction

The precise reconstruction of interaction vertices ("primary vertices", PV) is an essential ingredient in the analysis described in this paper. The initial estimate of the PV is based on an iterative clustering of tracks ("seeding"). Only tracks with hits in the VELO are considered. For each track the distance of closest approach ("DOCA") with all other tracks is calculated and tracks are clustered into a seed if the DOCA is

less than 1 mm. Then the position of the seed is obtained in an iterative procedure. The point of closest approach between all track pairs is calculated and the coordinates are used to discard outliers and determine the weighted average position. To improve the seed position into PV coordinates an iterative adaptive weighted least squares fit is used. In each iteration a new PV position is evaluated. Participating tracks are extrapolated to the z coordinate of the PV and assigned weights depending on their impact parameter with the PV. The procedure is repeated for all seeds, excluding tracks from previously reconstructed primary vertices, retaining only PVs with at least five tracks.

3.2.6 Performance

In 2010 the tracking system of LHCb performed as expected, with close to 100% sub-detector channels being operational. Next we summarise the results of some of the performance studies of the reconstruction efficiency and the precision of the measured track parameters.

The tracking efficiency for long tracks is evaluated using "tag and probe" method and K_S decays into two pions. After reconstructing the long track of one of the pions (the *tag*), the track of the other pion is searched using the constraint of a VELO segment and a calorimeter cluster. The efficiency of the T-stations and of the long-track reconstruction is estimated from the probability for finding the matching track segment in the T-stations. The obtained efficiency is shown in Fig. 3.12 as function of the transverse momentum of the *probe* track. For transverse momenta greater than 200 MeV the efficiency is above 95%.

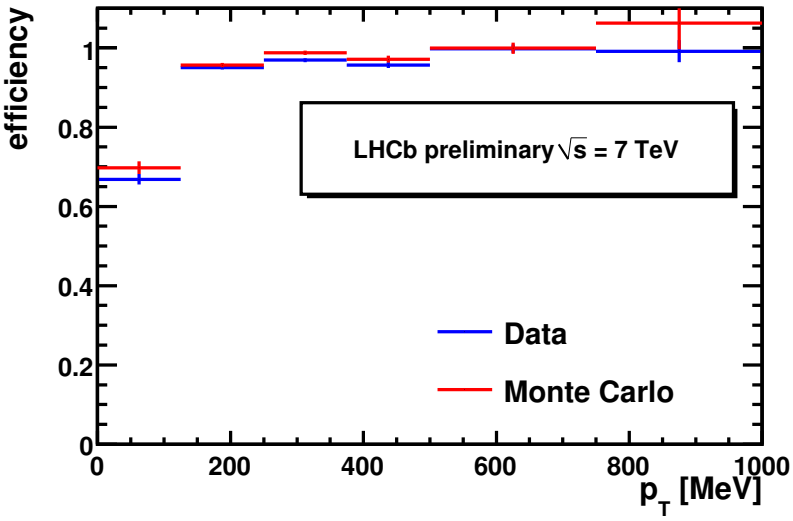

Figure 3.12: Long-track reconstruction efficiency, evaluated with "tag and probe" method and K_S decays into two pions.

The resolution of single hits in the VELO r-sensors is determined from the dis-

tance between the VELO sensor measurements and the long tracks they belong to. The obtained hit resolution is shown in Fig. 3.13 as function of the strip pitch. The analogue pulse height readout of the VELO allows one to obtain a resolution which is considerably better than the corresponding binary resolution. In the regions with 40 μm strip pitch the resolution is as good as 4 μm.

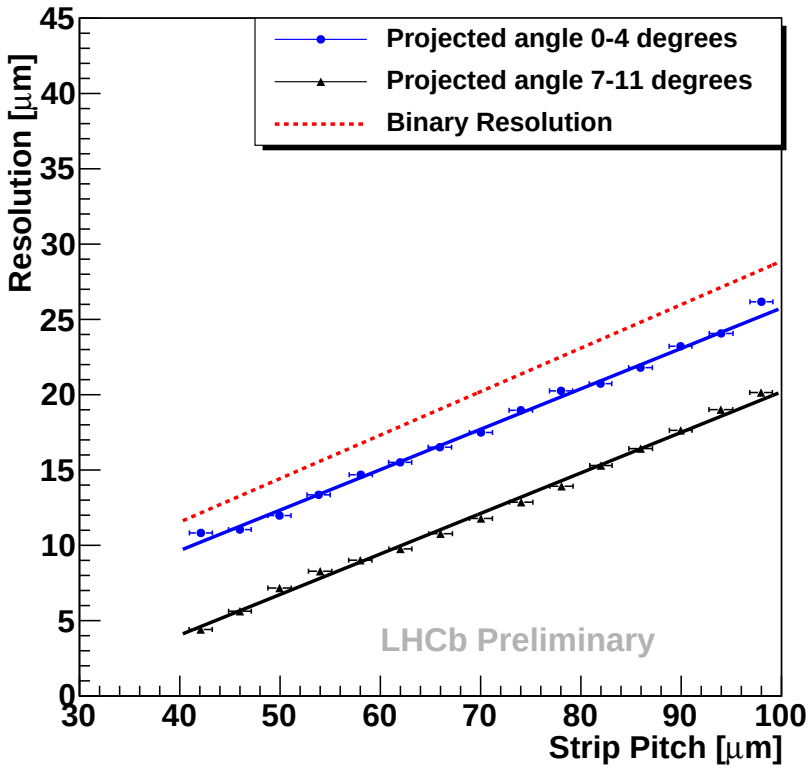

Figure 3.13: Hit resolution of the VELO r-sensors as function of the strip pitch. The results for two ranges of track angles (circles and triangles) are compared with the hit resolution obtained assuming digital detector behaviour (dashed line).

The primary vertex resolution is discussed in Section 7.3. For an average (25 track) vertex the resolution in the transverse and longitudinal coordinates is about 13 μm and 76 μm, respectively.

The impact parameter (IP) resolution plays an important role in the search for tracks from decays of long-lived particles. The distance of a track to the primary vertex (PV) is evaluated after refitting the PV without considering this track. The distribution of the distance in both transverse directions is fitted with a Gaussian and the resulting Gaussian width serves as an estimate of the IP resolution. The results are shown in Fig. 3.14 as function of $1/p_{\mathrm{T}}$.

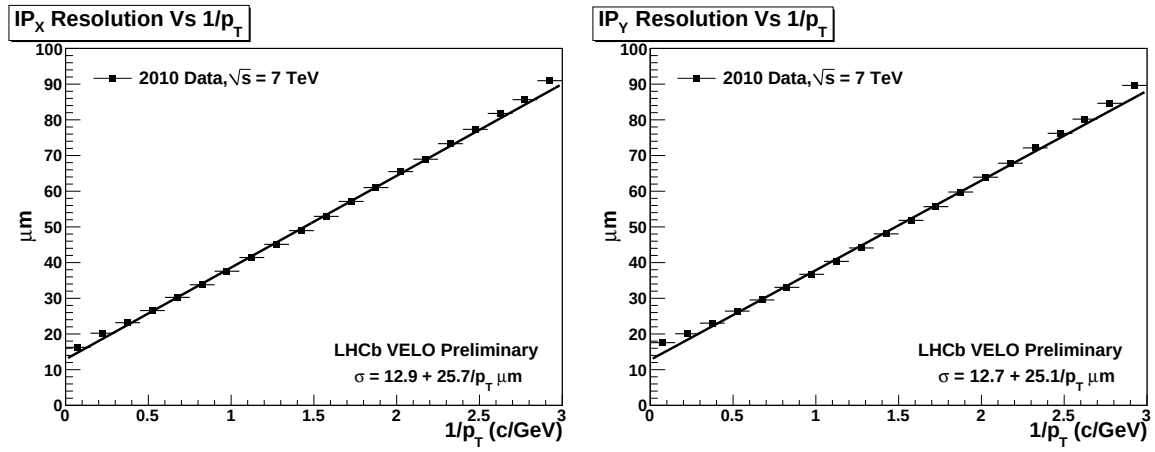

Figure 3.14: Impact parameter resolution in the x (left) and y (right) coordinates for long tracks as function of $1/p_{\mathrm{T}}$.

3.3 Calorimeters

The LHCb calorimeter system [1, 96] provides the identification of electrons, photons and hadrons as well as the measurement of their position and energy. Its measurements are essential for the event selection at the first trigger level (see Section 3.4.1.1) and for all physics analyses involving electrons, photons or neutral pions.

The calorimeter system consists of four planar detectors, located downstream of the RICH2 detector and the first muon station (see Fig. 3.3). The scintillating-pad detector (SPD) and the pre-shower (PS) are two planes of scintillating tiles, separated by a 15-mm thick (2.5 X_0) lead wall. The electromagnetic calorimeter (ECAL) and the hadronic calorimeter (HCAL) are located further downstream (see Fig. 3.15) and have been designed as sampling calorimeters made of alternating layers of scintillating tiles and lead (ECAL) or iron (HCAL) absorber. The scintillation light, produced in the detection layers, is transported to photomultiplier tubes through wavelength-shifting fibers. The total radiation length of the ECAL is about 25 X_0, while the thickness of the HCAL corresponds to 5.6 interaction lengths.

The large polar angle dependence of the particle flux motivated variable lateral segmentation of the calorimeters. The SPD, PS and ECAL are divided into three regions. The cells of the three detectors are placed and sized such that they cover the same polar angle (see Fig. 3.16). Given the dimensions of the hadronic showers and the less stringent requirements on the HCAL resolution, it is divided into two regions and cells with a larger size are used. The total number of cells in SPD/PS/ECAL is about 6000, while the HCAL contains about 1500 cells.

The ECAL and HCAL energy resolution have been measured in dedicated test beam experiments. The resolution is quantified using the parametrisation

$$\frac{\sigma(E)}{E} = \frac{a}{\sqrt{E}} \oplus b \oplus \frac{c}{E} \ ,$$

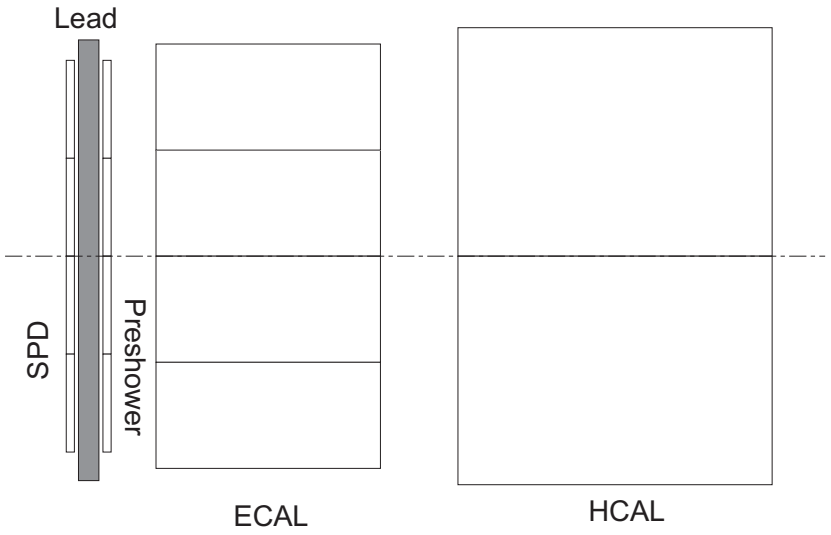

Figure 3.15: Schematic side view of the calorimeter system.

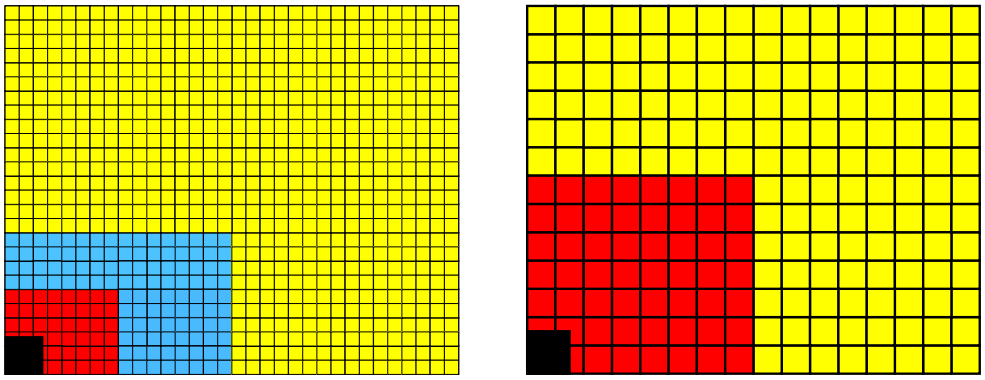

(a) SPD/PS/ECAL (b) HCAL

Figure 3.16: Lateral segmentation of the calorimeter system, indicated for one quarter of the corresponding sub-detector. All cells have a square shape. The SPD/PS/ECAL cells have dimensions of about 4, 6 and 12 cm in the inner, middle and outer regions, respectively. The HCAL cell sizes are about 13 and 26 cm in the inner and outer regions, respectively.

where a, b and c signify the stochastic, constant and noise terms, respectively and E is in GeV. Depending on the module type[✠] and beam conditions, the ECAL stochastic and constant terms were measured to be $8.5\% < a < 9.5\%$ and $b \approx 0.8\%$. The stochastic and constant terms of the HCAL resolution were measured to be $a = 69 \pm 5\%$ and $b = 9 \pm 2\%$.

[✠] The ECAL modules of the inner, middle and outer regions are segmented into 9, 4 and 1 cells, respectively.

3.4 Trigger system

3.4.1 LHCb trigger system

The LHCb trigger system [97] is made of two trigger levels: level-0 (L0), which is implemented in custom electronics and a software high level trigger (HLT), which is executed on a farm of commercial processors.

3.4.1.1 Level-0

The main purpose of the L0 trigger is to efficiently select c- and b-hadron events while reducing the rate of visible pp interactions [‡] to 1 MHz. As explained later in this section the L0 trigger plays an essential role in the selection of beam-gas interactions as well. The L0 trigger system uses information from three detectors - the pile-up veto system (PU), the calorimeters and the muon system. They synchronously send information to the L0 decision unit (L0DU) [98], where selection algorithms (L0 channels) are run. For every bunch-crossing (*i.e.* every 25 ns) the L0DU calculates four decisions and delivers them to the LHCb readout supervisor, ODIN [99]. The decisions that L0DU sends to ODIN are (definitions are given below):

1. the logical `OR` of the decisions of all L0 *physics* channels;
2. the decision of the `B1gas` L0 channel;
3. the decision of the `B2gas` L0 channel;
4. the decision of the `CALO` L0 channel.

ODIN uses the L0DU decisions and other inputs (*e.g.* L0 channel downscale factors, timing and bunch-crossing type information) in the process of making the judgement whether the full event information should be read-out. Notably, ODIN can request the reading of an event independently of the L0DU decision (*e.g.* for collecting calibration or trigger-unbiased data).

The measurement of the luminosity uses the following L0 quantities:

- PU multiplicity − the number of hits measured in one of the two PU stations;
- SPD multiplicity − the number of SPD cells with a hit;
- Hadron E_T^{max} − E_T of the hadron calorimeter cluster (2×2 cells) with highest transverse energy;
- ΣE_T − a measure of the total transverse energy deposited in the HCAL.

[‡] The LHC bunch-crossing frequency is 40 MHz. Not all bunch slots will be filled with protons and not all `bb` crossings will produce *visible* interactions, *i.e.* interactions with at least two charged particles with sufficient hits in the VELO and T1-T3 to allow them to be reconstructible. At nominal conditions the expected rate of crossings with at least one visible pp interaction is about 10 MHz.

and the following L0 trigger channels:

- `PU` – requires PU multiplicity greater than 3;
- `CALO` – defined as the logical `AND` of the conditions SPD multiplicity > 2 and Hadron $E_T^{max} > 240$ MeV;
- `B1gas` – requires minimal ΣE_T and vetoes events with large PU multiplicity;
- `B2gas` – requires minimal PU multiplicity and vetoes events with large ΣE_T.

Details about the beam-gas L0 channels are given in Section 3.4.2.2.

3.4.1.2 High level trigger

After ODIN requests an event to be read-out, the full information from all sub-detectors is sent to the event filter farm (EFF). The EFF consists of a pool of computers which run the high level trigger software code. There partial reconstruction of the event is performed and selection criteria are applied. The HLT is organised in two levels - HLT1 and HLT2. The first step in HLT1 is to perform a confirmation of the objects which triggered the event at level-0. In case of successful confirmation reconstruction of VELO tracks, primary vertices and addition of the information from other sub-detectors to the track candidates are performed. The candidate selections are based on impact parameter, transverse momentum, invariant mass and others. The typical rate of events selected by the HLT1 is about 30 kHz. The analysis of these events continues at the HLT2 where more complete event reconstruction, including pattern recognition using the full tracking system, is performed and many inclusive and exclusive selections are run. The events passing the HLT2 stage are written to disk and nominally have a rate of 2-3 kHz.

The structure of the HLT1 and HLT2 trigger levels is organised in `HLT Trigger Lines`, or just `Lines`. The `Lines` are logical and software code entities, which perform specific selections (*e.g.* `Hlt1SingleHadron`, `Hlt2B2HH`, etc.). Each HLT `Line` is a sequence of algorithms which provide a decision whether the event should be kept. Internally, the algorithms in each `Line` perform the prescaling (or rate-limiting), the reconstruction and the application of specific selection criteria. All `Lines` at each of the two HLT levels are executed independently of each other [⊛].

In LHCb the configuration of the L0 and high level triggers is mapped onto an 8-digit hexadecimal number, which uniquely labels the collection of settings of all L0 channels, HLT `Lines` and the involved event reconstruction algorithms. This hexadecimal number is called Trigger Configuration Key (TCK) and is used as a unique label for the trigger configuration.

[⊛] As explained later, one of the beam-gas trigger `Lines` is an exception. This `Line` runs in the end of the HLT1 and considers only events with already reconstructed r-z VELO tracks.

3.4.2 Beam gas trigger

For the online selection of beam-gas events a dedicated trigger has been developed and is used since the beginning of the LHC operation at the end of 2009. In 2010 the beam-gas trigger evolved following the changing beam conditions provided by the LHC. In this section we detail the layout of the trigger during the periods relevant for the absolute luminosity normalisation with the beam-gas imaging method. More precisely, we describe the beam-gas trigger strategy and the configuration of the beam-gas L0 and HLT triggers used in the data-taking of fills $1089 - 1122$ (TCKs 0x00051710 and 0x00081710) and $1444 - 1453$ (TCKs 0x002E002A and 0x002E002C). As the beam-gas trigger is identical in TCKs 0x00051710 and 0x00081710, in the following we refer only to the latter TCK. For the same reason we quote only TCK 0x002E002C as a trigger configuration used for recording the necessary amount of beam-gas interactions for the application of the beam-gas imaging method with October 2010 data. No improvement on the absolute luminosity normalisation was achieved with October 2010 data, due to increased uncertainty of the beam current measurement during the LHC operation with bunch trains (see Section 5.1) and therefore this measurement is not presented in this thesis. Nevertheless, we describe the beam-gas trigger configuration allowing to collect data for the application of the beam-gas imaging method in fills with large number of bunches.

3.4.2.1 Trigger Strategy

We use the following notation for the four possible types of bunch-crossings:

- bb : bunches of beam1 and beam2 are filled;
- be : bunch of beam1 is filled, bunch of beam2 is empty;
- eb : bunch of beam1 is empty, bunch of beam2 is filled;
- ee : bunches of beam1 and beam2 are empty.

We recall that beam1 is the clockwise beam, as seen from above. Beam1 enters LHCb from the VELO side. We use the standard nomenclature, where the colour code blue is used for this beam, while red is used for beam2 [5].

It is particularly important to record beam-gas events in bb crossings since these allow a direct normalisation of a reference cross-section in the pp collisions to be made. The beam-gas events in be and eb crossings can be used for studying the beam geometries and for measuring the z-dependence of the primary vertex resolution. These do not suffer from the pp 'background' and are relatively easy to identify. The events in ee crossings can be used for measuring the ghost charge (beam current in nominally-empty bunch slots) [75]. The measurement of the ghost charge in fills $1089 - 1122$ is described in Section 5.2.

3.4.2.2 L0

In this section we describe the beam-gas L0 trigger channels and the ODIN settings, which enable these triggers in the different bunch-crossings. The beam-gas L0 trigger channels exploit the directionality of the event – the products of the beam-gas interactions have the z-direction of the incoming proton bunch. Therefore we require activity in a detector upstream (negative z-direction) or downstream (positive z-direction) from the luminous region and veto the activity in the opposite direction. There are two L0 channels, `B1gas` and `B2gas`, aimed at selecting beam1-gas and beam2-gas interactions occurring in the VELO vicinity, respectively. The z-region of interest is roughly $|z| < 1.5$ m. The beam1-gas interactions are selected by requiring an energy deposition in the calorimeters (located at $z \approx 12$ m) and low activity in the PU detector. The PU sensors are located at $z \approx -0.3$ m and therefore can detect products of beam1-gas interactions occurring at $z < -0.3$ m. This necessitates the use of a tolerant PU veto requirement in the `B1gas` channel. The signature of the signal beam2-gas interactions is activity in the PU detector and no energy deposition in the calorimeters. Both beam-gas L0 channels use the variables PU multiplicity and ΣE_T. The conditions which constitute the two beam-gas channels are summarised in Table 3.2.

Table 3.2: Definitions of the beam-gas L0 trigger channels corresponding to trigger configuration keys 0x00081710 and 0x002E002C. Both conditions on ΣE_T and PU multiplicity need to be satisfied to get a positive decision of the relevant L0 channel (logical AND).

	`B1gas`		`B2gas`	
TCK	0x00081710	0x002E002C	0x00081710	0x002E002C
ΣE_T	> 3GeV	> 5GeV	< 5GeV	< 1GeV
PU multiplicity	< 40	< 30	> 9	> 9

Bunch-crossings of type be and eb For each bunch-crossing L0DU evaluates and sends to ODIN the decisions of the `B1gas` and `B2gas` channels (see Section 3.4.1.1). Positive decisions are respected by ODIN only in the corresponding bunch-crossing type: events with positive `B1gas` decision are read-out in crossings of type be, and events with positive `B2gas` decision are read-out in crossings of type eb.

Bunch-crossings of type ee The amount of protons in nominally empty bunch slots (ghost charge) can be measured with beam-gas or pp interactions in the different bunch-crossing types. Throughout 2010 the L0 *physics* channels were respected by ODIN in all types of bunch-crossings (including ee), while the beam-gas L0 channels were active in ee crossings only during the period encompassing fills 1364 to 1443 (note that this includes fill 1422, where absolute luminosity calibration was performed with the van der Meer scan method).

Bunch-crossings of type bb The amount of information available to the L0 (see Section 3.4.1.1) does not allow for efficient and pure selection of events containing beam-gas interactions (single beam-gas interaction or overlapped beam-gas and *pp* interactions). At L0 the beam-gas interactions can be selected in a parasitic manner, because they can overlap with an L0-triggering *pp* interaction in the same bunch-crossing. This implies a random selection of the beam-gas events and a reduction of their rate by the retention factor of the L0 trigger, which has a nominal value of about 1/10 (see Section 3.4.1.1). However, in the early data-taking period (up to fill 1122) the L0 *physics* trigger included several non-selective trigger channels, like `PU` and `CALO` (see Section 3.4.1.1), with high efficiency for triggering single beam-gas interactions.

With the increasing number of bunches in 2010 the physics L0 trigger became more stringent and the beam-gas interactions in `bb` crossings were selected at L0 only parasitically, which became insufficient for precise bunch-by-bunch measurements. Therefore in fills $1444-1453$ a special L0-ODIN beam-gas trigger was used, increasing the beam-gas trigger efficiency for a limited number of colliding bunches. The strategy was to activate the two beam-gas L0 channels for a few selected `bb` crossings※. As already mentioned, the veto requirement in the `B1gas` L0 channel is not strong, determining the high efficiency of this L0 channel for *pp* interactions. For improving the background rejection we have used the signal from the beam-loss scintillator (BLS) [100] as a veto for the *pp* interactions (can only be applied by ODIN).

3.4.2.3 HLT

In the high level trigger we execute a sequence of reconstruction and selection algorithms aimed at choosing events containing beam-gas interaction vertices. As mentioned in Section 3.4.1.2 the HLT selections are based on the `HLT Line` framework, which specifies their structure and the components they may use. In TCK 0x00081710 the beam-gas high level trigger consists of four HLT1 `Lines`, while in TCK 0x002E002C there are six HLT1 and two HLT2 beam-gas trigger `Lines`.

HLT1 Beam-Gas Lines The HLT1 beam-gas trigger selections start by checking the bunch-crossing type and the *ODIN Trigger Type*✣ of the event. Further, we select events which satisfy a certain L0 requirement and we apply a limit on their rate. Then we execute several reconstruction and selection algorithms, which aim at identifying events containing a beam-gas interaction vertex. We use r-z VELO tracks (see Section 3.2.4) to look for track accumulation around a point on the z axis (pseudo-vertex). The execution of the r-z tracking algorithm is included in all beam-gas `Lines`, except in the 'bb-Parasitic' `Line`, designed to profit from the fact that the VELO r-z

※ In fills 1444, 1450 and 1453 the beam-gas trigger was active in four BCIDs – 895, 901, 907 and 913.
✣ The *ODIN Trigger Type* is an ODIN flag which facilitates the recognition and the streaming of non-L0 or other special events. It can take 8 distinct values.

tracking is executed for the vast majority of the events entering the HLT and having bunch-crossing type bb. The 'bb-Parasitic' Line is executed last in the HLT1 sequence.

The accumulation of tracks around a point on the z axis is quantified in the following way. We fill a vector with the z positions of all reconstructed r-z VELO tracks at the point where they cross the z axis ($r = 0$). After sorting the vector we iteratively select every N_{min} consecutive values, where N_{min} is a parameter corresponding to the required minimal number of tracks in the pseudo-vertex. We calculate the min-to-max spread of every set of z values and compare them to a maximally allowed spread, Δz_{max}. The pseudo-vertex search is considered successful if we find a set of N_{min} values with min-to-max spread lower than Δz_{max}. The value of Δz_{max} is a linear function of z with a minimum, Δz^0_{max}, at $z = 0$ m. At $|z| = 2$ m Δz_{max} has a value which is twice bigger than Δz^0_{max}.

The beam-gas Lines selecting beam-gas interactions in bb crossings do not consider the luminous region, as the dominant source of interaction vertices in this z-range is pp collisions (depending on the beam conditions, the beam-gas fraction can be as low as 10^{-5}). A veto region of $\pm 5\sigma_z^{\text{lumi region}}$ around $z = 0$ ensures that less than 1 in a million pp vertices will be selected (in case that the pp vertices are normally distributed along the z axis). When a relatively low N_{min} is used, vertices from random combination of tracks may be produced. Due to the asymmetric VELO geometry, such vertices are observed predominantly in the upstream end of the VELO, which necessitates an expansion of the lower limit of the vetoed region (see Table 3.3).

In its final stage each beam-gas HLT1 Line limits the rate of selected events.

The essential properties of the beam-gas trigger Lines corresponding to TCKs 0x00081710 and 0x002E002C are summarised in Tables 3.3 and 3.4, respectively. More details about the pseudo-vertex algorithms can be found in [101].

The two HLT1 Trigger Lines present in TCK 0x002E002C and not in 0x00081710, namely bb-Enh.B1 and bb-Enh.B2, select only events which occur in bb crossings and which have *ODIN Trigger Type* equal to *BeamGasTrigger*. The trigger-type flag is set by ODIN for up to four BCIDs (see Section 3.4.2.2). This enhances the overall beam-gas trigger efficiency for the selected bunch-crossings.

In TCK 0x00081710 the selection of beam-gas interactions in the HLT was done with HLT1 Lines only and all selected events were passed transparently through HLT2 (and therefore written to disk).

HLT2 Beam-Gas Lines TCK 0x002E002C includes two HLT2 beam-gas Lines, which refine the selection done in HLT1 and allow a refined online beam-gas selection to be made. The algorithm sequence of both HLT2 Lines includes the reconstruction of 3D VELO tracks (see Section 3.2.4) and primary vertices (see Section 3.2.5). Later we pick out the reconstructed primary vertices with certain z position and number of tracks. At the final stage of each HLT2 Line we limit the rate of selected events. The

Table 3.3: Algorithm composition and settings of the HLT1 beam-gas `Lines` defined in TCK0x00081710. The cells with '-' signify the lack of a selection requirement for the corresponding HLT `Line`.

	B1gas	B2gas	bb-ForcedReco	bb-Parasitic
bunch-crossing type	be	eb	-	-
L0 requirement	`B1gas`	`B2gas`	$SPD > 2$ || $PU > 3$	$SPD > 2$ || $PU > 3$
L0 rate limit [kHz]	-	-	10	-
HLT BG Algorithms				
z-range limits [m]	$[-2.0; 0.6]$	$[0.0; 2.0]$	$[-2.0; 2.0]$	
exclude z-region [m]	-	-	$[-0.35; 0.25]$	
pseudo-vertex $\Delta z^0_{\max}$	14 mm			
pseudo-vertex $N_{\min}$	5			
Output rate limit [Hz]	25	25	25	25

Table 3.4: Algorithm composition and settings of the HLT1 beam-gas `Lines` defined in TCK0x002E002C. The cells with '-' signify the lack of a selection requirement for the corresponding HLT `Line`.

	B1gas	B2gas	bb-ForcedReco	bb-Parasitic	bb-Enh.B1	bb-Enh.B2
bunch-crossing type	be*	eb*	bb	bb	bb	bb
ODIN trigger type	-	-	-	-	`BGTrig`	`BGTrig`
L0 requirement	`B1gas`	`B2gas`	$SPD > 2$ || $PU > 3$	$SPD > 2$ || $PU > 3$	`B1gas`	`B2gas`
L0 rate limit [kHz]	15	15	5	-	50	50
HLT BG Algorithms						
z-range limits [m]	$[-1.5; 0.3]$	$[0.1; 1.5]$	$[-1.5; 1.5]$		$[-1.5; 0.3]$	$[0.1; 1.5]$
exclude z-region [m]	-	-	$[-0.3; 0.3]$			
pseudo-vertex $\Delta z^0_{\max}$	14 mm					
pseudo-vertex $N_{\min}$	5					
Output rate limit [Hz]	50	50	10	150	20	20

essential properties of the two HLT2 beam-gas `Lines` are summarised in Table 3.5.

* The B1gas and B2gas `Lines` in TCK 0x002E002C selected as well events in ee crossings, after prescaling by a factor 0.1.

Table 3.5: Reconstruction and selection stages of the HLT2 beam-gas `Lines`. The algorithm sequence and their essential properties correspond to TCK 0x002E002C. The reconstruction algorithms in these trigger `Lines` are executed only on events selected by the beam-gas HLT1 `Lines`.

	non-bb	bb
bunch-crossing type	not bb	bb
HLT requirement	pass B1 or B2 beam-gas HLT1 `Line`	pass any bb beam-gas HLT1 `Line`
Reconstruction Algorithms	3D VELO tracks and primary vertices	
Rec. vertex min. #tracks	12	12
Rec. vertex z requirement	$\lvert z\rvert < 1.0$ m	$\lvert z\rvert > 0.4$ m & $\lvert z\rvert < 1.0$ m
Output rate limit [Hz]	20	80

3.4.2.4 Performance of the beam-gas trigger

L0

The beam-gas interactions occurring in the VELO vicinity, $|z| \lesssim 1.5$ m, are considered as *signal*, while there are two types of background. First, there are the beam-gas interactions which occur at a long distance (several meters) from LHCb and therefore the respective collision point cannot be determined with high precision. In order to study the various distributions in the detector from *distant* beam-gas interactions Monte Carlo simulated events are used. The distribution of the PU multiplicity and ΣE_T in beam1-gas and beam2-gas collisions taking place within 10 m from the LHCb interaction point are shown in Fig. 3.17. The simulation uses the HIJING [102] event generator, which is interfaced with the LHCb simulation program (Gauss) [103]. The HIJING Monte Carlo program can be used to generate interactions between different types of projectiles and targets. Motivated by the dominant contribution of the Hydrogen gas in the LHC vacuum [66], protons were used both as projectiles and targets. For the results shown in Fig. 3.17 the proton beam has energy 5 TeV, corresponding to pp collisions with a center-of-mass energy 97 GeV (*cf.* 81 GeV at 3.5 TeV beam energy). The effect of the higher beam energy is considered small as far as the z-dependence of the distributions is concerned. The full LHCb geometry ($-2 \lesssim z \lesssim 20$ m) is used in the simulation, but no material or LHC magnets in the region upstream of LHCb ($z < -2$ m) have been taken into account. This incomplete geometry description leads to an overestimation of the distant beam1-gas background. As can be seen from Fig. 3.17 no significant reduction of the distant beam-gas background can be achieved with the use of the PU multiplicity and ΣE_T variables, available at L0. The identification of such background at the HLT is straightforward.

The second type of background is due to pp collisions of the two LHC beams. Nominally no pp interactions are expected in non-bb crossings. However, it is possible

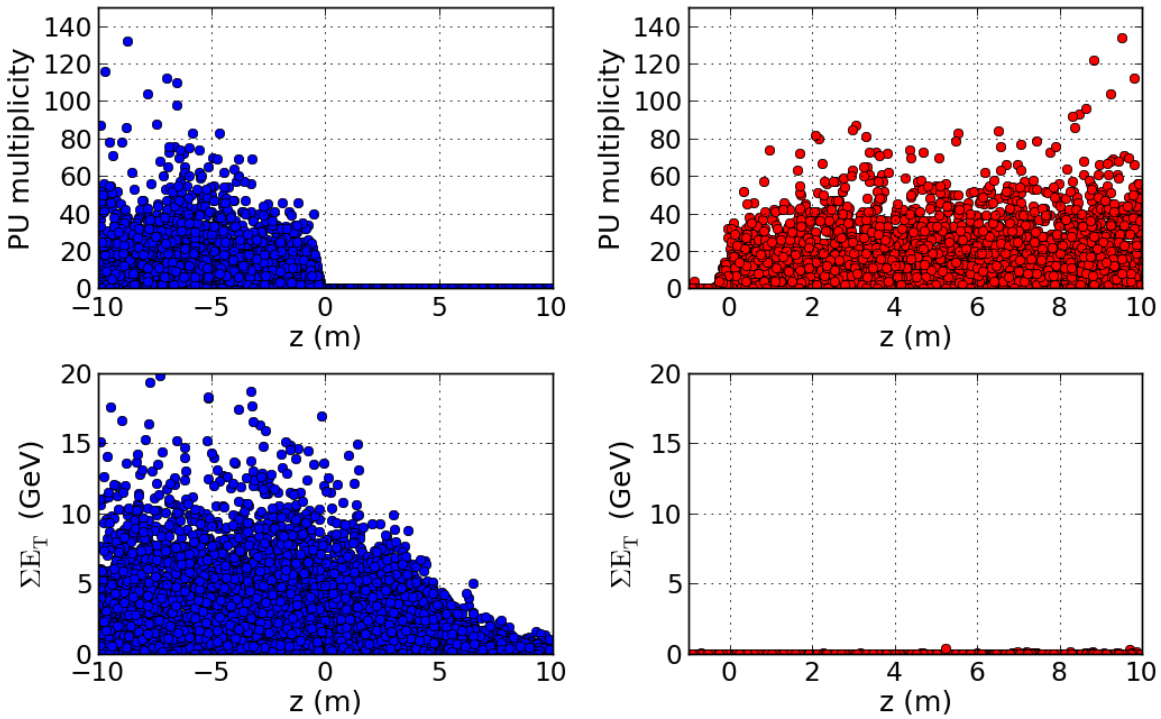

Figure 3.17: PU multiplicity and ΣE_T distributions of beam-gas interactions as a function of the z position of the primary vertex. The beam1(2)-gas events are shown on the left (right). The drop in the PU multiplicity at $z \approx 0.3$ m corresponds to the location of the PU sensors. Similar situation occurs for the ΣE_T distribution for beam1-gas interactions (the hadronic calorimeter is located at $z \approx 14$ m), while, as expected, the beam2-gas interactions deposit no energy in the HCAL.

for beam current to appear in nominally empty bunch slots during injection from the SPS or due to misbehaviour of the LHC beam capture (RF) system. This can result in pp collisions between protons in non-nominal and nominal bunches[♦]. Given the limited bandwidth for events passing the L0 trigger (nominally, 1 MHz), the retention of inelastic pp interactions by the beam-gas trigger needs to be minimised. For this purpose the two beam-gas L0 trigger channels veto events with high activity in the direction opposite to the incoming beam.

In the evaluation of the beam-gas trigger efficiency and the pp background retention of the beam-gas L0 trigger low-bias data, collected by LHCb in fill 1089, have been used. The signal and background samples are defined as follows. The signal beam1(2)-gas events occur in be (eb) crossings and are selected by the L0 `CALO` (`PU`) trigger channels. There must be an offline reconstructed vertex with at least 10 tracks and with a z position in the range $-1500 < z < 500$ mm for beam1-gas events, and in the range $0 < z < 1500$ mm for beam2-gas events. The background pp events occur in bb crossings and are selected by the L0 `CALO` or `PU` trigger channels. There must be an

♦ More details about the measurement of the beam current in non-nominal bunch slots can be found in Chapter 5.

offline reconstructed vertex with at least 10 tracks and with a z position in the range $-150 < z < 150$ mm. The obtained signal efficiency and background retention of the beam1-gas and beam2-gas L0 channels are shown in Figs. 3.18 and 3.19, respectively.

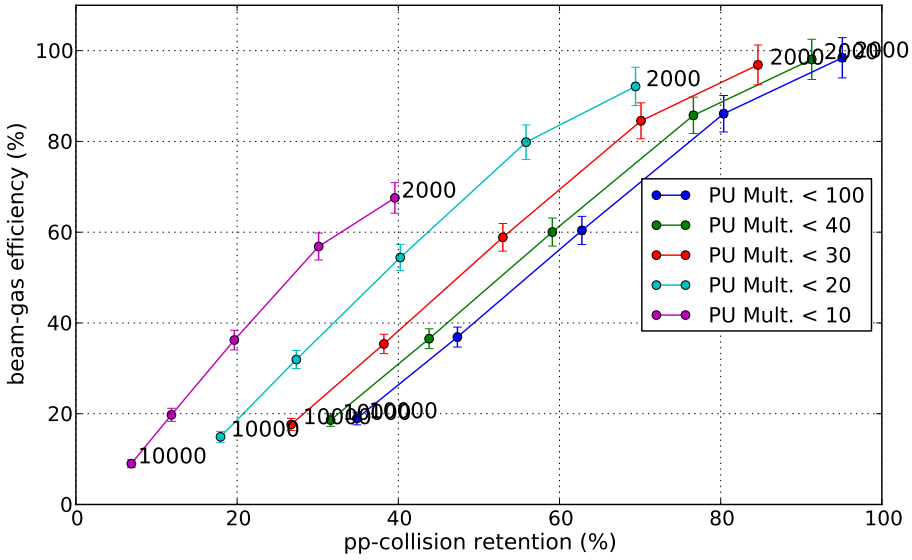

Figure 3.18: Signal efficiency and background retention of the beam1-gas L0 channel, obtained from LHCb data, recorded in fill 1089. The different curves correspond to different *veto* requirements (PU multiplicity $< X$), while the points on each curve correspond to different *activity* requirement ($\Sigma E_T > Y$). The ΣE_T requirement changes in equal steps between the minimal and maximal values, indicated on the figure in MeV.

HLT

Studies related to the high level trigger for beam-gas interactions, using Monte Carlo simulated data, are described in [101].

Using the fact that in fill 1089 the HLT was not rejecting events, the efficiency of the different beam-gas HLT `Lines` can be estimated from the ratio of selected and total number of signal events. The signal events are defined by the requirement for an offline reconstructed vertex with at least 10 tracks. The z regions $-1500 < z < 500$ mm and $0 < z < 1500$ mm are used for the vertices reconstructed in be and eb crossings. The same z regions are used for bb crossings, but the luminous region ($-350 < z < 250$ mm) is excluded. To be identified as beam1-gas (beam2-gas) interaction the vertex is required to have only forward-going (backward-going) tracks. The relevant L0 trigger requirements have been imposed as well (see Table 3.3). The efficiency of the beam-gas HLT `Lines` is shown in Table 3.6. Generally, high efficiency is achieved for beam-gas vertices with 10 or more tracks. The lower efficiency of the bb-Parasitic `Line` and its asymmetry with respect to the two beams can be explained by the fact that this trigger selection considers only events where the VELO r-z tracking has been done in another HLT `Line`. As expected, in the fills where its L0 rate limit is not exceeded (see

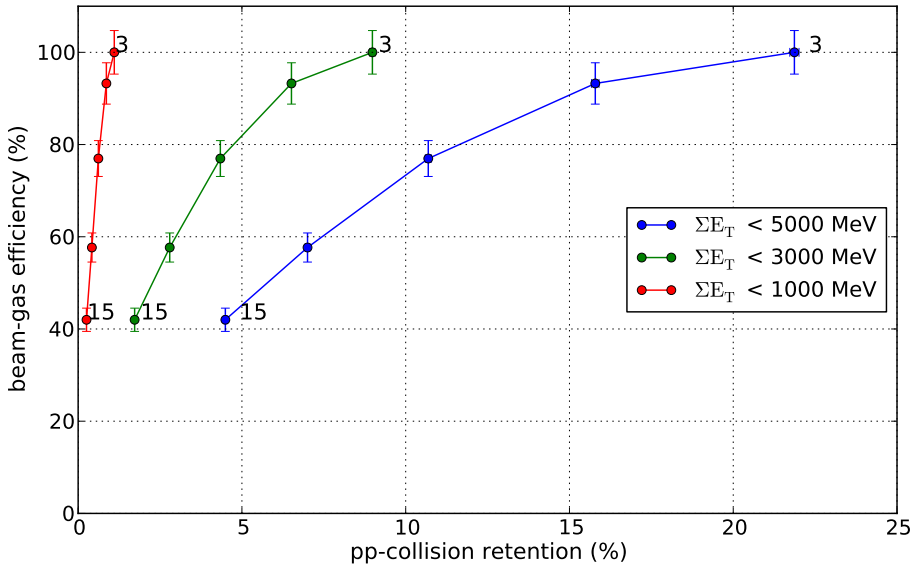

Figure 3.19: Signal efficiency and background retention of the beam2-gas L0 channel, obtained from LHCb data, recorded in fill 1089. The different curves correspond to different *veto* requirements ($\Sigma E_T < X$), while the points on each curve correspond to different *activity* requirement (PU multiplicity $> Y$). The PU multiplicity requirement changes in equal steps between the minimal and maximal values, indicated on the figure.

Table 3.3), the bb-ForcedReco `Line` has higher efficiency than the bb-Parasitic `Line`.

Table 3.6: Efficiency (in percent) of the HLT beam-gas `Lines`, measured with low-bias LHCb data, recorded in LHC fill 1089.

HLT `Line`	Efficiency for beam1-gas	Efficiency for beam2-gas
B1gas	99 ± 3	-
B2gas	-	98 ± 3
bb-ForcedReco	98 ± 4	98 ± 3
bb-Parasitic	84 ± 4	68 ± 3

3.4.3 Trigger for relative luminosity measurement

An unbiased trigger selection is used for the measurement of the relative luminosity. Random triggers are created, which initiate the full readout of the LHCb detector. These are called "LumiTriggers". The readout supervisor (ODIN) takes care of generating these LumiTriggers by defining a quasi-random number and deciding on a crossing-by-crossing basis whether such a random trigger is issued for the particular crossing. Four separate random-numbers are generated, one for each crossing type (bb, be, eb, ee). During normal physics data-taking, the overall rate is chosen to be 997 Hz,

with 70% assigned to bb, 15% to be, 10% to eb and the remaining 5% to ee. The events taken during crossing types other than bb are used for background subtraction and beam monitoring.

After a processing step in the High Level Trigger, a small number of "counters" are defined for each of these random LumiTriggers which store *e.g.* the number of channels which fired in different sub-detectors or the number of reconstructed tracks and vertices (see Section 4.1). The values of these counters are stored as integer numbers in a specific bank in the raw data, a "LumiBank". If for the event the only positive HLT decision is due to the luminosity trigger, only the LumiBank is retained for storage and apart from some other bookkeeping data, the raw detector data are discarded. The event size is then reduced by a factor 500. These events are called "nano-events".

3.4.4 Trigger for van der Meer scans

In this section we describe the LHCb trigger configuration used to collect data in LHC fills 1059 and 1422, where van der Meer scans were performed in LHCb. The absolute luminosity normalisation analysis is described in Chapter 6.

During the April scans (fill 1059) the event rate was low and it was possible to record all events containing interactions. The non-selective L0 channels PU and CALO (see Section 3.4.1.1) were used, while the HLT was only tagging, but not rejecting the events.

The event rates during the October scans (fill 1422) were significantly higher and therefore a selective trigger, composed of the OR of three independent criteria, was used. The first decision accepts random LumiTriggers (see Section 3.4.3) with a total rate of 22.5 kHz, distributed among the different bunch-crossings as follows: 20 kHz in bb crossings, 2 kHz in be and eb crossings, and 0.5 kHz in ee crossings. It is possible to record such a high rate of events (recall that the nominal rate of events written to disk is 2 kHz) because the random "nano-events" contain only the information necessary to measure the relative luminosity and therefore are of very small size. The second decision uses L0 CALO triggers with a rate limit of 1 kHz. The third decision collects events for the beam-gas analysis. As detailed in Section 7.5.5, the measured rates of beam-gas interactions in be and eb crossings are used to set a limit on the transverse inhomogeneity of the residual gas. In 2010, the beam-gas data collected in VDM fills was not sufficient to perform absolute luminosity normalisation with the BGI method.

Chapter 4

Measurement of the relative luminosity

As discussed in Section 1.2.2, the luminosity of a pair of colliding bunches[⋆] can be written in the following way (*cf.* Eq. (1.9)):

$$L = N_1 N_2 f (2c \cos^2 \alpha) \cdot (\text{Overlap Integral}) , \tag{4.1}$$

where N_i $(i = 1, 2)$ are the number of particles in the two bunches, f is the revolution frequency, c is the speed of light, and α is the half crossing angle between the beams. The Overlap Integral depends on the crossing angle, the bunch profiles and their offsets in space and time. The direct methods for absolute luminosity determination provide estimates of the quantities entering Eq. (4.1). Below, a short summary is given of how these quantities are determined in the measurements presented in this thesis. The absolute luminosity of the full data-set collected by the experiment is determined using the so obtained absolute normalisation and a systematic measurement of the relative luminosity.

At the LHC, two different devices are used for the measurement of the intensity of the individual bunches, $N_{1,2}$ (see Section 2.2.3). The FBCT measurements are used to determine the relative populations of the individual 25 ns bunch slots, while the absolute normalisation is obtained with the DCCT. The nominally empty bunch slots which contain beam current below the FBCT threshold (ghost charge) will be visible only to the DCCT. Therefore, the ghost charge needs to be subtracted from the DCCT measurements before the normalisation takes place.

The revolution frequency, f, is an essential operational parameter of any collider. It is determined by the particles' velocity and the collider circumference, and can be estimated with sufficiently high precision. The revolution frequency at the LHC is 11.245 kHz [5].

The beam crossing angle, 2α, can be measured by the LHC, using the beam position

[⋆] In case of multiple colliding bunches, their contributions to the total luminosity are summed.

monitors situated in the inner triplet magnets [79], or by the experiments, using beam-gas interaction vertices (see Section 7.2).

The measurements of the Overlap Integral with the van der Meer scan and beam-gas imaging methods are presented in Chapters 6 and 7, respectively. With the VDM method the relevant beam parameters are determined by scanning the two beams across each other in the two transverse directions and recording the observed interaction rate. With the beam-gas imaging method, the beam angles, profiles and transverse offsets are determined from reconstructed beam-gas interaction vertices. The precision of the measured beam parameters is improved by applying the constraints relating the position and the size of the separate beams and their luminous region (see Eq. (7.2)).

In an experiment, the absolute luminosity is obtained only for short periods of data-taking. To be able to perform cross-section measurements on any selected data sample, the relative luminosity must be measured consistently during the full period of data-taking. The systematic determination of the relative luminosity in all data-taking periods requires specific procedures to be applied in the trigger, in the data-acquisition, processing and final analysis [104].

The basic principle used in LHCb is to acquire luminosity data together with the physics data and store it in the same files. During further processing of the physics data the relevant luminosity data are kept together in the same storage entity. In this way, it remains possible to select only part of the full data-set for physics analysis and still keep the capability to determine the corresponding luminosity.

In this chapter we first describe the procedure to determine the relative luminosity using several independent variables and methods. Later we outline how these variables are measured online and how the relative luminosity information is handled during the different data-processing stages.

4.1 Luminosity counters

Luminosity counters are variables which give access to the (relative) instantaneous luminosity and are easily measurable on-line. The following luminosity counters are used:

- number of hits in the SPD;
- transverse energy deposition in the calorimeters, $\sum E_{\mathrm{T}}$;
- number of hits in the PU;
- number of r-z tracks in the VELO;
- number of backward r-z tracks in the VELO;
- number of vertices reconstructed from 3D VELO tracks.

The first three counters are obtained directly from the hardware (L0) trigger (see Section 3.4.1.1), while the last three counters are the result of partial event-reconstruction

in the HLT (see Sections 3.2.4 and 3.2.5).

The luminosity is proportional to the average number of visible proton-proton interactions in a beam-beam crossing, $\mu_{\rm vis}$. Considering a single pair of colliding bunches, this can be shown by dividing both sides of Eq. (1.1) by the bunch revolution frequency f:

$$\frac{R_{\rm vis}}{f} \equiv \mu_{\rm vis} = \frac{L\sigma_{\rm vis}}{f} \ , \tag{4.2}$$

where $R_{\rm vis}$ is the interaction rate of the process with cross-section $\sigma_{\rm vis}$. The subscript "vis" is used to indicate that Eq. (4.2) holds for an arbitrary definition of the visible cross-section. For practical purposes, *effective* processes are chosen which allow easy determination of the interaction rate and $\mu_{\rm vis}$, like, for example, the process producing at least two r-z VELO tracks (see Section 3.2.4). Appropriate subscripts will be used (*e.g.* "VELO") to indicate the properties of such processes.

LHCb is recording the values of the luminosity counters listed above during all periods of data-taking using randomly triggered events (see Section 3.4.3). With any of these counters the average number of visible pp interactions per crossing, and therefore the relative luminosity, can be determined using several different approaches. In 2010 LHCb used the "zero-count" method (see Section 4.2.3). In addition, the recorded luminosity-counter spectra are used for systematic studies.

4.2 Methods for the determination of the average number of visible pp interactions per crossing

4.2.1 Average of the counter distribution

In case of linear response of the detectors providing luminosity counters, there should be proportionality between the mean of the counter distribution and $\mu_{\rm vis}$. Toy Monte Carlo studies show that this simple approach is very accurate [105]. However, the method is not robust against non-linearity of the detector response (*e.g.* saturation at large $\mu_{\rm vis}$).

4.2.2 Fit to the counter distribution

A possible approach to determine $\mu_{\rm vis}$ is to perform a fit to the luminosity counter spectrum. For the application of this method, the detector response to a single proton-proton interaction needs to be determined. This procedure yields precise results and is robust against saturation of the detector response. More details about the method are given below.

Let us consider the luminosity counter distribution that we would obtain observing a large number of events containing one and only one pp interaction. After normalising this distribution we obtain the one-interaction PDF for this counter, I. The

counter distribution that we would get if there were exactly two interactions in the same event is the convolution of I with itself✦. Later we are going to use the Fourier transform of these distributions, where the convolution of two functions is replaced by the multiplication of their Fourier transforms. We are going to signify the Fourier transformed functions with the superscript "F". Considering the counter distribution P_{sig}, obtained for pp collisions following the Poisson distribution we have the following expression [105]:

$$P^F_{\text{sig}} = \sum_{n=0}^{\infty} \frac{e^{-\mu_{\text{vis}}} {\mu_{\text{vis}}}^n}{n!} (I^F)^n = \exp(\mu_{\text{vis}}(I^F - 1)) \ , \tag{4.3}$$

In the presence of background with PDF P_{bgr}, the Fourier transform of the observed counter distribution P_{obs} will be:

$$P^F_{\text{obs}} = P^F_{\text{bgr}} P^F_{\text{sig}} \ , \tag{4.4}$$

From Eqs. (4.3) and (4.4) we can get an expression for I:

$$I = \left(\frac{1}{\mu_{\text{vis}}} \ln(P^F_{\text{obs}}/P^F_{\text{bgr}}) + 1 \right)^{F^{-1}} \tag{4.5}$$

For the determination of I we need to measure μ_{vis} and the counter PDFs corresponding to signal + background and background only.

In Fig. 4.1 one-interaction PDFs obtained from data are shown for several counters. Spikes at zero are clearly visible for VELO and SPD counters. It has been checked that the peaks are correlated and it is believed that they are due to diffractive events.

Equation (4.5) is invariant under the two simultaneous transformations: $I \to \alpha I + (1-\alpha)\delta$, $\mu_{\text{vis}} \to \mu_{\text{vis}}/\alpha$, where α is a constant and δ is a Dirac δ-function. This arbitrary scale does not influence the relative luminosity monitoring. Once determined with sufficient precision, the one-interaction PDFs can be used to determine μ_{vis} by fitting the observed counter distribution to (4.4) multiplied by the total number of events in the observed spectrum. This provides a robust and precise method to monitor μ_{vis}. However, the "fit" method is computationally intensive and at present is not used for the measurement of the relative luminosity at LHCb.

✦ This can seen from the following. We consider the general case where two distinct processes produce counter distributions $P_1(x)$ and $P_2(x)$, respectively. We are interested in the counter distribution that we would observe if the two processes take place at the same time. Initially, we consider that the first process produces a fixed number of counter hits (say x_0) for every event, *i.e.* $P_1(x) = \delta(x - x_0)$. In this case, the counter spectrum corresponding to the simultaneous occurrence of the two processes will be $P_2(x)$ shifted to the right by x_0, *i.e.* $P_{12}(x) = P_2(x - x_0)$. Next, we represent a generic distribution $P_1(x)$ as a sum of entries in many bins, $P_1(x) = \int P_1(x_0)\delta(x - x_0)dx_0$. Using the already obtained transformation induced by $\delta(x - x_0)$ we conclude that the counter spectrum corresponding to the simultaneous occurrence of the two processes will be $P_{12}(x) = \int P_1(x_0)P_2(x - x_0)dx_0$, which coincides with the definition of a convolution of $P_1(x)$ and $P_2(x)$.

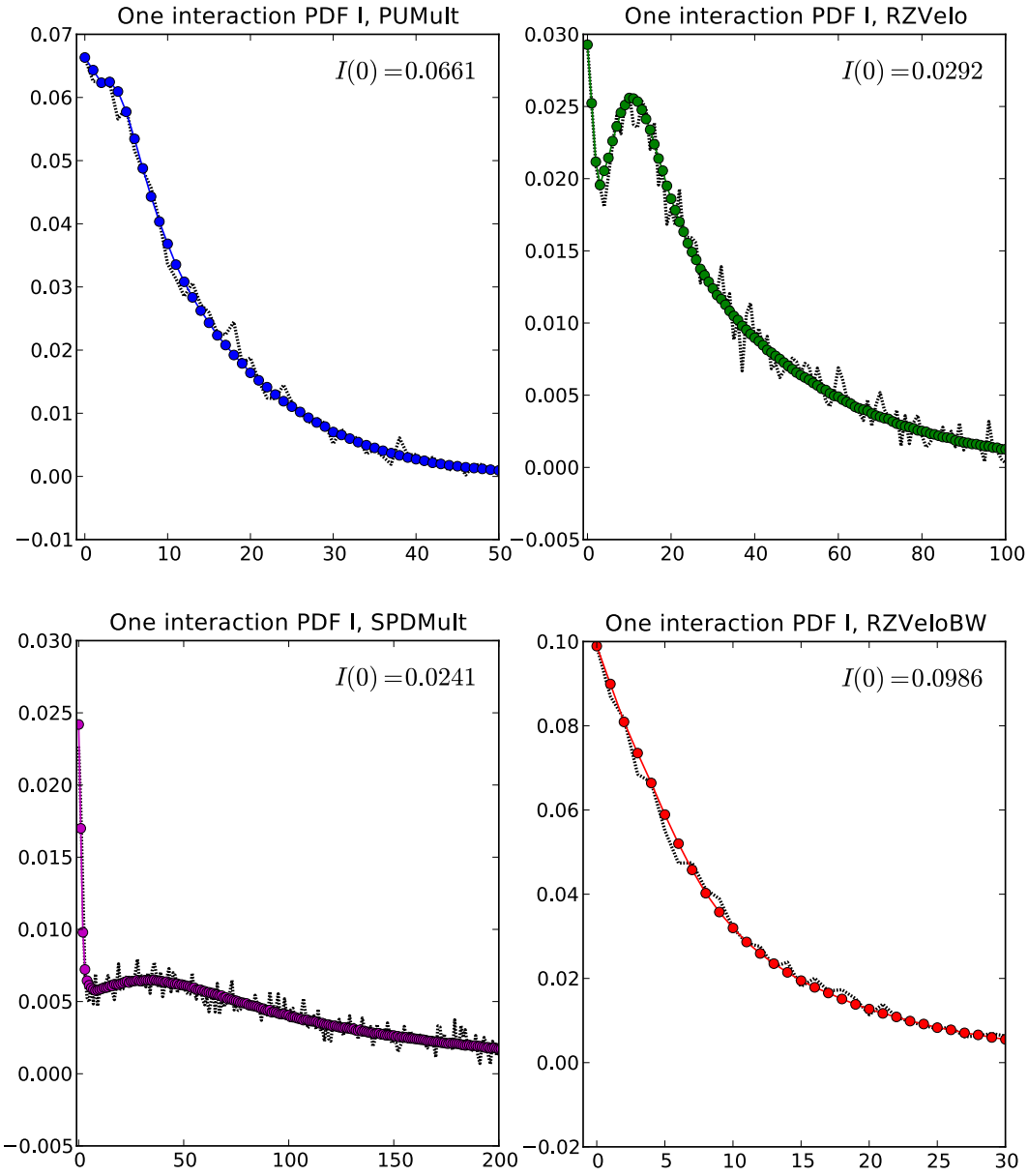

Figure 4.1: One-interaction PDFs of different luminosity counters: PU multiplicity (top left), SPD multiplicity (bottom left), r-z VELO tracks (top right) and backward r-z VELO tracks (bottom right). The measured one-interaction spectrum is shown with a fine-dashed line. Its spiky shape is due to high frequencies in the Fourier transforms I^F, which arise from statistical fluctuations of adjacent bins in the signal and background spectra. The smoother distribution, shown with filled circles is obtained by applying a high-frequency cut-off on I^F.

4.2.3 Zero-count method

Assuming that the number of visible proton-proton interactions follows a Poisson distribution μ_{vis} can be determined from the fraction of events producing zero interactions. The "zero-count" method provides reliable results with no dependence on possible detector response non-linearity.

The probability to have zero interactions in the crossings of type bb, P_0^{bb}, is mea-

sured from the fraction of "empty" events in a sample of randomly triggered events (see Section 3.4.3). An empty event is defined by applying a counter-specific threshold below which it is considered that no primary interactions occurred in the corresponding bunch-crossing. The contribution of backgrounds is accounted for in the following way. Consider a counter x which can not take negative values. Suppose there are two independent sources (*e.g.* beam-beam and beam-gas interactions) contributing to x and individually they give spectra P^{sig} and P^{bgr}. The resulting spectrum is the convolution $P = P^{\text{sig}} \otimes P^{\text{bgr}}$ (see Section 4.2.2). Since both sources can not produce a negative x, a zero sum means zero contributions from P^{sig} and P^{bgr}, so that $P_0 = P_0^{\text{sig}} P_0^{\text{bgr}}$ and $\ln P_0 = \ln P_0^{\text{sig}} + \ln P_0^{\text{bgr}}$. Therefore, $\ln P_0$ is an additive quantity and in the presence of backgrounds their contribution $-\ln P_0^{\text{bgr}}$ can be subtracted. The background distribution should not necessarily follow a Poisson law. The value of $-\ln P_0^{\text{bgr}}$ is estimated from the crossings where one bunch is filled and the other is empty. In the crossings with pp-collisions it is renormalised assuming that the dominating beam-gas background is proportional to the beam currents.

As already mentioned, we define an "empty" event as having $x \leq x_0$ with some threshold x_0. The above arguments hold only for $x_0 = 0$ since we assumed that $x = x_1 + x_2 = 0$ implies $x_1 = x_2 = 0$. If $x_0 > 0$, some systematic error appears. Toy MC studies show that the magnitude of this systematic plays an important role only when a significant fraction of the counter probability distribution for signal events is contained in the excluded counter range [105]. As will be shown later, the systematic associated with the relative luminosity measurement is estimated from the stability of counter ratios during the relevant period of data-taking.

The zero-count method is both robust and easy to implement. To evaluate the number of visible pp interactions per crossing μ_{vis}, backgrounds are subtracted using:

$$\mu_{\text{vis}} = -\left(\ln P_0^{\mathsf{bb}} - \ln P_0^{\mathsf{be}} - \ln P_0^{\mathsf{eb}} + \ln P_0^{\mathsf{ee}}\right) \ , \tag{4.6}$$

where $P^i (i = \mathsf{bb}, \mathsf{ee}, \mathsf{be}, \mathsf{eb})$ are the probability density functions (PDFs) of a counter measured for the four different bunch-crossing types. The P^{ee} contribution is added because it is also contained in the P^{be} and P^{eb} terms.

The number of r-z tracks reconstructed in the VELO is chosen as the best and the most stable counter. For the purpose of the zero-count method "empty" events are defined as having zero or one track. The systematics associated with this choice of threshold is negligible since the average interaction produces ~ 30 tracks in the VELO. Modifications and alignment variations of the VELO also have negligible impact on the method, since the efficiency for reconstructing at least two tracks in an inelastic event is close to 100%. The stability of the counter is demonstrated in Fig. 4.2 which shows the ratio of the relative luminosities determined with the zero-count method from the multiplicity of hits in the PU layer of the VELO and from the number of r-z VELO tracks. Apart from a few threshold updates in the PU hardware, the PU was also stable throughout LHCb 2010 running, and we use it as a cross-check. Figure 4.3a

covers the whole period of LHCb operation in 2010, with both low and high number of interactions per crossing. Similar cross-checks have been made with the counter based on the number of reconstructed vertices. These three counters have different systematics, and by comparing their ratio as a function of time and instantaneous luminosity we conclude that the relative luminosity measurement has a systematic error of 0.5%. The assignment of this error is supported by Fig. 4.2 (taking into account that the *visible* spread of ±1% in the ratio $\mu_{\rm PU}/\mu_{\rm VELO}$ corresponds to about $\pm 2\sigma$) and by Fig. 4.3a (taking into account that the "steps" in the ratio $\mu_{\rm PU}/\mu_{\rm VELO}$ are attributed to known maintenance changes to the PU system).

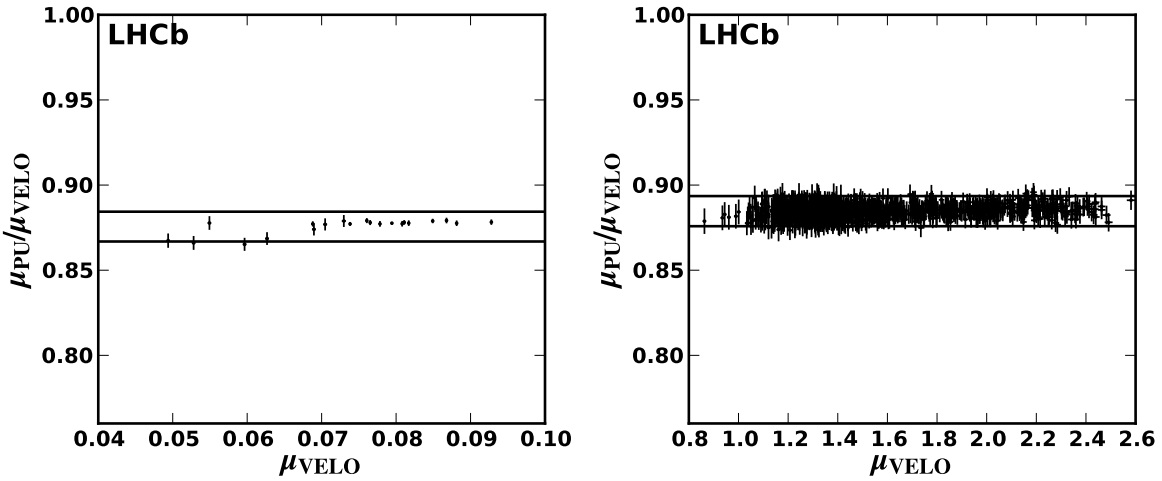

Figure 4.2: Ratio of the average numbers of interactions per crossing $\mu_{\rm PU}/\mu_{\rm VELO}$ determined with the zero-count method from the number of hits in the PU layer and the number of r-z VELO tracks, versus $\mu_{\rm VELO}$. The deviation from unity is due to the difference in acceptance. The left (right) panel uses runs from the beginning (end) of the 2010 running period with lower (higher) values of $\mu_{\rm VELO}$. The horizontal lines indicate a ±1% variation.

4.3 Systematic effects

Spill-over occurs either due to time misalignment of event windows or because the signal does not fit into 25 ns. The spill-over results into an increased average detector response in ee crossings immediately after beam-beam crossings and therefore leads to an overestimation of the background to the relative luminosity. If there is no time misalignment, spill-over is relevant only for the SPD and PU detectors (see Fig. 4.4).

The effect of the spill-over can be minimised by ignoring events from ee crossings near bb crossings. Since the detector noise for the selected counters is small ($< 10^{-5}$ relative to the typical values measured during bb crossings), it is a good approximation to ignore the ee subtraction altogether. The integral relative luminosity computed from the SPD counter decreases by 0.5% when the correction is applied. The effect on other counters is less than 0.1%. In filling schemes with consecutive bunches (bunch trains),

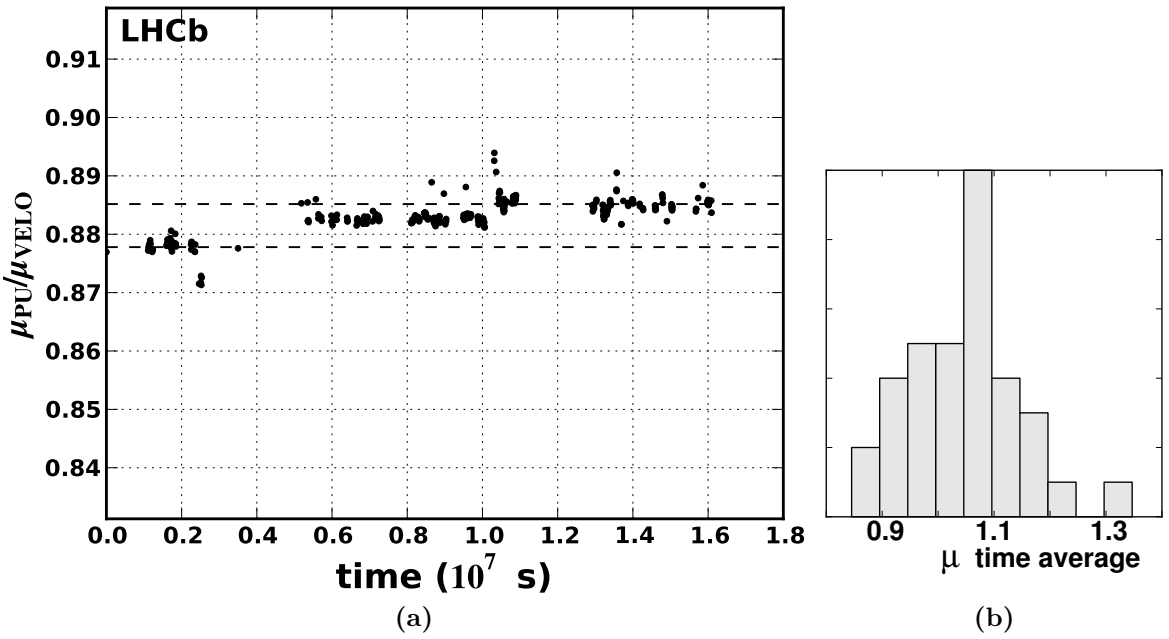

(a) (b)

Figure 4.3: (a) Ratio between μ_{vis} values obtained with the zero-count method using the number of hits in the PU and the track count in the VELO as function of time in seconds relative to the first run of LHCb in 2010. The period spans about half a year. The dashed lines show the average value of the starting and ending periods and differ by $\sim 1\%$. The changes in the average values between the three main groups coincide with known maintenance changes to the PU system. The excursion near $1.05\,10^7$ s is due to background introduced by parasitic collisions at 37.5 m from the IP to which the two counters have different sensitivity. The isolated points are due to runs with low statistics. (b) Spread of μ_{vis} defined by the zero-count method of the VELO counter for the different bunches of fill 1308 averaged over time. The RMS is 10%.

the effect grows and introduces larger errors. Study with 2011 data using 50 ns bunch trains showed that the effect of the spill-over is less than 0.1% for the VELO counter, about 1% for the PU counter, and $\mathcal{O}(10)\%$ for the SPD counter.

The number of protons, beam sizes and transverse offsets at the interaction point vary across bunches. Thus, the μ_{vis} value varies across bb crossings. A histogram of these μ_{vis} values for fill 1308 with 35 colliding bunches is shown in Fig. 4.3b. The spread in μ_{vis} is about 10% of the mean value. Due to the non-linearity of the logarithm function one first needs to calculate the μ_{vis} values for the different bb BCIDs and then take their average. However, for short time intervals the statistics are insufficient to determine μ_{vis} per BCID, while one cannot assume μ_{vis} to be constant when the intervals are too long (due to *e.g.* beam current decay and emittance growth). If the spread in the instantaneous μ_{vis} of all bb BCIDs is known, the effect of neglecting this spread in calculating the average value of μ_{vis} can be estimated. The difference between the naively computed (biased) μ_{vis} value and the true one is:

$$\mu_{\text{vis}}^{\text{biased}} - \mu_{\text{vis}}^{\text{true}} = -\ln\langle P_0^{\text{i}}\rangle - (-\langle \ln P_0^{\text{i}}\rangle) = \langle \ln(\frac{P_0^{\text{i}}}{\langle P_0^{\text{i}}\rangle})\rangle \ , \tag{4.7}$$

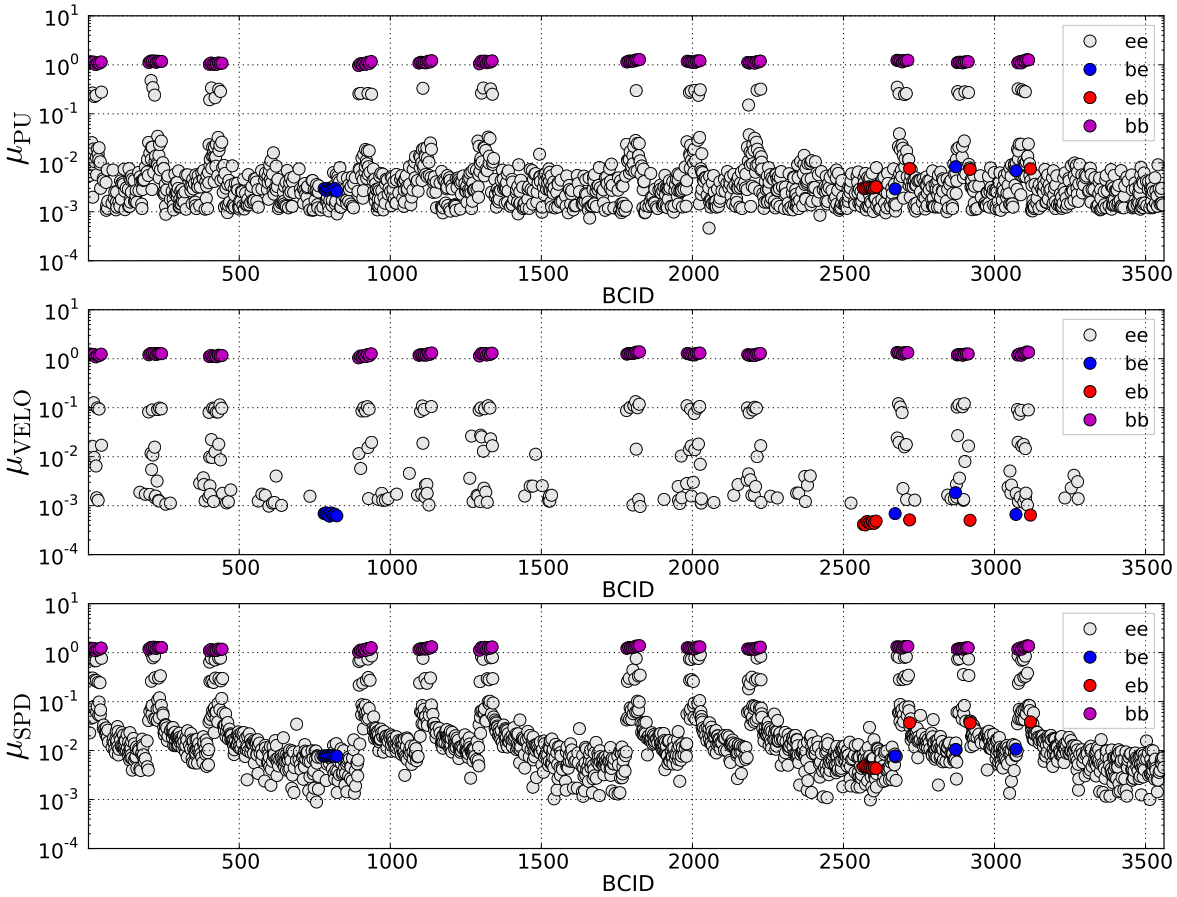

Figure 4.4: Average number of interactions per crossing obtained with the zero-count method and the PU (top), VELO (center) and SPD (bottom) counters. The values represent the separate BCID time-averaged results in fill 1372. The different colors correspond to the different types of bunch-crossings (ee, be, eb and bb). The effect of the spill-over is negligible for the VELO counter, while significantly increased detector response is observed in up to a few (PU) and up to a few hundred (SPD) ee crossings following bb BCIDs. With the event statistics available in a fill with duration of 15 h (see Section 3.4.3), the sensitivity to μ_{vis} in ee crossings is limited to about 10^{-3}.

where the average applies over all bb BCIDs i. The last equality uses the fact that taking the average over i of $\langle P_0^{\mathrm{i}} \rangle$ does not have any effect. Therefore, the biased μ_{vis} value can be calculated over short time intervals and a correction for the spread of μ_{vis} can be applied by computing $P_0^{\mathrm{i}}/\langle P_0^{\mathrm{i}} \rangle$ over long time intervals. The integral relative luminosity increases by about 0.5% when the correction is applied and we include a systematic uncertainty of 0.5% to account for this effect. The magnitude of the correction due to the spread of μ_{vis} is only weakly dependent on the luminosity counter used.

4.4 Data handling

The online selection of events used for measuring the relative luminosity (LumiEvents) has been described in Section 3.4.3. All LumiEvents are written to the full physics-event data stream and an additional copy is stored in the LumiStream. The LumiStream is three orders of magnitude smaller than the stream containing all data. During the off-line processing of the full physics stream a minimal summary of the contents of the LumiEvents is made and stored in a "File Summary Record" (FSR). The event processing is organised on a file-by-file basis, where a raw file typically contains the event data of a few minutes of data-taking. The granularity of the relative luminosity information is one raw file. A small number (more than one) of full raw physics-event streams is written on-line and events are stored randomly in one of the streams. It is not excluded that, due to data-handling problems, not all files are transmitted to the final data selection. Thus, it is important to keep the relative luminosity normalisation data together with the physics data. Files with reconstructed data (DSTs) are merged on a run basis and contain the data for a multiple of runs. During all these steps the luminosity summary data are transmitted, but their granularity is not further reduced by a summation process. Thus, time-dependent calibration constants can be applied to the counter information at a later stage.

During the final analysis stage the event data and luminosity data are available on the same files. The relative luminosity estimates are integrated (when necessary after time-dependent calibration) and the absolute calibration factor is applied. The absolute calibration factor is universal and is the result of the luminosity calibration procedures described in Chapter 6 and Chapter 7.

Chapter 5

Beam intensity measurement

In this chapter, the bunch current data analysis used in the LHCb absolute luminosity measurements with the VDM and BGI methods is presented. The beam current results are obtained following the prescriptions given in [75] and [106].

The individual bunch populations N_i (of each beam) are obtained assuming that the sum of populations of all nominally filled bunches $i = 1, ..., n$, as measured by the FBCT, is equal to the total beam intensity, measured with the DCCT, after subtracting a possible amount of "ghost" charge N_{ghost} (the LHC beam current transformers are introduced in Section 2.2.3). The ghost charge is defined as the beam current not visible to the FBCT, *i.e.* the total beam current contained in all 25 ns bunch slots with populations below the FBCT threshold. A common scale factor to transform FBCT signals into bunch populations can be defined as:

$$a = \frac{N_{\text{tot}} - N_{\text{ghost}}}{\sum_{i=1}^{n} S_i} \ , \tag{5.1}$$

where N_{tot} is the DCCT measurement of the total beam current, N_{ghost} is the total ghost charge, and S_i are the FBCT measurements of the individual bunch intensities (the sum runs over all nominally filled slots, $i = 1, ..., n$). Then, the individual bunch populations are:

$$N_i = a\, S_i \tag{5.2}$$

In this chapter we present consecutively the DCCT, ghost-charge, FBCT and satellite bunch measurements, and we conclude with a summary of the DCCT and FBCT uncertainties.

5.1 Total beam current

The absolute response of the DCCTs needs to be calibrated and any time dependent effects need to be understood. Calibrations are performed during technical stops, where a high-precision external current source is used to evaluate the absolute scale of the

DCCT response. According to the specifications, a precision of 1% or better can be reached for beams with intensity above 3×10^{11} [78]. However, with the lower beam intensities in the April-May 2010 fills, the noise ($O(10^9)$ charges) and the baseline variations have relatively bigger importance and bring larger contribution to the overall uncertainty. The noise subtraction is determined by taking the average DCCT readings over long periods of time during periods without beam before and after the relevant fills (see Fig. 7.3). The subtraction is given by the interpolation of the data outside the fill. The uncertainty introduced by the noise is estimated during periods without beam. The average of the A and B systems of the DCCT (see Section 2.2.3) is used for the final result.

The DCCTs were subject to extensive studies throughout 2010. An observation has been made that the DCCT response becomes non-linear for fills with closely-spaced bunches (bunch trains). The lack of precise estimation of this effect in the rapidly changing beam conditions in the last months of the LHC operation in 2010 resulted in large uncertainty on the absolute bunch intensity. Consequently, no competitive absolute luminosity calibration with the BGI method could be performed in this period. Later, the source of the filling scheme dependence of the DCCT readings has been identified and hardware changes were made. Laboratory test of the new DCCT hardware showed that the bunch pattern dependency is reduced to less than 1% (see Fig. 5.1).

A large number of calibration checks of the DCCT absolute scale were performed in 2011. Regular measurements in the LHC tunnel as well as on the surface, where the DCCT data acquisition hardware is located, show that the DCCT absolute scale is stable within 0.05%. Further monitoring will make it possible to determine if a seasonal effect is present and to estimate the uncertainty of the DCCT absolute scale.

5.2 Ghost charge measurement

A measurement of the ghost charge is performed by LHCb for the VDM and BGI fills used in the present analysis. The rates of beam-gas events produced by "ghost" and nominal protons are measured using a "low bias" trigger. The ghost fraction is determined from their ratio.

5.2.1 Event selection

In the April-May 2010 running period the LHCb trigger configuration included several low bias level-0 trigger channels (for an overview of the LHCb trigger system see Section 3.4.1). The used L0 channels `CALO` and `PU` have high efficiency for selecting events with a beam1-gas and beam2-gas interaction, respectively. In this period of data-taking no discrimination between the different types of bunch-crossings was made and all events selected by these trigger channels were recorded. On the other hand, the dedicated beam-gas L0 trigger channels were enabled only in `be` and `eb` bunch-crossings

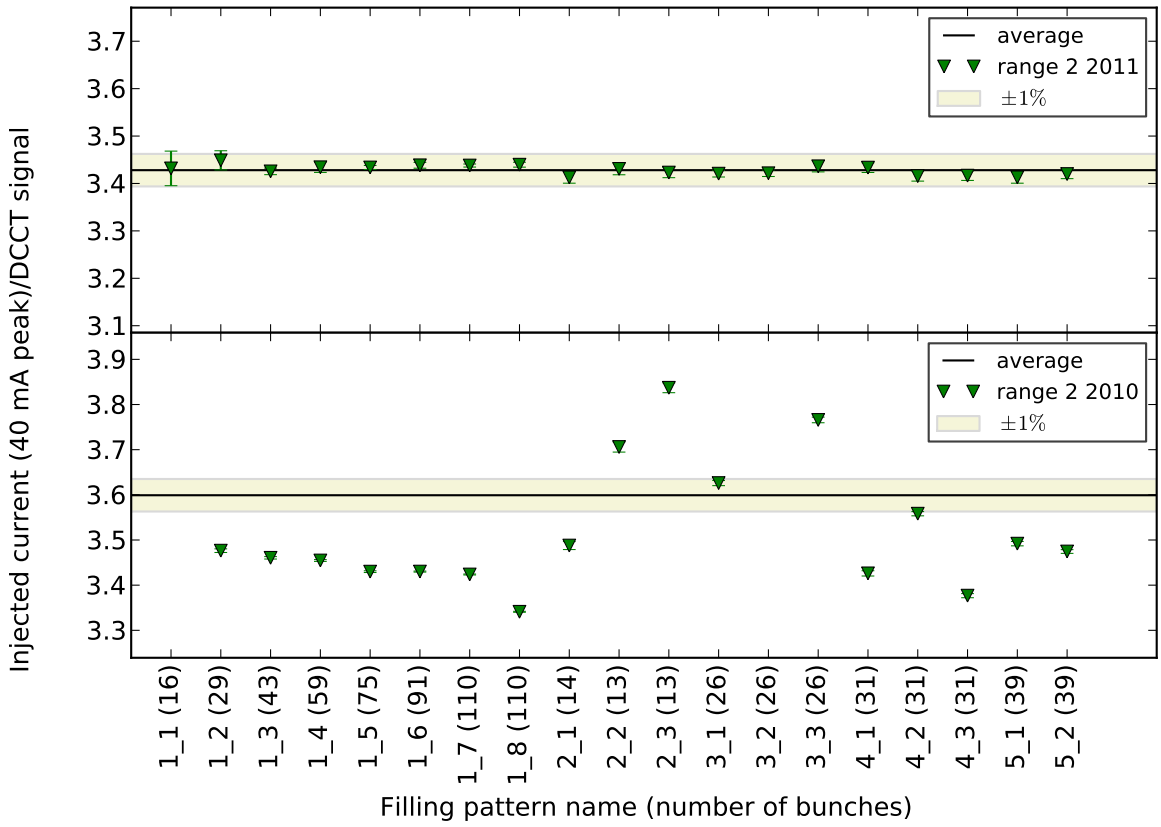

Figure 5.1: Stability of DCCT signal against variations in the LHC bunch pattern. The ratio between the injected current and raw DCCT signal is shown for various patterns of the injected current, simulating possible bunch train structures. The bottom part of the figure shows the DCCT response measured in 2010, where a strong dependence on the filling pattern is observed. On the top, the measurements done with the modified DCCT hardware used in 2011 are shown, where the filling pattern dependence is reduced to below 1%.

and therefore cannot be used for the measurement of the ghost charge, as one needs to measure the beam-gas rates in ee bunch-crossings too.

Two different configurations of the high-level trigger were used during the two fill ranges 1058-1090 (VDM and BGI analysis) and 1101-1122 (BGI analysis). In the former fills there were 1 or 2 colliding bunch pairs, while in the latter fills this number increased to 8. The individual bunches contained about 2.10^{10} protons and the average number of visible interactions per bunch-crossing was about 0.1. For this reason in fills 1058-1090 the HLT was configured not to reject events and all L0 triggers were written to disk (the LHCb design rate of events written to disk is 2 kHz). For the ghost charge measurement in these fills the events selected by the L0 `CALO` and `PU` channels are used. In fills 1101-1122 the HLT switched to a more selective mode. Beam-gas events were selected with the dedicated beam-gas `HLT Lines` (see Section 3.4.2). For the ghost charge measurement in these fills, in addition to the already mentioned L0 selection, we require that the events pass the beam-gas `BBForcedReco Line`. As can be

seen from Table 3.3 none of the other beam-gas HLT Lines can be used: the B1(2)gas Lines do not select events in ee bunch-crossings, while the BBParasitic Line processes only events, where the tracking has already been executed in another trigger Line and therefore has decreased efficiency for events containing single beam-gas interactions. The usage of the BBForcedReco beam-gas Line implies that only beam-gas interactions outside the luminous region will be selected. It has been checked that the rate limits of the trigger Line were not reached and therefore no effects due to rate limiters are expected. During the October VDM scan (fill 1422) the beam-gas L0 channels were activated for ee crossings in order to monitor the background rate and to estimate the ghost charge. The trigger used for the ghost charge measurement in this fill consists of the beam-gas L0 channels and the B1gas and B2gas HLT Lines.

In the April-May 2010 running period random triggers selected all of the bb bunch-crossings and fractions of the be ($\sim 21\%$), eb ($\sim 14\%$) and ee ($\sim 2 \times 10^{-3}\%$) crossings [75]. Currently the LHCb readout system does not allow the full events of two consecutive (25 ns) crossings to be read-out and therefore all crossings after the bb ones are blocked. As a result no ghost charge estimate can be given for the crossings after bb and a corresponding systematic uncertainty needs to be taken into account in the final results for the ghost charge.

The data are reconstructed with settings maximising the vertex finding efficiency for beam-gas events in the large z-region. Only 3D VELO tracks are used (see Section 3.2.4). In addition to the trigger requirements described above, the events in non-bb crossings are subject to the following selection. We require a reconstructed vertex with at least three tracks and z position $|z_{vtx}| < 2$ m. The transverse position of the vertex is required to satisfy both $|x_{vtx}| < 2$ mm and $|y_{vtx}| < 2$ mm. It was found that in the cases where more than one vertex is reconstructed (about 5% of all events) the corresponding z positions are close to each other and hint for a multiple reconstruction of the same interaction. Events with multiply reconstructed vertices are not considered in the present analysis. Distinction is made between vertices which have their tracks pointing all into the forward, or all into the backward direction or into both directions (the forward direction in LHCb is defined by the vector pointing from the VELO towards the muon system, see Fig. 3.3). Later we refer to such events as forward, backward and mixed events, respectively.

The vast majority of the vertices in be (eb) crossings are of the forward (backward) type. In both crossing types approximately 1% of the vertices contain tracks in the "wrong" direction (*i.e.* backward tracks in be crossings and forward tracks in eb crossings). A possible explanation are imperfections in the algorithm determining the directionality of the tracks. Later on, only forward (backward) events are considered in be (eb) crossings. In ee crossings both forward, backward and mixed vertices are observed. As an example, the bunch-crossing identifier (BCID) distributions of the forward, backward and mixed vertices in ee bunch-crossings in fill 1089 are shown in Fig. 5.2. The relation between the LHCb BCID and the LHC RF bucket numbers is given in Section 2.2.2.

For the case of forward and backward *ghost* vertices, about half of the events are observed in a "near-bunch", *i.e.* within ± 3 BCIDs of a nominally filled bunch. The mixed *ghost* vertices are predominantly concentrated around the bb crossings. The BCID distribution of the events near nominally filled bunches are shown in the zoomed insertions in Fig. 5.2.

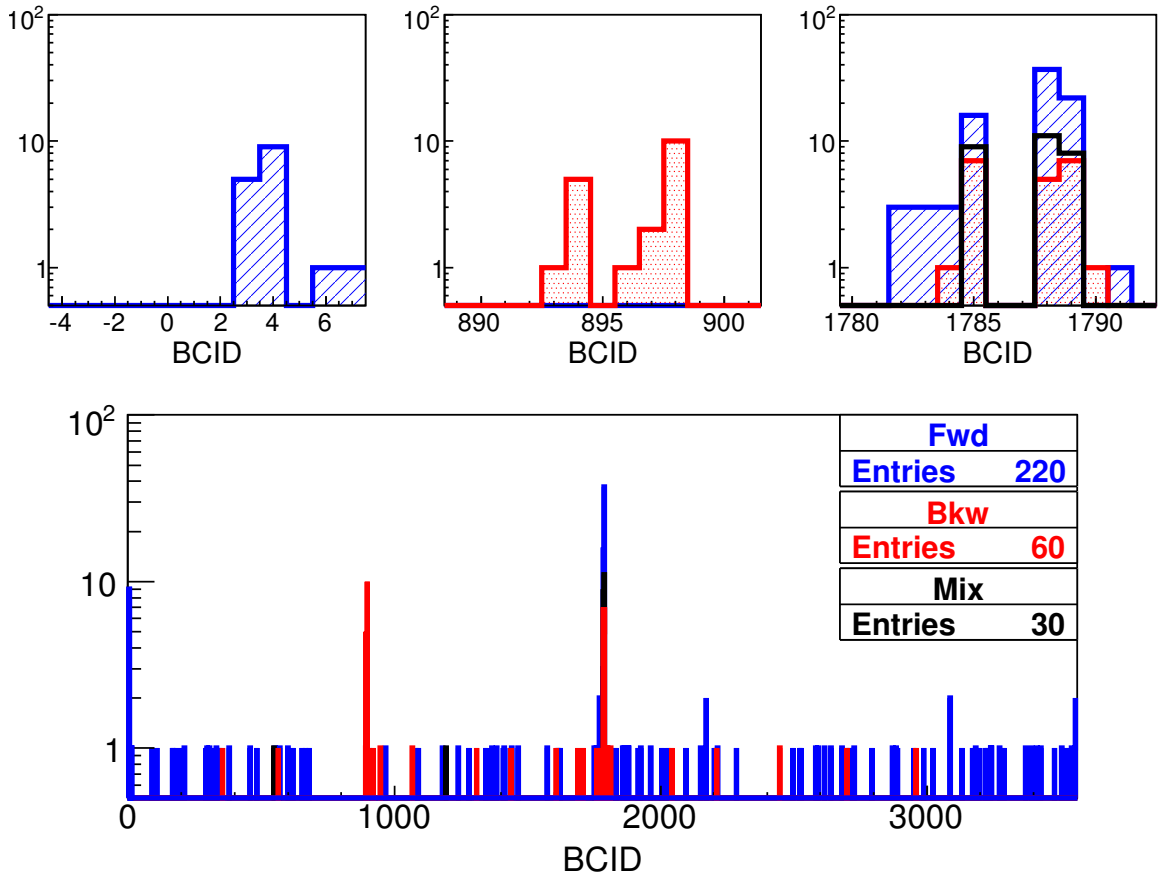

Figure 5.2: Number of forward (blue, hatched), backward (red, dotted) and mixed (black, empty) events in ee bunch-crossings as a function of BCID, in fill 1089. The inserted zooms at the top show the distributions near the nominally filled crossings with IDs 1, 895 and 1786, which are of types be, eb and bb, respectively. As explained in the text, all triggers in BCID 1787 were blocked.

The x-z distribution of the forward, backward and mixed vertices reconstructed in ee bunch-crossings is shown in Fig. 5.3. The distributions of forward and backward vertices show similarity with the distributions for be and eb bunch-crossings (the net crossing angle is clearly visible) and therefore these events are attributed to beam-gas interactions. The mixed events are concentrated in the luminous region and are attributed to inelastic pp interactions. We evaluate the fraction of pp interactions that could be misidentified as forward or backward events due to asymmetric distribution of the produced tracks or due to geometrical inefficiency. The estimates, obtained from

simulated minimum-bias events, are about 10 and 1% for the forward and backward case, respectively. A correction is applied to take this observation into account.

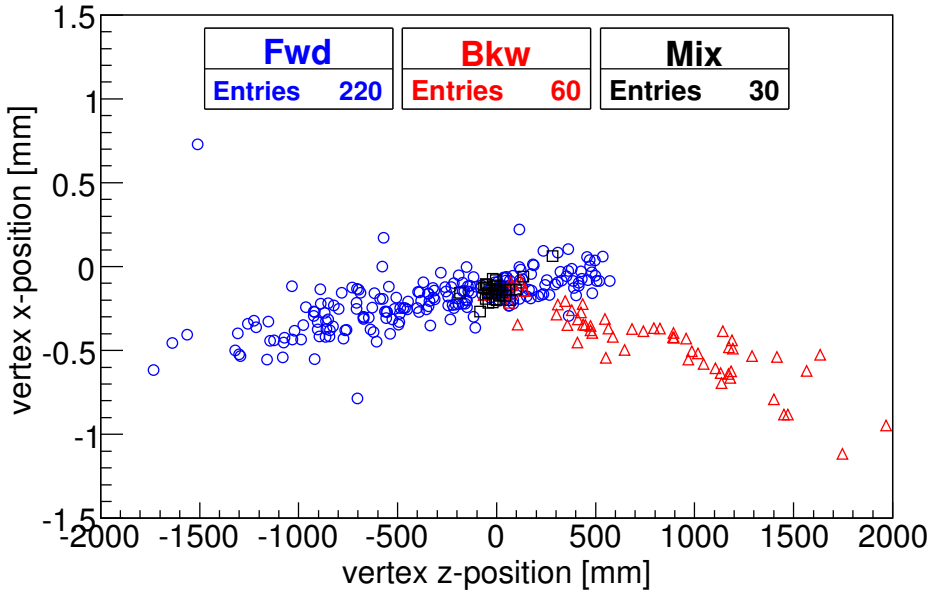

Figure 5.3: Distribution of reconstructed vertices in ee crossings in the $x-z$ plane for fill 1089. The forward events are indicated by blue circles, the backward events – by red triangles and the mixed events – by black squares.

The number of events measured in the various crossing types are summarised in Table 5.1 for the VDM and BGI fills used in this analysis. The ghost charge fraction of beam1(2) is obtained from the ratio of the number of beam1(2)-gas events in ee and be (eb) bunch-crossings, normalised to the relative population of the bunches taking part in be (eb) crossings. For beam1 the following formula is used:

$$f_{\text{ghost},1} = \frac{N_{\text{ghost},1}}{N_{\text{tot},1}} = \frac{F_{\text{ee}}}{F_{\text{be}}} \times \frac{\sum\limits_{i\in\text{be}} S_i}{\sum\limits_{i=1}^{n} S_i}\,, \tag{5.3}$$

where F_{ee} and F_{be} are the numbers of forward events in ee and be crossings and S_i is the population of bunch i from beam1. The sum in the denominator runs over all bunches of beam1. Similarly, the ghost fraction for beam2 is obtained from:

$$f_{\text{ghost},2} = \frac{N_{\text{ghost},2}}{N_{\text{tot},2}} = \frac{B_{\text{ee}}}{B_{\text{eb}}} \times \frac{\sum\limits_{i\in\text{eb}} S_i}{\sum\limits_{i=1}^{n} S_i}\,, \tag{5.4}$$

where B_{ee} and B_{eb} are the numbers of backward events in ee and eb crossings and S_i is the population of bunch i from beam2. The sum in the denominator runs over all

Table 5.1: Number of beam-gas events measured in be, eb and ee bunch-crossings in different LHC fills. The event selection procedure is described in the text. "near bunch" stands for all slots that are within ±3 BCIDs of a nominally filled bunch slot. The subsets of events summed over these slots are given in parentheses.

Fill number	Events in be	Events in eb	Events in ee (near bunch)					
			Forward		Backward		Mixed	
1059	1454	1425	4	(4)	0	(0)	0	(0)
1089	12277	11341	220	(95)	60	(39)	30	(28)
1090	5896	4579	52	(31)	40	(37)	31	(30)
1101	5880	6818	114	(27)	85	(61)	6	(5)
1104	26835	30276	273	(117)	246	(211)	1	(0)
1117	12163	15688	91	(28)	69	(28)	1	(1)
1118	10054	11469	117	(21)	61	(22)	0	(0)
1122	22571	30030	196	(88)	227	(128)	5	(2)
1422	16228	10813	140	(87)	155	(109)	82	(80)

bunches of beam2. The resulting ghost fractions are given in Table 5.2.

It is important to note that this method of ghost charge determination has an intrinsic time granularity of 25 ns - the individual 2.5 ns buckets within one BCID slot cannot be resolved due to the lack of precise timing information. The LHCb trigger efficiency depends on the time of the interaction with respect to the phase of the clock (which is centred at the nominal RF bucket). This timing-phase dependence and the unknown distribution of the ghost charge in the 25 ns slots introduce a systematic uncertainty which is evaluated below.

5.2.2 Systematic corrections

Inhibited BCIDs. As already mentioned, taking data in the bunch slots right after the bb crossings was not possible, which has the effect of underestimating the total amount of ghost charge. However, measurements of CMS, which focus on a smaller window around the bb crossings and with a finer granularity, allow one partially to "bridge the gap" between the nominally filled bucket and the bb +2 crossing monitored by LHCb. It was shown that the measurements of LHCb underestimate the ghost fractions by less than 0.2% [75]. In the present analysis, no correction is made for the inhibited BCIDs.

Timing-phase dependence of the trigger efficiency. The timing of the LHCb trigger is optimised for interactions in the nominal RF buckets and its efficiency depends on the time of the interaction with respect to the phase of the clock (modulo 25 ns). A measurement of the trigger efficiency was performed by shifting the clock, which is

Table 5.2: Results for the ghost fractions in beam1 and beam2 (in percent). The errors given reflect the statistical uncertainty from the number of beam-gas events. "near bunch" stands for all slots that are within ±3 BCIDs away from a nominally filled bunch slot. The ghost fractions concentrated in these slots are given in parentheses.

Fill number	beam1 ghost fraction $f_{\mathrm{ghost},1}$ (%) all slots	(near bunch slots)	beam2 ghost fraction $f_{\mathrm{ghost},2}$ (%) all slots	(near bunch slots)
1059	0.14 ± 0.07	(0.14 ± 0.07)	0.00 ± 0.04	(0.00 ± 0.04)
1089	0.88 ± 0.06	(0.38 ± 0.04)	0.26 ± 0.03	(0.17 ± 0.03)
1090	0.42 ± 0.06	(0.24 ± 0.04)	0.44 ± 0.07	(0.40 ± 0.07)
1101	0.97 ± 0.09	(0.23 ± 0.04)	0.62 ± 0.07	(0.45 ± 0.06)
1104	0.51 ± 0.03	(0.22 ± 0.02)	0.41 ± 0.03	(0.35 ± 0.02)
1117	0.37 ± 0.04	(0.12 ± 0.02)	0.22 ± 0.03	(0.09 ± 0.02)
1118	0.58 ± 0.05	(0.10 ± 0.02)	0.27 ± 0.03	(0.10 ± 0.02)
1122	0.33 ± 0.02	(0.15 ± 0.02)	0.29 ± 0.02	(0.16 ± 0.01)
1422	0.20 ± 0.02	(0.12 ± 0.01)	0.36 ± 0.03	(0.25 ± 0.02)

usually synchronised with the LHC bunch-crossing time, by 5, 10 and 12.5 ns and by comparing the total beam-gas rates in the nominal crossings. The efficiency drop for different time shifts of the clock phase is shown in Fig. 5.4.

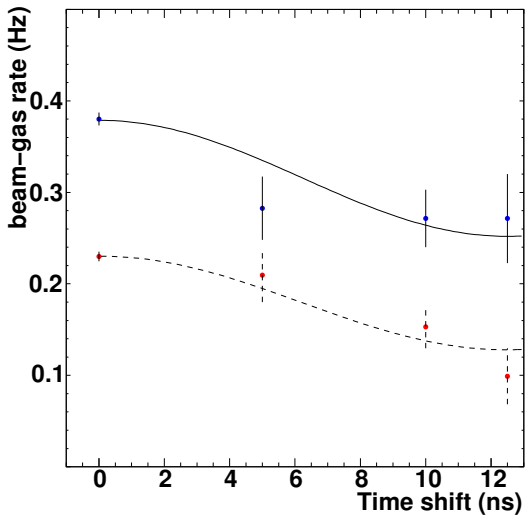

Figure 5.4: Beam-gas rate as function of clock phase as a measure of the relative trigger efficiency. The curves indicate fits to the function $R_{\max}\,(\epsilon_{\mathrm{fit}} + (1-\epsilon_{\mathrm{fit}})\,\cos(2\pi\Delta t/25\ \mathrm{ns}))$; the average normalised to the value at zero phase shift determines the phase-average of the trigger efficiency for a random distribution of ghost charge to be $\epsilon_{\mathrm{fit}} = 0.83 \pm 0.04$ and 0.78 ± 0.04 for the first (solid line) and the second beam (dashed line), respectively.

While for the nominal bunches we expect most of the protons to be contained in the nominal RF buckets, no information is available for the distribution of the ghost protons and a systematic error for the trigger efficiency needs to be taken into account.

We consider two extreme cases - when all ghost charge is contained within the nominal RF buckets and, thus, the relative timing efficiency is 100%, and when the efficiency is at the average level for 5, 10 and 12.5 ns points. The latter should be below the efficiency averaged over *all* RF buckets in a 25 ns slot. We take the average between these two extremes as an approximation of the efficiency and half of the difference between them as an error. This estimate is given as $\epsilon_{\text{average}}$ in Table 5.3.

Table 5.3: Ratio of the average rate measured with 5, 10, 12.5 ns time shifts and the rate at zero (first row). Estimation of the efficiency due to timing by using the average values (second row). Average efficiency from the fit to the sum of a cosine and a constant (third row).

	Beam1	**Beam2**
5, 10, 12.5 ns average	0.73	0.67
$\epsilon_{\text{average}}$	0.86 ± 0.14	0.84 ± 0.16
ϵ_{fit}	0.83 ± 0.04	0.78 ± 0.04

By assuming an approximate behaviour of the trigger efficiency another estimate can be obtained. We also fit the four available points at 0, 5, 10 and 12.5 ns to a periodic function $R_{\text{max}}\left(\epsilon_{\text{fit}} + (1-\epsilon_{\text{fit}})\cos(2\pi\Delta t/25\text{ ns})\right)$ (see Fig.5.4). This function has been obtained from $A + B\cos(2\pi\Delta t/25\text{ ns})$, by denoting its maximum (at $\Delta t = 0$), $A + B$, with R_{max} and its average in the range $\Delta t \in [0; 12.5]$ ns, $A/(A+B)$, with ϵ_{fit}. The value of the latter parameter gives the average trigger efficiency within one 25 ns slot (assuming that the efficiency is symmetric with respect to $\Delta t = 0$). The obtained ϵ_{fit} values are close to the central efficiency values $\epsilon_{\text{average}}$, as can be seen in Table 5.3.

The trigger efficiency correction $\epsilon_{\text{average}}$ is applied to the ghost charge estimates from Table 5.2. The final ghost charge correction factor f_{g} is estimated per fill as follows:

$$f_{\text{g}} = \left(1 - \frac{g_1 \pm \Delta g_1}{0.86 \pm 0.14}\right) \times \left(1 - \frac{g_2 \pm \Delta g_2}{0.84 \pm 0.16}\right) , \tag{5.5}$$

where $g_{1,2}$ and $\Delta g_{1,2}$ are the ghost charge estimates and errors from Table 5.2 and the numbers in the denominators are the trigger efficiency corrections $\epsilon_{\text{average}}$ from Table 5.3. The values of $1 - f_{\text{g}}$ used in the BGI analysis are given in Table 7.3. It should be noted that the ghost fraction corrections used in the BGI analysis used previous estimates of the ghost charge and differ slightly (about 10%, except in fill 1090, where the relative difference is almost 30%) from the ghost fraction corrections obtained from the numbers given in this section. Given the small overall effect that the new ghost charge estimates bring (about 0.1%), it was found unjustified to update the BGI results.

The estimates of the ghost charge in the VDM fills are given in Section 6.5.2.

5.2.3 Ghost charge measurement in LHC fills 1653 and 1658

Van der Meer scans were performed in LHC fills 1653 and 1658 (March 2011). Below, the LHCb ghost charge measurements in these two fills are presented, although the absolute luminosity measurements by LHCb using these data are not discussed in this thesis.

The ghost charge measurement procedure is identical to the one used for the April-May 2010 data, while a modified trigger configuration was used. At L0, the events selected by the two dedicated beam-gas channels (see TCK 0x002E002C in Table 3.2) were retained in ee, be and eb crossings. At HLT, dedicated beam-gas `Lines` processed the events with a beam-gas L0 trigger, reconstructing tracks and primary interaction vertices. The vertex selection criteria used in the two HLT `Lines` running over events in ee crossings are identical to the vertex selection criteria used in the HLT `Lines` running over events in be/eb crossings. The off-line ghost charge determination is made using formulas 5.3 and 5.4. The applied off-line vertex selection cuts are: z position within 2 m to $z = 0$, radial position smaller than 4 mm, and number of tracks per vertex larger than 4.

The BCID distributions of the off-line selected forward, backward and mixed vertices in ee bunch-crossings in fill 1653 is shown in Fig. 5.5. The corresponding x-z position distributions of the forward, backward and mixed vertices is shown in Fig. 5.6. The observed beam crossing angle confirms that these are beam-induced interactions. No qualitative difference is observed in the distributions corresponding to fills 1653 and 1658.

The acquired beam-gas data allowed the ghost charge measurement to be performed with high statistical precision using only a subset of the data. The result of the ghost charge measurements using 2-hour-long periods of data taking are shown in Figs. 5.7 and 5.8. The increase of the ghost charge with time is due to the increase of the beam-gas interaction rates measured in ee crossings (the beam-gas interaction rates in be and eb crossings decrease during the fill, with a rate compatible with the beam intensity lifetime). No evidence has been found that the increase of the ghost charge is related to the LHCb detector or trigger.

Ghost charge estimates for each of the VDM scan periods in fills 1653 and 1658 are made using LHCb data collected in the corresponding time period. Due to the lack of data during the CMS scan, an estimate of the ghost charge is obtained from a straight-line fit to the measurements made during the ALICE, ATLAS and LHCb scans. The raw and the final, trigger-efficiency corrected results for the ghost charge are given in Table 5.4. The *raw* ghost charge is obtained using formulas (5.3) and (5.4). The *final* ghost charge results are obtained from the raw results, after applying the trigger efficiency correction $\epsilon_{\text{average}}$ given in Table 5.3.

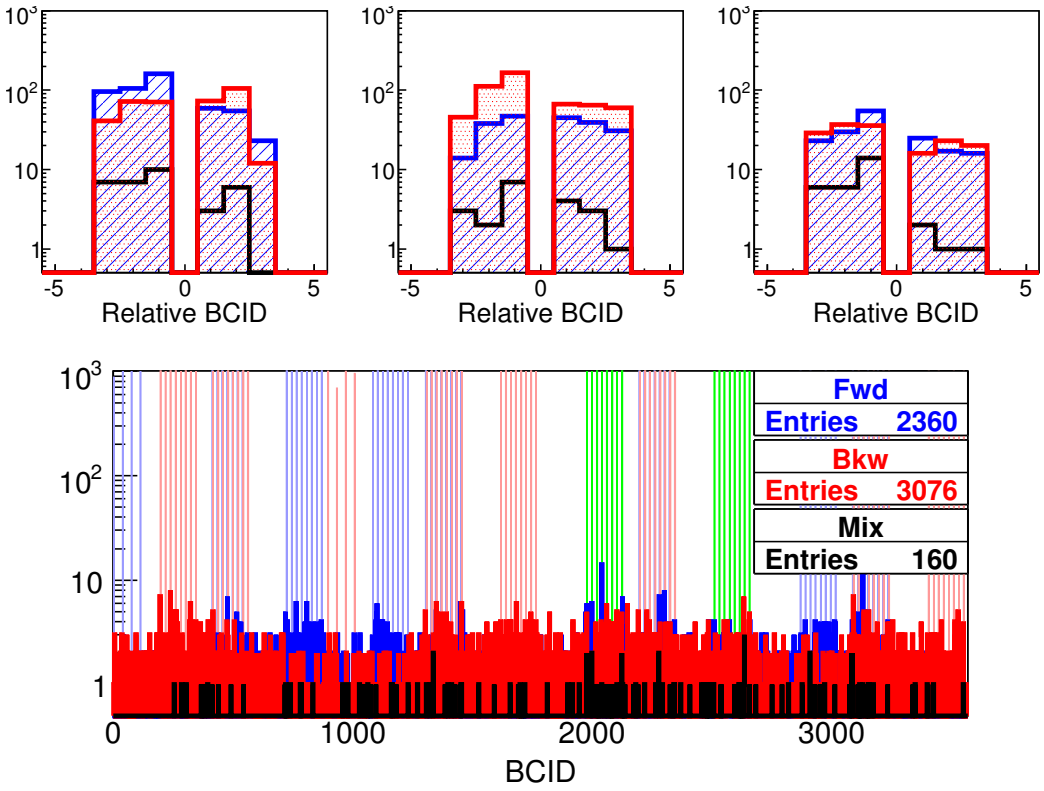

Figure 5.5: Bottom: Number of forward (blue, hatched), backward (red, dotted) and mixed (black, empty) events in ee bunch-crossings as a function of BCID in fill 1653. The thin vertical lines indicate the BCID of the be (blue), eb (red), and bb (green) crossings. Top: the summed BCID distributions near the nominally filled be (left), eb (middle) and bb (right) crossings.

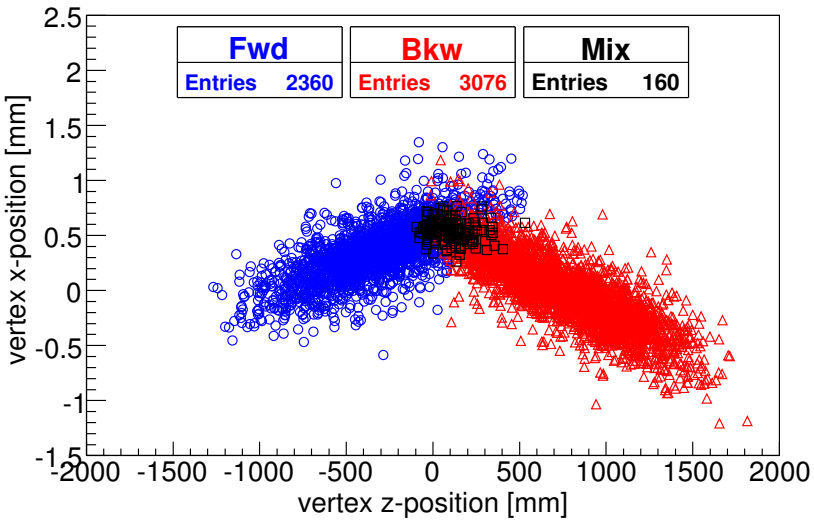

Figure 5.6: Distribution of reconstructed vertices in ee crossings in the $x-z$ plane for fill 1653. The forward events are indicated by blue circles, the backward events – by red triangles and the mixed events – by black squares.

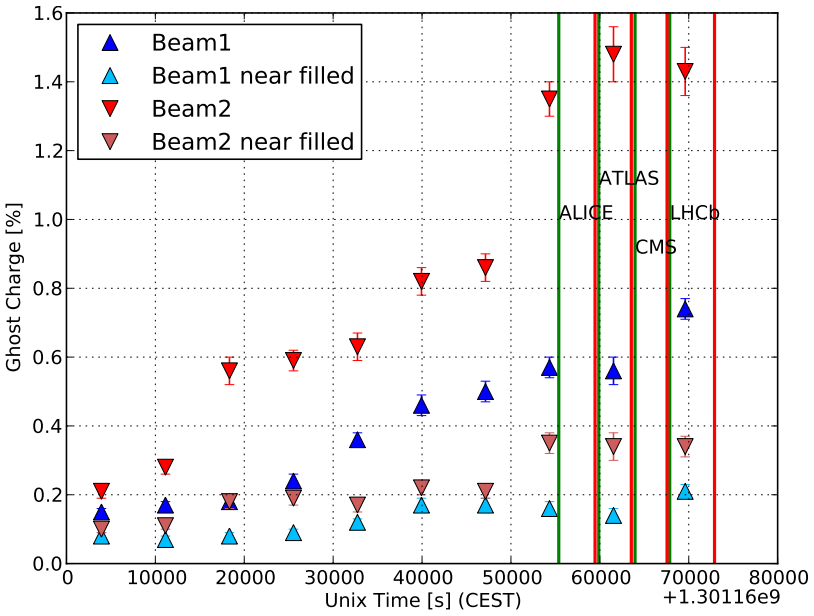

Figure 5.7: Time evolution of the ghost charge in fill 1653. The different markers indicate the total and the near-bunch (±3 BCID from the nominally filled bunches) ghost charge in the two LHC beams. No trigger-efficiency correction has been applied. The vertical lines indicate the start and end times of the van der Meer scans in the IP of ALICE, ATLAS, CMS and LHCb.

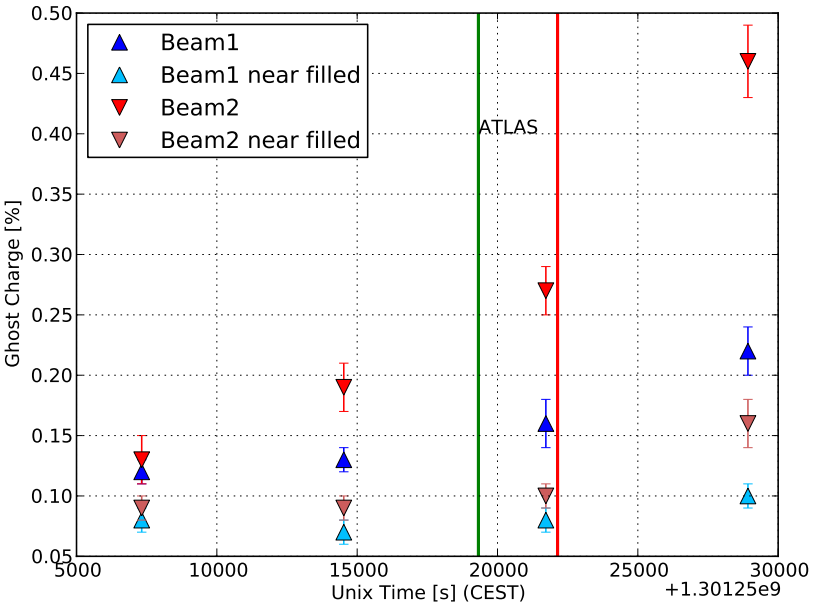

Figure 5.8: Time evolution of the ghost charge in fill 1658. The different markers indicate the total and the near-bunch (±3 BCID from the nominally filled bunches) ghost charge in the two LHC beams. No trigger-efficiency correction has been applied. The vertical lines indicate the start and end times of the van der Meer scans in ATLAS.

5.3 Bunch-by-bunch fractions

For the case of the FBCT, small timing errors and imperfections in the transformer response may result in 2–5% of the signal of a specific bunch to appear in the next 25 ns slot [75]. A correction for this spill-over effect can be applied by adding the signals measured in BCIDs "X" and "X+1" and assigning the sum to BCID "X" (nominally BCID "X+1" is empty). However, due to the fact that the FBCT readings are used only for the determination of the *relative* bunch populations the spill-over effect is reduced. Consequently, no spill-over correction is made in the present analysis. Other essential properties of the FBCT measurements are the offset of the electronic channels and the proportionality with the individual bunch charge. These have been cross-checked

Table 5.4: Ghost charge measurements during the VDM scans in fills 1653 and 1658.

	UTC Epoch time [s]		Raw Ghost Charge [%]		Trig. eff. corrected Ghost Charge [%]	
	Middle of scan	Duration of scan	beam1	beam2	beam1	beam2
Fill 1653						
ALICE	1301217420	4080	0.57 ± 0.04	1.57 ± 0.08	0.66 ± 0.12	1.87 ± 0.37
ATLAS	1301221710	3660	0.56 ± 0.06	1.47 ± 0.13	0.65 ± 0.13	1.75 ± 0.37
CMS	1301225760	3600	0.64 ± 0.03	1.44 ± 0.02	0.74 ± 0.13	1.71 ± 0.33
LHCb	1301230380	5040	0.70 ± 0.04	1.38 ± 0.09	0.81 ± 0.14	1.64 ± 0.33
Fill 1658						
ATLAS	1301270730	2800	0.18 ± 0.03	0.27 ± 0.04	0.21 ± 0.05	0.32 ± 0.08

with the ATLAS BPTX system [107], which provides a totally independent estimate of the relative bunch populations. This comparison shows a good linearity within the probed bunch current ranges, and small discrepancies between the offsets, which is interpreted as an effective relative offset [106]. As described in Section 6.3, a possible way to estimate these offsets and reduce the systematics associated with the relative bunch signals is to use the cross-section measurements obtained with the different colliding bunch pairs in a fill. In addition, an evidence has been found that the FBCT measurements are sensitive to the bunch length and position. Detailed studies of such effects are planned to be made in the future.

5.4 Satellite bunches

Satellite bunches are defined as beam current captured in RF buckets (see Section 2.2.2) that are within a few ns of the nominally filled bunches, *i.e.* within the same 25 ns slot. Satellite bunches can be detected by the LHC experiments when there is no (or a very small) crossing angle between the two beams, or during van der Meer scans where the beam separation in the plane of the crossing angle may lead to collisions between nominal and satellite bunches (see Fig. 6.15).

The amount of beam current contained in satellite bunches is estimated from the relative number of inelastic pp interactions in displaced interaction regions[⋆]. The LHCb satellite bunch analysis of the October VDM scan is discussed in Section 6.5.2. The ATLAS and CMS analyses of the four VDM fills in April-May 2010 show mutually consistent results and indicate that in the worst case (fill 1089) the satellite populations

[⋆] The charge at 5 ns steps from the main bunches is likely due to satellite bunches coming from the injector (SPS) which works with 200 MHz cavities. When the crossing angle between the two beams is small these satellite bunches collide with the nominal bunches at locations displaced by a multiple of ± 75 cm from the nominal interaction point.

in the buckets located at ±5 ns from the main bunch are about 0.2% of the main bunch [75]. The satellite populations in the buckets at ±10, ±15 and ±20 ns from the main bunches are an order of magnitude smaller. The correction due to satellite bunches is negligible in comparison to the total error and therefore is not taken into account (except for the VDM fill 1422; see Section 6.5.2).

5.5 Uncertainties

Three main sources of uncertainty have been identified for the measurements of the absolute bunch intensity [75, 106]. The exact uncertainty values used in the absolute luminosity measurement with the VDM and BGI methods are given in the respective chapters.

1. The uncertainty on the DCCT baseline offset. It is considered to be uncorrelated between the two LHC rings and from fill to fill. The importance of the DCCT baseline offset is smaller in fills with bigger total beam intensity;
2. The reproducibility of the DCCT absolute scale, based on three absolute calibrations performed in 2010. The observed peak-to-peak variation of the absolute scale are 2%, which is used to set an upper limit on the absolute scale uncertainty: ±2% (100% confidence level). Due to the lack of complete understanding of the source of these variations, these errors are conservatively treated as correlated between the two beams and between fills. The associated uncertainty on the bunch intensity product is 2.7% (68.2% confidence level);
3. The uncertainty of the FBCT measurements are estimated from a comparison to the ATLAS BPTX signals. This systematic uncertainty is considered to be uncorrelated between the two beams and from fill to fill [106]. Depending on the fill, the associated error on the bunch intensity product is between 2 and 3%. As discussed in Section 6.3, in VDM scans with multiple colliding bunches this uncertainty can be reduced by calibrating the relative bunch intensities with a fit to the cross-sections obtained for each individual colliding pair.

These three uncertainties and the uncertainty of the ghost charge determination are combined as uncorrelated errors.

Chapter 6

The van der Meer scan method

This chapter presents the LHCb measurements of an effective cross-section with the VDM method, using data collected in two dedicated LHC fills in April and October 2010. The author of this thesis has no direct contribution to the analysis leading to the absolute luminosity normalisation with the VDM method. The text in this chapter is reproduced from [10] and is included in this thesis for a comparison with the BGI method and its results (see Chapter 7).

The van der Meer scan method, introduced in Section 1.2.2, provides a direct determination of an effective cross-section σ_{vis} by separating the two colliding beams and measuring a counting rate proportional to the rate of inelastic pp interactions. Due to the bunched structure of the LHC beams, the beam separation scan needs to be performed in the $x-y$ plane (in contrast to the ISR which used continuous beams, the beam overlap at the LHC depends on the horizontal separation too). For two colliding bunches and under the assumption that the bunch shapes can be factorised in their x and y components, the cross-section σ_{vis} can be measured using the equation:

$$\sigma_{\text{vis}} = \frac{\int R(\Delta_x, \Delta_{y_0})\mathrm{d}\Delta_x \int R(\Delta_{x_0}, \Delta_y)\mathrm{d}\Delta_y}{N_1\, N_2\, f\, \cos\alpha\, R(\Delta_{x_0}, \Delta_{y_0})} \tag{6.1}$$

where N_1 and N_2 are the intensities of the two colliding bunches, which need to be taken from an independent measurement, α is the half crossing angle and $R(\Delta_x, \Delta_y)$ are the event rates corresponding to the process with cross-section σ_{vis}. These rates are measured when the beams are displaced by Δ_x and Δ_y with respect to the nominal "working" point (x_0, y_0). The scans consist of creating offsets Δ_x and Δ_y such that practically the full profiles of the beams are explored. The derivation of this formula can be found in [62].

By substituting $R(\Delta_x, \Delta_y)$ with $f\,\mu_{\text{vis}}(\Delta_x, \Delta_y)$, where μ_{vis} is the average number of interactions per bunch-crossing corresponding to σ_{vis}, Eq. (6.1) can be written in the following way:

$$\sigma_{\text{vis}} = \frac{\int \mu_{\text{vis}}(\Delta_x, \Delta_{y_0})\mathrm{d}\Delta_x \int \mu_{\text{vis}}(\Delta_{x_0}, \Delta_y)\mathrm{d}\Delta_y}{N_1\, N_2\, \cos\alpha\, \mu_{\text{vis}}(\Delta_{x_0}, \Delta_{y_0})} \tag{6.2}$$

This form is used in the cross-section calculations presented here.

In this chapter a description is given of the experimental conditions and the used beam scan procedures, followed by a discussion on the effects from the varying emittance and beam intensity during the scans. Later are described the cross-section determination and the averaging of the results obtained from the different colliding bunches. Finally, the associated systematic uncertainties are addressed and the cross-section results are summarized.

6.1 Experimental conditions during the van der Meer scans

VDM scans have been performed in LHCb during dedicated LHC fills in the beginning and at the end of the 2010 running period – one in April and one in October. The main beam characteristics are summarised in Table 6.1.

Table 6.1: Beam parameters and trigger selections used in the LHCb van der Meer scans. $N_{1,2}$ is the typical number of protons per bunch, $n_{\rm tot}$ ($n_{\rm coll}$) is the total number of (colliding) bunches per beam, ${\mu_{\rm vis}}^{\rm max}$ is the average number of visible interactions per crossing at the beam positions with maximum rate, $\tau_{N_1 N_2}$ and τ_L are the decay times of the bunch intensity product and of the luminosity, respectively. More details about the VDM trigger can be found in Section 3.4.4.

	25 Apr	**15 Oct**
LHC fill	1059	1422
$N_{1,2}$ (10^{10} charges)	1	7-8
$\beta^\star$ (m)	2	3.5
$n_{\rm coll}/n_{\rm tot}$	1/2	12/16
${\mu_{\rm vis}}^{\rm max}$	0.03	1
$\tau_{N_1 N_2}$ (h)	950	700
τ_L (h)	30	46
Trigger	minimum bias	22.5 kHz random minimum bias (R_{max} <1 kHz) beam-gas

In both fills two scans were performed [⋆], where either both beams moved symmetrically or only one at a time. The two different scanning strategies were used in order to look for systematic effects related to the displacement of the beams. Beam movements recorded with LHC beam position monitors (BPMs, see Section 2.2.3) up- and downstream of LHCb are shown in Fig. 6.1. In the following analysis we do not use this information quantitatively, since temperature effects may result in drifts of the BPM readings [79]. The precise beam positions are calculated from the LHC magnet

⋆ As previously mentioned, one VDM scan at the LHC consists of sweeping the two beams with respect to each other in the horizontal and vertical planes.

currents and cross-checked with the vertex measurements using the LHCb VELO, as described in Section 6.4.

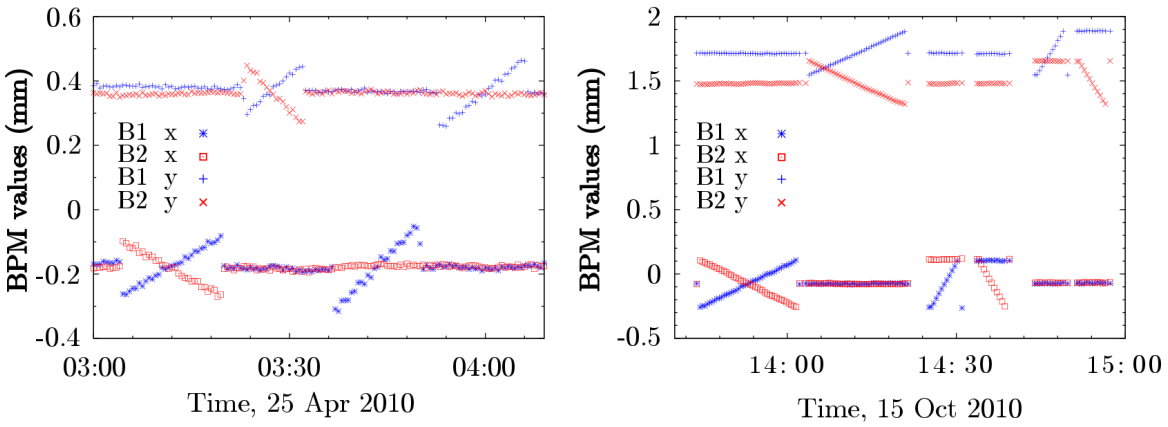

Figure 6.1: Position of the beams as function of time during the April (left) and October (right) scans. The values shown are obtained after averaging the measurements of the LHC BPMs located at about 20 m on either side of the IP, and provide information about the beam displacement at the IP (and not about the absolute beam position at the IP). The top (bottom) curves show the $y_{1,2}$ ($x_{1,2}$) coordinates of the two beams. Both in April and October there were two scans in $\Delta_x = x_1 - x_2$ and $\Delta_y = y_1 - y_2$. In the first scan both beams moved symmetrically, while in the second scan either only the first beam was moved (April) or the first beam in the beginning and the second beam in the end (October).

In April, the maximal beam separation was achieved only in the first scan, as in the second scan only the first beam was allowed to move away from its nominal position (details about the steering of the beams at the IP can be found in Section 2.2.4). In the second scan in October both beams moved one after the other, covering the optimal beam separation range. However, the beam steering procedure was such that in the middle of the scan the first beam jumped to an opposite end point and then returned, so that the beam movement was not continuous. This unwanted feature of the beam steering procedure potentially increases hysteresis effects in the LHC magnets controlling the beam separation. In addition, the second scan in October has fewer data points, as twice larger step-size was used. Therefore, we use the second scan only as a cross-check and to estimate systematic errors.

During the April scans the event rate was low and it was possible to record all events containing interactions. A loose minimum bias selection was used at the first trigger level (see Section 3.4.4). In October, the bunch intensities were higher by a factor ~ 7.5. Therefore, in spite of the slightly broader beams (the optics defined a $\beta^\star$ value of 3.5 m instead of 2 m, used in April), the interaction rate per colliding bunch pair was higher by a factor of ~ 30. There were twelve colliding bunch pairs instead of just one in April. Therefore, the selective trigger described in Section 3.4.4 was used.

As discussed later, the systematic error in the VDM cross-section measurements in both the April and October scans is dominated by uncertainties in the beam in-

tensities. In April, the error on the bunch current product is higher (5.6%) due to the uncertainties of the DCCT baseline offset, the DCCT scale and the relative bunch intensities (see Section 5.5). In October, the error from the DCCT baseline offset is reduced, due to the higher beam intensities. In addition, in the latter measurement the uncertainty of the relative bunch intensities is eliminated by fitting the results from the multiple colliding bunches (see Section 6.3). Therefore, the overall beam-current error in October is largely dominated by the DCCT scale uncertainty (2.7%) [106]. The results from the April and October scans are consistent, and in the following emphasis is put on the first scan taken in October, which provides the best overall precision.

6.2 Time stability

The relative evolution of the individual bunch intensities during the period of the two LHCb scans in October is shown in Fig. 6.2. The LHC filling scheme was chosen in such a way that all bunches collided only in one experiment (except for ATLAS and CMS where the bunches are always shared). There were twelve colliding bunch pairs in LHCb, three in ATLAS/CMS and one in ALICE. It is interesting to note that the LHCb bunches demonstrated the best time stability. During each of the two scans the bunch intensities changed by about 0.1% and the decay time of the bunch intensity product $\tau_{N_1 N_2}$ was about 700 hours. Therefore, we do not normalise the interaction rates at every scan point by the bunch intensity product $N_1 N_2$, but instead we use one average intensity product for each of the two scans. This is done to avoid the noise associated with the $N_{1,2}$ measurement. The used average bunch intensities are given in Table 6.2. The same procedure is applied for the April scans, where the decay time of the bunch intensity product was about 950 hours.

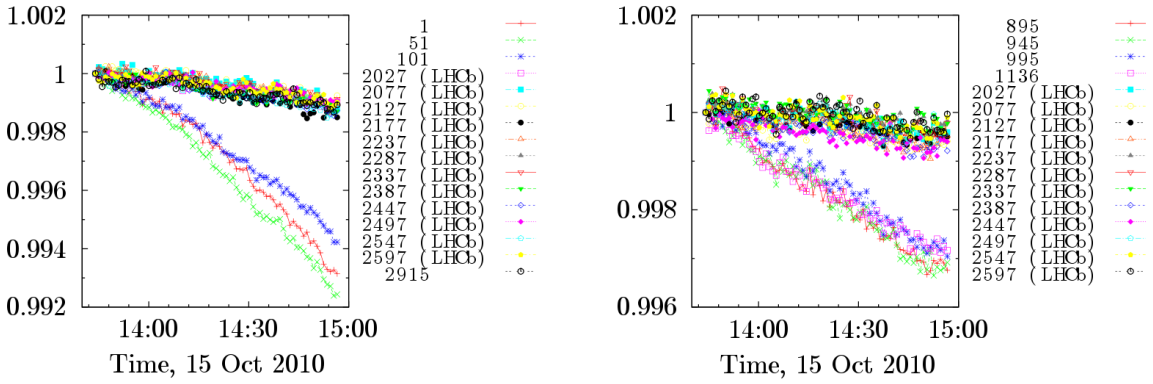

Figure 6.2: Relative evolution of the individual bunch charges measured with the FBCT (channel A) during the two LHCb scans in October. The left (right) panel corresponds to the first (second) beam. The bunches with shorter decay time collided in ATLAS/CMS or in ALICE.

In addition to the beam intensity drop, the luminosity stability can be limited

Table 6.2: Average bunch intensities (in 10^{10} particles) in the two October scans. The first 12 rows are the FBCT measurements in bunch-crossings (BX) with collisions at LHCb, while the last two lines give the FBCT and DCCT measurements of the total beam intensities (*i.e.* the sum over all 16 bunches of each beam). The uncertainties of the beam current measurement are discussed in Section 6.6.

	Scan 1		Scan 2	
BX	N_1	N_2	N_1	N_2
2027	8.425	7.954	8.421	7.951
2077	7.949	7.959	7.944	7.957
2127	7.457	7.563	7.452	7.561
2177	6.589	7.024	6.584	7.021
2237	7.315	8.257	7.311	8.255
2287	7.451	7.280	7.446	7.278
2337	7.016	7.219	7.012	7.217
2387	7.803	6.808	7.798	6.805
2447	7.585	7.744	7.580	7.742
2497	7.878	7.747	7.874	7.745
2547	6.960	6.244	6.955	6.243
2597	7.476	7.411	7.472	7.409
All, FBCT	120.32	119.07	120.18	118.99
DCCT	120.26	119.08	120.10	118.98

by variations of the bunch profiles, caused for example by emittance growth✦. The stability of the transverse beam sizes is evaluated by measuring the average number of visible interactions per crossing each time the beams are brought to their nominal positions, as shown in Fig. 6.3.

The luminosity decay time is measured to be 46 hours (30 hours in April). This corresponds to 0.7% luminosity drop during the first (longer) scan along either Δ_x or Δ_y (0.9% in April). As already mentioned, for the cross-section determination with the VDM method one needs to measure the integral of the average number of interactions per crossing, $\mu_{\rm vis}$, over the Δ_x and Δ_y displacements (see Eq. (6.2)). In each of the LHCb scans the initial scan points were at large beam separation and therefore at low interaction rate. After several steps have been made the two beams face each other and maximum interaction rate is observed. The scan continues until the rate drops to zero again. Effectively, the drop in the luminosity during the time of a scan in one direction enhances the left side of the *VDM-profile*§ and reduces its right side. Let $\int g_0\,\mathrm{d}t$ be the time integral of the VDM-profile for the case of constant luminosity. The integration

✦ The beam emittance was defined in Section 2.2.1.

§ Here, the term *VDM-profile* is used to signify the trend curve of the luminosity or the average number of interactions per crossing, $\mu_{\rm vis}$, obtained during the beam separation scan in one coordinate. For an example of VDM-profiles see Fig. 6.4.

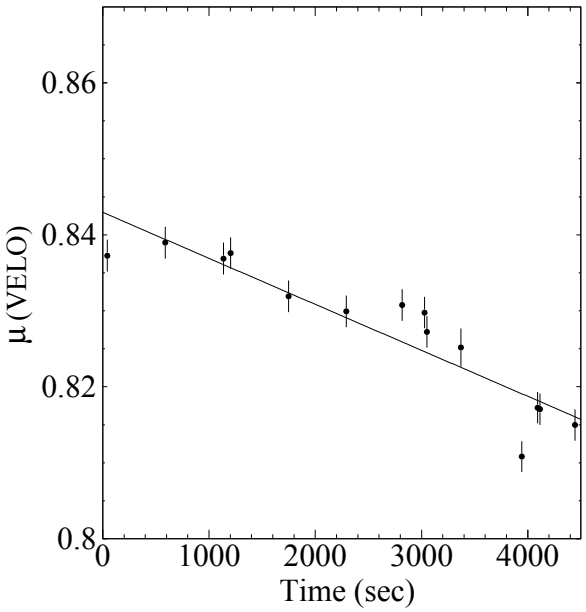

Figure 6.3: Evolution of the number of visible interactions per crossing at the nominal beam positions during the two October scans. A visible interaction is defined as an event producing at least two r-z VELO tracks. The values on the vertical axis correspond to the average over all 12 colliding bunch-pairs. In the first (second) scan the nominal point parameters were measured three (four) times both during the Δ_x scan and the Δ_y scan. The line indicates a first-order polynomial fit to the data points. The luminosity decay time is 46 hours.

is done over the time of the scan, which is of the order of 20 min. In case of Gaussian beam profiles g_0 is Gaussian as well. For the case of exponentially falling luminosity the time integral of the VDM-profile has the form:

$$\int g_0 \left(1 - \frac{t}{\tau} + \frac{1}{2}\left(\frac{t}{\tau}\right)^2 + O\left(\frac{t}{\tau}\right)^3\right) \mathrm{d}t \tag{6.3}$$

where we have written the first three terms in the Taylor expansion of the exponent. The luminosity decay time in the October VDM scan was $\tau \approx 40$ h. Considering only the first term, we would get a VDM-profile integral equal to the one obtained in the constant-luminosity case ($\tau \to \infty$). The second term does not contribute, because g_0 is symmetric. The integral of the third term, normalised to $\int g_0 \, \mathrm{d}t$ gives $\frac{\sigma^2}{2} \times \frac{1}{\tau^2} \approx 3.4 \times 10^{-7}$, where we have used $\sigma = 2$ min[❖] for the Gaussian width of g_0. Therefore, the distortion of the VDM-profile due to a slowly decaying luminosity can be neglected. The other term in Eq. (6.2), that is affected by the luminosity decrease during the scan, namely the term proportional to the interaction rate at the nominal beam position, μ_{vis} (Δ_{x_0},Δ_{y_0}) is measured in the beginning, in the middle and at the end of every scan. By taking their average, the effect of the slowly decreasing luminosity

❖ The temporal width of the VDM-profile Gaussian g_0 is estimated using spatial width of 80 μm and the time and the size of a single step in the scan: 25.6 s and 17.8 μm, respectively. For comparison, a full scan in Δ_x or Δ_y sweeps the range ± 355.9 μm and takes about 20 min.

is reduced. Therefore, the systematic error due to the luminosity drop is much less than 0.7% and is neglected in this analysis. The reproducibility of the luminosity, when the beams are in their nominal positions, is discussed further in Section 6.5.3.

The stability of the bunch profiles has been checked also by monitoring the size of the luminous region. A comparison of the transverse widths of the luminous region when the two beams are at their nominal position during the two Δ_x and Δ_y scans shows no variation within the statistical uncertainty (0.5%). This fact also indicates that the emittance growth is negligible. In addition, in the following it will be demonstrated that the widths of the VDM-profiles are stable as well.

6.3 Cross-section determination

As was mentioned in the beginning of this chapter, the VDM method allows an effective cross-section, σ_{vis}, to be measured with the use of Eq. (6.2). The half crossing angle between the beams was 270 and 170 μrad in the April and October scans, respectively. The correction due to this angle is proportional to $1/\cos\alpha$ and plays an insignificant role (the correction is of the order of 10^{-8}). An arbitrary process can be used to measure the average number of interactions per crossing μ_{vis} during the VDM scan and to determine the corresponding σ_{vis}. Once σ_{vis} is measured in a VDM scan, the associated μ_{vis} is used in physics fills to determine the accumulated absolute luminosity ($L = \frac{f\,\mu_{\text{vis}}}{\sigma_{\text{vis}}}$). Therefore, it is important to choose an interaction process, which allows μ_{vis} to be measured precisely for various beam conditions (*e.g* in 2010 the average number of inelastic pp interactions per crossing at IP8 varied roughly between 0.1 and 2, while the time between two consecutive bb crossings varied between more than 1000 and 150 ns). As discussed in Chapter 4, as a main relative luminosity monitor we chose the process which produces at least two r-z VELO tracks.

The twelve colliding bunch pairs of the VDM scan in October are analyzed individually. The dependence of μ_{vis}, summed over all bunches, as function of the separation Δ_x and Δ_y is shown in Fig. 6.4. The two scans in each direction are overlaid. The second scan is taken at the same points, but a twice as large step size has been used. One can see that the overlap of the VDM-profiles obtained in the two Δ_y scans is not perfect – there is a shift between the two curves of 7 μm on the left side and 4 μm on the right side. The reason for this apparent non-reproducibility is not understood. It may be attributed to hysteresis effects, enhanced in the second scan. Similar curves for the April scans are shown in Fig. 6.5, where a shift is present between the two Δ_x VDM-profiles.

The mean and the RMS width of the VDM-profiles shown in Fig. 6.4 are listed in Table 6.3. There is no evidence for an emittance growth as the widths of the two VDM-profiles are the same within the statistical errors. Single-Gaussian fits to the VDM-profiles of the individual bunches yield a χ^2 per degree of freedom between 2.7 and 4.3, while double-Gaussian fits provide a much better description of the data and

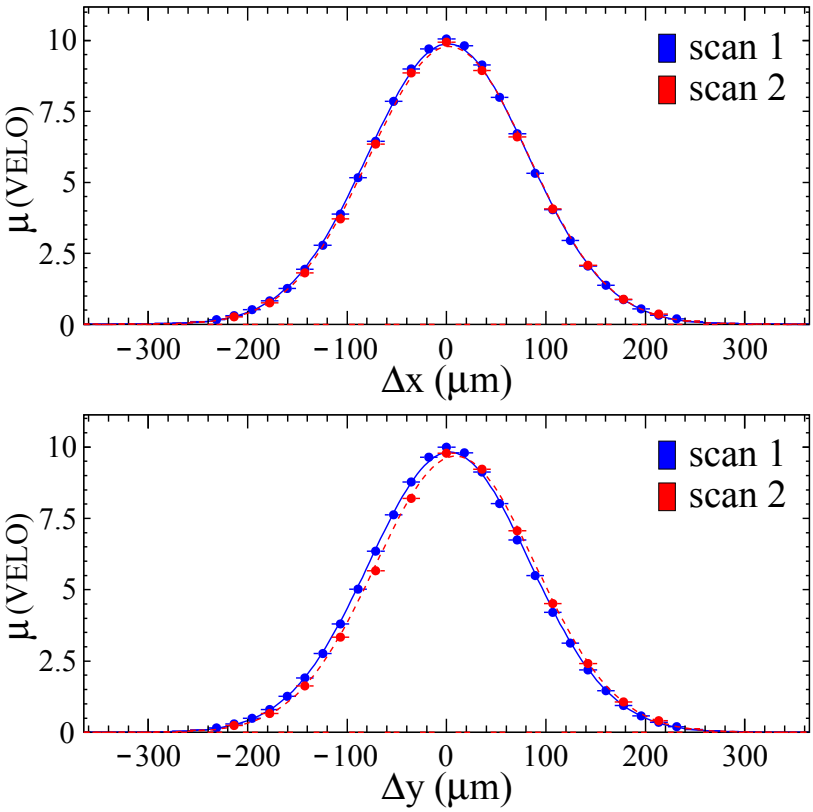

Figure 6.4: The average number of interactions per bunch-crossing, μ_{VELO}, summed over the twelve colliding bunches, versus the separations Δ_x (top) and Δ_y (bottom) in the October VDM scans. The first (second) scan is represented by the blue/dark (red/shaded) points and the solid (dashed) lines. The spreads of the centers and the widths obtained for each colliding pair are small compared to the widths of the VDM-profiles, so the shown sum gives a good illustration of the shape.

Table 6.3: October VDM scans (I and II): mean and RMS width of the VDM-profiles showing the average number of interactions per crossing, μ_{VELO}, summed over all twelve colliding bunches, as a function of the beam separations Δ_x and Δ_y. The statistical errors are 0.05 μm in the mean position and 0.04 μm in the RMS.

	Scan	**Δ_x scan**	**Δ_y scan**
Mean (μm)	I	1.3	3.1
	II	2.8	9.2
RMS (μm)	I	80.6	80.8
	II	80.5	80.7

are therefore used in the analysis. The single-Gaussian fits yield cross-sections typically 1.5 to 2% higher than the ones obtained with a double-Gaussian. It is found that the fit errors can be reduced by approximately a factor two if the fits of the Δ_x and Δ_y curves are performed simultaneously and the value measured at the nominal point

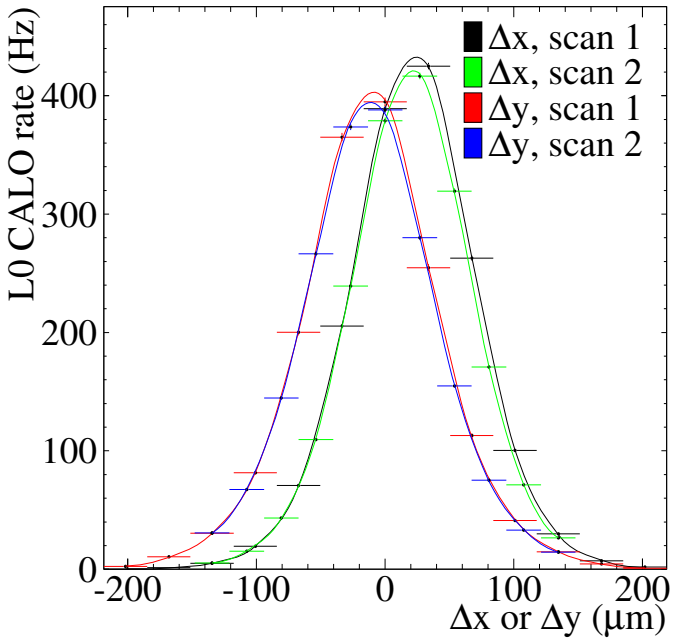

Figure 6.5: The L0 CALO trigger rate, corrected for the probability of multiple interactions, showing the dependence of the luminosity on the beam separations during the April VDM scans. The four curves, corresponding to the two scans in Δ_x and the two scans in Δ_y, are overlaid. The VDM-profiles obtained in the Δ_y scan have lower height because the two beams were not precisely centered in x.

$\mu_{\rm vis}(\Delta_{x_0},\Delta_{y_0})$ is constrained to be the same in both scans. The first fit parameter is chosen to be $\int \mu_{\rm vis} {\rm d}\Delta_x \int \mu_{\rm vis} {\rm d}\Delta_y / \mu_{\rm vis}(\Delta_{x_0}, \Delta_{y_0})$, the term appearing in Eq. (6.2), so that the correlation of both integrals and the value at the nominal point is correctly taken into account in the resulting fit error. The other fit parameters are ($i = x, y$): the integral of the VDM-profile along Δ_i, the widths of the two double-Gaussian components, σ_{1i} and $\sigma_{2i} = \sqrt{\sigma_{1i}^2 + \Delta\sigma_i^2}$ and a common mean for the two double-Gaussian components. In total there are nine fit parameters. The used parametrisation for σ_{2i} ensures that $\sigma_{2i} > \sigma_{1i}$. The relative normalisation of the two double-Gaussian components and the value at the nominal point, $\mu_{\rm vis}(\Delta_{x_0},\Delta_{y_0})$, are obtained from the fit. The χ^2 per degree of freedom is between 0.7 and 1.8 for all bunches.

In both October scans the product of the average bunch intensities $N_1 N_2$ of the twelve colliding bunches (see Table 6.2) have an RMS spread of 12%. As discussed later, the analysis of the individual bunch pairs yields cross-sections consistent within the statistical errors (the typical statistical error in the first scan is 0.3%). The sensitivity of the method is high enough that it is possible to calibrate the *relative* bunch populations $N^i_{1,2} / \sum_{j=1}^{16} N^j_{1,2}$ measured with the FBCT system by assuming that the latter has a linear response. Here i runs over the twelve bunches colliding in LHCb and j over all 16 bunches of each beam. By comparing the relative bunch intensities from the FBCT with the independent measurement of the same quantities provided by the

ATLAS BPTX [107], it is observed that both may have a non-zero offset [75, 106]. Therefore, the twelve cross-section measurements are fitted with three parameters: the common cross-section $\sigma_{\rm vis}$ and the FBCT offsets for the two beams $N^0_{1,2}$. The twelve measurements $\sigma^{\rm meas}_{{\rm vis},i}$ $(i = 1, ..., 12)$ are fitted to the function

$$\sigma^{\rm fit}_{{\rm vis},i} = \sigma_{\rm vis} \prod_{b=1,2} \left[\frac{(N^i_b - N^0_b)}{N^i_b} \frac{\sum^{16}_{j=1} N^j_b}{\sum^{16}_{j=1}(N^j_b - N^0_b)} \right] , \tag{6.4}$$

which uses the relative populations N^i_b corrected for the FBCT offset N^0_b and takes into account that the total beam intensities measured with the DCCT constrain the sums of all bunch intensities obtained from the FBCT values. The results of this fit are shown in Fig. 6.6, where the data points are drawn without offset correction and the horizontal bars represent the fit function of Eq. (6.4). The use of FBCT offsets improves the description of the points compared to the straight-line fit which does not use a correction for the FBCT offsets. The χ^2 per degree of freedom and other relevant results of the two fits (with and without the FBCT offsets) are summarised in Table 6.4. This table shows also the results when the ATLAS BPTX system [107] is used instead of the FBCT system.

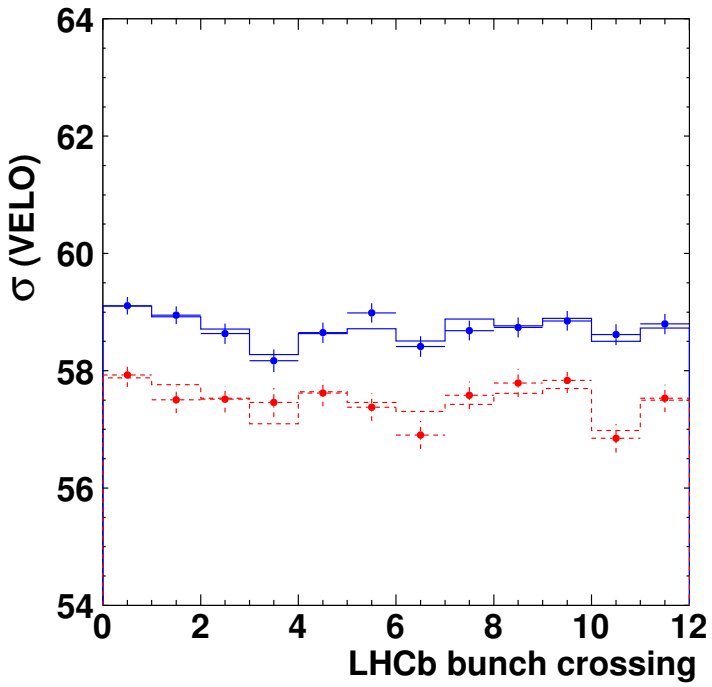

Figure 6.6: The measured ($\sigma^{\rm meas}_{{\rm vis},i}$, circles with error bars) and fitted ($\sigma^{\rm fit}_{{\rm vis},i}$, lines) cross-sections obtained for each of the twelve colliding bunch-pairs ($i = 1, ..., 12$) in the October VDM fill. The upper (lower) set of circles and lines is obtained in the first (second) scan, respectively. The difference between the results of the two scans is due to a unknown systematic, most probably related to the different beam displacement procedures of the two scans.

The uncertainties of the FBCT and BPTX offsets obtained in the first scan are $(0.10 - 0.12) \times 10^{10}$, or 1.5% relative to the average bunch intensity

Table 6.4: Results for the effective cross-section $\sigma_{\rm vis}$ obtained with fits to the twelve bunches colliding in LHCb, using data collected in the October VDM scans, together with the results of the April scans. At the top are the results of the fit to the cross-sections $\sigma^{\rm meas}_{{\rm vis},i}$ obtained for each colliding bunch-pair ($i = 1, ..., 12$) in October. Below them are the results of the fit to the offset-corrected cross-sections $\sigma^{\rm fit}_{{\rm vis},i}$ obtained for each colliding bunch-pair. The October results use the relative bunch-intensity measurements of either the FBCT (center) or the ATLAS BPTX (right) systems. $N^0_{1,2}$ are the FBCT or BPTX offsets in units of 10^{10} charges, obtained from the fit to $\sigma^{\rm fit}_{{\rm vis},i}$. The cross-section obtained in October with the FBCT measurements with offsets determined by the fit is used as a final VDM luminosity calibration. The results of the two October scans are not combined because of the large (2.1%) difference between them. The first scan is preferred to the second scan because in the first scan twice more scan steps were made. The 2.1% discrepancy between the two scans is included as a systematic uncertainty of the measured $\sigma_{\rm vis}$. The results of the April scans using the single bunch-pair colliding at LHCb are reported on the last row.

October scans

	FBCT		**ATLAS BPTX**	
	Scan1	**Scan2**	**Scan1**	**Scan2**
	no offsets		*no offsets*	
$\sigma_{\rm vis}$ (mb)	58.73 ± 0.05	57.50 ± 0.07	58.63 ± 0.05	57.46 ± 0.07
χ^2/ndof	23.5 / 11	21.9 / 11	66.5 / 11	23.5 / 11
	with offsets		*with offsets*	
$\sigma_{\rm vis}$ (mb)	**58.73 ± 0.05**	57.50 ± 0.07	58.62 ± 0.05	57.45 ± 0.07
N^0_1	0.40 ± 0.10	0.29 ± 0.15	−0.10 ± 0.12	−0.23 ± 0.17
N^0_2	−0.02 ± 0.10	0.23 ± 0.13	−0.63 ± 0.12	−0.34 ± 0.15
χ^2/ndof	5.8 / 9	7.6 / 9	6.9 / 9	7.3 / 9

April scans

	Scan1	**Scan2**
$\sigma_{\rm vis}$ (mb)	59.6 ± 0.5	57.0 ± 0.5

$\langle N_{1,2} \rangle = 7.5 \times 10^{10}$. The sensitivity of the method is therefore very high, in spite of the fact that the RMS spread of the intensity products $N_1\ N_2$ is only 12%. In future scans it may be advantageous to use bunches with intensities as different as possible to increase the sensitivity to the offsets and also to probe other effects like beam-beam interaction which may be visible only at high intensities.

The offset and cross-section errors given in Table 6.4 are only statistical. Since the fit to $\sigma^{\rm fit}_{{\rm vis},i}$ yield good χ^2 values, the systematics related to the properties of the individual colliding bunches (*e.g.* bunch intensity and emittance) are expected to be at a lower or at a comparable level. The largest relative difference between the central values of $\sigma_{\rm vis}$ obtained with FBCT and BPTX is 0.2%. This value is used as an estimate for the systematics corresponding to the determination of the relative bunch intensity product. The relative cross-section error is 0.09%. The magnitude of this error coincides with the expectation from combining 12 independent measurements

with uncertainties of 0.3% (the latter is the typical statistical uncertainty of the cross-sections determined from each bunch-pair). All principal sources of systematic errors which will be discussed below (DCCT scale uncertainty, hysteresis, and ghost charges) cancel when comparing bunches within a single scan.

In spite of the good agreement between the bunches within the same scan, there is an overall 2.1% discrepancy between the two scans. The reason is not understood, and may be attributed to a potential hysteresis effect or similar effects resulting in uncontrollable shifts of the beam as a whole. As described in Section 6.6, we use the results of the first scan with the FBCT offsets determined by the fit as the final VDM luminosity determination. The 2.1% uncertainty, estimated from the discrepancy with the second scan is the second largest systematic error in the cross-section measurement after the uncertainties in the beam intensities. If the DCCT accuracy will improve in the future, the discrepancy error may become a dominating uncertainty.

In the April data the situation is similar: the discrepancy between the cross-sections obtained from the two scans is $(4.4 \pm 1.2)\%$, the results are given in Table 6.5. Since the April measurement is performed using corrected trigger rates proportional to the luminosity, instead of r-z VELO tracks, the results have to be corrected for the difference in acceptances. The correction factor is determined by applying the two conditions to random triggers and is $\sigma_{\mathrm{VELO}}/\sigma_{\text{April trigger}} = 1.066$. For the April data the Δ_x and Δ_y curves are fitted separately. To obtain the average number of interactions per bunch crossing from the trigger rates we use the well-known LHC revolution frequency, 11.245 kHz.

Table 6.5: Cross-section results from the April VDM scans. R is the L0 `CALO` trigger rate, corrected for the small probability of multiple interactions and is, thus, proportional to the luminosity. σ_{VELO} is the cross-section of the interaction with at least two r-z VELO tracks.

	Scan 1	**Scan 2**
$\int R\, d\Delta_x$ (cm Hz)	5.107 ± 0.017	4.875 ± 0.016
$\int R\, d\Delta_y$ (cm Hz)	5.094 ± 0.025	4.994 ± 0.016
$R(\Delta_{x_0}, \Delta_{y_0})$ (Hz)	392	383
$N_1 N_2$ (10^{20})	1.056	1.056
σ_{VELO} (mb)	**59.6**	**57.0**

6.4 Length scale calibration

The beam separation values Δ_x and Δ_y are calculated from the LHC magnet currents at every scan step. There is a small non-reproducibility in the results of two scans, as can be seen in Figs. 6.4 and 6.5. The non-reproducibility may be the result of wrong positioning of the two beams. Therefore, it is important to check the Δ_x and Δ_y values as predicted by the magnet currents, and in particular their scales which enter linearly in the cross-section (Eq. (6.2)).

Two different length-scale calibration methods were used at LHCb. The first method was applied on the data collected during the two VDM scans in April. The LHCb measurements of the position of the luminous region during the two scans in Δ_x and Δ_y were used to cross-check LHC length-scale [108]. These measurements showed that the LHCb and the LHC length-scales are identical within 2%.

In October, another length scale calibration method was used. This method was preferred to the one used in April, because it constitutes a relatively quick procedure (the time needed is similar to the time for a single VDM scan in one coordinate), which allows a direct comparison of the LHC and the LHCb length-scales to be made. For the application of this length-scale calibration method the two beams were moved in five equidistant steps in Δ_x and Δ_y, keeping the nominal separation between the beams constant. The movement of the centre of the luminous region is shown in Fig. 6.7. The shaded regions distinguish periods with fixed beam positions which were used in the following analysis. During the scan along x the beam separation was $(\Delta_x, \Delta_y) = (-80\ \mu\text{m}, 0)$, which corresponds approximately to the width of the Δ_x VDM-profile, Σ_x [10]:

$$\Sigma_x = \sqrt{\sigma_{1x}^2 + \sigma_{2x}^2 + 4(\sigma_{\otimes z})^2 \tan^2 \alpha}\ , \tag{6.5}$$

where $\sigma_{\otimes z}$ is the width of the luminous region in the z coordinate and σ_{ix} is the width of beam i ($i = 1, 2$). A similar equation can be written for Σ_y. This separation was chosen in order to maximise the derivative $dL/d\Delta_x$, *i.e.* the sensitivity of the luminosity to a possible difference in the length scales for the two beams. If during the length calibration scan one of the beams makes a larger step than the other beam, the separation Δ_x, and therefore the luminosity, will change. Similarly, the beam separation used in the Δ_y scan was $(\Delta_x, \Delta_y) = (0, 80\ \mu\text{m})$.

The behaviour of the measured luminosity during the length scale calibration scans is shown in Fig. 6.8. As one can see, the points show a significant deviation from a constant. This effect may be attributed to different length scales of the two beams. More specifically, we assumed that the real positions of the beams $x_{1,2}$ could be obtained from the values $x_{1,2}^0$ obtained from the LHC magnet currents by applying a correction with size parameter ϵ_x:

$$x_{1,2} = (1 \pm \epsilon_x/2)\, x_{1,2}^0\ , \tag{6.6}$$

and similarly for $y_{1,2}$. If we assume that the Δ_x VDM-profile is Gaussian and has width Σ_x, we get:

$$\frac{1}{L}\frac{dL}{d(x_1 + x_2)/2} = -\epsilon_x \frac{\Delta_x}{\Sigma_x^2} \tag{6.7}$$

Here, $\Delta_x = 80\ \mu$m is the fixed nominal beam separation. (A similar equation holds for the y coordinate.) From the slopes observed in Fig. 6.8 we obtain $\epsilon_x = 2.4\%$ and $\epsilon_y = -1.9\%$. The luminosity changes coherently in the different bunches, as can be seen in Fig. 6.9.

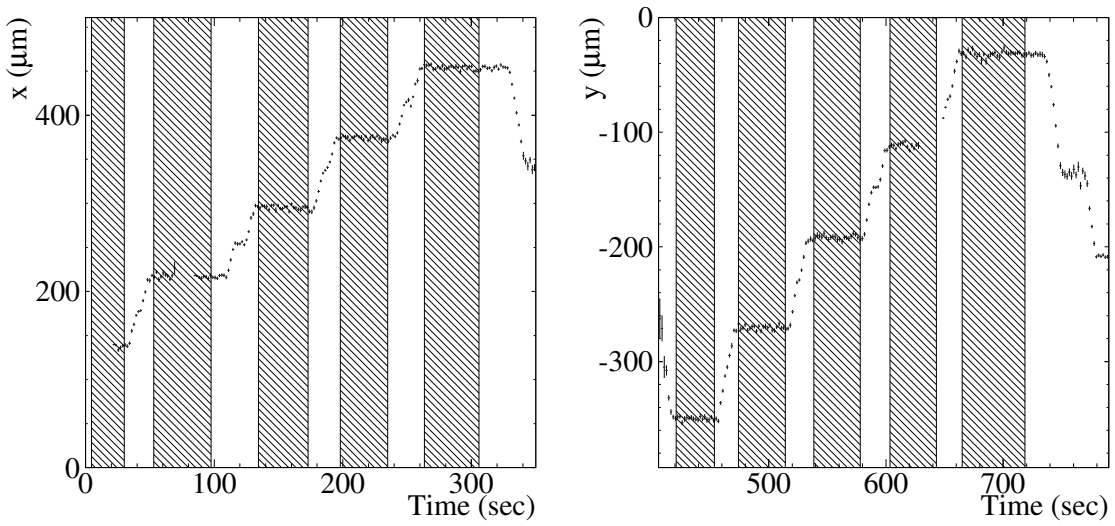

Figure 6.7: Evolution of the centre of the luminous region in x (left) and in y (right) during the length scale calibration scans in October. The shaded areas indicate the periods used in the analysis. During the first (second) scan the beams were moved in five equidistant steps of 80 μm along x (y) with a constant separation $\Delta_x = -80\,\mu$m, $\Delta_y = 0$ $(0,\, 80\,\mu\text{m})$.

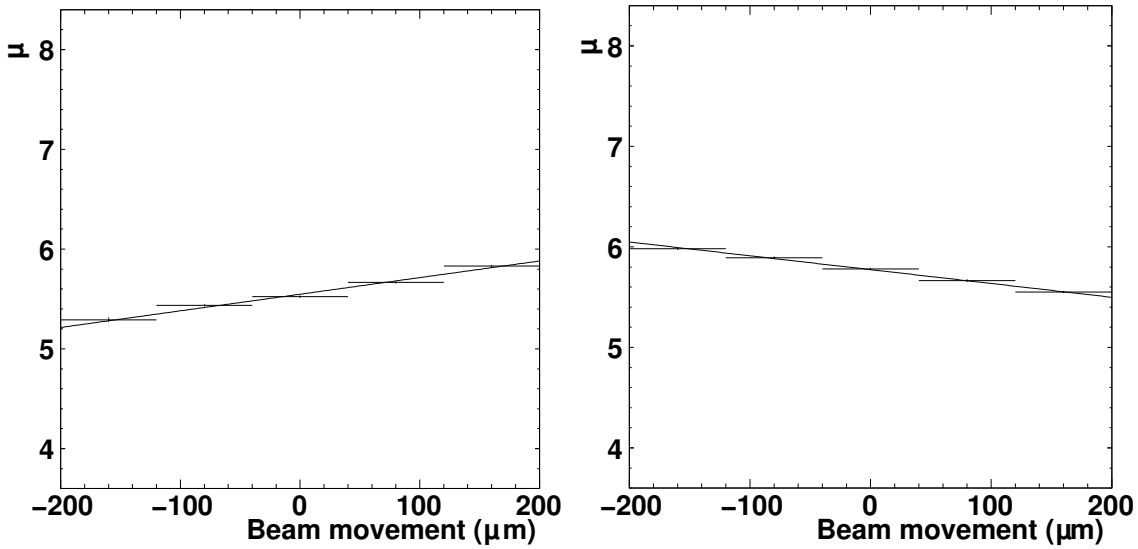

Figure 6.8: Average number of interactions per crossing, μ_{VELO}, summed over the twelve colliding bunches, versus the centre of the luminous region. The curves indicate straight-line fits. The left (right) panel corresponds to the x (y) length scale calibration scans performed in October.

Since $\Delta_x = (x_1^0 - x_2^0) + \epsilon\,(x_1^0 + x_2^0)/2$, the Δ_x correction depends on the nominal mid-point between the beams $(x_1^0 + x_2^0)/2$. In the first scan this nominal point was kept at zero. Therefore, no correction is needed. During the second scan the mid-point between the beams moved with nominal positions $0 \to 355.9$ μm $\to 0$. Therefore, a correction to the Δ_x values in Fig. 6.4 is required. The central point should be shifted to the right (left) for the x (y) scan. The left (right) side is thus stretched and the

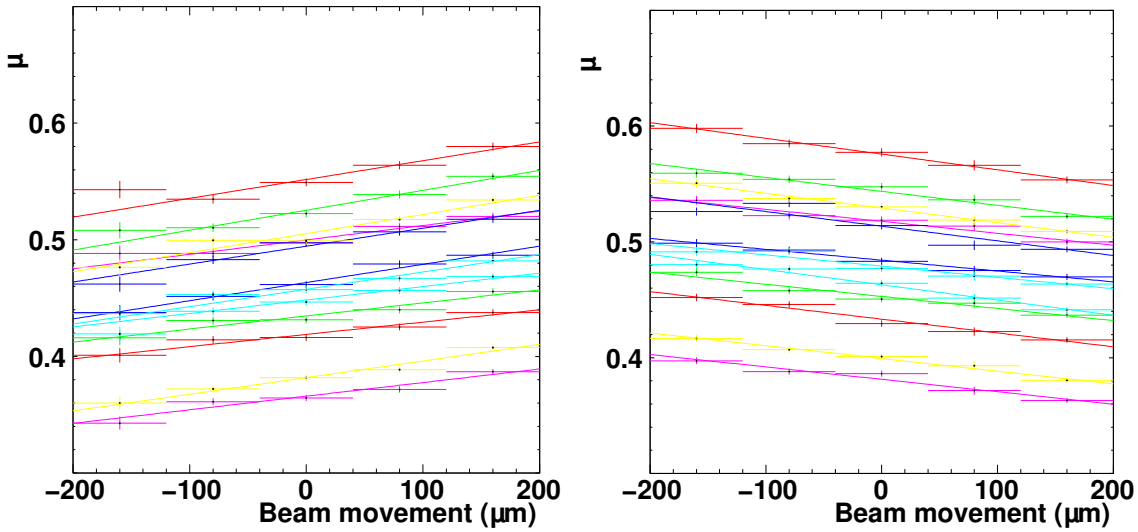

Figure 6.9: Average number of interactions per crossing, μ_{VELO}, versus the centre of the luminous region for each individual pair of bunches. The curves indicate straight-line fits. The left (right) panel corresponds to the x (y) length scale calibration scans performed in October.

opposite side is shrunk. The corrected curves are shown in Fig. 6.10. One can see, that the shift between the scans is reduced in y, but appears now in x, so that the discrepancy cannot be fully explained by a linear correction alone.

The correction which stretches or shrinks the VDM-profile measured in the second scan influences their integrals and the resulting cross-sections very little. The latter changes on average by only 0.1%, which we take as an uncertainty and which we include into the systematic error. The results in Table 6.4 are given with the correction applied.

During a simultaneous parallel translation of both beams, the centre of the luminous region should follow the beam positions regardless of the bunch shapes. Since the centre of the luminous region is approximately at $(x_1 + x_2)/2 = (x_1^0 + x_2^0)/2$ and similarly for y, the corrections due to $\epsilon_{x,y}$ are negligible. The luminous centre can be determined using vertices measured with the VELO. This provides a precise cross-check of the common beam scales $(x_1^0 + x_2^0)/2$ and $(y_1^0 + y_2^0)/2$. The result is shown in Fig. 6.11. The LHC and VELO length scales agree within $-0.97 \pm 0.17\%$ and $-0.33 \pm 0.15\%$ in x and y, respectively. The transverse position measurement of the length scale with the VELO is expected to be very precise owing to the fact that it is determined by the strip positions of the silicon sensors with a well-known geometry. For the cross-section determination we took the more precise VELO length scale and multiplied the values from Table 6.4 by $(1 - 0.0097)\,(1 - 0.0033) = 0.9870$. In addition, we conservatively assign a 1% systematic error to the common scale uncertainty.

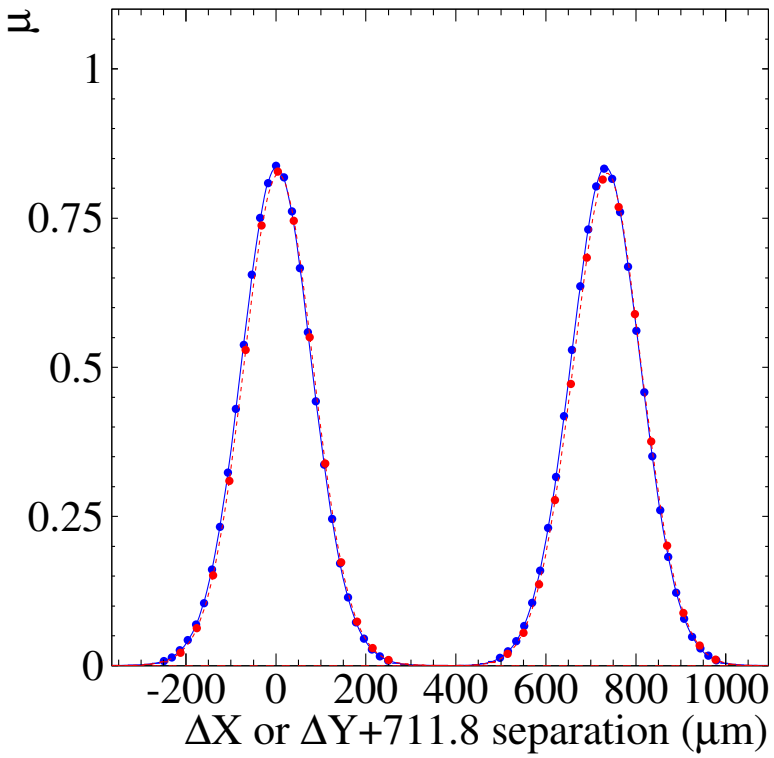

Figure 6.10: The same as Fig. 6.4, but with the $\epsilon_{x,y}$ correction, as discussed in the text. The Δ_x and Δ_y curves are displayed one beside the other for illustration purposes.

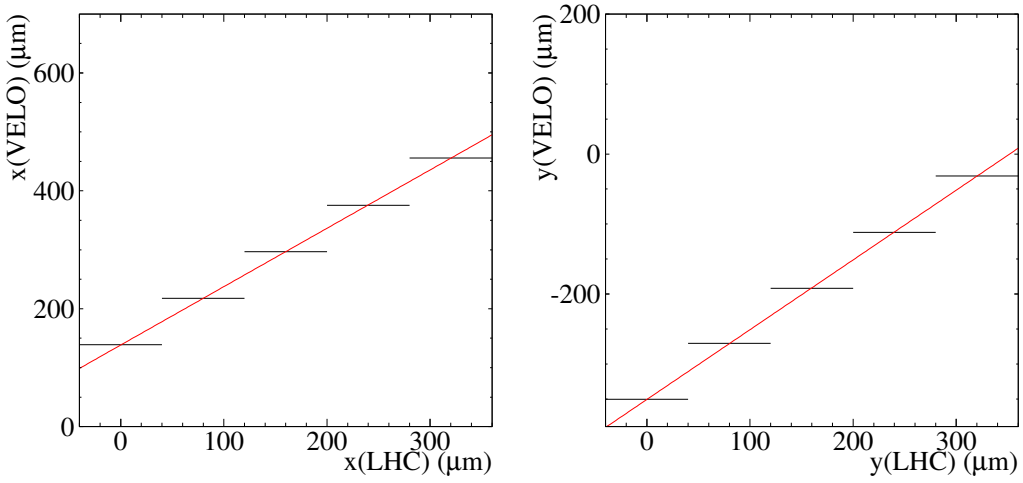

Figure 6.11: Centre of the luminous region determined from vertices reconstructed with VELO tracks, versus the position predicted by the LHC magnet currents. The horizontal bars represent the bin widths. The points are fitted to a linear function. The slope calibrates the common beam scale.

6.5 Systematic errors

6.5.1 Coupling between the x and y coordinates in the LHC beams

The LHC ring is tilted with respect to the horizontal plane, while the VELO detector is aligned with respect to a coordinate system where the x axis is in a horizontal plane [109]. The van der Meer equation (Eq. (6.2)) is valid only if the particle distributions in x and in y are independent. To check this condition the movement of the centre of the luminous region along y is measured during the length scale scan in x and vice versa, as shown in Fig. 6.12. The slope is within errors compatible with the expected tilt of the LHC ring of 13 mrad at LHCb [109] with respect to the vertical and the horizontal axes of the VELO. Due to this tilt the LHC and VELO length scales differ by $1 - \cos(13\text{ mrad}) = 0.84 \times 10^{-4}$ both in x and y. The corresponding correction to the cross-section is negligible.

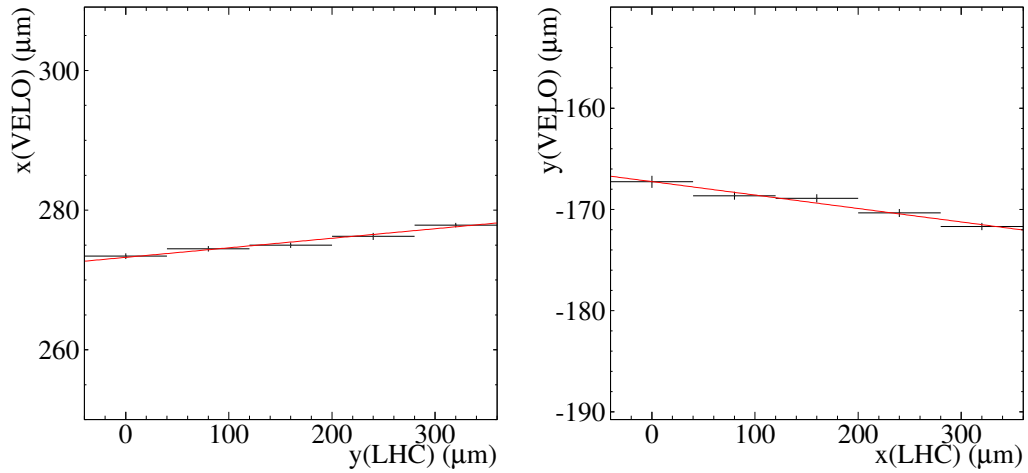

Figure 6.12: Position of the centre of the luminous region in x during the length scale scan in y (left) and vice versa (right). The points are fitted to a linear function. The slope is compatible with the expected 13 mrad tilt of the LHC ring at LHCb.

In addition, the correlation of the x and y dependence of the vertex distribution is checked. To obtain enough statistics, data collected in a period with head-on colliding beams are used. These data were taken after the VDM scans at LHCb, during fill 1422. Figure 6.13a shows the RMS of the vertex distribution in y at different x intervals ("slices") and vice versa. The RMS luminous width has been estimated without unfolding the vertex resolution. The apparent horizontal (resp. vertical) luminous size exhibits a marked dependence on the vertical (resp. horizontal) coordinate; the relative variation is similar in the two planes, suggesting a possible x-y correlation. However, the corresponding distributions, using a sample of vertices reconstructed with > 40 tracks and, thus, with better resolution, are much more flat, see Fig. 6.13b. Clearly,

due to the fact that the vertex resolution in x and y is correlated with the number of tracks making up the vertex, the tails of the distribution of the measured x position of vertices in the luminous region contain more poorly measured vertices, which also leads to a larger RMS in y. It is therefore plausible that the large apparent correlation observed in Fig. 6.13a is caused by the simultaneous degradation of the vertex resolution in both planes, rather than by residual x-y coupling in the colliding bunches.

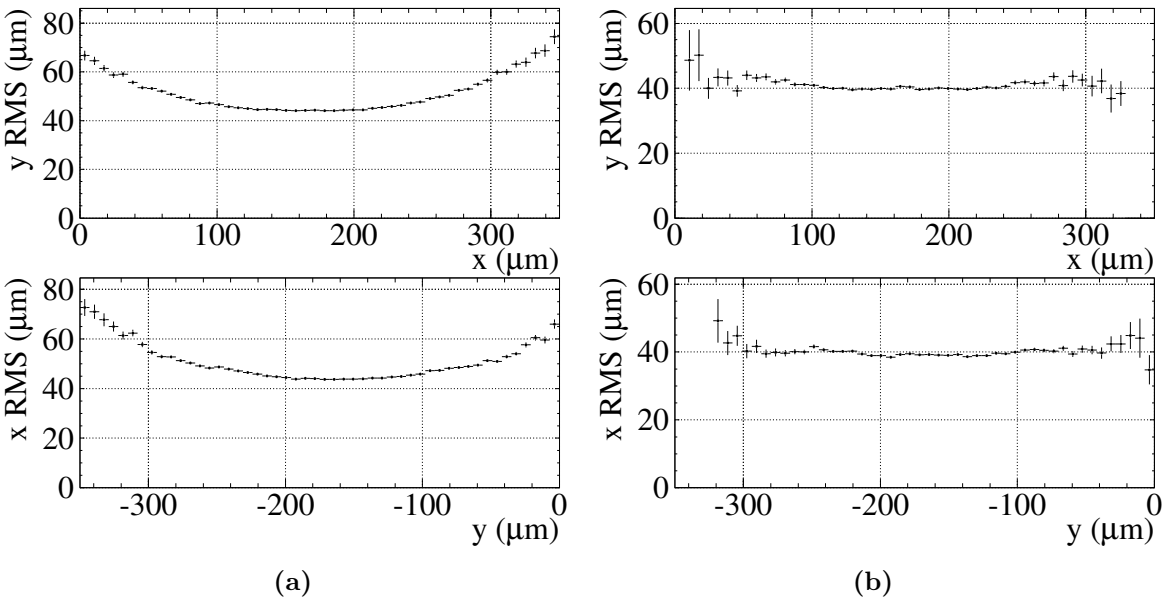

Figure 6.13: RMS width of the luminous region in the y coordinate for different x slices (top plots) and vice versa (bottom plots). The left (right) panels show the results obtained using all reconstructed vertices (only the vertices with more than 40 tracks). The data were collected with head-on beams during fill 1422.

It is better to measure the possible x-y correlation by examining the two-dimensional vertex map and by determining the centre position in one coordinate for different values of the other coordinate. Figure 6.14 shows the x-y profile of the luminous region. The centre positions of the y coordinate lie on a straight line with a slope of 79 mrad. As discussed in [10], a correction to this value needs to be made in order to take into account the fact that the LHC ring is tilted with respect to the horizontal plane (and therefore, with respect to the LHCb coordinate frame). According to [10], the cross-section correction due to the non-zero correlation between the x and y coordinates is 0.3%. This correction is not applied to the measured cross-section, but an uncertainty of 0.3% is added to the overall systematic error.

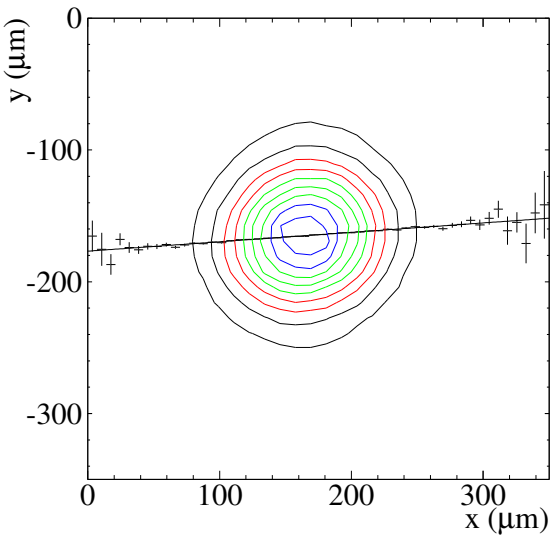

Figure 6.14: Contours of the distribution of the x-y coordinates of the luminous region. The points represent the y-coordinates of the centre of the luminous region in different x slices. The straight line fit to the points is shown as well.

6.5.2 Ghost charge and satellite bunches during the VDM scans

As discussed in Section 5.2, a small fraction of ("ghost") protons, contained in non-nominal bunch slots, has been observed in the fills used in the beam-gas analysis. The ghost charge contribution to the total LHC beam current should be subtracted from the DCCT value before the sum of the FBCT bunch intensities is constrained by the DCCT measurement of the total current. The ghost charge in the April and October VDM fills is estimated using the method described in Section 5.2. The results are summarised in Table 6.6. The cross-section correction due to the ghost charge is $\frac{0.12\pm0.06}{0.86\pm0.14} + \frac{0.00\pm0.03}{0.84\pm0.16} = 0.14 \pm 0.08\%$ in April and $\frac{0.20\pm0.02}{0.86\pm0.14} + \frac{0.36\pm0.03}{0.84\pm0.16} = 0.66 \pm 0.10\%$ in October. These estimates use the numbers from Table 6.6 and the trigger efficiency corrections due to timing, as given in Table 5.3.

Table 6.6: First two rows: total fraction of events outside nominally-filled BCIDs in October (fill 1422) and fractions localised in ±3 BCIDs around bb crossings. The same information for the April VDM fill (1059) are given in the bottom two rows.

	Beam1	**Beam2**
Fraction in Oct., %	0.20 ± 0.02	0.36 ± 0.03)
(in ±3 BX)	(0.12 ± 0.01)	(0.25 ± 0.02)
Fraction in Apr., %	0.12 ± 0.06	0.00 ± 0.03)
(in ±3 BX)	(0.12 ± 0.06)	(0.00 ± 0.03)

Satellite bunches may surround the nominally filled RF buckets (see Section 5.4). Due to the beam crossing angle in IP8, the nominal RF buckets and the RF buckets located a few ns from them are separated in x, and therefore, do not collide. However, when the beams are separated during the VDM scan in Δ_x, collisions between nominal and satellite bunches can occur, as illustrated in Fig. 6.15.

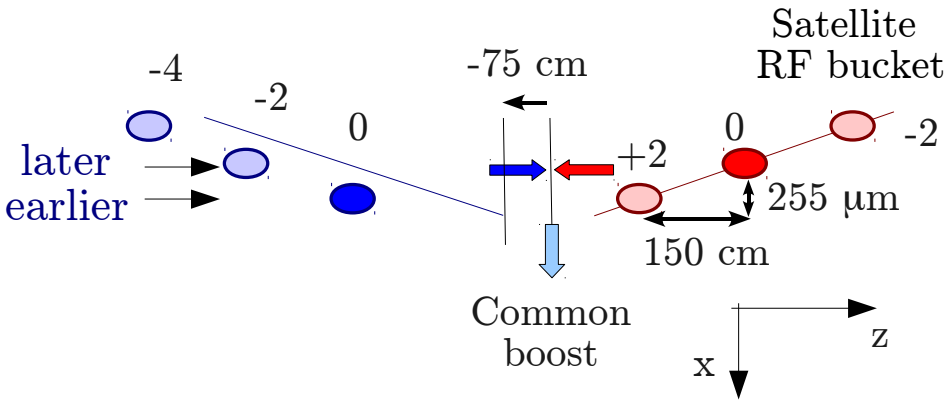

Figure 6.15: Collisions of protons from the nominal RF bucket in one beam and from the ±2 satellite RF buckets of the other beam during the van der Meer scan.

The z distribution of vertices accumulated with the minimum bias trigger in the October VDM fill is shown in Fig. 6.16. To estimate the satellite populations, the number of vertices at $z = 0$ and ±75 cm versus the separation in x is determined, see Fig. 6.17. Since the rate of the minimum bias events is modified by the rate limiter in the HLT, the vertex distributions are weighted with coefficients determined from a sample of random triggers. Assuming that the trigger and reconstruction efficiencies and distributions of particles in the nominal and the satellite ±2 RF buckets are similar, the fraction of the charge in the satellite RF buckets is determined to be 0.1%. This effect is not corrected for, but an additional systematic error of 0.1% is assigned to this uncertainty.

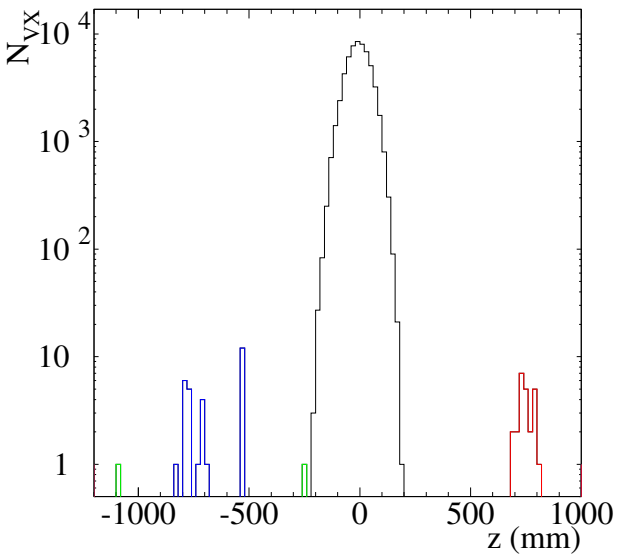

Figure 6.16: The z distribution of vertices in the minimum bias sample during the first Δ_x scan. Vertices at ±75 cm are due to interactions of protons in the nominal RF bucket with protons in the ±2 satellite RF buckets.

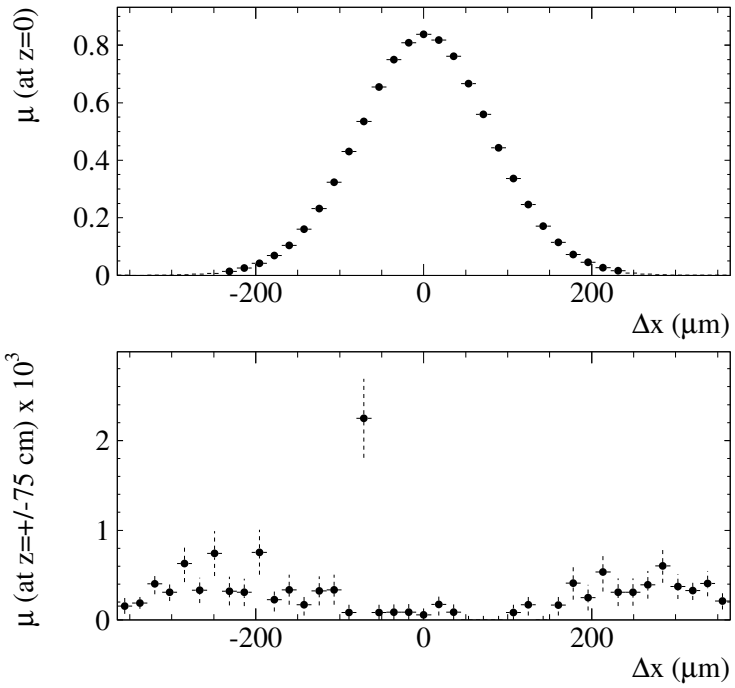

Figure 6.17: The average number of visible interactions per bunch crossing μ_{vis} at $z = 0$ (top) and at $z = \pm 75$ cm (bottom) versus the beam separation Δ_x corrected for the trigger-rate limiter of the minimum bias sample. It is assumed that the trigger and reconstruction efficiencies and the distributions of the particles in the nominal RF bucket and the satellite RF buckets are the same.

6.5.3 Reproducibility of the luminosity at the nominal beam positions

Figure 6.3 shows the evolution of the luminosity as a function of time for the periods where the beams were at their nominal positions during the VDM scan. One expects a behaviour which follows the loss of intensity and the emittance growth. Since these effects occur at large time-scales compared to the duration of the scan, the dependence on these known effects can be approximated by a linear evolution. As shown in Fig. 6.3, the luminosity did not always return to the expected value when the beams returned to their nominal positions. The χ^2/ndof with respect to the fitted straight line is too large (40/12), thus, the non-reproducibility cannot be attributed fully to statistical fluctuations alone and another systematic effect is present. The origin of this effect is not understood but it may be similar to the one which causes the non-reproducibility of the beam positions observed in the shift of the VDM-profile in the consecutive VDM scans (see Figs. 6.4 and 6.5). To take this observation into account a systematic error is estimated in the following way. The amount which should be added in quadrature to the statistical error of μ_{vis} (0.25%) to produce a χ^2/ndof equal to one is 0.4%. Since the absolute scale of the μ_{vis} measurement enters the cross-section linearly (see Eq. (6.2)), the systematic error of 0.4% is assigned to the cross-section measurement.

6.5.4 Cross-check with the z position of the luminous region

A cross-check of the width of the VDM-profile as a function of Δ_x is made by measuring the movement of the z position of the centre of the luminous region during the first VDM scan in the x coordinate in October (see Fig. 6.18). According to reference [110], if the widths of the two colliding beams are identical, the slope should be equal to:

$$\frac{\mathrm{d}z_{\otimes}}{\mathrm{d}\left(\Delta_x\right)} = -\frac{\sin 2\alpha}{4}\frac{\sigma_z^2 - \sigma_x^2}{\sigma_x^2\cos^2\alpha + \sigma_z^2\sin^2\alpha}\ , \tag{6.8}$$

where $\sigma_{x,z}$ are the beam widths in the corresponding directions and $\mathrm{d}z_{\otimes}$ is the induced shift in the z coordinate of the centre of the luminous region. We approximate σ_z as $\sqrt{2}\sigma_{\otimes z}$, where $\sigma_{\otimes z}$ is the width of the luminous region in the z coordinate.

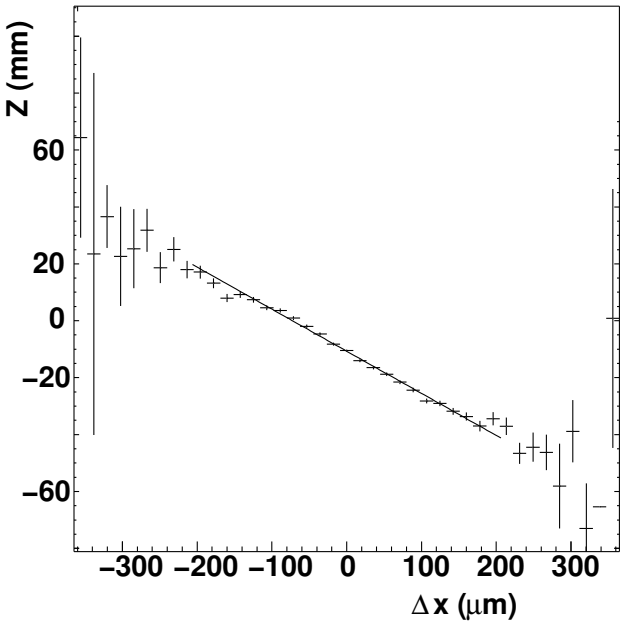

Figure 6.18: Movement of the centre of the luminous region in z during the first scan in Δ_x taken in October.

Using the slope observed in Fig. 6.18 one gets the expected width of the Δ_x VDM-profile, $\Sigma_x = \sqrt{2}\sigma_x = 78\ \mu$m, in agreement with the measured value of 80 μm.

6.5.5 Summary of the systematic errors

A summary of all systematic errors taken into account in the absolute luminosity calibration is given in Table 6.7 and Table 6.8 for the van der Meer scans in April and October, respectively.

6.6 Results of the van der Meer scans

The cross-section results obtained with the VDM scans are given in Table 6.9. We recall that the effective cross-section defined by interactions with at least two r-z VELO

Table 6.7: Summary of relative cross-section uncertainties for the van der Meer scan in April. The last column contains the correction to the cross-section measurements given in Table 6.5.

Source	uncertainty (%)	correction (%)
DCCT (baseline and scale) and FBCT	5.6	
Ghost charge	0.08	+0.14
Satellite bunches in ±2 RF	negligible	
N_1N_2 drop	negligible	
Emittance growth	negligible	
Length scale	2	
Difference between scans	4.4	
VELO track stability	0.5	
Total	7.5	

Table 6.8: Summary of relative cross-section uncertainties for the van der Meer scan in October. The last column contains corrections to the cross-section measurements given in Table 6.4 obtained with FBCT intensities with fitted offsets.

Source	uncertainty (%)	correction (%)
DCCT scale	2.7	
FBCT offset	0.2	
Ghost charge	0.15	+0.66
Satellite bunches in ±2 RF	0.1	
N_1N_2 drop	negligible	
Emittance growth	negligible	
Working point stability	0.4	
Length scale	1	-1.3
Beam scale difference	0.1	
x-y coupling	0.3	
Difference between scans	2.1	
VELO track stability	0.5	
Total	3.64	

tracks σ_{VELO} is used in the analysis. The results of the two measurement periods are consistent.

Table 6.9: Cross-section of the interaction producing at least two r-z VELO tracks, measured in the two van der Meer scans in April and in October.

	σ_{VELO} (mb)	relative uncertainty (%)		
		total	systematic	statistical
April	59.7	7.5	7.4	0.9
October	**58.35**	3.64	3.64	0.09

During the second scan in October the beam movements were not continuous, so the results might suffer from hysteresis effects. In the second scan in April only one beam moved which restricted the separation range. Therefore, only the results of the first scans in April and October are shown in Table 6.9. Both in the April and in the October measurements the difference observed in the results of the two scans is included as a systematic error. The complete list of systematic errors taken into account is given in Tables 6.7 and 6.8. These tables show also the corrections which are applied to the results given in Tables 6.5 and 6.4. The systematic uncertainties are uncorrelated and therefore added in quadrature. Since the first scan taken in October has much reduced systematic errors compared to the April scans, it is retained as the final result of the VDM method.

Chapter 7

The beam-gas imaging method

The development of precise micro-vertex detectors opened the possibility for the application of a novel method for determining the absolute luminosity. The recently proposed beam-gas imaging method (BGI) [6] relies on the vertex detection of beam-gas interactions to measure directly the geometrical properties and the overlap integral of the individual colliding bunches. The absolute luminosity can be determined by combining this information with a measurement of the bunch intensity (see Eq. (4.1)). Once calibrated by this method, a reference cross-section of an effective pp reaction is used for the systematic evaluation of the absolute luminosity (see Chapter 4). This chapter describes the application of the BGI method for the absolute luminosity normalisation at LHCb with data collected in May 2010.

The measurements presented in this chapter use the residual gas in the beam vacuum pipe as a visualising medium. At nominal conditions the expected rate of beam-gas interactions which can be reconstructed with the LHCb vertex detector is of the order of 0.1 Hz per bunch (see Section 1.2.2) and therefore several hours of data-taking are necessary for achieving satisfactory statistical precision of the measured bunch profiles (see Section 7.4.1). Corrections need to be made in order take into account the effects of potential beam instabilities. An important prerequisite for the application of the BGI method is the knowledge of the transverse density profile of the visualising gas, as it has direct influence on the measured beam profiles.

By introducing a controlled pressure bump in the LHCb vertex region the time for collecting the needed beam-gas statistics can be reduced, which would improve the measurement systematics. The required target gas thickness is much smaller than the LHC residual gas density, and the induced radiation is not larger than the one caused by beambeam collisions [6].

Compared to the VDM method, the disadvantage of a small rate is balanced by the advantage that the BGI method is non-disruptive, the beams do not move. This means that possible beam-beam effects are constant and potential effects which depend on the beam displacement, like hysteresis, are avoided. Furthermore, the beam-gas imaging method is applicable during physics fills.

The BGI method requires a vertex resolution comparable to or smaller than the transverse beam sizes. The knowledge of the vertex resolution is necessary to unfold the resolution from the measured beam profiles. The uncertainty in the resolution plays an essential role in determining the systematic error.

The half crossing angle between the beams, α, is small enough to justify setting $\cos^2\alpha = 1$ in Eq. (1.9). In the approximation of a vanishing correlation between the transverse coordinates, the x and y projections can be factorised. At the level of precision required, the bunch shapes are well described by Gaussian distributions. Thus, their shapes are characterised in the x-y plane at the time of crossing by their widths σ_{ji}, their mean positions ξ_{ji} $(i = x, y)$, and by their RMS lengths σ_{jz}. The index j takes the values 1 and 2 according to the two beams. With these approximations, Eq. (1.9) reduces for a single pair of colliding bunches to [79]:

$$L = \frac{N_1 N_2 \, f}{2\pi\sqrt{1+\tan^2\alpha(\sigma_{1z}^2+\sigma_{2z}^2)/(\sigma_{1x}^2+\sigma_{2x}^2)}} \prod_{i=x,y} \frac{1}{\sqrt{\sigma_{1i}^2+\sigma_{2i}^2}} \exp\left(-\frac{1}{2}\frac{(\xi_{1i}-\xi_{2i})^2}{\sigma_{1i}^2+\sigma_{2i}^2}\right), \tag{7.1}$$

where the denominator of the first factor in the product corrects for the crossing angle. The analysis is applied for each individual colliding bunch pair, *i.e.* bunch populations, event rates and beam profiles are considered per bunch pair. Thus, each colliding bunch pair provides an internally consistent measurement of the same effective cross-section. The observables σ_{ji} and ξ_{ji} are extracted from the transverse distributions of the beam-gas vertices reconstructed in the bb crossings of the colliding bunch pairs (see Section 7.2).

The beam overlap integral is then calculated from the two individual bunch profiles. The simultaneous determination of the position and the size of the *pp* luminous region provides additional constraints on the bunch parameters. In the approximation of Gaussian bunches the luminous region positions $\xi_{\otimes i}$ and transverse widths $\sigma_{\otimes i}$ are:

$$\xi_{\otimes i} = \frac{\xi_{1i}\sigma_{2i}^2 + \xi_{2i}\sigma_{1i}^2}{\sigma_{1i}^2+\sigma_{2i}^2} \quad \text{and} \quad \sigma_{\otimes i}^2 = \frac{\sigma_{1i}^2\sigma_{2i}^2}{\sigma_{1i}^2+\sigma_{2i}^2}, \tag{7.2}$$

This equation is valid only for a zero crossing angle. It will be shown in Section 7.5.2 that the approximation is justified for this analysis. The *pp*-interaction vertices are identified by requiring $-150 < z < 150$ mm and their distribution is used to measure the parameters of the luminous region of the corresponding bunch pair. Owing to the higher statistics of *pp* interactions compared to beam-gas interactions, the constraints of Eq. (7.2) provide the most significant input to the overlap integral.

The longitudinal bunch sizes σ_{jz} are extracted from the longitudinal distribution of the *pp*-collision vertices*. Because σ_{jz} are approximately 1000 times larger than σ_{jx}, the crossing angle reduces the luminosity by a non-negligible factor equal to the first square root term in Eq. (7.1). The case of non-collinear beams is described in

* In fact, only the combination $(\sigma_{1z}^2+\sigma_{2z}^2)$ can be obtained.

more detail in Section 7.4.2.

This chapter is organised as follows: we begin with an overview of the data-taking conditions during the fills used in the present analysis. Later, the data selection and analysis procedures are outlined in Section 7.2. The evaluation of the vertex resolution is described in Section 7.3, while the beam profile and overlap integral measurements are discussed in Section 7.4. The systematic uncertainties in the overlap integral measurements with the BGI method are addressed in Section 7.5. Finally, we conclude with a summary of the absolute luminosity normalisation results.

7.1 Data-taking conditions

The data used for the results described in the BGI analysis were taken in May 2010. In the data taken after this time the proton beam intensity and visible pp event rate were too high to select beam-gas events at the trigger level. In October a more selective trigger was in place and sufficient data could be collected. However, in this period difficulties were observed with the DCCT data with LHC filling schemes using bunch trains (see Fig. 5.1). It should be noted that the VDM data taken in October used a dedicated fill with individually injected bunches so that this problem was not present.

In the selected fills, there were 2 to 13 bunches per beam in the machine. The number of colliding pairs at LHCb varied between 1 and 8.

The online selection of events containing beam-gas interactions was performed with the dedicated level-0 and HLT beam-gas triggers, described in Section 3.4.2.

7.2 Analysis and data selection procedure

The standard vertex reconstruction algorithms in LHCb are optimised for pp interaction vertices close to $z = 0$. This specific optimisation is removed for this particular analysis such that no explicit bias is present in the track and vertex selection as a function of z. The resolution of the vertex measurement has to be known with high precision. Details of the resolution study are given in Section 7.3.

The BGI method relies on the unambiguous selection of beam-gas interactions, also during bb crossings where an overwhelming majority of pp collisions is present. The beam-gas fraction can be as low as 10^{-5} depending on the beam conditions. The criteria to distinguish beam-gas vertices from pp interactions exploit the small longitudinal size of the beam spot (luminous region). Beam1(2)-gas vertices in bb crossings are identified by requiring their z-position to satisfy $z < -250$ mm ($z > 250$ mm). The vetoed region corresponds approximately to $\pm 6\,\sigma_{\otimes}$, meaning that the background from pp interactions in the beam-gas selection region can be neglected (a similar cut is used in the beam-gas trigger, see Table 3.3). As an additional requirement, only vertices with exclusively

forward (backward) tracks are accepted as beam1(2)-gas interactions. The vertices are required to have more than 10 tracks, which allows a precise determination of the collision point to be made (see Section 7.3). A further selection on the distance from the measured beam axis is applied, $|\mathrm{d}r| < 2$ mm, to reject vertices from interactions in the VELO material and random associations of tracks. The z-distribution of vertices in bb, be and eb bunch-crossings is shown in Fig. 7.1.

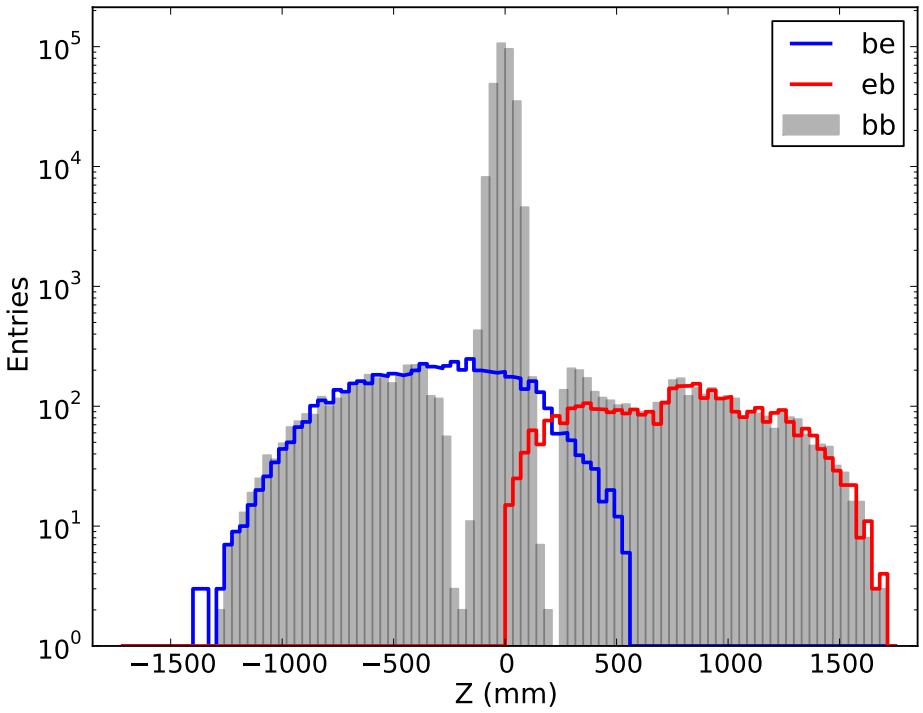

Figure 7.1: Distribution of the z-position of vertices in bb, be and eb bunch-crossings. The data shown are from fill 1117, where each beam contained six bunches, half of which collided in LHCb. The vertices are selected by applying requirements on the track-asymmetry, the number of tracks per vertex and the vertex radial position (see text). The peak around $z = 0$, which corresponds to pp interactions in bb crossings, is downscaled by a factor 100.

Due to the worsening of the resolutions for large distances from $z = 0$ and due to the presence of pp interactions near $z = 0$, to determine the width of the colliding bunches the selection regions are limited to $-700 < z < -250$ mm for beam1 and $250 < z < 800$ mm for beam2✦. For the measurement of the beam angles the vertices are allowed to extend up to 1000 mm from $z = 0$ (avoids magnetic field for $z > 1000$ mm and bad resolution for $z < -1000$ mm). The selection of pp events requires $150 < z < 150$ mm and only accepts vertices with more than 20 tracks. The background of beam-gas interactions in the pp interaction sample is negligible owing to the high pp event rate.

The transverse profiles of the two beams are measured for each individual colliding

✦ The vertex resolution for beam2 has a weaker z dependence, so the sensitivity is improved by enlarging the selection region beyond $z = 700$ mm.

bunch by projecting the vertex position parallel to the beam direction. The direction of the beam is determined on a fill-by-fill basis using the beam-gas interactions observed in be and eb crossings, which are free of pp interactions [§]. The $x-z$ and $y-z$ distribution of beam-gas vertices in be and eb crossings are shown in Fig. 7.2. Depending on the fill, the direction of the beam axis can be determined with a precision of 1 to 5 μrad.

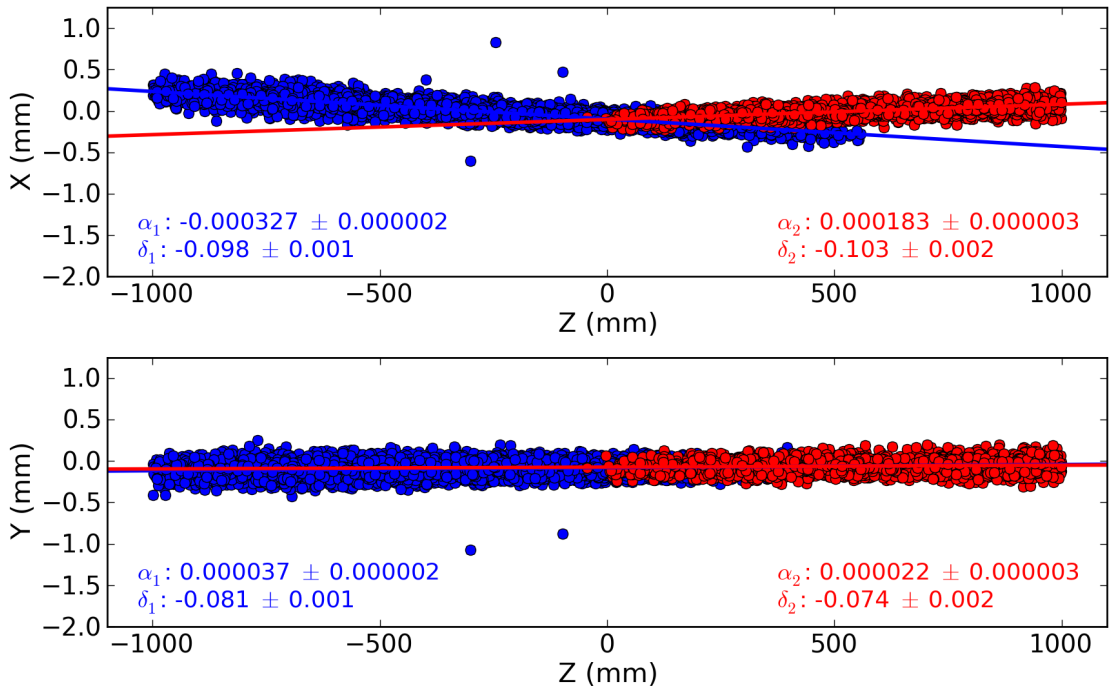

Figure 7.2: Position of reconstructed beam-gas vertices in the $x-z$ (top) and $y-z$ (bottom) planes in LHC fill 1117. Interaction vertices in be (eb) bunch-crossings are represented by blue (red) dots. The beam angles $\alpha_{1,2}$ and offsets $\delta_{1,2}$ are obtained from straight line fits. The measured beam crossing angles in the horizontal and vertical planes are 510 ± 5 and 15 ± 5 μrad, respectively, to be compared with the expected values of 540 and 0 μrad.

Out of the many LHC fills only seven are selected for the BGI analysis. The first selection criteria are based on the stability of beam intensities and emittances as observed by the LHC beam instrumentation. In addition, it is required that all necessary data (DCCT, FBCT, luminosity counters and vertex measurements) are present during a sufficiently long period (roughly 5 hours, depending on the beam intensity). A list of used fills is given in Table 7.1. The table shows the total number of bunches and the ones colliding at LHCb, the typical number of protons per bunch, the measured beam slopes with respect to the LHCb reference frame, and the duration of the period used for the analysis.

The beam intensities for one of the selected fills are shown in Fig. 7.3 as a function

[§] Generally, depending on the beam conditions and the filling scheme, (undesired) pp interactions can be observed in be and eb crossings. In this case forward-backward track-asymmetry and z-position cuts can be used to filter-out the pp vertices. However, no such problem arose in the present analysis.

Table 7.1: LHC fills used in the BGI and VDM analyses. The second and third columns show the total number of (colliding) bunches n_{tot} (n_{coll}), the fourth - the typical intensity per bunch, the fifth - the period of time used for the analysis and the sixth and seventh - the measured angles (in mrad) of the individual beams with respect to the LHCb reference frame (the uncertainties in the angles range from 1 to 5 μrad). The last two columns give the typical number of events *per bunch* used in the BGI vertex fits for each of the two beams.

Fill	n_{tot}	n_{coll}	N	**time (h)**	α_1	α_2	**analysis**	**events 1**	**events 2**
1059	2	1	$1\,10^{10}$				VDM 1		
1089	2	1	$2\,10^{10}$	15	0.209	-0.371	BG 1	1270	720
1090	2	1	$2\,10^{10}$	4	0.215	-0.355	BG 2	400	300
1101	4	2	$2\,10^{10}$	6	-0.329	0.189	BG 3	730	400
1104A	6	3	$2\,10^{10}$	5	0.211	-0.364	BG 4	510	350
1104B	6	3	$2\,10^{10}$	5	0.211	-0.364	BG 5	520	350
1117	6	3	$2\,10^{10}$	6	-0.327	0.185	BG 6	700	500
1118	6	3	$2\,10^{10}$	5	-0.332	0.181	BG 7	500	400
1122	13	8	$2\,10^{10}$	3	-0.329	0.182	BG 8	300	250
1422	16	12	$8\,10^{10}$				VDM 2		

of time.

The analysis is applied for each individual colliding bunch pair, *i.e.* bunch populations, event rates and beam profiles are considered per bunch pair. Thus, each colliding bunch pair provides an internally consistent measurement of a visible cross-section. The beam intensity and size cannot be assumed to be constant during the analysis period. Therefore, the DCCT and FBCT data and the vertex measurements using *pp* interactions are binned in periods of 900 seconds. The choice of the period length is not critical. The chosen value maintains sufficient statistical precision while remaining sensitive to variations of the beams. The distributions of beam-gas interactions do not have sufficient statistics and are accumulated over the full periods as shown in Table 7.1.

The analysis proceeds by determining a time-weighted average for the bunch-pair intensity product and the width and position of the *pp* beam spot. The weighting procedure solves the difficulty introduced by short periods of missing data by a logarithmic interpolation for the beam intensities and a linear interpolation for the beam spot. The averages defined by the latter procedure can be directly compared to the single measurement of the profiles of the single beams accumulated over the full period of multiple hours. A systematic error is assigned to this averaging procedure.

7.3 Vertex resolution

The measured vertex distribution is a convolution of the true width of each beam with the resolution function of the detector. Since the resolution is comparable to the

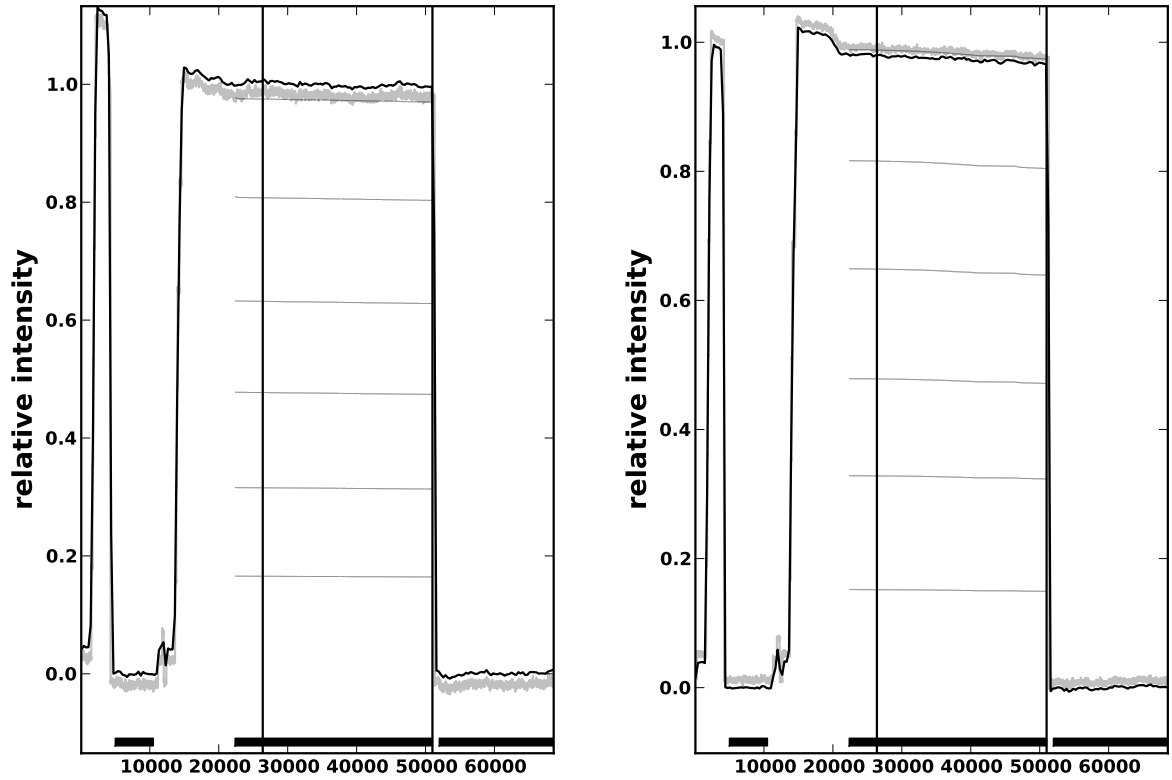

Figure 7.3: Beam intensity measurements as a function of time for fill 1117. The horizontal axis shows the time in seconds with an arbitrary offset. The beginning and the end of the period used for the BGI analysis are indicated by vertical lines. All intensities are relative to the average of the DCCT during the stable beam period. The dark bar near the horizontal axis indicates the periods used for the determination of the DCCT offset (during the time with no beam), and the "stable-beam" period (during the flat top). The grey shaded lines show the raw DCCT values and the black line - their offset-corrected average over periods of 300 s. The thin dotted lines show the cumulative FBCT value for the bunches in the beams.

bare beam size (approximately 35 μm), it is crucial to understand this effect, and to be able to unfold it from the reconstructed values.

The vertex resolution is measured using data on an event-by-event basis. The principle is to reconstruct the same primary vertex twice, and to consider the residual between these two points. This is achieved by splitting the track sample of each event into two (see below), and attempting to make a vertex from each independent set of tracks.

The vertex resolution is parametrised as a function of the multiplicity, or number of tracks used to reconstruct the vertex, and as a function of the z position of the interaction. Beam-gas vertices alone are used to measure the positions and spatial extent of each beam; however, these events are rare in comparison to pp vertices. To avoid binning the beam-gas vertices in both number of tracks and z position, inelastic pp events are initially used to measure the dependence of the resolution on the number

of tracks, at the z position of the luminous region. Once this dependence is known, the beam-gas vertices are used to find the z dependence of the resolution.

7.3.1 Dependence on the track multiplicity of the vertex

The resolution as a function of the number of tracks in a vertex is determined using inelastic pp events, which occur around $z = 0$. These events are plentiful. All events which pass the LHCb trigger are initially considered. The raw event is reconstructed using the default tracking and vertexing algorithms and a larger z range is used in the track reconstruction algorithm. The increase of the tracking z window from $-170 < z < 120$ mm to $-1200 < z < 1200$ mm ensures efficient reconstruction of tracks coming from beam-gas interactions in the VELO vicinity. Exactly the same reconstruction for both the pp and beam-gas events is used.

The reconstructed tracks from each event are split into two independent sets. This is done at random, with no momentum ordering of tracks and no requirement that the same number of tracks are put into each set. For each track in the event a uniformly distributed random number between 0 and 1 is drawn and the track is assigned to one of the two sets using a threshold value of 0.5. The vertex reconstruction algorithm is run on each set of tracks, and if exactly one vertex is found from each track collection it is assumed to be the same original interaction. Both vertices must pass a loose selection, requiring that the vertex lies in the beam region, and has a reasonable χ^2 value. If the number of tracks making each of these two vertices, N_{Tr}, is the same[❖], the residuals in x and y are calculated. Later, these residuals are filled in separate histograms, accumulating the results in each of the two transverse directions and for every N_{Tr}. Each residual histogram is fitted with a Gaussian. The resolution for each particular number of tracks is calculated as the σ of the fitted Gaussian divided by $\sqrt{2}$, as there are two resolution contributions in each residual measurement. The resolutions are then binned as a function of the number of tracks, as shown in Fig. 7.4. The transverse resolution for an average (25 track) vertex is calculated to be 13 μm, which agrees with the resolution of the default reconstruction used for standard physics analyses.

The set of resolution estimates, obtained for all accessible N_{Tr} are fitted with the following function, which parametrises the vertex resolution as a function of the number of tracks in a vertex, N_{Tr}:

$$\sigma_{\mathrm{res}} = \frac{A}{N_{\mathrm{Tr}}^{B}} + C \tag{7.3}$$

The values of the function parameters obtained from the fit are given in Table 7.2. The overall accuracy of the parametrisation is determined by applying the track-split method on Monte Carlo simulated events. As described in Section 7.5.1, the vertex

[❖] In practice, the number of tracks making a vertex ranges from 5, the required minimum, to around 100. However, given the track split method divides the total number of tracks in two, it is difficult to measure the resolution past 40 tracks. In any case, beam-gas vertices tend to have lower multiplicities than pp vertices, so this does not limit the precision of the measurement.

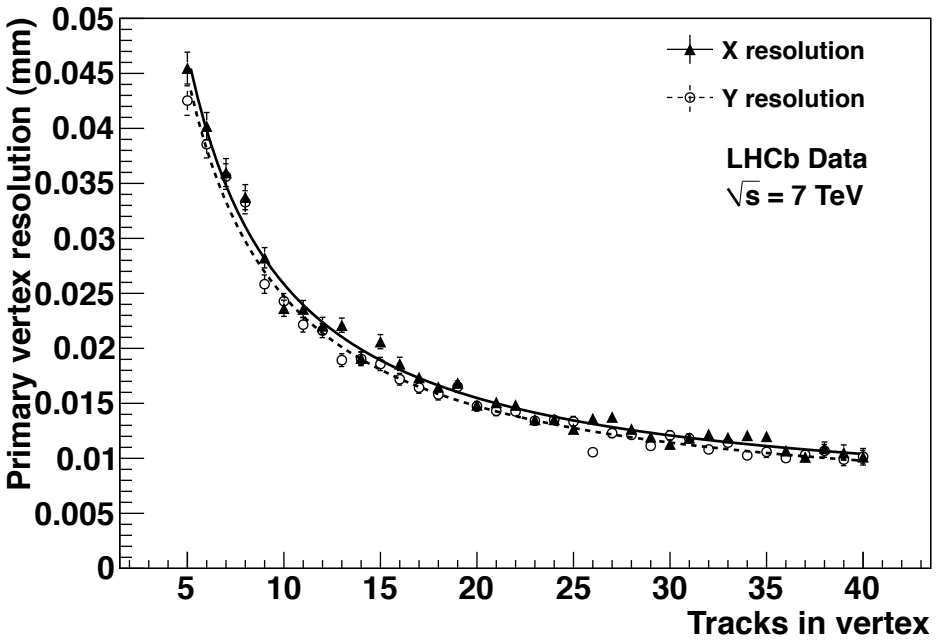

Figure 7.4: VELO primary vertex resolution $\sigma_{\rm res}$ in the transverse directions x and y for pp interactions as a function of the number of tracks in the vertex.

resolution parametrisation as function of $N_{\rm Tr}$ is found to be better than 5%.

Table 7.2: Fit parameters for the resolution for pp interactions as a function of number of tracks, for the transverse coordinates x and y. Parameters correspond to those in Eq. (7.3). The errors in the fit parameters are correlated and therefore do not represent the overall accuracy of the parametrisation.

	x	y
Factor A (mm)	0.215 ± 0.020	0.202 ± 0.018
Power B	1.023 ± 0.054	1.008 ± 0.053
Constant C (10^{-3} mm)	5.463 ± 0.675	4.875 ± 0.645

VELO is asymmetric in the x and y coordinates. For example, to facilitate the alignment procedure, its sensors overlap in the vertical plane. Therefore, no attempt is made to average the resolution parametrisation in the x and y coordinates (the same argument holds for the vertex resolution parametrisation as function of z).

The parametrisation as function of $N_{\rm Tr}$ is used in the calculation of the z dependence of the resolution, to take into account the resolution component determined by the number of tracks.

7.3.2 Dependence on the z position of the vertex

The dependence of the vertex resolution as function of z is determined using beam-gas interactions occurring in be and eb bunch-crossings. The events are reconstructed

in the same manner as *pp* vertices, and again, the total track sample is randomly split into two. As with the *pp* analysis, if both sets of tracks yield exactly one good-quality reconstructed vertex, then it is assumed to be the same underlying beam-gas interaction. However, in contrast to the *pp* analysis, every beam-gas event which yields two vertices with $N_{\mathrm{Tr}} \geq 5$ is used, without requiring that the two vertices are reconstructed with an equal number of tracks. For each of the transverse directions $\xi = x, y$ we define a z-dependent correction factor F_z as:

$$F_z = \frac{\xi_1 - \xi_2}{\sqrt{\sigma^2_{N_{\mathrm{Tr}_1}} + \sigma^2_{N_{\mathrm{Tr}_2}}}} \tag{7.4}$$

Here, the index $1, 2$ signifies the vertices obtained from the two track samples in the event, and ξ_1 and ξ_2 are the measured vertex positions. The quantities $\sigma_{N_{\mathrm{Tr}_{1,2}}}$ are the resolutions σ_{res} for vertices with N_{Tr_1} and N_{Tr_2} tracks, occurring near $z = 0$, as defined in Eq. (7.3). The correction factors F_z show by how much the *pp* resolution at $z \approx 0$ must be multiplied in order to find the resolution for a vertex with the same number of tracks, at a certain position in z. F_z are calculated for a large number of events and the values are filled in separate histograms, holding the results in several bins in z. These histograms are fitted with a Gaussian and the Gaussian width is used as an estimate of the final z correction factors of the vertex resolution (see Fig. 7.5).

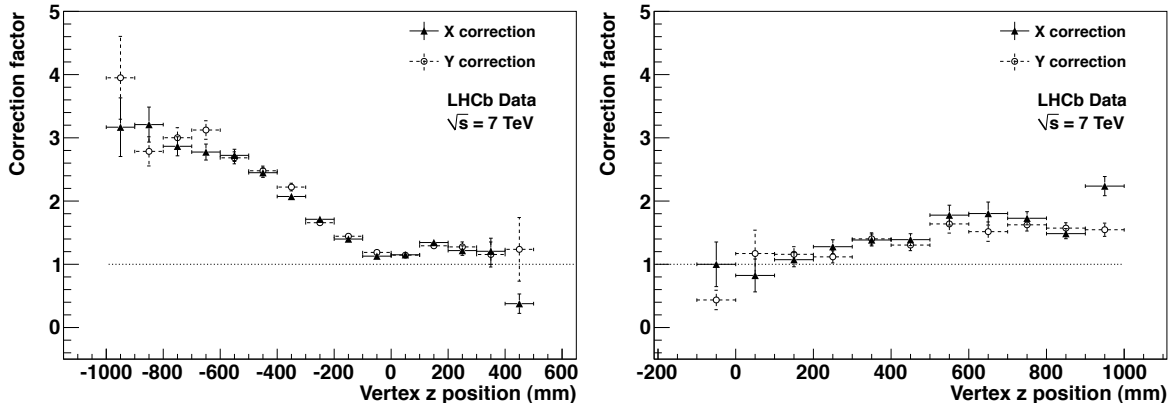

Figure 7.5: The z dependence of the correction factor F_z in x and y for beam1-gas (left) and beam2-gas (right) interactions.

In order to better understand the behaviour of the resolution as a function of z, it is instructive to consider the geometry of the VELO (see Fig. 3.5). Since LHCb is designed to study physics in the forward region of phase space, the interaction region is slightly off-centre, and is surrounded by a region of closely packed r-ϕ measuring silicon modules. Figure 7.5 shows that around the interaction point of $z = 0$ the correction factor is close to one, which signifies that the resolution is nearly independent of the type of event, whether *pp*, beam1-gas or beam2-gas. This is not initially obvious, as beam-gas events normally have tracks going only in one of the z directions, while

usually the products of inelastic pp interactions fly in both z directions. The correction factor increases approximately linearly as the vertices move away from the interaction region. For small shifts from $z = 0$ this is explained by the geometry of the VELO becoming non-optimal, as the vertex position becomes displaced with respect to the closely packed region of silicon modules. For larger displacements, the distance from the beam-gas vertex to the first track hits in the silicon modules becomes larger, so increasing the distance by which the tracks must be extrapolated to find the vertex.

The most upstream VELO sensor is located at $z = -175$ mm, the most downstream sensor is located at $z = 750$ mm, and therefore the geometrical middle is at $z = 287.5$ mm. This explains to some extent the asymmetric behaviour of the correction factor on both sides of the interaction region. In addition, this asymmetry is enhanced by the fact that four VELO station slots, located between $z = 320$ mm and $z = 550$ mm, are not populated with sensors [111].

7.3.3 Resolution unfolding

The subtraction of the vertex resolution from the measured vertex distributions is done independently in the two transverse coordinates. The procedure assumes that the beams have Gaussian shapes and that the effect of the vertex resolution can be parametrised as a superposition of Gaussian functions. We use the fact that the convolution of two Gaussian distributions with widths σ_1 and σ_2 is again a Gaussian, with width $\sigma = \sqrt{\sigma_1^2 + \sigma_2^2}$.

Due to the dependence of the resolution on the number of tracks and on z, the effective resolution function is defined as a sum of N Gaussian functions $g_n(x; \sigma_n)$, centred at zero, with scalar coefficients c_n:

$$R(x) = \sum_{n=1}^{N} c_n g_n(x; \sigma_n) \tag{7.5}$$

The effective resolution function is obtained by accumulating for each vertex entering the vertex distributions its expected resolution on the basis of the number of tracks in the vertex and its z position (see Sections 7.3.1 and 7.3.2). In this way, the two-dimensional resolution parametrisation is used to generate a one-dimensional resolution distribution. The latter is subsequently divided in N bins. The number of entries in each bin gives the weight coefficient c_n and the average resolution in each bin gives the corresponding value of σ_n. Six bins are sufficient to give a good description of the resolution.

The physical beam shape is assumed to be described by a Gaussian with amplitude a, position ξ and width σ. The measured vertex distribution $M(x)$ is a convolution

of the physical beam shape, $f(x; a, \xi, \sigma)$, and the resolution function $R(x)$:

$$M(x) = \int_{-\infty}^{+\infty} \sum_{n=1}^{N} c_n g_n(x - t; \sigma_n) f(t; a, \xi, \sigma) dt \,, \tag{7.6}$$

Using the basic algebraic properties of the convolution and defining $\sigma_n^* = \sqrt{\sigma_n^2 + \sigma^2}$ Eq. (7.6) can be rewritten as:

$$M(x) = \sum_{n=1}^{N} c_n f_n(x; a, \xi, \sigma_n^*) \,, \tag{7.7}$$

Finally, the physical beam position, ξ, and width, σ, are obtained by fitting this function to the data.

7.4 Measurement of beam profiles and overlap integral

7.4.1 Measurement of beam profiles

In Fig. 7.2 the position of the vertices of beam-gas interactions of the single beams in be and eb crossings is shown in the x-z and y-z planes. The straight line fits provide the beam angles in the corresponding planes. Generally, agreement between the expected and measured beam angles is observed. Whereas we can use the non-colliding bunches to determine the beam directions, the colliding bunches are the only relevant ones for luminosity measurements.

The transverse bunch profiles are obtained from the projected beam-gas vertex distributions onto a plane perpendicular to the beam direction. The data are selected according to the criteria given in Section 7.2. As an example, the x and y profiles of one colliding bunch-pair are shown in Fig. 7.6. The true bunch size is obtained after deconvolving the vertex resolution following the procedure described in Section 7.3.3. The resolution function and true bunch profile are drawn separately to show the importance of the knowledge of the resolution.

In Fig. 7.7 the fits to the luminous region of the same bunch pair are shown, both for the duration of the full fill and for a short period of 900 s. The distributions for the full fill deviate from Gaussian (bad χ^2 is obtained in the fit) due to the emittance growth of the beam. This is not the case for the shorter period where the fit describes the data satisfactorily. The resolution at $z = 0$ is small compared to the size of the luminous region. This fact and the larger number of tracks emerging in inelastic pp interactions, compared to beam-gas events, makes it possible to reach small systematic uncertainties in the luminosity determination by using the constraints of the beam parameters provided by Eqs. (7.2).

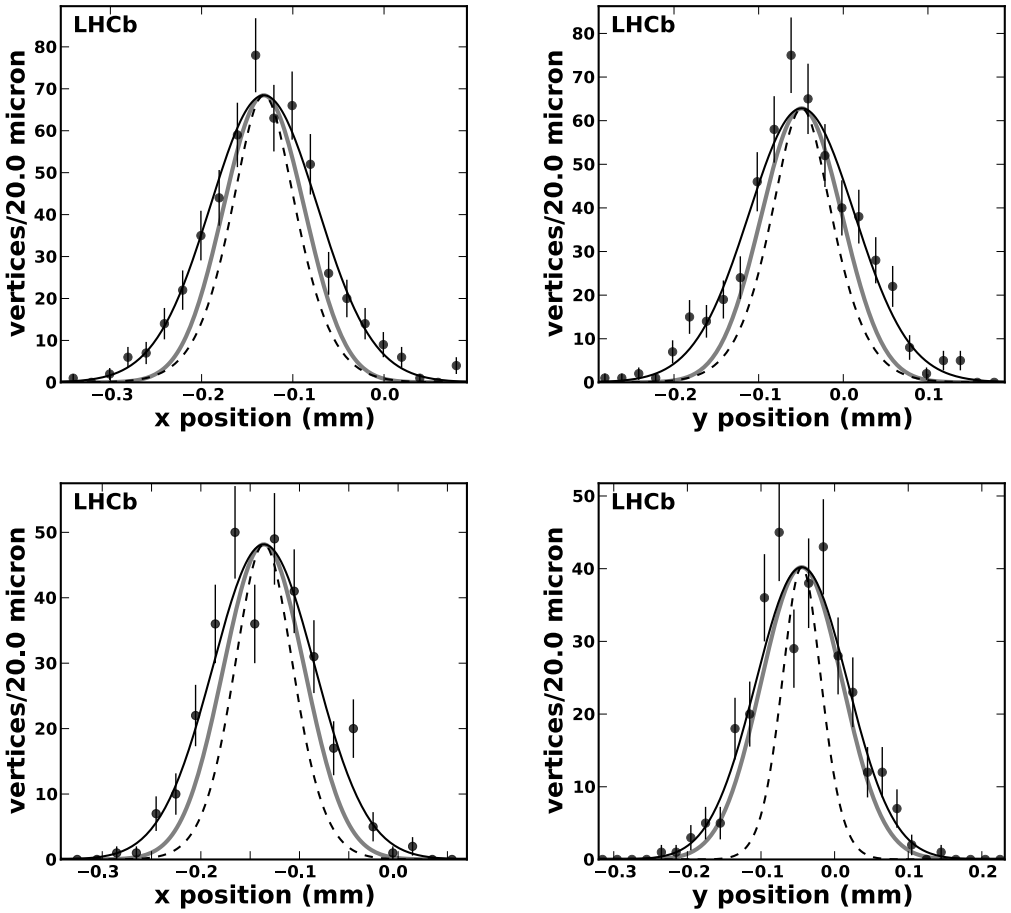

Figure 7.6: Transverse profiles of two bunches colliding in LHCb (bunch-crossing ID 2186) in fill 1104, obtained from the projected position distributions of beam-gas vertices. The bunch of beam1(2) appears at the top (bottom). The left (right) panels show the distributions in x (y). The Gaussian fit to the measured vertices is shown as a solid black line together with the resolution function (dashed) and the unfolded bunch profile (thick grey line). Note the variable scale of the the horizontal axis.

For non-colliding bunches it is possible to measure the width of the beam in the region of the interaction point (IP) at $z = 0$ since there is no background from pp collisions. One can compare these measurements with the bunch widths obtained from vertices outside the IP region, which need to be used for the colliding bunches. With the present focusing of the beams no measurable difference is expected.

Figures 7.8 and 7.9 show the consistency of the two beam width measurements. We see that within errors the width ratios are consistent with unity, which is a significant confirmation of the correctness of the resolution parametrisation, which includes a large z-dependent correction.

For the colliding bunches we can compare the width of the luminous region, as measured from pp interaction vertices, with the width obtained using the second relation in (7.2) and the beam-gas vertex distribution of the individual colliding bunches

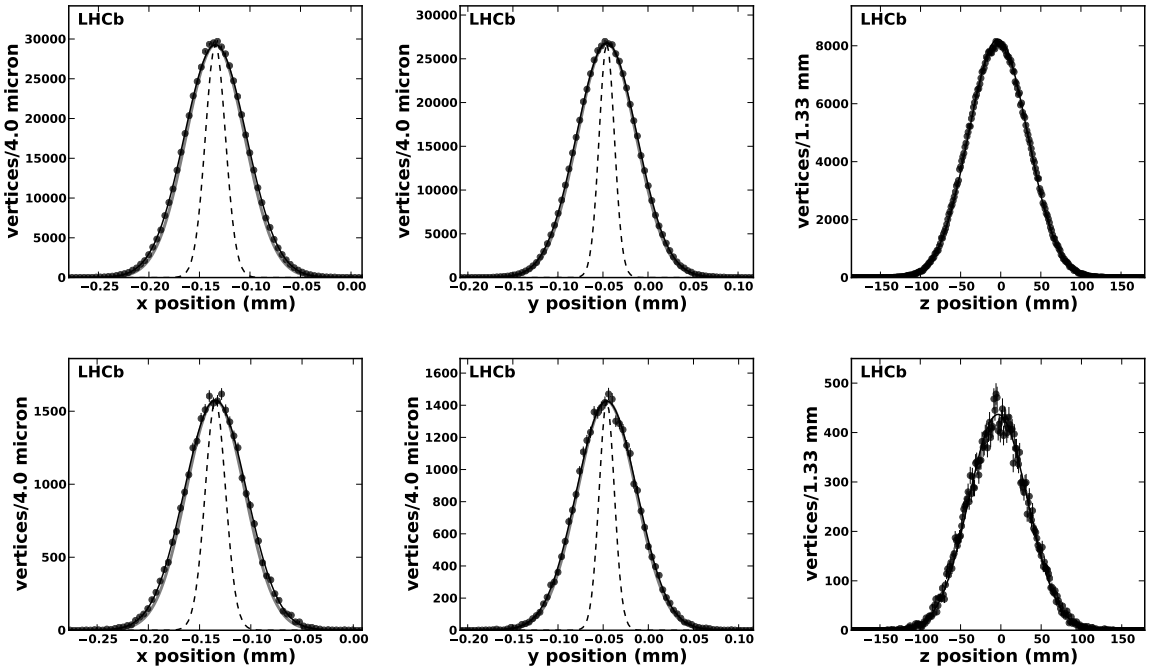

Figure 7.7: Distribution of the transverse and longitudinal position of pp interaction vertices of two bunches colliding in LHCb (bunch-crossing ID 2186) in fill 1104. The data corresponding to the full fill are shown at the top, while data corresponding to 900 s, in the middle of the fill, are at the bottom. The x, y and z distributions appear in the left, middle and right panels, respectively. The Gaussian fit to the measured vertices is shown as a solid black line together with the resolution function (dashed) and the unfolded luminous region (solid grey line). Owing to the good resolution, the grey curves are close to the solid curves and are therefore not clearly visible in the figures. The fit to the z coordinate neglects the vertex resolution. Note the variable scale of the the horizontal axis.

outside the IP region. Figure 7.10 shows that there is overall consistency. In addition to the data used in the BGI analysis described here, also higher statistics data from later fills are used for this comparison. The cross-check reaches a precision of 1–1.6% for the consistency of the width measurements at large z compared to the measurement at $z = 0$. This provides a good evidence for the correctness of the parametrisation of the z dependence of the vertex resolution and confirms that relations (7.2), valid for Gaussian bunches, can be used.

The relations (7.2) are used to constrain the width and position measurements of the single beams and the luminous region in both coordinates separately. Given the high statistics of the luminous region the pp events have the largest weight in the luminosity calculation. The beam-gas measurements determine the width ratio of the two beams: $\rho_i = \sigma_{2i}/\sigma_{1i}$ $(i = x, y)$.

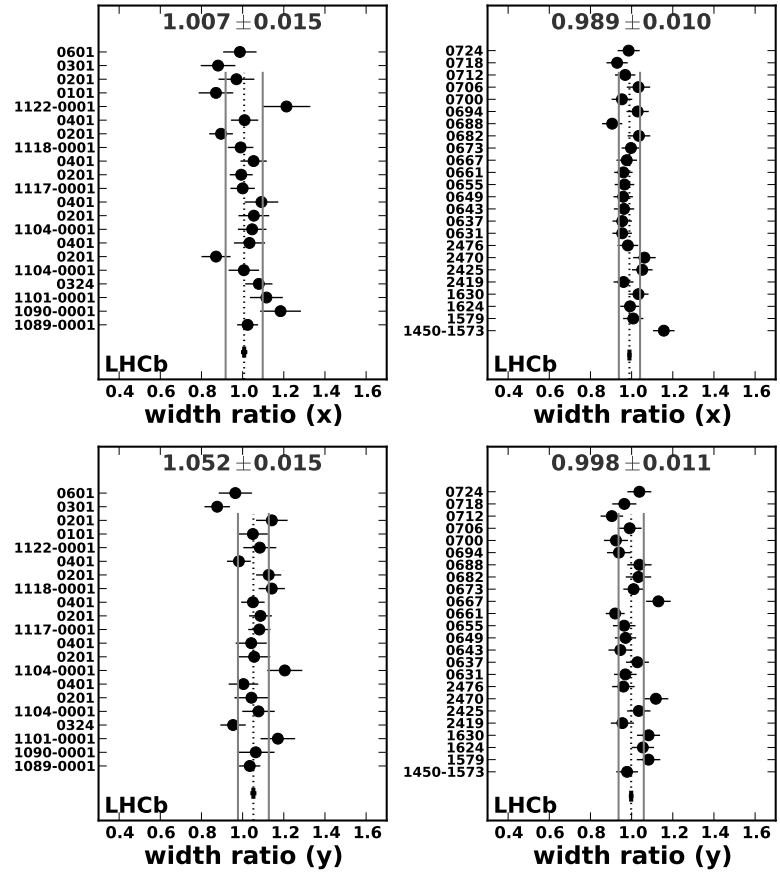

Figure 7.8: Comparison of the width (corrected for resolution) measured far from the IP and near the IP for beam1. The left panel shows the results for bunches in the fills with $\beta^\star = 2$ m optics used in this analysis, the right panel shows bunches in a fill taken with $\beta^\star = 3.5$ m optics. The fill and bunch numbers are shown on the vertical axis. The vertical dotted line and the point at the bottom indicate the weighted average of the individual measurements. The error bar of the bottom point represents the corresponding uncertainty in the average. The same information is given above the data points. The solid lines show the standard deviation of the data points.

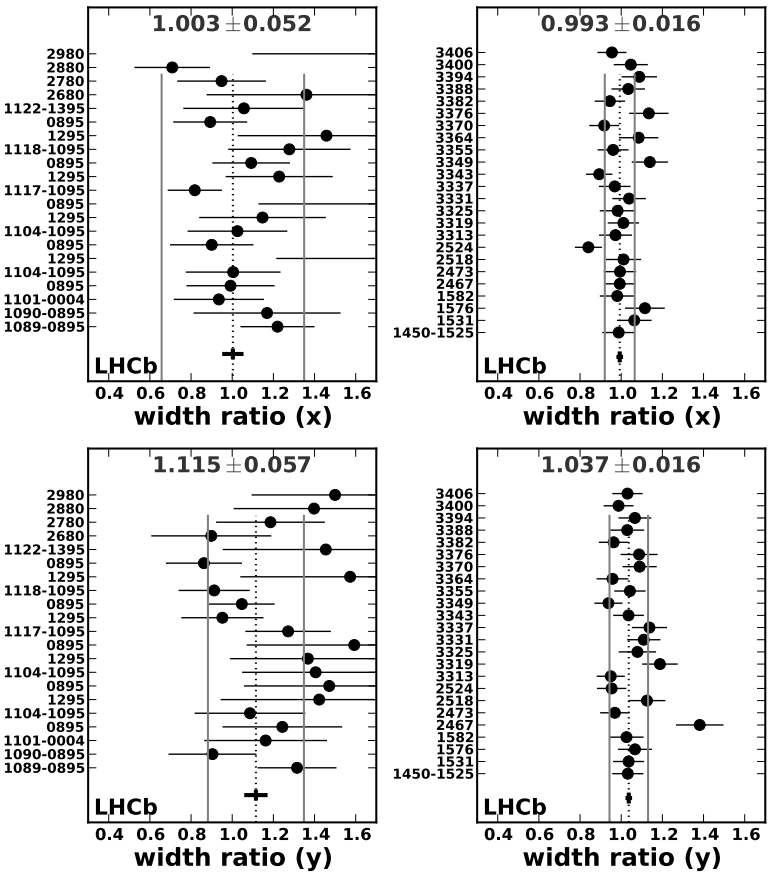

Figure 7.9: The same as Fig. 7.8 for beam2.

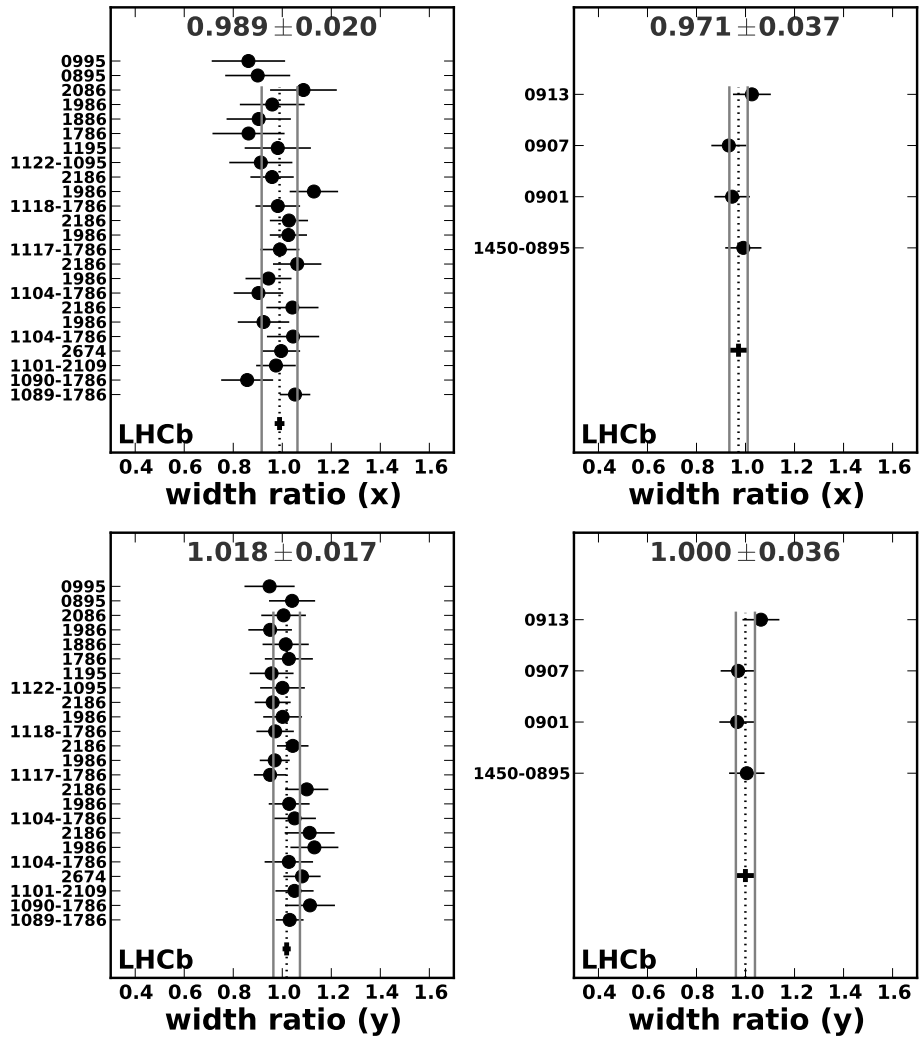

Figure 7.10: Comparison of the prediction for the luminous region from measurements based on individual bunches, with the direct measurement of the luminous region width for colliding bunches. The left panel shows the results for bunches in the fills with $\beta^\star = 2$ m optics used in this analysis, the right panel shows four colliding bunches in a fill taken with $\beta^\star = 3.5$ m optics. The fill and bunch numbers are shown on the vertical axis. The vertical dotted line and the point at the bottom indicate the weighted average of the individual measurements. The error bar of the bottom point represents the corresponding uncertainty in the average. The same information is given above the data points. The solid lines show the standard deviation of the data points.

7.4.2 Measurement of the overlap integral

The overlap integral of two Gaussian bunches, colliding with no offset and zero crossing angle is (*cf.* Eq. (7.1)):

$$A_{\text{eff}}^{-1} = \frac{1}{2\pi\sqrt{\left({\sigma_{1x}}^2 + {\sigma_{2x}}^2\right)\left({\sigma_{1y}}^2 + {\sigma_{2y}}^2\right)}}\,, \tag{7.8}$$

where we have introduced the effective overlap area A_{eff} to signify the inverse of the overlap integral. In terms of the widths of the luminous region $\sigma_{\otimes i}$ and the width ratios of the two beams ρ_i, the overlap integral is:

$$A_{\text{eff}}^{-1} = \frac{1}{2\pi} \prod_{i=x,y} \frac{\rho_i}{(1+\rho_i^2)\sigma_{\otimes i}}\,, \tag{7.9}$$

where we have used the second equation in (7.2). Equation (7.9) shows clearly the weight of the measurement of the width of the luminous region in the luminosity determination.

In the presence of a crossing angle and an offset between the beams, the luminosity decreases due to the imperfect overlap between the two beams. As described in [79], in this case the overlap integral can be expressed as the product of (7.8) and three correction factors. Two of the corrections account for the crossing angle (**S**) and offset (**T**) alone, while the third correction (**U**) needs to be taken into account only when the two effects are present simultaneously. The explicit form of the correction factors is the following:

$$\begin{aligned}
\mathbf{S} &= \frac{1}{\sqrt{1+\sum_{i=x,y}\dfrac{\sigma_{1z}^2+\sigma_{2z}^2}{\sigma_{1i}^2+\sigma_{2i}^2}\tan^2\alpha_i}} \\
\mathbf{T} &= \prod_{i=x,y} \exp\left(-\frac{1}{2}\frac{(\xi_{1i}-\xi_{2i})^2}{\sigma_{1i}^2+\sigma_{2i}^2}\right) \\
\mathbf{U} &= \exp\left[\mathbf{S}^2\,\frac{\sigma_{1z}^2+\sigma_{2z}^2}{2}\left(\sum_{i=x,y}\frac{(\xi_{1i}-\xi_{2i})\tan\alpha_i}{\sigma_{1i}^2+\sigma_{2i}^2}\right)^2\right]
\end{aligned} \tag{7.10}$$

In the fills used in the present analysis the half crossing angle α_i is about 250 and 0 μrad in the horizontal and vertical planes, respectively. Taking into account that the ratio of the longitudinal and lateral sizes of the bunches is of the order of 10^3 we see that a crossing angle in the vertical plane of the order of 10 μrad will generate a contribution of 10^{-4} in the sum of the expression for **S**. Therefore we can safely neglect the potential small crossing angle in the vertical plane. This approximation brings the **S** correction factor to its form used in Eq. (7.1), namely:

$$\mathbf{S} \equiv C_\alpha = \left[1+\tan^2\alpha(\sigma_{1z}^2+\sigma_{2z}^2)/(\sigma_{1x}^2+\sigma_{2x}^2)\right]^{-\frac{1}{2}} \tag{7.11}$$

For $\alpha = 250$ μrad and $(\sigma_{1z}^2+\sigma_{2z}^2)/(\sigma_{1x}^2+\sigma_{2x}^2) = 10^3$ the correction due to crossing angle is: $1/\sqrt{1+0.0625} \approx 0.97$.

The correction due to offsets in the beam positions, **T**, is taken into account in Eq. (7.1). For head-on beams this correction equals unity. Equations (7.2), relating

the positions and widths of the two beams and the luminous region, are used as a constraint to improve the overall precision.

The angle-offset interference correction, **U**, is not considered in the calculation of the luminosity as its effect is negligible when we consider the beam parameter values of the present analysis. This can be seen from the following. As the crossing angle in the vertical plane is much smaller than the angle in the horizontal plane we consider only the x term in the **U** correction formula. We rewrite the **U** correction as follows:

$$\mathbf{U} = \exp\left(\frac{\mathbf{S}^2}{2}\,\frac{\Sigma_z^2\alpha_x^2}{\Sigma_x^2}\,\frac{(\xi_{1x}-\xi_{2x})^2}{\Sigma_x^2}\right),$$

where we used the symbol Σ_i^2 to signify $\sigma_{1i}^2+\sigma_{2i}^2$ $(i=x,z)$. In this rough estimation the deviation of **S** from unity can be neglected. As already mentioned, the ratio of the longitudinal and lateral bunch sizes is of the order of 10^3 and using $\alpha_x = 250$ μrad we notice that $\dfrac{\Sigma_z^2\,\alpha_x^2}{\Sigma_x^2}$ is smaller than 0.1. Therefore the exponent argument of the **U** correction is approximately equal to:

$$0.05\left(\frac{\Delta\xi_x}{\Sigma_x}\right)^2 \tag{7.12}$$

Requiring the expression (7.12) to be smaller than 10^{-3} leads to the requirement that $\dfrac{\Delta\xi_x}{\Sigma_x}$ must be smaller than 0.14 ¶. As these are the typical relative offsets observed in most fills used in the present analysis (see Table 7.3), the **U** correction is neglected.

By examining both relations of Eq. (7.2) a system of two constraint equations and six measurable quantities emerges for each transverse coordinate separately. This fact is exploited in a combined fit where the individual beam widths σ_{1i}, σ_{2i}, and the luminous region width $\sigma_{\otimes i}$ together with the corresponding position values ξ_{ji} and $\xi_{\otimes i}$ are used as input measurements. Several choices are possible for the set of four fit-parameters, trivially the set σ_{1i}, σ_{2i}, ξ_{1i}, ξ_{2i} can be used. The set Σ_i (as defined above), ρ_i, $\Delta_\xi = \xi_{1i} - \xi_{2i}$ and $\xi_{\otimes i}$ is used which makes it easier to evaluate the corresponding luminosity error propagation. The results for the central values are identical, independently of the used fit-parameter set.

7.5 Corrections and systematic errors

In the following, corrections and systematic error sources affecting the BGI analysis will be described. We consider uncertainties in the vertex resolution description, crossing angle effects, biases, the effect of drifts and the gas pressure. The uncertainty of the beam intensity normalisation was already discussed in Chapter 5.

¶ For $\Sigma_x^2 = 50$ μm, this corresponds to 7 μm offset between the beams.

7.5.1 Resolution

The uncertainty of the resolution induces potentially a significant systematic error in the luminosity measurement. One way to estimate the uncertainty of the resolution parametrisation is to use simulated events and to compare the resolution determined with the "data" method (which proceeds by splitting the tracks of the event in two groups and reconstructing two vertices; see Section 7.3) and the resolution obtained by comparing the simulated and reconstructed vertex positions. The pp vertex resolutions obtained with these two methods are shown in Fig. 7.11 as function of the number of tracks in the vertex. The uncertainty in the number of tracks (N_{Tr}) dependence at $z = 0$ is estimated in this way to be no larger than 5%.

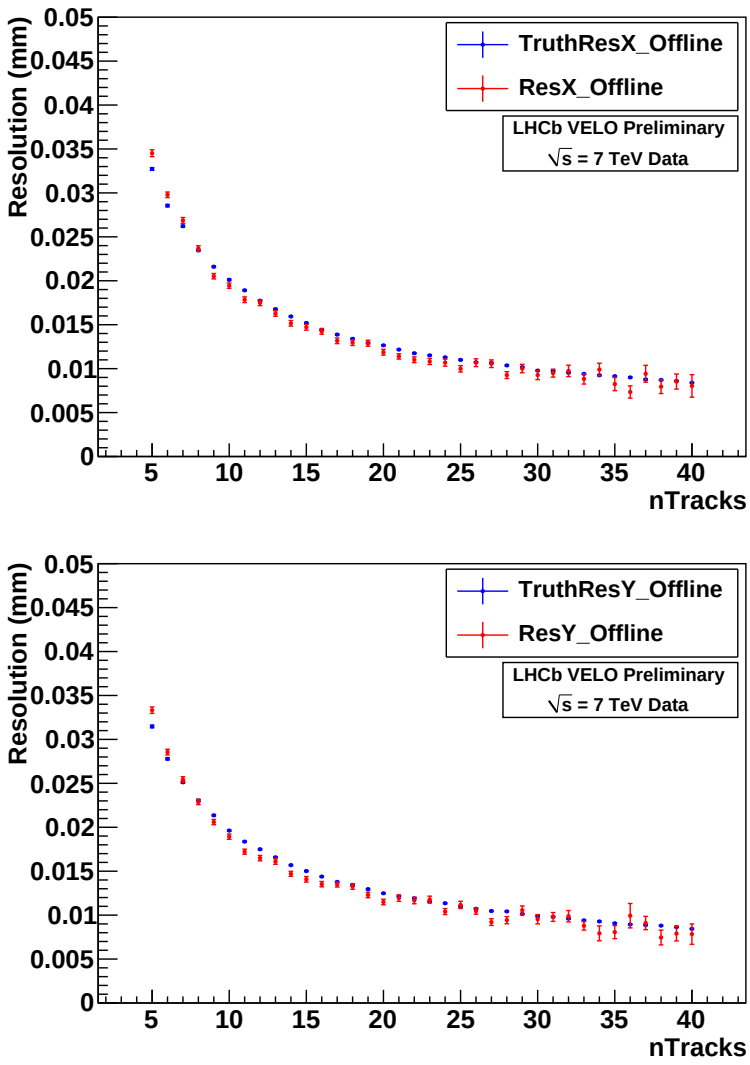

Figure 7.11: Comparison of the primary vertex resolution obtained with the MC-truth and "data" methods. The resolutions in the x and y coordinates are shown in the top and bottom panels, respectively.

The uncertainty in the z dependence of the resolution is estimated from data collected by LHCb, using the upper and lower limits of the error bars in Fig. 7.5 (relative variations of about $\pm 10\%$). The comparisons of the fits to the vertex distributions in different z ranges described in the previous section justify this choice.

The effect of these systematic errors of the resolution on the measured widths of the individual beams and the luminous region are shown in Figs. 7.12 and 7.13, respectively.

The effect of the uncertainties in the N_{Tr} and z dependence on the final results are estimated by repeating the analysis varying the resolution within its uncertainty. The conservative approach is taken to vary the different dependencies coherently in both x and y and for the dependence on N_{Tr} and z simulataneously. The resulting uncertainties in the cross-section depend on the widths of the distributions and are therefore different for each analysed bunch pair.

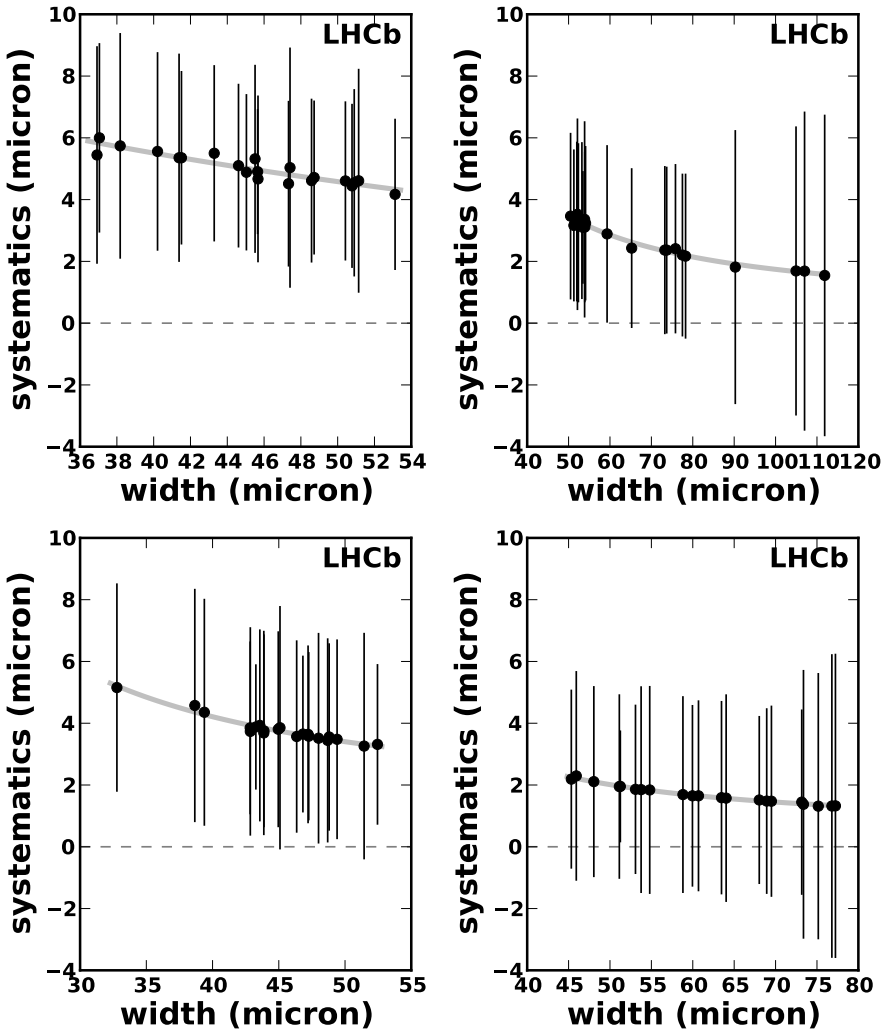

Figure 7.12: Systematic error of the resolution indicating the difference between the beam widths obtained with the upper and lower extremes of the vertex resolution, versus the beam width obtained with the central values of the vertex resolution. The top (bottom) panels correspond to beam1(2); the x-coordinate is shown on the left and the y-coordinate - on the right. The error bars indicate the statistical error of the individual fits. The statistical error in the determination of the systematic error is much smaller owing to the fully correlated data-sets. The parametrisation of the systematics is shown as a shaded line.

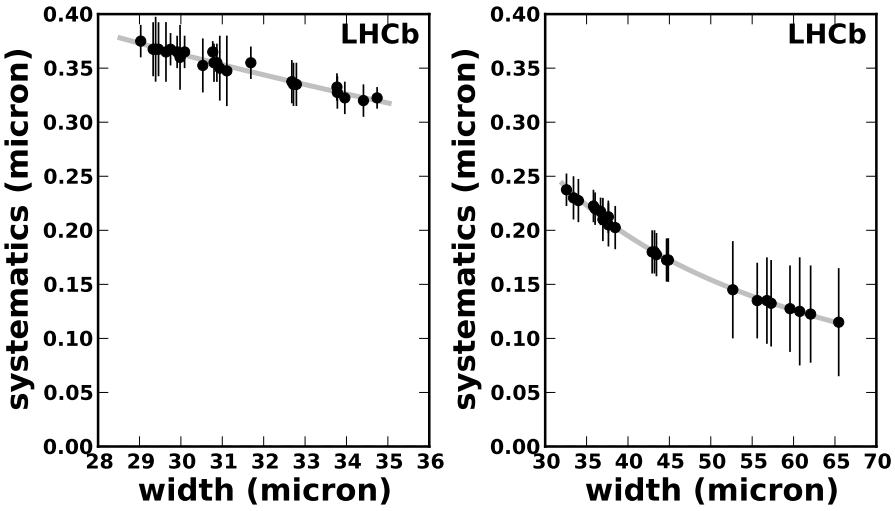

Figure 7.13: Systematic error of the resolution, obtained as the difference between the luminous region widths obtained with the upper and lower extremes of the vertex resolution, versus the width obtained with the parametrisation using the central values for the resolution. The x-coordinate is shown on the left and the y-coordinate - on the right. The error bars indicate the statistical error of the individual fits; the statistical error in the determination of the systematic error is much smaller owing to the fully correlated data-sets. The parametrisation of the systematics is shown as a shaded line.

An independent cross-check of the resolution using the *beam-beam imaging* method [62] is discussed in [10].

7.5.2 Crossing angle effects

The expression for the luminosity (Eq. (7.1)) contains a correction factor for the crossing angle C_α, which has the form given in Eq. (7.11) [79]. For a vanishing crossing angle and equal bunch lengths, the longitudinal beam size σ_z is obtained from the beam spot assuming that the two beams have equal size, by $\sigma_z = \sqrt{2}\sigma_{\otimes z}$. In the presence of a crossing angle the measured length of the luminous region depends on the lengths of the bunches, the crossing angle and the transverse widths of the two beams in the plane of the crossing angle. The bunch lengths need not necessarily be equal. Evaluating the overlap integral of the two colliding bunches over the time of the bunch crossing, one finds for the luminous length:

$$\sigma_{\otimes z} = \left[\frac{\tan^2 \alpha}{\sigma^2_{\otimes x}} + \frac{4 \cos^2 \alpha}{\sigma^2_{1z} + \sigma^2_{2z}} \right]^{-\frac{1}{2}} \tag{7.13}$$

Solving for $\sigma_{1z}^2 + \sigma_{2z}^2$, the right-hand side of Eq. (7.11) can be written in terms of the measured quantities α, $\sigma_{\otimes z}$, $\sigma_{\otimes x}$, σ_{1x}, and σ_{2x}:

$$C_\alpha = \left[1 + \frac{4\,\sin^2\alpha\,\sigma_{\otimes z}^2}{(1-(\tan\alpha\,\sigma_{\otimes z}/\sigma_{\otimes x})^2)\,(\sigma_{1x}^2+\sigma_{2x}^2)}\right]^{-\frac{1}{2}} \tag{7.14}$$

The dependence of the estimate of $\sigma_{\otimes z}$ on σ_z and of the overall correction on σ_x is shown in Fig. 7.14 for a typical value of the parameters. The difference with respect to a naive calculation assuming equal beam sizes and using the simple $\sqrt{2}$ factor to obtain the bunch lengths from the luminous region length is in all relevant cases smaller than 1%. For the beam conditions in May 2010 the value of the crossing angle correction factor C_α is about 0.95 (see Table 7.3). To take into account the accuracy of the calculation conservatively a 1% systematic error is assigned to this factor.

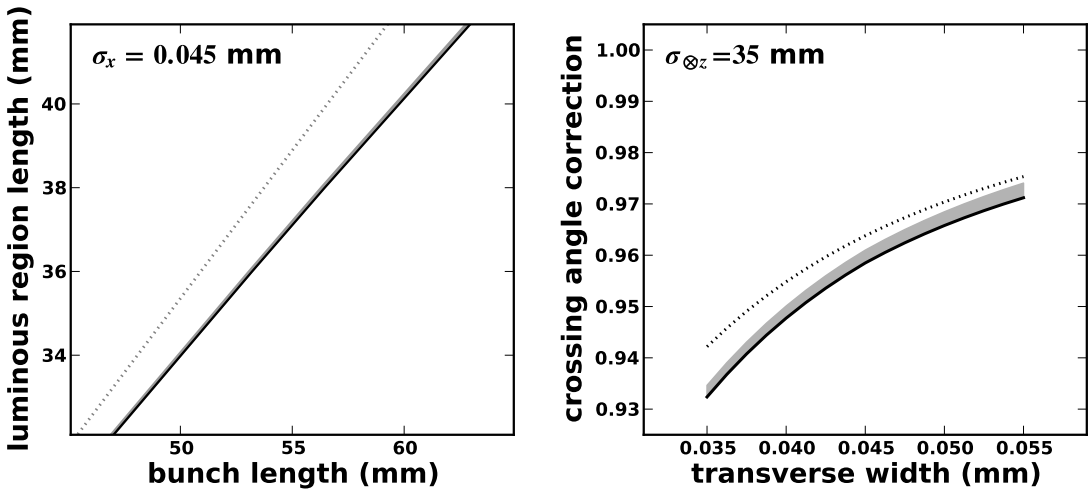

Figure 7.14: Left panel: the dependence of the length of the luminous region $\sigma_{\otimes z}$ on the single bunch length σ_z under the assumption that both beams have equal length bunches. The dotted line shows the $\sqrt{2}$ behaviour expected in the absence of a crossing angle. The solid black line shows the dependence for equal transverse beam sizes $\sigma_x = 0.045$ mm, the shaded region shows the change for $\rho = 1.2$ keeping the average size constant. Right panel: the dependence of the luminosity reduction factor C_α on the transverse width of the beam σ_x for a value of $\sigma_{\otimes z} = 35$ mm. The solid line shows the full calculation for $\rho = 1$ (equal beam widths) with the shaded area the change of the value up to $\rho = 1.2$, keeping the transverse luminous region size constant. The dotted line shows the result of the naive calculation assuming a simple $\sqrt{2}$ relation for the length of the individual beams. All graphs are calculated for a half crossing angle $\alpha = 0.2515$ mrad.

There are other small effects introduced by the beam angles. The average angle of the beams is different from 0 in the LHCb coordinate system. This small difference introduces a broadening of the measured transverse width of the luminous region, since the projection is taken along the nominal z axis of LHCb. Another effect is more subtle. The expression for the width of the luminous region (Eq. (7.2)) assumes a vanishing

crossing angle. It is still valid for any crossing angle if one considers the width for a fixed value of z. When applying Eq. (7.2) as a function of z one can show that the centre of the luminous region is offset if in the presence of a non-vanishing crossing angle the widths of the two beams are not equal. Thus, when these two conditions are met, the luminous region is rotated by an angle given by ($i = x, y$):

$$\tan\phi_i = \tan\alpha_i \frac{1-\rho_i^2}{1+\rho_i^2} \ , \tag{7.15}$$

where $\rho_i = \sigma_{2i}/\sigma_{1i}$. With the parameters observed in this analysis the effect of this rotation is smaller than 10^{-3}.

7.5.3 Bias due to unequal beam sizes and beam offsets

According to Eq. (7.9), the overlap integral for two bunches colliding with no offset and zero crossing angle can be expressed as a function of the transverse width of the beam spot $\sigma_{\otimes i}$ and the ratio of the widths of the two bunches ρ_i ($i = x, y$). Owing to the high statistics of inelastic pp interactions, the value of $\sigma_{\otimes i}$ is the best measured quantity entering the overlap integral. The measurement of the bunch-width ratio is associated with larger statistical uncertainty. When the colliding bunches in a pair have similar, but non-equal, widths the "ρ-correction" factor[✠] $2\rho/(1+\rho^2)$ is close to unity, but can only take values smaller than one (see Fig. 7.15a). Thus, when the precision of measuring ρ is similar to its difference from unity, the experimental estimate of the ρ-factor is biased towards smaller values. In the present case the deviation from unity is compatible with the statistical error of the ρ measurement for each colliding bunch pair. These values are typically 15% in the x coordinate and 10% in the y coordinate.

The bias is estimated as the difference between the ρ-factor calculated for a given ρ_0 and the average of the ρ-factors calculated for Gaussian-distributed ρ-values centred at ρ_0 and with spread corresponding to the uncertainty of the ρ-measurement. In this way the magnitude of the ρ-factor bias is estimated to be about 1% in x and 0.5% in y (see Fig. 7.15b).

A similar situation occurs for the offset factor for non head-on colliding bunches (see **T** correction factor, defined in (7.10)). The offsets are also in this case compatible with zero within the statistical errors and the correction can only take values smaller than one. The *offset* bias can be estimated as in the case of width-ratio bias described above. The variation of the offset correction and the associated bias are shown in Fig. 7.16 as function of the offset. The average expected offset bias is approximately half of the magnitude of the width-ratio bias effect.

Since these four sources of bias (ρ and offset in both transverse coordinates) act in the same direction, their overall effect is no longer negligible and is corrected for on a bunch-by-bunch basis. We assume a systematic error equal to half of the correction, *i.e.*

[✠] This is the term in Eq. (7.9), which involves ρ, multiplied by 2.

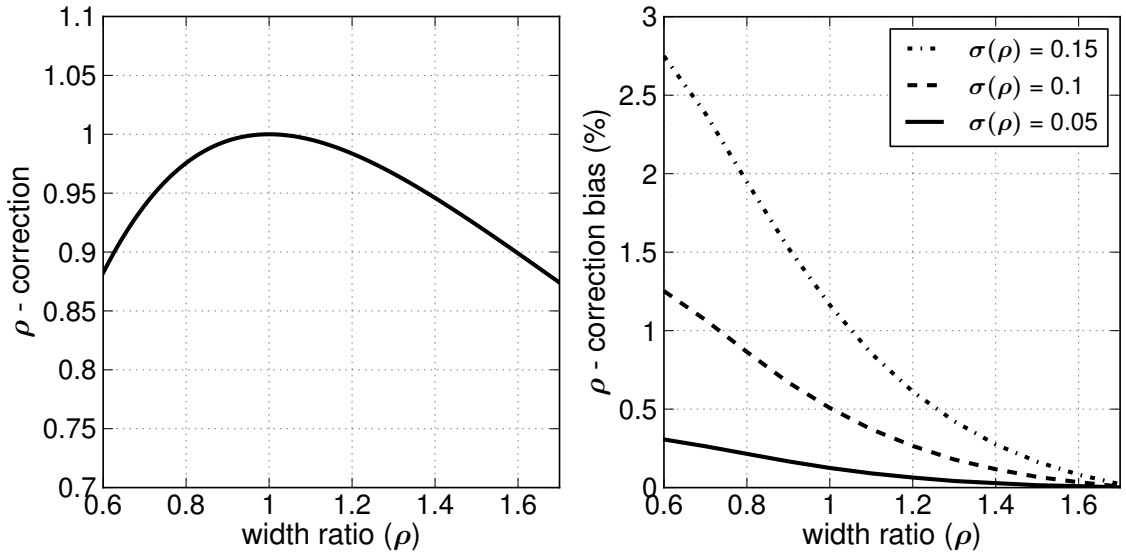

(a) (b)

Figure 7.15: (a) Dependence of the ρ-correction factor on ρ. (b) Bias in the estimated ρ-correction as function of ρ. As indicated by the different lines, the bias is bigger when the uncertainty in the ρ measurement is larger.

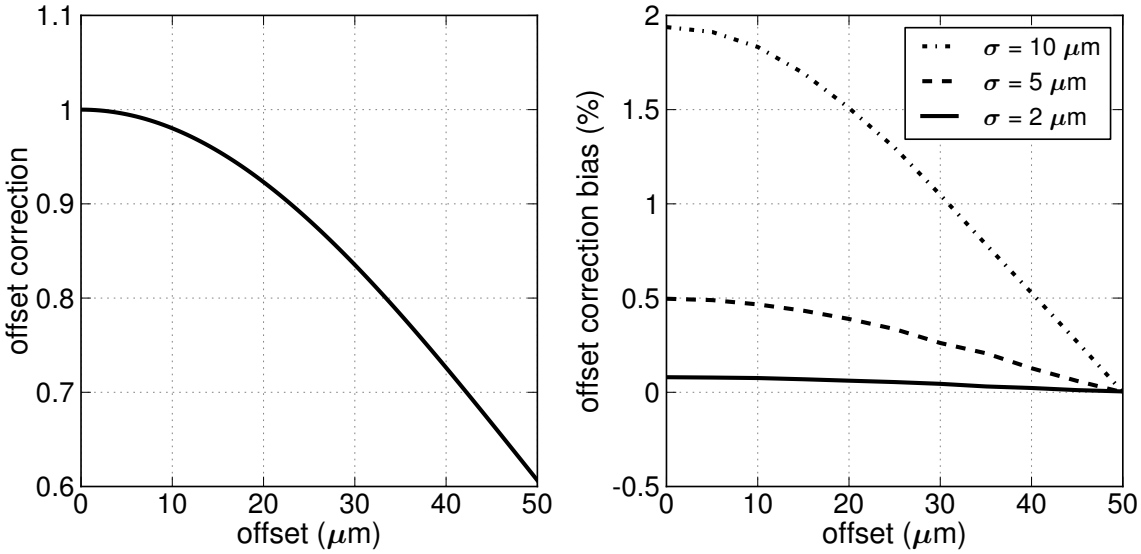

(a) (b)

Figure 7.16: (a) Dependence of the offset correction factor on the offset of the two beams. (b) Bias in the estimated offset correction as function of the offset. As indicated by the different lines, the bias is bigger when the uncertainty (σ) of the measured beam width and offset is larger. For the calculations we assumed $\sqrt{\sigma_1^2 + \sigma_2^2} = 50$ μm.

typically 1.5%. The correction and the associated uncertainty depend on the measured central value and its statistical precision and therefore vary from fill to fill.

7.5.4 Time dependence and stability

The beam and data-taking stability are taken into account when selecting suitable fills to perform the beam-gas imaging analysis. This is an essential requirement given the long integration times needed to collect sufficient statistics for the beam-gas interactions. A clear beam-intensity decay and emittance growth is observed over these long time periods. It is checked that these variations are smooth and that the average position and size of the luminous region is a good approximation to be used together with the average beam profiles measured with vertices of beam-gas interactions. As an example, the time variation of the transverse position and width of the luminous region of one colliding bunch pair is shown in Fig. 7.17. The data shown correspond to a period of 5 hours during fill 1104. This fill contains two stable periods which have been analyzed separately. One observes a smooth decrease of the beam intensities and a smooth increase of the widths of the luminous region translating into a decrease of the luminosity. No significant movement of the luminous region is observed, consistent with the general impression of a very stable central orbit maintained by the LHC machine.

The time variation of quantities determining the interaction rate of the same bunch pair from fill 1104 are shown in Fig. 7.18. In this figure it is clear that the variation of *specific* μ_{VELO}, *i.e.* the ratio of μ_{VELO} and beam intensity product is explained within a precision of a few percent by the increase of the luminous region alone. Thus, the effect of any possible drift in the mis-alignment of the two beams or different emittance growth of the two beams is small.

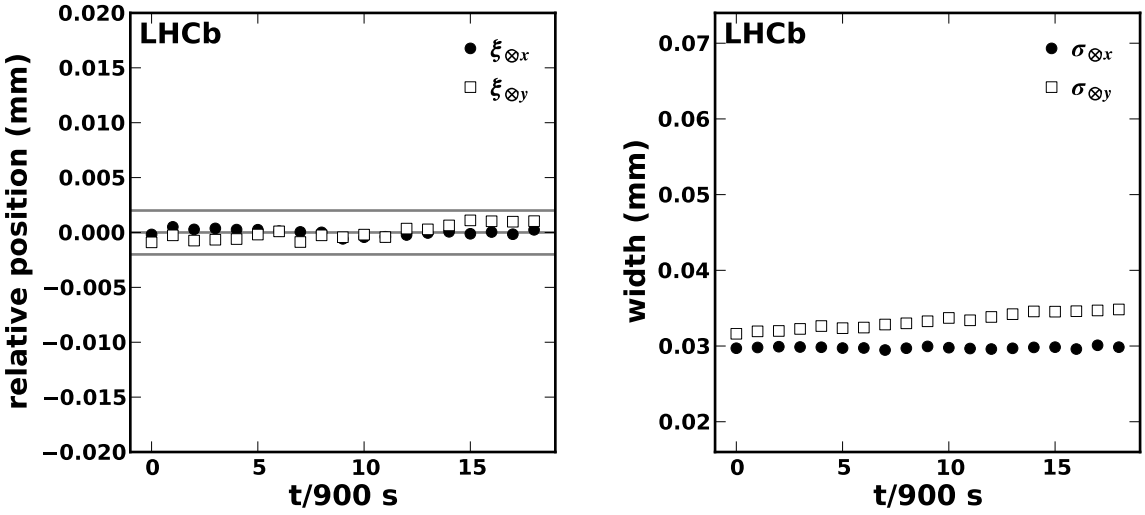

Figure 7.17: Time dependence of the mean position of the luminous region (left) and the width of the luminous region (right) during a 5 hour period in fill 1104 for one colliding bunch pair. The horizontal coordinate is shown as full circles and the vertical coordinate as open squares.

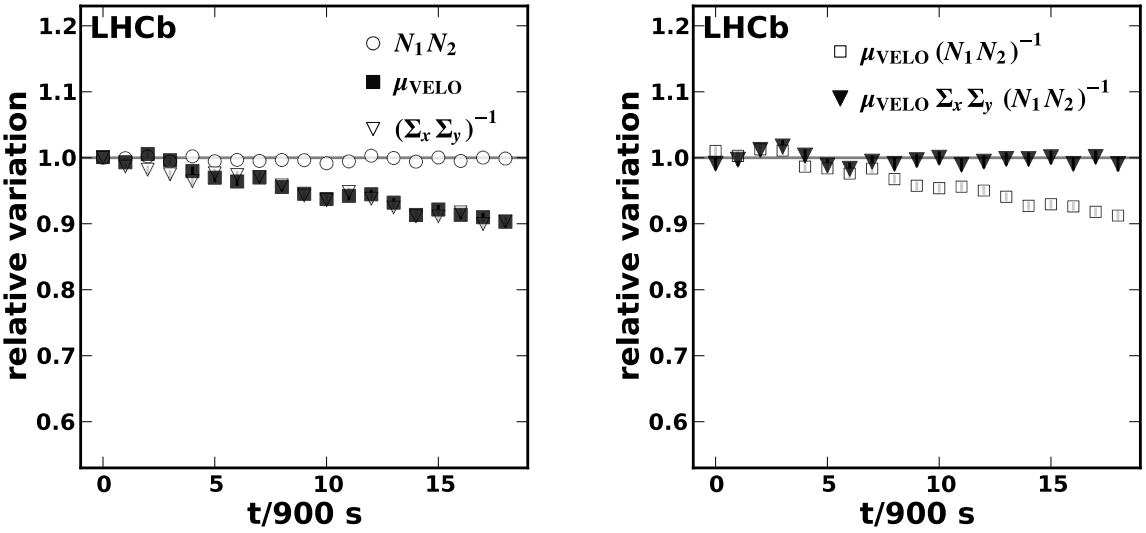

Figure 7.18: Left panel: beam intensity product (open circles), observed $\mu_{\rm VELO}$ (full squares) and overlap integral of the two bunches $A_{\rm eff}^{-1}$, calculated with (7.8) (open triangles). Right panel: time dependence of the $\mu_{\rm VELO}/(N_1\,N_2)$ (open squares) and $\mu_{\rm VELO}$ normalised by $A_{\rm eff}^{-1}$ and the beam intensity product $N_1\,N_2$ (full triangles). All trends are normalised to unity in the beginning of the period and shown for a 5 hour period in fill 1104 for one colliding bunch pair.

With the interpolation and averaging procedure explained above, systematics introduced by these variations errors are minimised and are estimated to amount to less than 1%.

7.5.5 Gas pressure gradient

The BGI method uses the interactions of the beams with the residual gas to produce an image of the beam profiles. In case of non-uniformity of the gas pressure in the plane transverse to the beam direction, the obtained image will be distorted with respect to the true one. Therefore for the luminosity measurement with the BGI method it is important to know the level of inhomogeneity of the residual gas and to take into account its effect on the measured overlap integral.

A measurement of the residual gas homogeneity is performed by displacing the beams and recording the rate of beam-gas interactions at these different beam positions. Figure 7.19 shows the results of these measurements made during fill 1422 for displacements in the x coordinate with a maximum difference 0.3 mm. The slope of the summed beam1-gas and beam2-gas rates, obtained from a straight line fit to the measured rates is 0.14 ± 0.17 Hz/mm. A 95% CL upper limit of 0.62 Hz/mm is set for the gradient.

Using these measurements we evaluate the relative variation of the overlap integral δ_I for the cases with and without gas inhomogeneity. We consider the simple case of two Gaussian bunches with equal transverse widths (σ) for both beams and in both transverse coordinates, and colliding with no offset and zero crossing angle. When the profiles of beam1-gas and beam2-gas interactions are used *directly* to determine

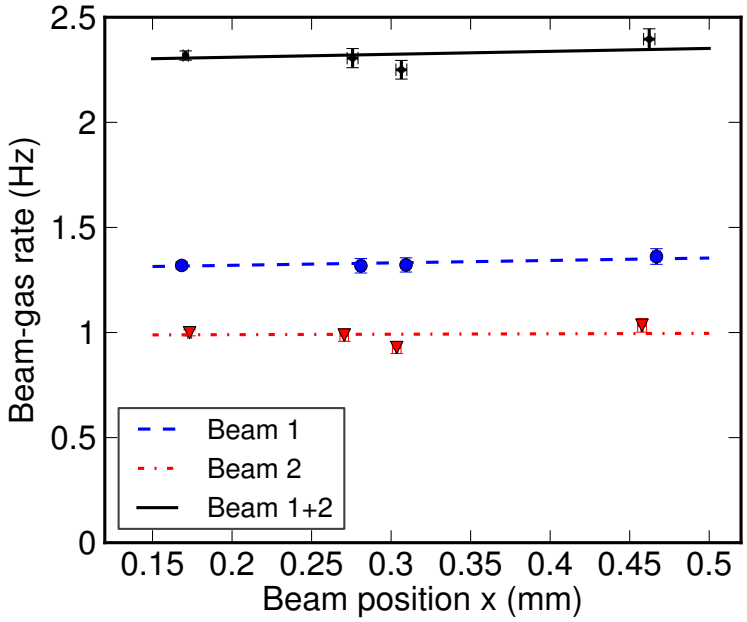

Figure 7.19: Measurement of the rate of beam-gas events as function of beam displacement for beam1 (dashed line and full circles), beam2 (dash-dotted line and triangles) and their sum (solid line and diamonds). The lines show a linear fit to the data points.

the overlap integral for the cases with and without pressure gradient, $I(a \neq 0)$ and $I(a = 0)$, the relative variation of the overlap integral is:

$$\delta_I = \frac{I(a \neq 0) - I(a = 0)}{I(a = 0)} = \frac{a^2\,\sigma^2}{2\,b^2}\ , \tag{7.16}$$

where a is gas pressure gradient and b the base rate. For this calculation we use bunch profiles of the form $G^y_{1,2}(y) = b\,G_0(y)$, and $G^x_{1,2}(x) = b\,G_0(x)$ for the case of no pressure gradient and $G^x_{1,2}(x) = (ax + b)\,G_0(x)$ for the case with pressure gradient. G_0 are normal Gaussians centred at zero and having the same width σ.

With the measured limit on the gradient, the maximum relative effect on the overlap is then estimated to be less than 4.2×10^{-4} ‡. In addition, the BGI method uses the width of the luminous region measured using *pp* interactions as a strong constraint. The gas pressure gradient does not affect the measurement of the luminous region and in practice it enters the luminosity calculation only through the measurements of the individual widths, which are mainly used to determined the ratio between the two beams. These are equally affected, thus, the overall effect of an eventual gas pressure gradient is much smaller that the estimate from Eq. (7.16) and can safely be neglected in the analysis.

‡ This calculation uses $a = 0.62$ Hz/mm, $\sigma = 0.1$ mm and $b = 2.14$ Hz.

7.6 Results of the beam-gas imaging method

With the use of the beam-gas imaging method we performed seven independent measurements of an effective reference cross-section. As in the case for the VDM measurements, we determine the cross-section for producing at least two tracks in the VELO, σ_{VELO}.

Some values relevant for the effective cross-section determination with the BGI method are shown in Table 7.3 for each colliding bunch pair used in the analysis. The beam currents, needed for the BGI method as an essential ingredient, are obtained following the same procedure as described in [75] (see Chapter 5).

The main uncertainties contributing to the overall precision of the cross-section measurement come from the measurement of the beam intensity product and the determination of the beam overlap integral. The bunch intensity normalisation error has components from the DCCT scale, the DCCT baseline fluctuations and FBCT offsets. The systematic error in the overlap integral is the quadratic sum of the effect of the resolution uncertainties, the treatment of the time dependence, the treatment of the bias due to the non-linear dependencies in ρ and $\Delta(\xi)$, and the crossing angle corrections. It also takes into account small deviations of the beam shape from a single Gaussian observed in the VDM scans. An additional systematic uncertainty is assigned to the measurement of the relative luminosity.

Each colliding bunch pair provides a self-consistent effective cross-section determination. The consistency of each of these measurements is shown in Fig. 7.20. The error bars are the combined errors with the end-marks indicating the uncorrelated errors. Some fill-related systematics are visible, as expected from the size of the correlated errors.

For multi-bunch fills the results for the cross-sections determined from each colliding bunch-pair are averaged, taking the correlations into account. The results of the averaging procedure, applied on a per-fill basis are shown in Fig. 7.21 and summarised in Table 7.4. The second column in the latter table provides information which errors are treated as correlated or uncorrelated between the bunches inside a fill and between the different fills.

Inside a fill, the FBCT offset uncertainty is treated taking into account the fact that the sum is constrained. The correlation between the individual bunch-to-bunch errors is not known, because we do not know exactly the absolute scale of the FBCT error, and because the bunch positions, bunch lengths and the satellite content can influence the FBCT measurements. We use an approximate procedure to propagate the errors from the individual bunch pairs to find the error of the average between bunches. The result of this calculation shows that by combining n_{b} bunch pairs, the FBCT error reduces by $n_{\mathrm{b}}^{-0.2}$. With this procedure the fill-to-fill variations of the cross-section (after subtracting the common scale errors) are consistent with the standard deviation of the individual cross-section measurements. An independent toy Monte Carlo study showed results compatible with the ones obtained with the approximate

Table 7.3: Values relevant for the measurement of the effective cross-section using the BGI method, measured per bunch. The first column shows the fill and bunch number, the second and third - the width of the luminous region in the x and y coordinates in μm, the fourth and fifth - the values of ρ, the sixth and seventh - the values of $\Delta\xi$ normalised to Σ, the eighth and ninth - the corrections due to the ghost charge and the crossing angle in %, and the last column - the average value of the product of the bunch intensities in units of 10^{20} charges.

fill - bunch	$\boldsymbol{\sigma_x}$ ($\boldsymbol{\mu}$m)	$\boldsymbol{\sigma_y}$ ($\boldsymbol{\mu}$m)	$\boldsymbol{\rho_x}$	$\boldsymbol{\rho_y}$	$\boldsymbol{\Delta\xi_x/\Sigma_x}$	$\boldsymbol{\Delta\xi_y/\Sigma_y}$	$\boldsymbol{1-f_{\mathrm{g}}}$ (%)	$\boldsymbol{1-f_{\mathrm{c}}}$ (%)	$\boldsymbol{N_1N_2}$ ($\boldsymbol{10^{20}}$)
1089 - 1786	30.49	35.53	1.20	1.21	0.19	-0.00	1.40	7.38	3.95
1090 - 1786	31.40	35.25	1.26	1.12	0.07	0.05	1.30	5.07	3.65
1101 - 2674	34.49	36.15	1.14	1.16	-0.30	-0.02	2.00	3.94	4.98
1101 - 2109	33.51	37.05	1.16	1.00	-0.29	-0.13	2.00	4.20	4.91
1104A- 2186	28.75	32.01	1.06	1.32	0.08	-0.06	1.20	6.80	4.98
1104A- 1986	29.61	32.88	1.14	1.00	0.15	-0.15	1.20	6.13	4.83
1104A- 1786	29.46	33.45	1.25	1.12	-0.01	-0.03	1.20	6.06	4.94
1104B- 2186	29.77	36.36	1.19	1.20	0.12	-0.04	1.20	8.08	4.84
1104B- 1986	30.46	37.05	1.13	1.18	0.11	-0.04	1.20	7.69	4.71
1104B- 1786	30.51	37.86	1.10	1.13	0.11	0.02	1.20	7.68	4.82
1117 - 2186	33.44	44.23	1.16	1.09	0.05	-0.12	0.75	3.44	4.83
1117 - 1986	34.08	44.52	1.04	1.06	0.09	-0.13	0.75	3.47	4.93
1117 - 1786	33.62	44.52	1.08	1.21	0.18	-0.21	0.75	3.54	4.40
1118 - 2186	32.40	42.45	1.09	1.20	-0.28	-0.20	1.10	3.76	4.87
1118 - 1986	32.47	42.91	1.03	1.16	-0.13	-0.13	1.10	3.72	4.70
1118 - 1786	32.43	42.73	1.24	1.30	-0.04	-0.14	1.10	3.53	4.97
1122 - 0995	28.98	52.27	1.07	1.56	0.07	0.20	0.70	4.49	3.92
1122 - 0895	28.97	57.40	1.34	1.14	0.07	-0.09	0.70	4.04	4.97
1122 - 2086	29.59	63.67	1.01	1.03	-0.04	0.07	0.70	4.38	4.74
1122 - 1986	29.24	60.72	1.00	1.01	-0.05	0.12	0.70	4.50	4.69
1122 - 1886	30.67	68.91	1.25	1.11	0.06	-0.04	0.70	3.89	4.42
1122 - 1786	30.54	61.87	1.06	1.19	-0.15	0.17	0.70	4.02	4.29
1122 - 1195	29.09	56.56	1.11	1.24	0.08	0.03	0.70	4.54	5.11
1122 - 1095	30.14	58.41	1.18	1.20	-0.10	-0.04	0.70	4.15	5.20

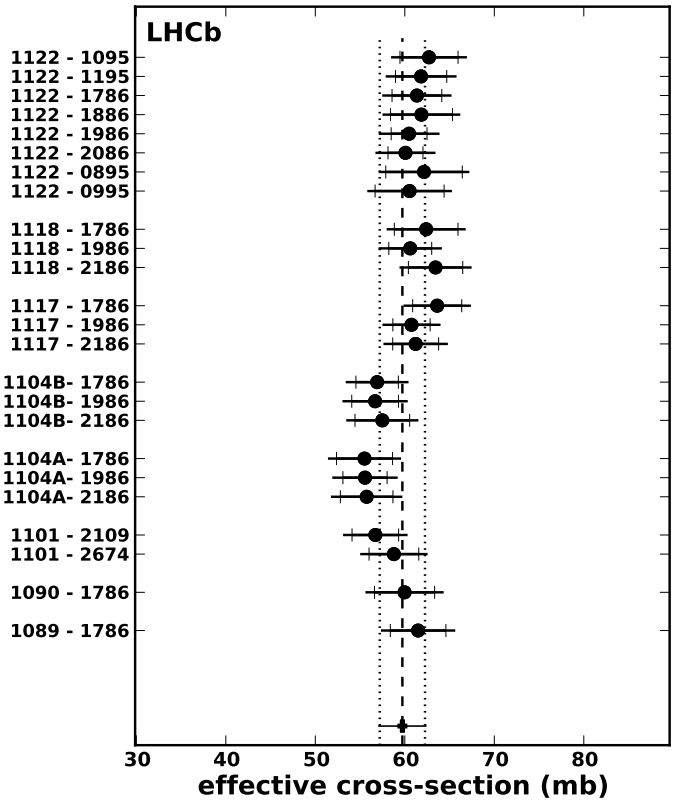

Figure 7.20: Results of the beam-gas imaging method for the effective visible cross-section of the interaction producing at least two r-z VELO tracks. The results are shown for each colliding bunch pair separately. The vertical scale label indicates the fill and bunch number. The error-bar mark of each measurement separates the uncorrelated from the total uncertainty. The dashed vertical line and the marker at the bottom indicate the weighted average. The bottom error bar corresponds to its total error. The dotted vertical lines show the standard deviation of the data points.

procedure mentioned above. The study takes into account the fact that in each beam the bunch intensity sum is constrained, to estimate the relative variation of the average cross-section after shifting all FBCT measurements with a fixed amount (FBCT offset). A strong dependence of the obtained power parameter on the Monte Carlo inputs was observed. Choosing different fraction of colliding bunches or bunch intensity spread the power parameter varied roughly between -0.4 and -0.2. The exact bahaviour of the FBCT error scaling in fills with multiple colliding bunches has small importance as the total fill-averaged FBCT uncertainty contributes only 5% to the total cross-section error (in quadrature). The results given in this thesis assume $n_{\mathrm{b}}^{-0.2}$ behaviour of the average FBCT error.

On a fill-by-fill basis the statistics, DCCT baseline noise, ghost charge and FBCT offset are treated as uncorrelated errors. Their quadratic sum is given in Table 7.4 in the row labeled "Weight". The DCCT baseline noise and the ghost charge are treated as correlated when bunches within one fill are combined. The average across fills of each uncorrelated error is calculated as the "canonical" error of a weighted average, *i.e.*

$1/\sigma^2 = \sum_{i=1}^{7} 1/\sigma_i^2$. The total uncorrelated error in each fill (the row labeled "Weight") is used as a weight to calculate the weighted average of the correlated errors across fills (the correlated errors are used as "values" in the weighted average).

Finally, the independent cross-section measurements in each fill are averaged, taking all correlations into account. The final beam-gas result for the effective cross-section is: $\sigma_{\mathrm{VELO}} = 59.9 \pm 2.7$ mb. The uncertainty without the DCCT scale error and the relative luminosity normalisation is 2.2 mb. The latter combination of uncertainties is in common with the VDM method.

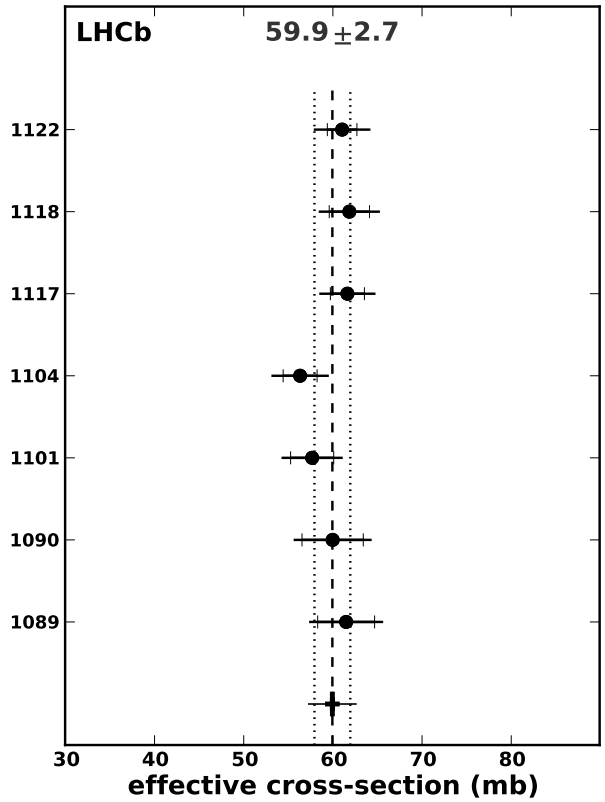

Figure 7.21: Results of the beam-gas imaging method for the effective visible cross-section of the interaction producing at least two r-z VELO tracks. The results for each fill are obtained by averaging over all colliding bunch pairs. The error-bar mark of each measurement separates the uncorrelated from the total uncertainty. The dashed vertical line and the marker at the bottom indicate the weighted average. The bottom error bar corresponds to its total error. The dotted vertical lines show the standard deviation of the data points. The observed spread is in good agreement with the expectations from the uncorrelated errors.

Table 7.4: BGI method effective cross-section measurements per fill and overall average (third column). All errors are quoted as percent of the values. The error components are labelled in the second column by *u*, *f* or *c* depending on whether they are uncorrelated between bunches and fills, correlated between bunches and uncorrelated between fills, or fully correlated between bunches and fills, respectively. The grouping of the systematic errors into (partial) sums is expressed as an indentation in the first column of the table. *Statistics* is the error from the fits to the transverse beam distributions. The *Overlap syst* row is the combination of *Crossing angle* (uncertainties in the crossing angle correction) and *Width syst*, which is a combination of *Resolution syst* (the systematic error in the vertex resolution for pp and beam-gas events), *Trend syst* (treatment of time-dependence) and *Bias syst* (ρ and offset biases). The overall *Beam normalisation* error is obtained from the uncertainties of the *DCCT scale*, *DCCT baseline*, *Ghost charge* and *FBCT offset*. *Relative lumi* is the error associated to the stability of the relative normalisation. *Weight* is calculated as the quadratic sum of *Statistics*, *DCCT baseline*, *Ghost charge* and *FBCT offset*, and is used in the averaging of the correlated errors. *Total Systematics* is the combination of *Overlap syst*, *Beam normalisation*, and *Relative lumi*, and can be broken down into *Uncorrelated systematics* and *Correlated systematics*. The *Total* error is the combination of *Statistics* and *Total Systematics*. Finally, *Excluding norm* is the uncertainty excluding the overall normalisation errors: *DCCT scale* and *Relative lumi*.

		average	**1089**	**1090**	**1101**	**1104**	**1117**	**1118**	**1122**
Cross-section (mb)		**59.94**	61.49	59.97	57.67	56.33	61.63	61.84	61.04
Statistics	u	0.96	4.06	4.73	3.09	2.56	1.89	2.66	1.82
Overlap syst		3.35	3.33	3.58	3.21	3.70	3.00	3.15	3.49
Crossing angle	c	1.00	1.00	1.00	1.00	1.00	1.00	1.00	1.00
Width syst		3.20	3.18	3.43	3.05	3.56	2.83	2.99	3.34
Resolution syst	c	2.56	2.79	2.74	2.54	2.86	2.37	2.47	2.44
Trend syst	c	1.00	1.00	1.00	1.00	1.00	1.00	1.00	1.00
Bias syst	c	1.61	1.14	1.81	1.35	1.89	1.19	1.35	2.05
Beam normalisation		2.88	4.21	4.21	3.91	3.48	3.65	3.67	3.37
DCCT scale	c	2.70	2.70	2.70	2.70	2.70	2.70	2.70	2.70
DCCT baseline	f	0.10	0.97	1.01	0.43	0.29	0.29	0.29	0.14
Ghost charge	f	0.19	0.70	0.65	1.00	0.60	0.38	0.55	0.35
FBCT offset	f	0.91	3.00	3.00	2.61	2.10	2.41	2.41	1.98
Relative lumi	c	0.50	0.50	0.50	0.50	0.50	0.50	0.50	0.50
Weight		1.38	5.19	5.73	4.19	3.38	3.10	3.64	2.72
Total Systematics		4.45	5.39	5.55	5.08	5.11	4.75	4.87	4.88
Uncorrelated syst	f	0.93	3.23	3.23	2.83	2.20	2.46	2.49	2.02
Correlated syst	c	4.33	4.32	4.51	4.22	4.61	4.07	4.18	4.44
Total		4.55	6.75	7.29	5.95	5.71	5.11	5.55	5.20
Excluding norm		3.63	6.17	6.75	5.28	5.01	4.31	4.82	4.42

Chapter 8

Conclusion

In 2010 two direct methods are used for the absolute luminosity normalisation at LHCb. The measurement performed with the van der Meer scan method using dedicated fills in April 2010 and October 2010 has an overall relative uncertainty of 3.6% (see Table 6.8). The final VDM result is based on the October data alone which give significantly lower systematic uncertainties. The beam-gas imaging method is applied on data collected in May 2010 using the residual gas pressure and provides an absolute luminosity normalisation with uncertainty of 4.6% (see Table 7.4). There is a good agreement between the effective cross-section measurements with the two methods (see Table 8.1). Whereas the VDM data have been taken during dedicated fills, no dedicated data-taking periods have yet been set aside for the BGI method. It is therefore remarkable that this method can reach a comparable precision.

The common DCCT scale error represents a large part of the overall uncertainty for the results of both methods and is equal to 2.7%. To determine the average of the two results the common scale is removed before calculating the relative weights. Table 8.1 shows the ingredients and the results of the averaging procedure. The combined result has a 3.4% relative error. Since the data-sets used for physics analysis contain

Table 8.1: Averaging of the VDM and BGI results and additional uncertainties when applied to larger data-sets.

	Average	**VDM**	**BGI**
Cross-section (mb)	58.8	58.4	59.9
DCCT scale uncertainty (%)	2.7	2.7	2.7
Uncorrelated uncertainty (%)	2.0	2.4	3.7
Cross-section uncertainty (%)	3.4	3.6	4.6
Relative normalization stability (%)	0.5		
Use of average value of μ_{vis} (%)	0.5		
Additional uncertainty for other data-sets (%)	0.7		
Total uncertainty for large data sets (%)	3.5		

only a subset of all available information (see Chapter 4), a small additional error is introduced *e.g.* by using μ_{vis} information averaged over bunch crossings. Together with the uncertainty introduced by the long term stability of the relative normalization this results in a final uncertainty in the integrated luminosity determination of 3.5%. The conservative approach has been taken to assign a 0.5% uncertainty representing the relative normalisation variation to all data-sets and not to single out one specific period as reference.

The results of the presented absolute luminosity normalisation measurements are published in [10], where in addition, a cross-check of the cross-section results is performed using a recently proposed complementary approach [62].

The results of the absolute luminosity measurements are expressed as a calibration of the visible cross-section σ_{vis}. As discussed in Section 1.1.2, this calibration is used to determine the cross-sections of different reactions in pp collisions at $\sqrt{s} = 7$ TeV. In particular, the inclusive ϕ cross-section measurement [24] uses the absolute luminosity calibration presented in this thesis.

The relative normalization and its stability have been studied for the data taken with LHCb in 2010 (see Chapter 4). Before the normalization can be used for other data-sets, an appropriate study of the relative normalization stability needs to be performed.

Next, we discuss the optimal data-taking conditions for the application of the VDM and BGI methods, and the prospects for improving the precision of the relative and absolute luminosity measurements.

The determination of the relative luminosity is sensitive to sub-detector instabilities and background coming from interactions outside the luminous region. The spill-over effects in sub-detectors used for measuring the relative luminosity lead to overestimation of the background in the bunch-crossings after bb (see Section 4.3). Such a background may change over time and therefore needs to be monitored regularly. In this respect, the LHC operation with bunches spaced at 25 ns offers additional challenge. Furthermore, special care is needed for determining the background from parasitic collisions in fills with small ($\mathcal{O}(10)$ μrad) net crossing angle in the horizontal plane. Such a situation may occur in fills where the external and the internal (induced by the LHCb dipole magnet) crossing angles cancel each other. Therefore, comprehensive systematic studies are needed of all periods of data taking in order to improve the current relative normalisation precision of 0.7% (includes the 0.5% uncertainty from the stability of the relative normalization and the 0.5% uncertainty introduced by using μ_{vis} averaged over all colliding bunches).

A significantly improved accuracy in the DCCT scale, which is the single largest uncertainty in the absolute luminosity calibration (see Tables 6.8, 7.4 and 8.1), can be expected already in 2011 (see Section 5.1). This would open the possibility for beam intensity normalisation with a precision close to 1%.

The main uncertainty in the VDM result, apart from the scale error, is given by the lack of reproducibility found between different scanning strategies. Dedicated tests will have to be designed to understand these differences better [112].

The nominal luminosity at LHCb is in the range $2 - 5 \times 10^{32}$ cm^{-2} s^{-1}. In fills with several hundred or more bunches, measures need to be taken to decrease the luminosity from the maximum achievable to the optimal one. This can be done by using broader beams ($\beta^\star$ of 3–10 m, depending on the number of colliding bunches), by displacing the beams at the interaction point (see below), or by a combination of the latter two. As can be seen from Table 7.4, the largest uncertainty in the determination of the beam overlap with the BGI method is due to the error in the vertex resolution. To reduce this uncertainty relatively larger beam sizes are necessary. The usage of large values of $\beta^\star$ such as 10 m would allow the luminosity error originating from the vertex resolution to be reduced by at least a factor of two (see Figs. 7.12 and 7.13).

In 2011 the reduction and the leveling of the LHCb luminosity is achieved with a vertical separation and regular adjustment of the distance between the beams at the interaction point ($\beta^\star = 3$ m is used). This operational procedure has the following implications for the application of the BGI method during physics fills. Firstly, the limited duration of the leveling steps (it is of the order of 10 min and depends on the luminosity lifetime) restrains the time for collecting beam-gas data at fixed beam positions, which increases the uncertainty of the measured beam positions and widths. Studies are needed on the possibility for improving the precision by combining the data collected in the different leveling steps. Secondly, the uncertainty of the luminosity coming from the uncertainty of the beam positions depends on the separation between the two beams – the larger the luminosity derivative ($dL/d\Delta y$), the larger the effect from the beam position error. The large beam separation and the frequent adjustment of their position obstruct the achievement of maximal precision with the beam-gas imaging method.

A controlled pressure bump in the LHCb interaction region would allow us to apply the beam-gas imaging method in a shorter period, at the same time decreasing the effects from the variation of the beam parameters and increasing the precision of the beam overlap measurement.

Finally, it is very advantageous to perform beam-gas measurements in the same fill as the van der Meer scans [112]. This would allow cross-checks to be made with a precision which does not suffer from intensity scale uncertainties. Furthermore, a number of parameters, such as the relative beam positions and the ratio of the sizes of the two beams, that limit the precision of the BGI method can be constrained independently using the VDM scan data. The precision of the VDM method does, in principle, not depend on $\beta^\star$. Therefore, the usage of the large values of $\beta^\star$ preferred by the BGI method would also be acceptable for the VDM method. In addition to any dedicated VDM fills, a convenient moment to perform these measurements would be the TOTEM/ALPHA runs.

The expectations are that a future combined application of the van der Meer scan and beam-gas imaging methods in a dedicated fill with the parameters outlined above can improve significantly the already achieved precision of 3.4%. Currently, the physically motivated goal of 2% on the absolute luminosity determination seems achievable, while the possibility for improving the accuracy down to the 1% level can be assessed better when the discussed measurements are performed.

Bibliography

[1] LHCb Collaboration, *The LHCb Detector at the LHC*, J. Instrum. 3 (2008) S08005, IOP and SISSA, URL.

[2] LHCb Collaboration, *Reoptimized Detector Design and Performance*, Technical Design Report, CERN-LHCC-2003-030, URL.

[3] LHCb Collaboration, *LHCb, a Large Hadron Collider beauty experiment for precision measurements of CP-violation and rare decays*, Technical Proposal, CERN-LHCC-98-004, URL.

[4] L. Evans and P. Bryant (eds.), *LHC Machine*, J. Instrum. 3 (2008) S08001, IOP and SISSA, This is an abridged version of the LHC Design Report, URL.

[5] O.S. Brüning et al. (eds.), *LHC Design Report, vol.1 The LHC Main Ring*, 2004, URL.

[6] M. Ferro-Luzzi, *Proposal for an absolute luminosity determination in colliding beam experiments using vertex detection of beam-gas interactions*, Nucl. Instrum. Methods Phys. Res. A **553** 3 (2005) 388-399, URL(CDS).

[7] LHCb Collaboraion, *Prompt K^0_S production in pp collisions at $\sqrt{s} = 0.9$ TeV*, Phys. Lett. B **693** (2010) 6980, URL(ARXIV.ORG).

[8] V. Balagura, *Luminosity measurements in the first LHCb data*, in proceedings of the 2010 Rencontres de Moriond (QCD), La Thuile, 2010, URL.

[9] P. Hopchev, *The beam-gas method for luminosity measurement at LHCb*, in Proceedings of the XLVth Rencontres de Moriond, 2010, Electroweak Interactions and Unified Theories, Moriond, p.479, URL(ARXIV.ORG).

[10] LHCb Collaboration, *Absolute luminosity measurements with the LHCb detector at the LHC*, J. Instrum. 7 (2012) P01010, IOP and SISSA, URL(ARXIV.ORG).

[11] The ATLAS Collaboration, *Luminosity determination in pp collisions at $\sqrt{s} = 7$ TeV using the ATLAS detector at the LHC*, Eur. Phys. J. C **71** (2011) 1630, URL(ARXIV.ORG).

[12] CMS Collaboration, *Measurement of CMS Luminosity*, CMS-PAS-EWK-10-004, URL.

[13] A complete review of the physics programme of each LHC experiment can be found at http://jinst.sissa.it/LHC/.

[14] J. Campbell, J. Huston, and W. Stirling, *Hard interactions of quarks and gluons: a primer for LHC physics*, arXiv:hep-ph/0611148, 2006, URL.

[15] J. Collins, D. Soper, and G. Sterman, *Factorization of Hard Processes in QCD*, arXiv:hep-ph/0409313, 2004, URL.

[16] MSTW Martin-Stirling-Thorne-Watt Parton Distribution Functions, URL.

[17] G. Altarelli and G. Parisi, *Asymptotic freedom in parton language*, Nucl. Phys. B **126** (1977) 298-318.

[18] CTEQ The Coordinated Theoretical-Experimental Project on QCD, URL.

[19] NNPDF approach to parton distribution functions, URL.

[20] R. Ellis, W. Stirling, and B. Webber, *QCD and collider physics*, Camb. Monogr. Part. Phys. Nucl. Phys. Cosmol. 8 1, 1996.

[21] K. Melnikov and F. Petriello, *Electroweak gauge boson production at hadron colliders through $O(\alpha_s^2)$*, arXiv:hep-ph/0609070, 2006, URL.

[22] A. Pich, *Quantum Chromodynamics*, arXiv:hep-ph/9505231v1, 1995, URL.

[23] R. Thorne et al., *Parton Distributions and QCD at LHCb*, arXiv:hep-ph/0808.1847, 2008, URL.

[24] LHCb Collaboration, *Measurement of the inclusive ϕ cross-section in pp collisions at $\sqrt{s} = 7$ TeV*, LHCB-PAPER-2011-007, URL.

[25] LHCb Collaboration, *Measurement of J/ψ production in pp collisions at $\sqrt{s} = 7$ TeV*, arXiv:hep-ex/1103.0423, URL.

[26] LHCb Collaboration, *Observation of J/ψ pair production in pp collisions at $\sqrt{s} = 7$ TeV*, CERN-PH-EP-2011-135, URL.

[27] LHCb Collaboration, *Measurement of the ψ(2S) production cross-section at $\sqrt{s} = 7$ TeV in LHCb*, LHCb-CONF-2011-026, URL.

[28] LHCb Collaboration, *Measurement of the Υ(1S) production cross-section at $\sqrt{s} = 7$ TeV in LHCb*, LHCb-CONF-2011-016, URL.

[29] LHCb Collaboration, *Prompt charm production in pp collisions at $\sqrt{s} = 7$ TeV*, LHCb-CONF-2010-013, URL.

[30] LHCb Collaboration, *Open charm and charmonium production at LHCb*, LHCb-PROC-2010-037, URL.

[31] LHCb Collaboration, *Measurement of $\sigma(pp \to b\bar{b}X)$ at $\sqrt{s} = 7$ TeV in the forward region*, arXiv:hep-ex/1009.2731, URL.

[32] LHCb Collaboration, W *and* Z *production at $\sqrt{s} = 7$ TeV with the LHCb experiment*, LHCb-CONF-2011-012, URL.

[33] LHCb Collaboration, *Central exclusive dimuon production at $\sqrt{s} = 7$ TeV*, LHCb-CONF-2011-022, URL.

[34] A. Martin et al., *Parton distributions for the LHC*, arXiv:hep-ph/0901.0002, 2009, URL.

[35] R. McNulty, *Potential PDF sensitivity at LHCb*, arXiv:hep-ex/0810.2550, 2008, URL.

[36] F. De Lorenzi, *PDF sensitivity studies using electroweak processes at LHCb*, in proceedings of the XVIII International Workshop DIS2010. arXiv:hep-ex/1011.4260, 2010, URL.

[37] M. Mangano, *Motivations and precision targets for an accurate luminosity determination at the LHC*, in procceedings of the LHC Workshop "Lumi Days", CERN, 2011, URL.

[38] J. Huston et al., *The PDF4LHC Working Group Interim Report*, arXiv:hep-ph/1101.0536, 2011, URL.

[39] J. Anderson, *Testing the electroweak sector and determining the absolute luminosity at LHCb using dimuon final states*, CERN-THESIS-2009-020, URL.

[40] S. Jadach, *Theoretical error of luminosity cross section at LEP*, arXiv:hep-ph/0306083, URL.

[41] See chapter 2 of G. Montagna, O. Nicrosini, and F. Piccinini, *Precision Physics at LEP*, arXiv:hep-ph/9802302, URL.

[42] A. Shamov and V. Telnov, *Precision luminosity measurement at LHC using two-photon production of $\mu^+\mu^-$ pairs*, arXiv:hep-ex/0207095, URL.

[43] TOTEM Collaboration, *TOTEM Technical Design Report*, CERN-LHCC-2004-002, URL.

[44] ATLAS Collaboration, *ATLAS Forward Detectors for Measurement of Elastic Scattering and Luminosity*, CERN-LHCC-2008-004, URL.

[45] V. Khoze et al., *Luminosity monitors at the LHC*, arXiv:hep-ph/0010163, URL.

[46] LHCb Collaboration, *Central Exclusive Dimuon Production at $\sqrt{s} = 7$ TeV*, LHCb-CONF-2011-022, URL.

[47] C. Bourrely, J. Soffer, and T.T. Wu, *Impact-picture phenomenology for $\pi^{\pm}p$, $K^{\pm}p$ and pp, $\bar{p}p$ elastic scattering at high energies*, arXiv:hep-ph/0210264, URL.

[48] U. Amaldi et al., *Precision measurement of proton-proton total cross-section at the CERN Intersecting Storage Rings*, Nucl. Phys. B **145** (1978) 367, URL(CDS).

[49] UA4 Collaboration, *Measurement of the proton-antiproton total and elastic cross sections at the CERN SPS collider*, Phys. Lett. **147**B 4-5 (1984) 392.

[50] CDF Collaboration, *Measurement of the antiproton-proton total cross section at $\sqrt{s} = 546$ and 1800 GeV*, Phys. Rev. D **50** (1994) 5550.

[51] E-811 Collaboration, *A measurement of the proton-antiproton total cross section at $\sqrt{s} = 1800$ GeV*, Phys. Lett. B **445** (1999) 419.

[52] V. Papadimitriou, *Luminosity measurements at hadron colliders*, FERMILAB-CONF-08-106-E, URL.

[53] M. Deile (TOTEM Collaboration), *The First Year at LHC: Diffractive Physics*, arXiv:hep-ex/0503042, URL.

[54] CMS Collaboration, *The CMS Experiment at the CERN LHC*, J. Instrum. 3 (2008) S08004, IOP and SISSA, URL.

[55] TOTEM Collaboration, *The TOTEM Experiment at the CERN Large Hadron Collider*, J. Instrum. 3 (2008) S08007, IOP and SISSA, URL.

[56] M. Deile et al., *Diffractive and total cross-section at the Tevatron and the LHC*, arXiv:hep-ex/0602021, URL.

[57] D. Bernard et al., *The real part of the proton-antiproton elastic scattering amplitude at the centre of mass energy of 546 GeV*, Phys. Lett. B **198** (1987) 583.

[58] W. Herr and B. Muratori, *Concept of luminosity*, in proceedings of "CERN Accelerator School 2003", URL.

[59] O. Napoly, *The luminosity for beam distributions with error and wakefield effects in linear colliders*, CERN-SL-92-34-AP, URL.

[60] C. Møller, *General properties of the characteristic matrix in the theory of elementary particles I*, K. Danske Vidensk. Selsk. Mat.-Fys. Medd. 23, 1, 1945.

[61] J. Bosser et al., *Transverse emittance measurement with a rapid wire scanner at the CERN SPS*, Nucl. Instrum. Methods A **235** (1985) 475.

[62] V. Balagura, *Notes on van der Meer Scan for Absolute Luminosity Measurement*, Nucl. Instrum. Methods Phys. Res. A **654** 1 (2011) 634-638, URL(ARXIV.ORG).

[63] S. van der Meer, *Calibration of the effective beam height in the ISR*, CERN-ISR-PO-68-31, URL.

[64] C. Rubbia, *Measurement of the luminosity of $p\bar{p}$ collider with a (generalized) Van der Meer Method*, CERN-$p\bar{p}$-Note-38, URL.

[65] G. Carboni et al., *Precise measurements of proton-antiproton and proton-proton total cross sections at the CERN Intersecting Storage Rings*, CERN-EP-84-163, URL.

[66] A. Rossi, *LHCb Vacuum Calculations*, Vacuum Technical Note 04-08, EDMS No: 458260 (2004).

[67] K. Nakamura et al. (Particle Data Group), *Data files and plots of cross-sections and related quantities in the 2010 Review of Particle Physics*, J. Phys. G **37**, 075021 (2010), URL.

[68] G. Bernardi, M. Carena, and T. Junk, *Higgs Bosons: Theory and Searches*, J. Phys. G **37**, 075021 (2010), URL.

[69] ATLAS Collaboration, *The ATLAS Experiment at the CERN Large Hadron Collider*, J. Instrum. 3 (2008) S08003, IOP and SISSA, URL.

[70] ALICE Collaboration, *The ALICE experiment at the CERN LHC*, J. Instrum. 3 (2008) S08002, IOP and SISSA, URL.

[71] C. Amsler et al. (Particle Data Group), *Accelerator physics of colliders*, Physics Letters B**667**, 1 (2008), URL.

[72] O. Sander, *Transverse emittance: Its definition, applications, and measurements*, AIP Conf. Proc. 212, p.127, 1989.

[73] J. Jowett, *Collision Schedules and Bunch Filling Schemes in the LHC*, LHC-Project-note-179, 1999, URL.

[74] R. Bailey and P. Collier, *Standard Filling Schemes for Various LHC Operation Modes*, LHC-Project-note-323, 2003, URL.

[75] G. Anders et al., *LHC Bunch Current Normalisation for the April-May 2010 Luminosity Calibration Measurements*, CERN-ATS-Note-2011-004 PERF, 2011, URL.

[76] J.J. Gras, M. Ludwig, and P. Odier, *The 2010 LHC DC BCT measurement system and its main sources of uncertainties*, CERN-LHC-Project-Note-432 (to be published), URL.

[77] D. Belohrad, J.J. Gras, and M. Ludwig, *The 2010 LHC ring Fast BCT measurement system and its main sources of uncertainties*, CERN-LHC-Project-Note-433 (to be published), URL.

[78] D. Belohrad et al., *Commissioning and First Performance of the LHC Beam Current Measurement Systems*, 1st IPAC, Kyoto, Japan, 23-28 May 2010, URL.

[79] S. White, *Determination of the absolute luminosity at the LHC*, CERN-THESIS-2010-139; LAL-10-154, URL.

[80] O. Brüning, W. Herr, and R. Ostojic, *A beam separation and collision scheme for IP1 and IP5 at the LHC for optics version 6.1*, LHC Project Report 315, 1999, URL.

[81] O. Brüning, W. Herr, and R. Ostojic, *A beam separation and collision scheme for IP2 and IP8 at the LHC for optics version 6.1*, LHC Project Report 367, 2000, URL.

[82] W. Herr, *Effects of PACMAN bunches in the LHC*, LHC Project Report 39, 1996, URL.

[83] R. Assmann et al., *LHC beam parameters for the physics run at 3.5 TeV*, LHC-OP-ES-0020 rev 3, EDMS No: 1059898 (2010), URL.

[84] R. Alemany, M. Lamont, and S. Page, *LHC modes*, LHC-OP-ES-0005-10-10, EDMS No: 865811 (2009), URL.

[85] E. Bravin et al., *Collision rate monitors for LHC*, in Proceedings of PAC07.

[86] LHCb Collaboration, *Search for the rare decays $B_s^0 \to \mu^+\mu^-$ and $B^0 \to \mu^+\mu^-$*, Phys. Lett. B **699** (2011) 330340, URL.

[87] LHCb Collaboration, *Roadmap for selected key measurements of LHCb*, LHCb-PUB-2009-029, URL.

[88] LHCb Collaboration, *LHCb RICH Technical Design Report*, CERN-LHCC-2000-037, URL.

[89] LHCb Collaboration, *LHCb Muon System Technical Design Report*, CERN-LHCC-2001-010, URL.

[90] LHCb Collaboration, *VELO Technical Design and Performance*, CERN-LHCC-2001-0011, URL.

[91] M. van Beuzekom et al., *Pile-up veto L0 trigger system for LHCb using large FPGA's*, 2002, URL.

[92] LHCb Collaboration, *LHCb inner tracker : Technical Design Report*, CERN-LHCC-2002-029, URL.

[93] LHCb Collaboration, *LHCb outer tracker : Technical Design Report*, CERN-LHCC-2001-024, URL.

[94] LHCb Collaboration, *LHCb magnet : Technical Design Report*, CERN-LHCC-2000-007, URL.

[95] E. Boss, *Reconstruction of charged particles in the LHCb experiment*, CERN-THESIS-2010-049, URL.

[96] LHCb Collaboration, *LHCb Calorimeters Technical Design Report*, CERN-LHCC-2000-036, URL.

[97] LHCb Collaboration, *LHCb Trigger Technical Design Report*, CERN-LHCC-2003-031, URL.

[98] R. Cornat, J. Lecoq, and P. Perret, *Level-0 Decision Unit for LHCb*, LHCb-2003-065, CERN, URL.

[99] R. Jacobsson, B. Jost, and Z. Guzik, *Readout supervisor design specifications*, LHCb-2001-012, CERN, URL.

[100] F. Alessio, *Beam, background and luminosity monitoring in LHCb and upgrade of the LHCb fast readout control*, CERN-THESIS-2011-047, URL.

[101] M. Ferro-Luzzi and P. Hopchev, *High-level trigger for beam-gas interactions in LHCb*, LHCb-2008-040 (internal note), 2008, URL.

[102] *HIJING Monte Carlo Model*, URL.

[103] *Gauss - the simulation program of the LHCb experiment*, URL.

[104] H. Dijkstra and O. Schneider, *Online and offline monitoring of the relative luminosity at LHCb*, LHCb-2008-034, URL.

[105] V. Balagura, *Analysis methods for luminosity data*, LHCb-INT-2009-001 (internal note), URL.

[106] G. Anders et al., *LHC Bunch Current Normalisation for the October 2010 Luminosity Calibration Measurements*, CERN-ATS-Note-2011-016 PERF, 2011, URL.

[107] C. Ohm and T. Pauly, *ATLAS beam pick-up based timing system*, Nucl. Instrum. Methods A **623** (2010) 558, URL.

[108] Y. Amhis et al., *Absolute Luminosity Measurements at* $\sqrt{s} = 7$ *TeV*, LHCb-INT-2011-018 (internal note), 2011, URL.

[109] C. Lasseur et al., *Géométrie du LHC : Points caractéristiques, Formules de Transformation*, CERN-LHC-Project-Note-95, 1997, URL.

[110] M. Ferro-Luzzi, *Luminosity and luminous region shape for pure Gaussian bunches*, LHCb-INT-2011-022 (internal note), URL.

[111] M. Ferro-Luzzi, *Definition of PU and VELO detector layout*, EDMS No: 719303 v2 (2006), URL.

[112] J. Panman, *Direct Luminosity Measurements at the LHC - summary*, in procceedings of the LHC Workshop "Lumi Days", CERN, 2011, URL.

Thesis summary

The *luminosity* of a particle collider is determined by the rate of the particlecollisions it produces. The *instantaneous* luminosity is defined as the ratio between the rate of interactions of a certain type and the cross-section (probability) for the reaction of interest. Knowledge of the instantaneous luminosity is necessary for the estimation of the expected signal and background rates, while a precise knowledge of the integrated luminosity is employed in a number of fundamental physics measurements, which allow us to improve our understanding of the theories describing the particle interactions. Also, the luminosity can be used to characterise the accelerator performance on an absolute scale.

In the first chapter of this thesis an overview is made of the possibility to constrain some of the existing hadroproduction models by measuring the cross-sections for the production of charm- and beauty-hadrons. Also, it is shown that the Drell-Yan and the electroweak-boson production measurements can be used to extract new information about the structure of the proton. The uncertainty of the absolute luminosity contributes directly to the precision of the measured cross-sections and therefore has direct impact on the possibility to achieve these new insights. Later, an overview is made of some of the most accurate direct and indirect methods for absolute luminosity determination at the The Large Hadron Collider (LHC). These include the van der Meer (VDM) and beam-gas imaging (BGI) methods which have been used for the absolute luminosity normalisation of the data taken by the LHC experiments in 2009 and 2010 [10, 11, 12].

In the second chapter an overview is given of the LHC layout, its operation and the physics goals of its experiments. Attention is drawn to technical details, operational procedures and beam instrumentation devices that play an essential role for the luminosity production and determination. These details complement the description of the LHCb detector and the analysis methods discussed in the subsequent chapters of this thesis.

The Large Hadron Collider beauty experiment (LHCb) [1, 2, 3] has been designed for indirect searches of *New Physics* through the study of rare b-hadron decays and CP-violation. Some of its core measurements aim at determining particle production asymmetries and branching fractions of specific decay channels. These rely on relative measurements which do not involve knowledge of the luminosity. However, LHCb is a forward spectrometer with a unique rapidity coverage and offers the possibility to

study the properties of particle production in hadron collisions in a hitherto unexplored kinematical region. The third chapter of this thesis begins with a brief overview of the LHCb experiment. Later are described the components which play an essential role in the absolute luminosity measurement: the tracking system, the calorimeters and the trigger system.

In an experiment, the absolute luminosity is obtained only for short periods of data-taking. To be able to perform cross-section measurements on any selected data sample, the *relative luminosity* must be measured consistently during the full period of data-taking. The systematic determination of the relative luminosity in all data-taking periods requires specific procedures to be applied in the trigger, in the data-acquisition, processing and final analysis [104]. The basic principle used in LHCb is to acquire luminosity data together with the physics data and store it in the same files. During further processing of the physics data the relevant luminosity data are kept together in the same storage entity. In this way, it remains possible to select only part of the full data-set for physics analysis and still keep the capability to determine the corresponding luminosity. The fourth chapter of this thesis describes the procedure to determine the relative luminosity at LHCb using several independent variables and methods. Also, it is outlined how these variables are measured online and how the relative luminosity information is handled during the different data-processing stages.

The second part of the thesis describes the LHCb measurements of the absolute luminosity with the VDM and BGI methods using data collected in 2010. The knowledge of the charge contained in the colliding bunches is essential for the application of both methods and therefore we start with a description of the bunch current measurements in chapter five. At the LHC, two different devices are used for the measurement of the intensity of the individual bunches. The measurements of the *fast beam current transformers* (FBCTs) are used to determine the relative populations of the individual 25 ns bunch slots, while the *DC current transformers* (DCCTs) provide absolute estimates of the charge in each of the two LHC beams. The bunch current results presented in this chapter are obtained following the prescriptions given in [75] and [106]. The individual bunch populations are obtained assuming that the sum of populations of all nominally filled bunches, as measured by the FBCT, is equal to the total beam intensities, measured with the DCCT, after subtracting a possible amount of "ghost" charge. The ghost charge is defined as the beam current not visible to the FBCT, *i.e.* the total beam current contained in all 25 ns bunch slots with populations below the FBCT threshold. In 2010 the ghost charge in the LHC beams were measured by LHCb using the ratio of the number of beam-gas interactions generated by nominally-empty and nominally-filled bunches. Chapter five of this thesis describes consecutively the DCCT, ghost-charge, FBCT and satellite bunch measurements in the fills used for absolute luminosity normalisation, and concludes with a summary of the DCCT and FBCT uncertainties.

The van der Meer scan method provides a direct determination of an effective cross-section by separating the two colliding beams and measuring a counting rate

proportional to the rate of inelastic pp interactions. Chapter six of this thesis presents the application of the VDM method at LHCb using data collected in two dedicated fills in April and October 2010. The author of this thesis has no direct contribution to the analysis leading to the absolute luminosity normalisation with the VDM method. The text in this chapter is reproduced from [10] and is included in this thesis for a comparison with the BGI method and its results.

In chapter six a description is given of the experimental conditions and the used VDM scan procedures, followed by a discussion on the effects from the varying emittance and beam intensity during the scans. Later are described the cross-section determination and the averaging of the results obtained from the different colliding bunches. Finally, the associated systematic uncertainties are addressed and the cross-section results are summarized. The results of the absolute luminosity measurements are expressed as a calibration of the effective cross-section σ_{VELO}, which corresponds to the pp collision process producing at least two tracks in the LHCb vertex detector. The measurements with the VDM method in April and October yield $\sigma_{\mathrm{VELO}} = 59.7$ and 58.4 mb, respectively. The corresponding uncertainties are 7.5 and 3.6%, in both cases dominated by the knowledge of the bunch intensity and the internal consistency of each measurement. Since the October scans provide a much reduced systematic errors compared to the April scans, the outcome of the former is retained as a final result of the VDM method.

The development of precise micro-vertex detectors opened the possibility for the application of a novel method for determining the absolute luminosity. The recently proposed beam-gas imaging method [6] relies on the vertex detection of beam-gas interactions to measure directly the geometrical properties and the overlap integral of the individual colliding bunches. The absolute luminosity can be determined by combining this information with a measurement of the bunch intensity. Chapter seven of this thesis describes the application of the BGI method for the absolute luminosity normalisation at LHCb with data collected in May 2010. The measurements presented in this chapter use the residual gas in the beam vacuum pipe as a visualising medium. At nominal conditions the expected rate of beam-gas interactions which can be reconstructed with the LHCb vertex detector is of the order of 0.1 Hz per bunch and therefore several hours of data-taking are necessary for achieving satisfactory statistical precision of the measured bunch profiles. An important prerequisite for the application of the BGI method is the knowledge of the transverse density profile of the visualising gas, as it has direct influence on the measured beam profiles. The BGI method requires a vertex resolution comparable to or smaller than the transverse beam sizes. The knowledge of the vertex resolution is necessary to unfold the resolution from the measured beam profiles. The uncertainty in the resolution also plays an essential role in determining the systematic error.

The reconstructed beam-gas interaction vertices are used to determine the beam angles, the transverse profiles of the colliding bunches and their transverse offsets at the interaction point. The simultaneous determination of the position and the size

of the *pp* luminous region provides additional constraints on the bunch parameters. These constraints allow a significant improvement to be made in the precision of the measured overlap integral. The analysis is applied for each individual colliding bunch pair, *i.e.* bunch populations, event rates and beam profiles are considered per bunch pair. Thus, each colliding bunch pair provides an internally consistent measurement of the same effective cross-section. As in the VDM measurements, the results of the absolute luminosity determination with the BGI method are expressed as a calibration of the effective cross-section σ_{VELO}. For multi-bunch fills the results for the cross-sections determined from each colliding bunch-pair are averaged, taking the correlations into account. The results in each of the seven considered fills are consistent and the observed spread is in good agreement with the expectations from the uncorrelated errors. The result for σ_{VELO} after averaging these seven measurements is 59.9 mb with a total uncertainty of 4.6%. The most dominant error sources are the beam intensity product and the knowledge of the vertex resolution.

In the concluding chapter eight the point is made that there is a good agreement between the effective cross-section measurements performed with the VDM and BGI methods in 2010 (see Table 8.1). Whereas the VDM data have been taken during dedicated fills, no dedicated data-taking periods have yet been set aside for the BGI method. It is therefore remarkable that this method can reach a comparable precision. The common DCCT scale error represents a large part of the overall uncertainty for the results of both methods and is equal to 2.7%. To determine the average of the two results the common scale is removed before calculating the relative weights. Table 8.1 shows the ingredients and the results of the averaging procedure. The combined result has a 3.4% relative error. Together with the uncertainty introduced by the long term stability of the relative normalization this results in a final uncertainty in the integrated luminosity determination of 3.5%. The results of the presented absolute luminosity normalisation measurements are published in [10]. Finally, a short discussion is presented of the optimal data-taking conditions for the application of the VDM and BGI methods, and the prospects for improving the precision of the relative and absolute luminosity measurements.

Résumé de la thèse

La *luminosité* d'un collisionneur de particules est déterminée à partir du taux de collisions de particules qu'il produit. On définit la luminosité *instantanée* comme le rapport entre le taux d'interactions pour une réaction donnée et la section efficace (probabilité) de la réaction considérée. La connaissance de la luminosité instantanée est nécessaire pour l'estimation des taux de signal attendu et de bruit de fond alors que la connaissance précise de la luminosité intégrée est utilisée dans un grand nombre de mesures de physique fondamentale qui nous permettent d'améliorer notre connaissance des théories décrivant les interactions des particules. La luminosité peut également être utilisée pour caractériser les performances de l'accélérateur.

Dans le premier chapitre de cette thèse, on donne un aperçu des possibilités de contraindre certains des modèles de hadroproduction en mesurant les sections efficaces de production des hadrons *charmés* et *beaux*. On montre également que les mesures de production du boson électrofaible et du mécanisme de Drell-Yan peuvent être utilisées pour extraire des informations nouvelles sur la structure du proton. L'incertitude sur la luminosité absolue contribue directement à la précision des sections efficaces mesurées et a donc un impact direct sur la possibilité d'atteindre ces nouvelles informations. On passe ensuite en revue quelques-unes des méthodes les plus précises pour la détermination directe et indirecte de la luminosité absolue au Grand Collisionneur Hadronique (LHC). Parmi ces dernières figurent les méthodes de van der Meer (VDM) et d'imagerie faisceau-gaz [beam-gas imaging] (BGI) qui ont été utilisées pour la normalisation absolue des données prises par les expériences au LHC en 2009 et 2010 [10, 11, 12].

Le deuxième chapitre commence par une brève description du LHC, son fonctionnement et les objectifs de physique de ses expériences. On met l'accent en particulier sur les détails techniques, les procédures opérationnelles et les dispositifs d'instrumentation des faisceaux qui jouent un rôle essentiel pour la détermination de la luminosité. Ces précisions techniques viennent en complément de la description du détecteur LHCb et des méthodes d'analyse discutées dans les chapitres suivants de cette thèse.

L'expérience LHCb (Large Hadron Collider beauty) [1, 2, 3] a été conçue pour la recherche indirecte de *Nouvelle Physique* à travers l'étude des désintégrations rares des hadrons beaux et de la violation de CP. Certaines des mesures cruciales ont pour but de déterminer les asymétries de production des particules et les rapports d'embranchement de canaux de désintégration spécifiques. Ces études reposent sur des mesures relatives

qui n'impliquent pas la connaissance de la luminosité. Cependant, LHCb est un spectromètre vers l'avant qui a une couverture en rapidité unique et qui offre la possibilité d'étudier les propriétés de la production des particules dans les collisions hadroniques dans une région cinématique jusqu'à présent inexplorée. Le chapitre 3 commence par une brève description de l'appareillage de l'expérience LHCb. On décrit ensuite plus en détail les éléments qui jouent un rôle essentiel dans la mesure de la luminosité absolue: trajectographie, calorimètres, système de déclenchement.

Dans une expérience, la luminosité absolue est mesurée seulement pendant de courtes périodes de prise de données. Pour pouvoir effectuer les mesures de sections efficaces sur n'importe quel échantillon de données, la *luminosité relative* doit être mesurée systématiquement durant la totalité de la période de prise de données. La détermination systématique de la luminosité relative dans toutes les périodes de prise de données nécessite d'appliquer des procédures spécifiques au déclenchement, à l'acquisition de données, au traitement des données et à l'analyse finale [104]. Le principe de base utilisé dans LHCb est d'acquérir en même temps les données sur la luminosité et les données de physique et de les stocker dans les mêmes fichiers. Durant le traitement ultérieur des données de physique, les données pertinentes sur la luminosité sont conservées ensemble sur le même support de stockage. De cette façon, il reste possible de sélectionner seulement une partie de l'ensemble complet des données pour une analyse de physique et d'être encore capable de déterminer la luminosité correspondante. Le chapitre 4 de la thèse décrit la procédure de détermination de la luminosité relative dans LHCb en utilisant différentes méthodes et variables indépendantes. On expose également la façon de mesurer ces variables en ligne et de traiter l'information sur la luminosité relative durant les différentes étapes du traitement des données.

La deuxième partie de cette thèse décrit les mesures de la luminosité absolue dans LHCb avec les méthodes VDM et BGI, en utilisant les données collectées en 2010. La connaissance de la charge contenue dans les paquets de protons en collision est essentielle pour l'application des deux méthodes et nous commençons donc le chapitre 5 par la description des mesures des courants des paquets de protons. Au LHC, deux dispositifs distincts sont utilisés pour la mesure de l'intensité des paquets individuels. Les mesures des *Fast Beam Current Transformers* (FBCT) sont utilisées pour déterminer les populations relatives des paquets individuels séparés par des intervalles de 25 ns tandis que les *DC Current Transformers* (DCCT) fournissent des estimations absolues de la charge dans chacun des deux faisceaux du LHC. Les résultats concernant le courant des paquets de protons présentés dans ce chapitre sont obtenus en suivant les procédures décrites dans les références [75] et [106]. Les populations d'un paquet individuel sont obtenues en supposant que la somme des populations de tous les paquets supposés *remplis*, telle que mesurées par le FBCT, est égale à la charge totale du faisceau, telle que mesurée par les DCCT, après soustraction d'une possible charge *fantôme*. La charge fantôme est définie à partir du courant du faisceau non visible par les FBCT, *c'est-à-dire*, le courant total du faisceau contenu dans tous les paquets espacés de 25 ns ayant une population inférieure au seuil des FBCT. En 2010, la charge

fantôme dans les faisceaux du LHC a été mesurée par LHCb en utilisant le rapport du nombre d'interactions faisceau-gaz générées par des paquets supposés vides à celui des interactions générés par les paquets supposés pleins. Le chapitre 5 de la thèse décrit successivement les mesures DCCT, de charge fantôme, FBCT des paquets ainsi que des paquets satellites dans les remplissages utilisés pour la normalisation absolue de la luminosité et conclut par un résumé des incertitudes sur les mesures DCCT et FBCT.

La méthode du balayage de van der Meer fournit une détermination directe d'une section efficace effective en séparant les deux faisceaux en collision et en mesurant un taux de comptage proportionnel au taux d'interactions inélastiques *pp*. Le chapitre 6 présente l'application de la méthode VDM à l'expérience LHCb en utilisant les données collectées au cours de deux remplissages spécifiques en avril et octobre 2010. L'auteur de la thèse n'a pas directement contribué à l'analyse conduisant à la normalisation de la luminosité absolue avec la méthode VDM. Le texte de ce chapitre est reproduit à partir de la référence [10] et n'est inclus dans cette thèse que pour comparaison avec la méthode BGI et ses résultats.

Le chapitre 6 commence par une description des conditions expérimentales et des procédures de balayage VDM utilisées, suivie d'une discussion sur les effets de la variation de l'émittance et de l'intensité du faisceau durant les balayages. On décrit ensuite la détermination de la section efficace la moyenne des résultats obtenus à partir des différents paquets en collision. Enfin, les erreurs systématiques sont traitées et les résultats sur la section efficace sont récapitulés. Les résultats sur les mesures de la luminosité absolue sont exprimés sous la forme d'une calibration de la section efficace effective σ_{VELO} qui correspond au processus de collision *pp* produisant au moins deux traces dans le détecteur de vertex de LHCb. Les mesures avec la méthode VDM en avril et octobre ont conduit respectivement à $\sigma_{\mathrm{VELO}} = 59.7$ et 58.4 mb. Les incertitudes correspondantes sont respectivement de 7.5% et 3.6% et sont dominées dans les deux cas par la connaissance de l'intensité des paquets et la cohérence interne des résultats. Puisque les résultats d'octobre ont des erreurs systématiques nettement plus faibles que ceux d'avril, ce sont eux qui sont finalement retenus comme résultats de la méthode VDM.

Le développement de détecteurs précis de micro-vertex a ouvert la possibilité d'appliquer une nouvelle méthode pour la détermination de la luminosité absolue. La méthode d'imagerie faisceau-gaz, récemment proposée [6] repose sur la détection du vertex des interactions faisceau-gaz pour mesurer directement les propriétés géométriques et l'intégrale de recouvrement des paquets individuels en collision. La luminosité absolue peut être déterminée en combinant cette information avec la mesure de l'intensité des paquets. Le chapitre 7 décrit l'application de la méthode BGI pour la normalisation de la luminosité absolue dans LHCb en utilisant les données collectées en mai 2010. Les mesures présentées dans ce chapitre utilisent le gaz résiduel dans la chambre à vide comme moyen de visualisation. Dans les conditions nominales, le taux attendu d'interactions faisceau-gaz qui peuvent être reconstruites avec le détecteur de vertex de LHCb est de l'ordre de 0.1 Hz par paquet et par conséquent, plusieurs heures de prise

de données sont nécessaires pour atteindre une précision statistique satisfaisante des profils de paquets mesurés. Un prérequis important pour l'application de la méthode BGI est la connaissance du profil de densité transverse du gaz servant à la visualisation car elle a une influence directe sur les profils de faisceau mesurés. La méthode BGI nécessite une résolution de vertex comparable ou plus petite que les tailles transversales des faisceaux. La connaissance de la résolution du vertex est nécessaire pour retirer les effets de la résolution des profils mesurés des faisceaux. L'incertitude sur la résolution joue également un rôle essentiel dans la détermination de l'erreur systématique.

Les vertex d'interactions faisceau-gaz reconstruits sont utilisés pour déterminer les angles des faisceaux, les profils transversaux des paquets et les décalages transversaux au point d'interaction. La détermination simultanée de la position et de la taille de la région d'interaction *pp* fournit des contraintes supplémentaires sur les paramètres des paquets. Ces contraintes permettent d'améliorer de façon significative l'intégrale de recouvrement mesurée. L'analyse est appliquée pour chaque paire de paquets en collision, *c'est-à-dire* que les populations des paquets, les taux d'événements et les profils de faisceau sont considérés par paires de paquets. Ainsi, chaque paire de paquet en collision fournit une mesure cohérente de la même section efficace effective. Comme dans les mesures VDM, les résultats de la détermination de la luminosité absolue avec la méthode BGI sont exprimés sous la forme d'une calibration de la section efficace effective σ_{VELO}. Pour des remplissages *multi-paquets*, les résultats pour la section efficace déterminés à partir de chaque paire de paquets en collision sont moyennés en tenant compte des corrélations. Les résultats pour chacun des sept remplissages considérés sont cohérents et la dispersion observée est en bon accord avec ce qui est attendu à partir des erreurs non corrélées. Le résultat pour σ_{VELO} en moyennant sur les sept mesures est 59.9 mb avec une incertitude totale de 4.6%. Les sources d'erreurs dominantes sont l'intensité du faisceau et la connaissance de la résolution du vertex.

En conclusion, dans le chapitre 8, on insiste sur le fait qu'il y a un bon accord entre les mesures de section efficace effective réalisées avec les deux méthodes en 2010: VDM et BGI (voir Table 8.1). Tandis que les données VDM ont été prises lors de remplissages spécifiques, la méthode BGI a pu être mise en œuvre pendant les prises de données normales. Il est donc remarquable que cette méthode puisse atteindre une précision comparable. L'erreur commune due au DCCT représente une grande partie de l'erreur globale sur les résultats des deux méthodes et est égale à 2.7%. Pour déterminer la moyenne des deux résultats, cette erreur commune est retirée avant de calculer les poids relatifs. La Table 8.1 montre les différents ingrédients et le résultat de la procédure pour effectuer la moyenne. Le résultat combiné a une erreur relative de 3.4%. Avec l'incertitude introduite par la stabilité à long terme de la normalisation relative, il en résulte une incertitude finale sur la détermination de la luminosité intégrée de 3.5%. Les résultats de ces mesures de la normalisation de la luminosité absolue ont été publiés dans la référence [10]. Enfin, on présente une brève discussion sur les conditions optimales de prise de données pour l'application des méthodes VDM et BGI et l'on explore les perspectives pour améliorer la précision des mesures de la luminosité relative et absolue.